

## Declaration

# Modelling to Predict the Reliability of Solder Joints

Stephen Walter Ridout

School of Computing and Mathematical Sciences,  
University Of Greenwich,  
Park Row, Greenwich,  
London, SE10 9LS,  
UK


A thesis submitted in partial fulfilment of the requirements of  
the University of Greenwich for the Degree of Doctor of Philosophy.

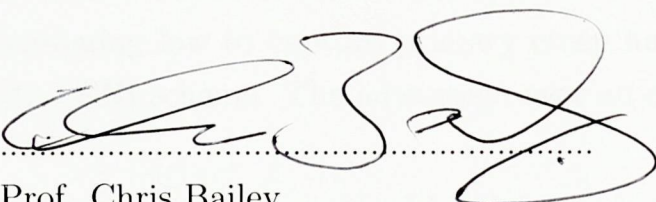
April 12, 2007

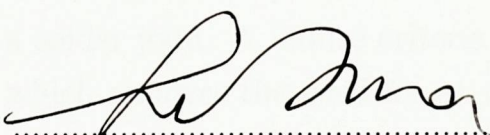


# Declaration

*I certify that this work has not been accepted in substance for any degree, and is not concurrently submitted for any degree other than that of Doctor of Philosophy (Ph.D.) of the University of Greenwich. I also declare that this work is the result of my own investigations except where otherwise stated.*

  
.....  
Stephen Ridout

  
.....  
Prof. Chris Bailey  
(Supervisor)

  
.....  
Dr. Hua Lu  
(Supervisor)



# Abstract

The work in this thesis investigates modelling methods to predict the reliability of solder joints under thermo-mechanical cycling. A literature review is presented covering analytical methods, creep laws and fatigue laws, and advanced damage mechanics methods. The use of FEA (Finite Element Analysis) to model creep along with a fatigue law to predict lifetime appears to be the most widely used and validated technique at present.

The FEA discretisation of elasticity problems is derived using the principle of minimum potential energy and implemented in the code FATMAN (Finite-element Analysis Tool, Multi-physics And Nonlinear).

A novel implicit solution scheme called LENI is proposed to allow modelling of creep in solder. The sinh law for steady-state creep and the Armstrong-Frederick kinematic hardening law to capture primary creep have been implemented in FATMAN using the LENI scheme. The advantage over an explicit discretisation is investigated.

An inverse analysis method for determining material properties is used to determine constants for the kinematic hardening law from experimental creep curves.

A damage law is presented which allows the prediction of crack propagation through a solder joint. A failure criteria based on the increase in electrical resistance is used, which removes the need for an empirical fatigue law.

The steady state creep law, the kinematic hardening law and the damage law are all applied to modelling of tests developed at the NPL (National Physical Laboratory) including novel crack detection tests, an isothermal fatigue test, and accelerated thermal cycling of resistors.

# Acknowledgements

I would like to thank my supervisor Chris Bailey for initiating this PhD and offering guidance throughout the past three years. My second supervisor Hua Lu provided much encouragement and technical advice for which I am grateful.

Thanks to my industrial supervisor Chris Hunt and colleague Milos Dusek at the NPL (National Physical Laboratory) who provided experimental results and many interesting discussions regarding their testing apparatus.

Thanks also to my parents for their support throughout my education.

This work was supported by the EPSRC (Engineering and Physical Sciences Research Council), through the Prime Faraday Partnership, as an Industrial Case Award. The industrial partner was the National Physical Laboratory who also financially supported the project as part of the Materials Processing Metrology Programme of the UK Department of Trade and Industry

Contents

# Contents

Declaration	i
Abstract	ii
Acknowledgements	iii
<b>1 Introduction</b>	<b>1</b>
1.1 Solder Joint Reliability . . . . .	2
1.2 Predicting solder reliability . . . . .	4
1.3 Software used . . . . .	4
1.4 Chapter contents . . . . .	6
1.5 Publications . . . . .	7
1.6 Areas of novelty . . . . .	8
<b>2 Literature Review: Modelling methods</b>	<b>10</b>
2.1 Analytical Methods . . . . .	12
2.2 Constitutive Law + Fatigue Law Methods . . . . .	14
2.2.1 FEA (Finite Element Analysis) . . . . .	15



Contents

2.2.2	Alternative numerical methods . . . . .	16
2.2.3	Solder Constitutive Laws . . . . .	19
2.2.4	Elasticity . . . . .	19
2.2.5	Creep . . . . .	20
2.2.6	Steady-state creep . . . . .	21
2.2.7	Primary creep . . . . .	22
2.2.8	Kinematic hardening . . . . .	23
2.2.9	Instantaneous Plasticity . . . . .	24
2.2.10	Fatigue laws . . . . .	25
2.3	Damage Mechanics Method . . . . .	27
2.3.1	J-integral . . . . .	28
2.3.2	Disturbed State Concept . . . . .	28
2.3.3	Cohesive zone . . . . .	29
2.3.4	Hybrid . . . . .	31
2.4	Discussion . . . . .	32
3	<b>FEA Theory</b>	<b>34</b>
3.1	Physics . . . . .	35
3.2	Discretisation . . . . .	36
3.2.1	Geometry . . . . .	36
3.2.2	The Element . . . . .	36
3.2.3	Shape Functions . . . . .	37



Contents

3.2.4	Degrees of Freedom . . . . .	39
3.2.5	Local & Global Derivatives . . . . .	39
3.2.6	Stress & Strain . . . . .	40
3.2.7	Elastic Energy . . . . .	42
3.2.8	Forces . . . . .	43
3.2.9	Energy Minimisation . . . . .	44
3.2.10	Calculating stiffness . . . . .	45
3.2.11	Boundary Conditions . . . . .	47
3.2.12	Need for DOF constraints . . . . .	48
3.2.13	Implementing DOF constraints . . . . .	49
3.3	Laplace equation (thermal / electrical) . . . . .	50
3.4	Solvers . . . . .	50
3.4.1	Cholesky Factorisation . . . . .	51
3.4.2	Preconditioned Conjugate Gradient Method . . . . .	51
3.4.3	Comparison of solvers . . . . .	52
3.5	Verifying accuracy compared to ANSYS . . . . .	57
4	<b>Solder Constitutive Law</b>	<b>59</b>
4.1	Creep Law . . . . .	60
4.1.1	Explicit and Implicit Time Discretisation . . . . .	60
4.1.2	LENI (Linear-Elastic / Nonlinear-Inelastic) Scheme . . . . .	61
4.2	Steady-state creep (explicit vs. implicit) . . . . .	64

Contents

4.2.1	Implementing using LENI Scheme . . . . .	64
4.2.2	Shear test (explicit) . . . . .	66
4.2.3	Stress relaxation . . . . .	67
4.2.4	Force-controlled vs. Displacement-controlled loading . . . . .	68
4.3	Kinematic Hardening Law . . . . .	70
4.3.1	Implementing using LENI . . . . .	71
4.4	Damage Law . . . . .	72
4.4.1	Damage evolution . . . . .	74
4.4.2	Explicit scheme . . . . .	75
4.4.3	Determining Lifetime . . . . .	75
4.4.4	Displacement-controlled cyclic loading . . . . .	76
4.4.5	Force-controlled cyclic loading . . . . .	78
4.4.6	Speeding up computation . . . . .	80
4.5	Summary . . . . .	81
5	Determining Material Constants	83
5.1	Inverse methods . . . . .	83
5.2	Creep tests . . . . .	85
5.2.1	Method . . . . .	86
5.2.2	Validation . . . . .	89
5.2.3	Fitting to experimental creep curves . . . . .	90
5.3	Damage . . . . .	92

Contents

5.4	Summary . . . . .	95
<b>6</b>	<b>Analysis: Fatigue Test</b>	<b>96</b>
6.1	Description of test . . . . .	96
6.2	Modelling Method . . . . .	98
6.3	Displacement Compensation . . . . .	99
6.4	Fatigue Cycling . . . . .	103
6.4.1	Load drop . . . . .	104
6.5	Electrical Resistance . . . . .	108
6.6	Conclusion . . . . .	110
<b>7</b>	<b>Analysis: Thermal Cycling of Resistor Joints</b>	<b>112</b>
7.1	Experimental Method . . . . .	113
7.2	Modelling method . . . . .	114
7.3	Modelling vs. Experiment . . . . .	116
7.4	Hysteresis Loops . . . . .	117
7.5	Sensitivity analysis . . . . .	122
7.5.1	Thermal profile parameters . . . . .	122
7.5.2	Effect of changing $t_{\text{dwell}}$ . . . . .	124
7.5.3	Effect of changing $t_{\text{ramp}}$ . . . . .	124
7.5.4	Effect of changing $T_{\text{low}}$ . . . . .	125
7.5.5	Effect of changing $T_{\text{high}}$ . . . . .	126



---

## Contents

---

7.6	Effect of constitutive law on lifetime predictions . . . . .	126
7.6.1	Different temperature profiles . . . . .	126
7.6.2	Different resistor sizes . . . . .	129
7.6.3	High Resolution Damage Simulation . . . . .	131
7.7	Conclusions . . . . .	133
<b>8</b>	<b>Analysis: Crack Detection Tests</b>	<b>134</b>
8.1	Introduction . . . . .	134
8.2	Cracks caused by Thermal Cycling . . . . .	135
8.3	Test Methods . . . . .	137
8.3.1	Pull Test . . . . .	138
8.3.2	3 Point bend test . . . . .	138
8.3.3	4 Point bend test . . . . .	140
8.3.4	Reverse 3 point bend test . . . . .	140
8.3.5	Thermal conductivity test . . . . .	141
8.4	Modelling Method . . . . .	141
8.5	Results . . . . .	143
8.5.1	Pull Test . . . . .	143
8.5.2	3-Point Bend Test Results . . . . .	149
8.5.3	4-Point Bend Test Results . . . . .	149
8.5.4	Reverse 3-Point Bend Test Results . . . . .	150
8.5.5	Thermal Conductivity Results . . . . .	150



Contents

8.6	Conclusion . . . . .	156
9	Conclusions	158
9.1	Future work . . . . .	160
A	Material Properties	162
A.1	Material Properties . . . . .	162
B	Sparse Matrix data structure	164

# Chapter 1

## Introduction

Engineering failures can be classified into three categories:

1. **Infant Mortality.** These are failures which occur early in the product's lifetime due to defects in production. (e.g. A solder joint did not form a good bond during the reflow process.)
2. **Random Failures.** These are failures which occur at a roughly steady rate over the product's lifetime. (e.g. A device was dropped to the floor causing a solder joint to completely break.)
3. **Wear-out Failures.** These are failures which occur due to gradual accumulation of damage over the product's lifetime. Wear-out failures increase in frequency toward the end of the product's lifetime. (e.g. Fatigue cracking in solder joints.)

The effect of these failure types on the overall failure rate is shown in figure 1.1, known as the bathtub curve due to its shape. The 'useful life' section of the curve is where the random failures dominate the failure rate.

This work focuses on the failure of solder joints due to ductile fatigue wear out mechanisms. Infant mortality and random failures are not considered.

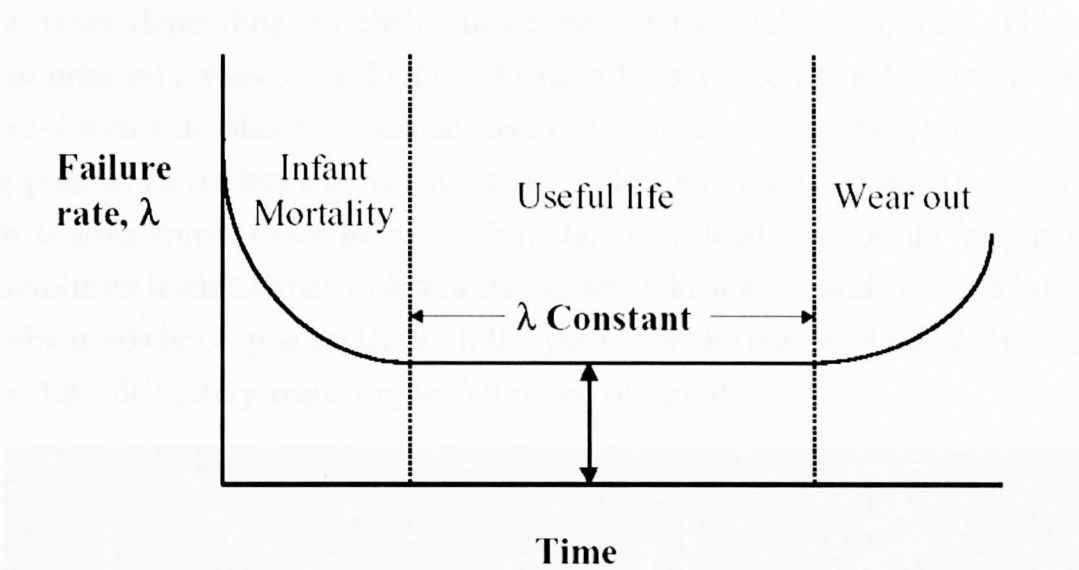


Figure 1.1: The idealised bathtub curve.

1.1 Solder Joint Reliability

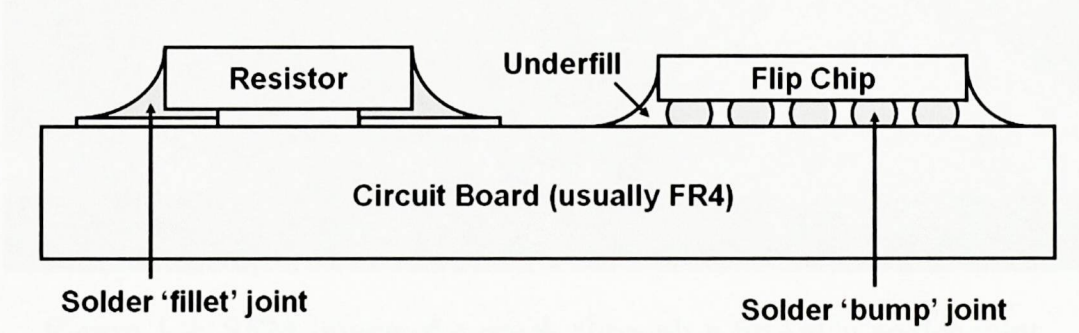


Figure 1.2: Two common types of soldered assemblies, a surface mount resistor and a flip chip.

Two of the more common types of chip assemblies tested are surface mount passives and flip-chips shown in figure 1.2. The circuit board is typically an organic material known as FR4 but alumina or other materials may be used. Two of the more common solder alloys are SnPb (Tin-Lead), which due to its Pb content is banned from use in most applications throughout Europe from July 2006 under the RoHS directive[1], and SnAgCu which is the most popular Pb-free replacement. Throughout the thesis SnPb refers to eutectic Sn37Pb and SnAgCu refers to Sn3.5Ag0.7Cu or to slight variations on these compositions.

The primary wear-out mechanism of solder joints is ductile fatigue fracture (low cycle fatigue). During operation or during testing, an electronic component will be subject to changes in temperature. This causes the materials to expand and contract at



## 1.1. Solder Joint Reliability

---

different rates depending on their coefficients of thermal expansion. This cycling results in internal stresses developing which, in turn, cause the solder to creep. Creep is a time-dependent plasticity which occurs in metals when they are close to their melting points. In solder, the melting point is low enough for creep to be significant at room temperature. Over many cycles, the creep leads to ductile fatigue damage which manifests itself as microvoids in the solder, which grow and coalesce into macro-cracks which slowly propagate through the joint over the course of its lifetime as shown in figure 1.3, ultimately resulting in failure of the joint.

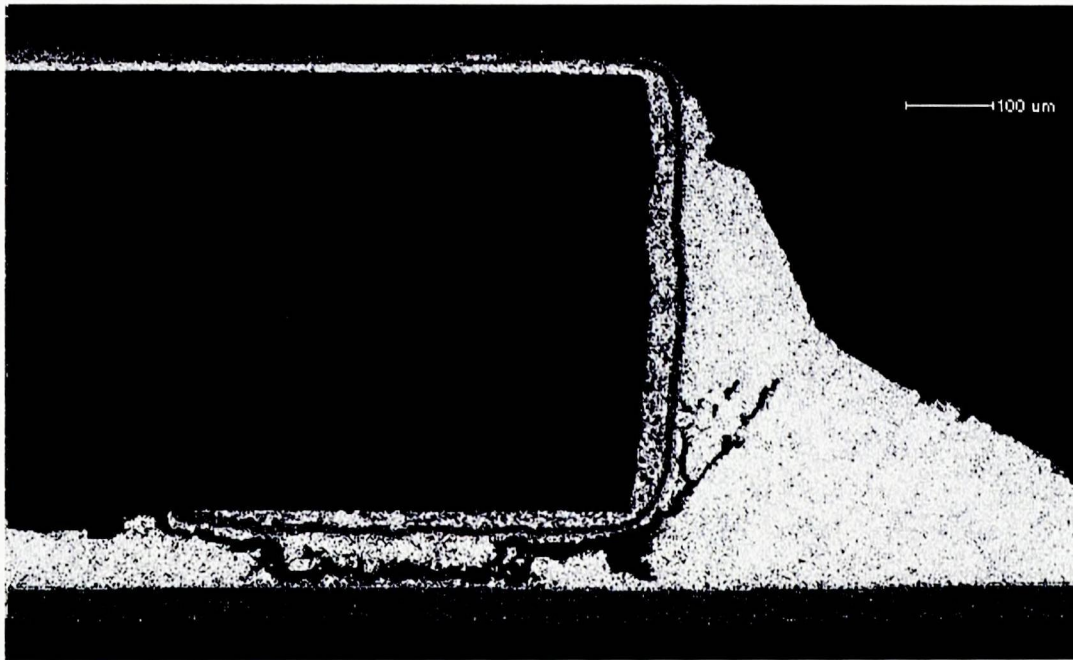


Figure 1.3: SEM image of a crack through a SnAgCu solder joint

The wear-out of solder joints due to ductile fatigue cracking can take many years under typical usage conditions. Therefore it is often unfeasible for companies to perform field tests due to the time and cost involved. Instead, accelerated tests are used which impose much harsher conditions on the joint, causing it to fail in a shorter time and allowing a judgement to be made on the product's reliability. The most popular accelerated test for solder joint reliability is thermal cycling, in which a soldered assembly is placed in an oven and subjected to a cyclic temperature profile representing conditions considerably harsher than expected field use. During cycling or at periodic intervals the samples will be monitored for electrical resistance/continuity. If the resistance shows a very large increase this indicates a crack has grown completely through the solder joint and the sample is considered to have failed. The number of cycles to failure in such a test is used as a measure of the reliability of a chip assembly.

Another accelerated test is the power cycling test, during which heat is periodically



---

## 1.2. Predicting solder reliability

---

generated from within a component. This results in an anisothermal temperature field more closely matching the conditions experienced in actual field use. This test is not as widely used as thermal cycling.

## 1.2 Predicting solder reliability

Since accelerated testing can be both time consuming and costly, modelling is a useful alternative, particularly in the early stages of design. By utilising ‘physics of failure’ based approaches, the effect of different designs on the solder reliability can be predicted. Current methods are described in detail in chapter 2 and are utilised in subsequent chapters.

## 1.3 Software used

All of the modelling work presented in this thesis is based upon FEA (Finite Element Analysis). This could have been accomplished either using a pre-existing code such as ANSYS, or by developing a new code. It was decided to develop a new code, called FATMAN (Finite-element Analysis Tool, Multiphysics And Nonlinear), in order to implement new constitutive laws and solution methods easily. In a commercial package like ANSYS the source code is not available which may have made implementation of novel schemes such as LENI (Linear-Elastic, Nonlinear-Inelastic) difficult or impossible.

An overview of the main software and experimental data used in this work is shown in figure 1.4. FemGV is used to create the FEA mesh, this is used in FATMAN, which performs an FEA simulation and produces results which can be visualised using FemGV. VisualDoc is an optimisation code which was integrated with FATMAN in order to determine material constants using inverse analysis.

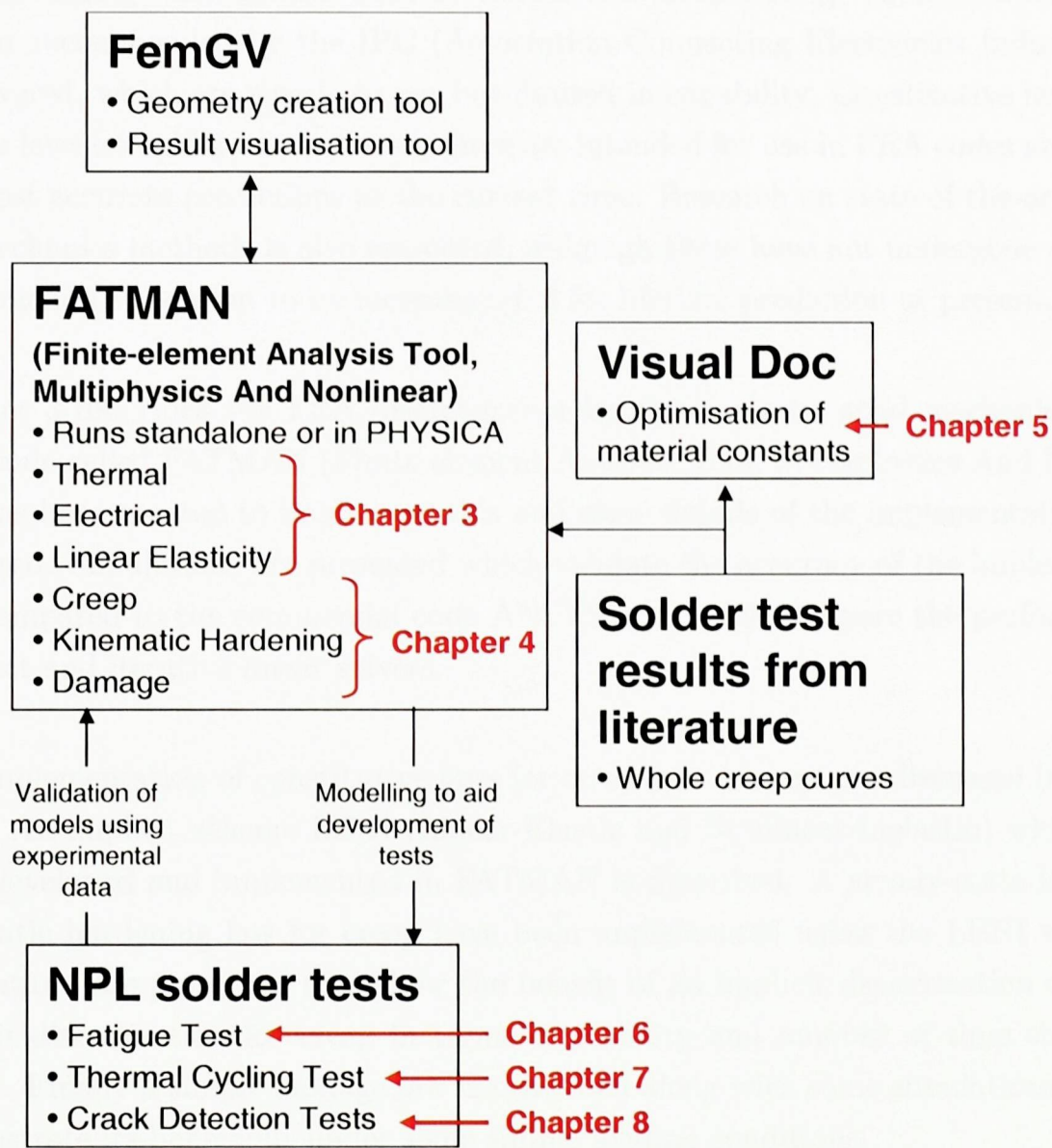


Figure 1.4: An overview of the software and experimental data used in this thesis



### 1.4 Chapter contents

Chapter 2 reviews the modelling methods available to predict the lifetime of SnPb and SnAgCu solder joints under thermo-mechanical cycling conditions such as power cycling, accelerated thermal cycling and isothermal testing. The methods do not apply to other damage mechanisms such as vibration or drop-testing. Analytical methods such as recommended by the IPC (Association Connecting Electronics Industries<sup>1</sup>) are covered, which are simple to use but limited in capability. Constitutive laws and fatigue laws for solder are reviewed, these are intended for use in FEA codes and offer the most accurate predictions at the current time. Research on state-of-the-art damage mechanics methods is also presented, although these have not undergone enough experimental validation to be recommended for lifetime prediction at present.

Chapter 3 describes the FEA discretisation for linear elastic solid mechanics. An FEA code called FATMAN (Finite element Analysis Tool, Multiphysics And Nonlinear) has been created to implement this and some details of the implementation are discussed. Simulations are presented which validate the accuracy of the implementation compared to the commercial code ANSYS and which compare the performance of direct and iterative linear solvers.

The implementation of constitutive laws for creep and damage are discussed in chapter 4. An implicit scheme LENI (Linear-Elastic and Nonlinear-Inelastic) which has been developed and implemented in FATMAN is described. A steady-state law and kinematic hardening law for creep have been implemented using the LENI scheme. Simulations are presented that show the benefit of an implicit discretisation over an explicit discretisation for creep in terms of stability and number of time steps required. Finally a simple damage law is described along with some simulations which demonstrate its behaviour under some simple loading conditions.

Chapter 5 describes the use of inverse analysis techniques to obtain material constants for the kinematic hardening creep law described in chapter 4. The ability of the kinematic hardening law to capture the primary and secondary regions of the creep curve is shown. The VisualDoc optimisation software was integrated with FATMAN to accomplish this. A method to determine the material constant in the damage law

---

<sup>1</sup>IPC used to be an acronym for Institute for Printed Circuits but has since undergone a name 'change' to IPC (in which the letters do not stand for anything).

---

## 1.5. Publications

---

is also presented.

Chapter 6 describes modelling on an isothermal fatigue test developed at the NPL. Modelling work is described which highlights a flaw in the initial design of the test – the intended displacement across the solder joint was not being achieved. A solution for this is offered that has been successfully applied experimentally by the NPL. Hysteresis curves are predicted using the steady-state creep law and load drops are predicted using the damage law and compared to experiment. The effect of crack length on pseudo-resistance (a value similar to electrical resistance) is also modelled.

Chapter 7 describes modelling of the thermal cycling of surface mount resistors with comparison to experimental data. The severity of 6 thermal cycle profiles is compared for 3 sizes of resistor and using the steady state creep law. The kinematic hardening law and damage law developed in chapter 4 are applied to determine the cycles to failure and compared to the sinh law. A sensitivity analysis is performed using the steady-state creep law which determines the effect of changes in the thermal profile on the predicted damage. Also, a high resolution simulation using the damage law predicts the crack propagation path in detail.

Chapter 8 describes modelling work on five novel tests developed by the NPL which aim to determine the presence and magnitude of cracks within the solder joints of a surface mount resistor. Four of the tests are mechanically based and one attempts to measure the change in the thermal conduction through the joints when a crack is present.

## 1.5 Publications

Four conference papers [2, 3, 4, 5] and two journal papers [6, 7] have been published from the work presented here:

1. The review of solder modelling methods presented in chapter 2 is based on a paper published in the journal *Fatigue and Fracture of Engineering Materials and Structures* [7].



---

## 1.6. Areas of novelty

---

2. The kinematic hardening law and damage laws presented in chapter 4 were presented in ESTC 2006 [5].
3. The modelling work on the crack detection tests developed by the NPL covered in chapter 8 was presented in EuroSimE 2004 [2] and has been published in the journal Microelectronics Reliability [6].
4. The work on the NPL fatigue test in chapter 6 was presented in EuroSimE 2005 [4].
5. The work comparing the effect of different thermal cycle profiles on the damage in resistor joints in chapter 7 was presented in EMAP 2004 [3].

## 1.6 Areas of novelty

To the best of the author's knowledge the following aspects of this work are novel:

1. The LENI (Linear-Elastic and Nonlinear-Inelastic) scheme to solve the implicit discretisation for creep. This has been implemented and compared to an explicit discretisation.
2. The use of electrical resistance increase to determine the point of failure in a damage mechanics simulation described on page 75.
3. The investigation into the effect of volume averaging on mesh dependence of the damage law under idealised fatigue cycling (chapter 4) and thermal cycling (chapter 7).
4. The method proposed to speedup the computation of damage simulations presented on page 80.
5. The determination of material constants for kinematic hardening using inverse analysis described in chapter 5.
6. The method to determine the material constant for the damage law from accelerated test data described in chapter 5.

## 1.6. Areas of novelty

---

7. The displacement compensation formula was developed in chapter 6 which aided the development of the NPL's fatigue test.
8. The work in chapter 6 predicting the increase in 'pseudo electrical resistance' across the joint in the fatigue test.
9. The sensitivity analysis, which investigates the effect of altering the ramp and dwell times as well as the high and low temperature extremes of a thermal cycling test. This is presented in chapter 7.
10. The use of the damage law to predict the crack propagation in a surface mount resistor joint in chapter 7.
11. The sensitivity of the crack detection tests in chapter 8 was predicted, aiding the NPL in the development of their tests.

## Chapter 2

# Literature Review: Modelling methods

Modelling is a useful tool used to supplement or replace accelerated tests, particularly in the early design stages. The modelling discussed here applies to creep induced ductile fracture only, and so will be suitable for modelling the damage which occurs due to typical thermal or power cycling of joints, but not to vibration or drop testing, or shear-strength testing. Most of the methods described can be applied to any solder alloy provided the correct material constants are known. Many methods exist, and there is no clear cut answer as to which is best. Figure 2.1 shows the classes of modelling methods which will be discussed in this chapter.

The methods in figure 2.1 increase in complexity going from top to bottom, the analytical method proposed by Engelmaier [8, 9] being simple to implement but with many caveats restricting its use in certain situations. The constitutive law + fatigue law class of methods (encompassing FEA and other alternatives) are very popular, providing more accurate predictions with fewer restrictions than analytical methods, however with increased setup time and computational cost. The damage mechanics based methods require considerably more effort both in implementation and computational cost and their predictive capability is currently unproven, however they promise to provide the most accurate predictions once they are developed further.

In reality the behaviour of solder joints is very complex and all the modelling methods



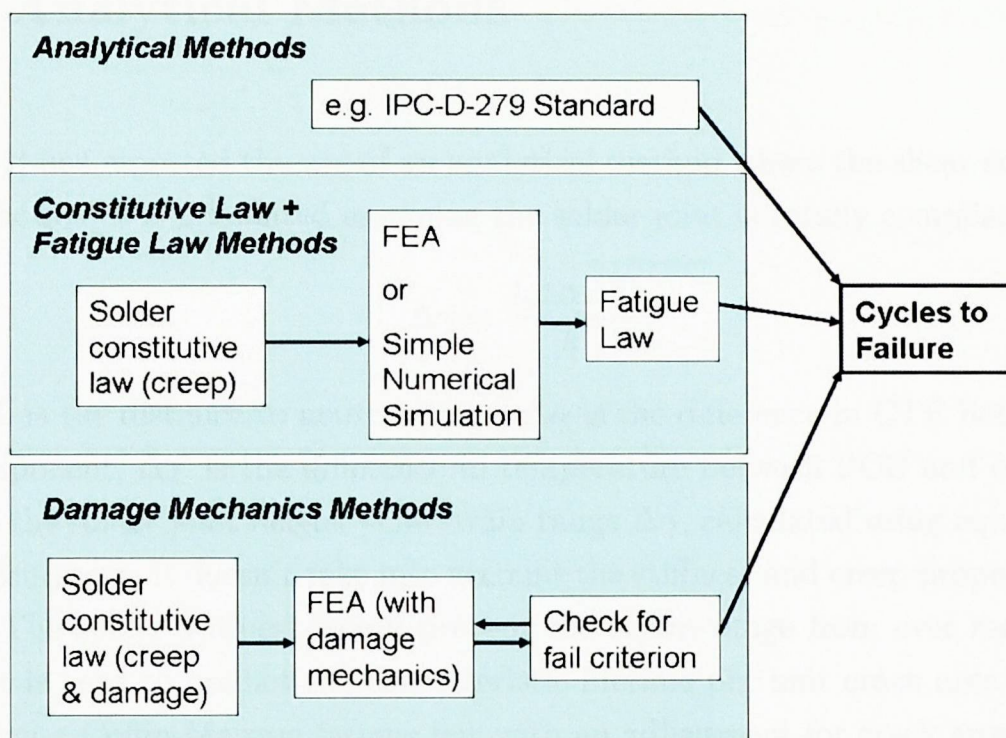


Figure 2.1: Modelling methods to predict lifetime of thermo-mechanically cycled joints

discussed must make many simplifications and omit certain aspects of the problem, for example the microstructural behaviour of the intermetallic particles in SnAgCu, or the differences between the Pb-rich and Sn-rich phases of SnPb. The constitutive law + fatigue law methods make fewer simplifications than the analytical methods, and the damage mechanics methods make even fewer simplifications but cannot capture all of the physics.

The methods discussed can be used to predict reliability under accelerated and field use conditions. However they cannot *accurately* predict field-use reliability as they have not been validated against field-use data, which is very sparse. The assumption is that the relative reliability of various components under accelerated conditions will be the same, or at least similar, under field-use conditions. Some models have been extrapolated to simulate field-use conditions [10], but this may produce misleading results.

In the formulas presented in this chapter,  $c_i$  refers to a material constant. Unless stated otherwise, similarly numbered constants in different equations don't represent the same quantities, e.g.  $c_1$  in equation (2.2) is not equal to  $c_1$  in equation (2.3).

## 2.1 Analytical Methods

Clech [11] has reported the use of an analytical method where the shear strain range  $\Delta\gamma$  in the solder is calculated assuming the solder joint is totally compliant:

$$\Delta\gamma = \frac{L\Delta\alpha\Delta T}{h} \quad (2.1)$$

Where  $L$  is the distance to neutral point,  $\Delta\alpha$  is the difference in CTE between PCB and component,  $\Delta T$  is the difference in temperature between PCB and component, and  $h$  is the solder joint height. The strain range  $\Delta\gamma$ , calculated using equation (2.1) is not accurate as it doesn't take into account the stiffness and creep properties of the solder. The solder stiffness would prevent the strain range from ever reaching this value. It is used to predict the characteristic lifetime per unit crack area of a single joint using a Coffin-Manson fatigue law with an adjustment for crack area  $A$ :

$$\frac{N_f}{A} = c_1 (\Delta\gamma)^{-c_2} \quad (2.2)$$

Where  $N_f$  is the number of cycles before failure. Predictions made using this method were correlated with a data set of 27 experimental data points covering different kinds of assemblies under different thermal profiles for SnAgCu solder. Despite not taking into account the creep behaviour of the solder at all, the accuracy of the predictions was in the range of  $\pm 2 \times 1$ .

A slightly different analytical approach is Engelmaier's model for predicting the lifetime of Sn37Pb joints recommended in the IPC-D-279 standard [9]. There are versions for both leaded and non-leaded components (leaded as in gull-wing lead, not to be confused with Pb) and they are very simple to use when compared with FEA modelling. The way it works is to assume the solder deforms to its maximum amount based on the CTE (coefficient of thermal expansion) of the substrate and component. This strain range is calculated for non-leaded joints using equation (2.3), this is very similar to the equation (2.1) used by Clech but with an added empirical factor  $c_1$ .

$$\Delta\gamma = c_1 \frac{L}{h} \Delta(\alpha\Delta T) \quad (2.3)$$

Following this, the standard Coffin-Manson fatigue law for predicting  $N_f$  (number of

---

<sup>1</sup>By saying  $x$  is in the range  $\pm y \times$ , the range being referred to is  $(x/y, xy)$



---

## 2.1. Analytical Methods

---

cycles to fail) has been modified to include temperature and frequency effects:

$$N_f = \frac{1}{2} \left[ \frac{\Delta\gamma}{2c_2} \right]^{1/c} \quad (2.4)$$

$$c(T, f) = -0.442 - 6 \times 10^{-4} \bar{T}_{SJ} + 1.74 \times 10^{-2} \ln \left( 1 + \frac{360}{t_D} \right) \quad (2.5)$$

Where  $t_D$  is the dwell time, and  $\bar{T}_{SJ}$  is the mean cyclic joint temperature for which a formula is provided [9]. This approach has been shown to predict lifetimes with an accuracy of  $\pm 2\times$  under the appropriate conditions [8]. However there are many conditions in which this law does not apply. A list of caveats from the IPC standard [9] are stated below along with a brief discussion of whether they also apply to the constitutive law + fatigue law methods.

1. **Solder joint quality:** This caveat is to ensure that the failure mechanism is actually ductile fatigue within the solder joint and not brittle failure at the interface which could be caused by poor materials choice (e.g. alloy 42 leads) or very small solder joint gaps ( $<75\text{nm}$ ). This caveat could be applied all the modelling methods covered in this paper, which are intended to predict the lifetime of joints which fail due to creep induced ductile fracture, not brittle failure.
2. **Large temperature excursions:** The damage mechanism changes in solder joints experiencing large temperature excursions ( $-50^\circ\text{C}$  to  $+80^\circ\text{C}$ ). Using a constitutive law + fatigue law method could capture the difference in solder behaviour within this temperature range. For example, Darveaux et. al. [10] validated a fatigue law for SnPb for temperature ranges up to  $-55^\circ\text{C}$  to  $+125^\circ\text{C}$ , and Syed [12] validated a similar law for SnAgCu up to the same range.
3. **High frequency/Low temperature:** For frequencies  $> 0.5\text{Hz}$  and/or temperatures  $< 0^\circ\text{C}$  the direct application of Coffin Manson may be more appropriate ( $c \simeq -0.6$ ). Under these conditions, creep induced fatigue may not be the primary failure mechanism, in which case none of the modelling methods discussed in this work would be suitable.
4. **Local expansion mismatch.** The local CTE mismatch between the solder joint and the board or component is not taken into account.



---

## 2.2. Constitutive Law + Fatigue Law Methods

---

For instance, an alumina component on an alumina substrate would generate no global strain in the solder and would, according to this model, experience no fatigue. However in reality, local strains will be generated at the solder/component and solder/substrate interfaces which would lead to damage. This damage mechanism is captured perfectly well by using FEA modelling with an appropriate constitutive law and fatigue model.

5. **Very stiff leads/very large expansion mismatches:** The analytical method does not make use of the Young's moduli of any of the materials so it cannot predict accurately the amount of strain which will occur in the joints, leads, component and substrate. When the package geometries and materials are similar this may not matter, but deviations from the norm could result in very inaccurate results. For instance, if we consider two assemblies, similar in all respects except that the component Young's modulus is high in one case and low in the other. The component with the high Young's modulus will cause a greater strain in the solder joints, but this model will predict the same lifetime for both. Using FEA will predict the strains occurring in the solder accurately based on the Young's modulus and other mechanical properties of the materials.

So of the five caveats, three would no longer be necessary if a Constitutive law + Fatigue law method were used instead. The Analytical methods, while simple to use, are limited in their applicability compared to the other methods.

## 2.2 Constitutive Law + Fatigue Law Methods

These methods work by running a transient simulation to predict the solder's stress strain behaviour during a thermal cycle. From this simulation, either the accumulated effective plastic strain per cycle ( $\varepsilon^{acc}$ ) or the accumulated strain energy density per cycle ( $\Delta W$ ) is extracted to be used in a fatigue law. First, the methods of modelling the mechanical response of an assembly under thermal cycling will be discussed (FEA and alternatives), followed by the various constitutive laws available, and finally the

fatigue laws.

### 2.2.1 FEA (Finite Element Analysis)

FEA (Finite Element Analysis) is a powerful and widely used numerical method which can be used to accurately predict the mechanical response of the solder joints and surrounding assembly under thermo-mechanical cycling. A detailed description of the FEA method is provided in chapter 3.

To use FEA requires considerably more investment in time than the analytical approaches mentioned so far, and detailed knowledge of the test being modelled. In order to use FEA to determine the fatigue life of solder joints under thermal cycling, the following steps are required:

1. Create geometry: The geometry of the model should strike an acceptable balance between accuracy and simplicity. Common simplifications to the geometry include:
  - (a) The intermetallic layer formed between the solder joint and the copper pads is usually ignored, due partly to its size and partly to the lack of material property data.
  - (b) Good judgement is needed in deciding what details of the actual geometry are important to include in the model and which are superfluous.
  - (c) Symmetry. Usually only a quarter of a surface mount resistor needs to be modelled, and only an eighth of a BGA or flip-chip.
2. Create mesh: Ideally we would obtain mesh independent results. This could be verified by performing simulations using progressively finer meshes until the results no longer change. However the presence of stress singularities often prevent this, in which case it is necessary to ensure that the mesh density is consistent when making comparisons between simulations. It is also important that the aspect ratio of elements is not too high as this can introduce numerical errors.
3. Specify material properties: It is crucial to use accurate material properties to obtain accurate results. When available, temperature dependent material



---

## 2.2. Constitutive Law + Fatigue Law Methods

---

properties should be used. The solder properties are discussed later in this chapter. Since the focus is on solder joint modelling the properties of the other materials involved are not discussed.

4. Specify boundary conditions: During typical thermal cycling regimes the temperature may be regarded as uniform throughout the sample. For very rapid thermal shock, or when there is heat generation from within a chip (e.g. during power cycling) then the temperature field will not be uniform and should be calculated throughout the mesh on each time step.
5. Apply Fatigue law: To apply the fatigue law, a  $\varepsilon_{acc}$  or  $\Delta W$  value needs to be extracted from the FEA simulation results. Since the variation in strain across a joint is captured, this raises the question of whether to average over the whole joint or only a portion of it. Two sources have been found which address this [12, 13] and both use an average value over a  $25\mu\text{m}$  layer at the top of the solder bump in a BGA package. Altering the size of this volume averaged region may alter the value of  $\varepsilon_{acc}$  or  $\Delta W$  significantly, so if the size needs to be changed, for example when modelling a different sized or shaped joint, then the fatigue law constants should ideally be re-calibrated with experimental data to ensure accurate predictions.

### 2.2.2 Alternative numerical methods

Alternatives to FEA include more simplified methods which capture the creep behaviour of the solder using a constitutive law but do not capture the geometry as accurately.

A simple example predicting only the prominent shear component of strain in a solder joint is shown in figure 2.2. In this example, the strain is assumed to be uniform throughout the solder joint thus making it suitable to model global strains only. The component and substrate have stiffnesses of  $k_c$  and  $k_s$  respectively and CTEs of  $\alpha_c$  and  $\alpha_s$  respectively. These are used to determine the forces imposed on the solder joint:

$$F_c = k_c (L\alpha_c\Delta T - u_c) \quad (2.6)$$

$$F_s = k_s (L\alpha_s\Delta T - u_s) \quad (2.7)$$



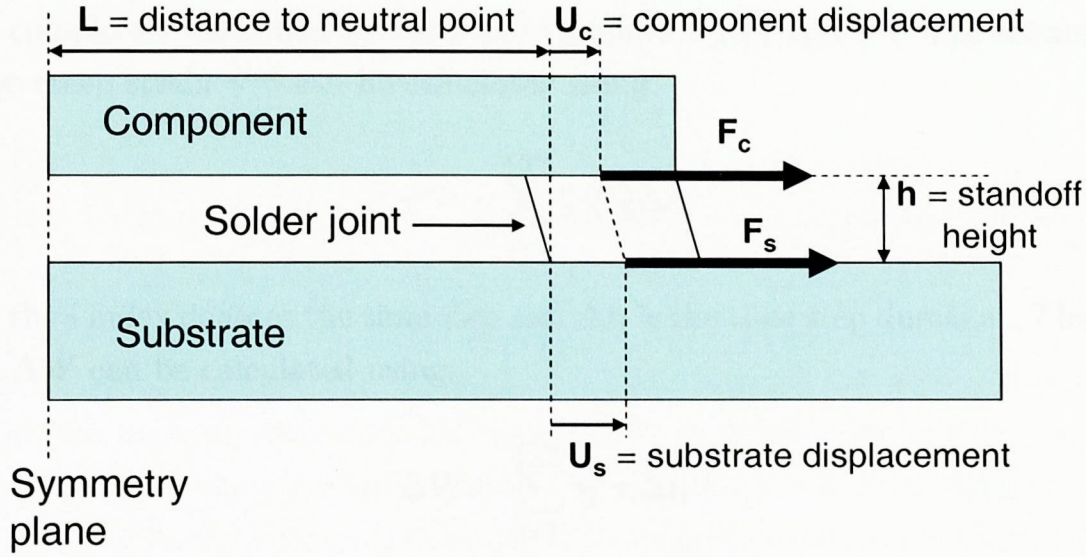


Figure 2.2: Example of a simple numerical model to predict the creep response in a solder joint.

Where  $\Delta T$  is the temperature relative to the stress-free temperature and  $F_c$  and  $F_s$  are the forces imposed on the solder joint by the component and substrate respectively. The total shear strain in the solder joint  $\gamma^{\text{total}}$  is given by:

$$\gamma^{\text{total}} = \frac{(u_c - u_s)}{h} \quad (2.8)$$

This is composed of elastic and plastic parts:

$$\gamma^{\text{total}} = \gamma^{\text{el}} + \gamma^{\text{cr}} \quad (2.9)$$

Where  $\gamma^{\text{el}}$  is the elastic strain component and  $\gamma^{\text{cr}}$  is the creep strain component. The creep strain changes over time depending on the stress in the solder  $\tau$ :

$$\dot{\gamma}^{\text{cr}} = \frac{\partial \gamma^{\text{cr}}}{\partial t} = f(\tau) \quad (2.10)$$

The stress in the solder  $\tau$  is related to the elastic strain by the shear modulus  $G$ :

$$\tau = G\gamma^{\text{el}} \quad (2.11)$$

The stress must be such that the forces are in equilibrium:

$$F_c = \tau A = -F_s \quad (2.12)$$

Where  $A$  is the cross sectional area of the solder joint. The above system is temporally discretised using an explicit or implicit scheme and the state of the system at each time

---

## 2.2. Constitutive Law + Fatigue Law Methods

---

step is completely described by the three variables  $u_c$ ,  $u_s$  and  $\gamma^{cr}$ . The accumulated effective creep strain  $\gamma^{acc}$  can be calculated using:

$$\gamma^{acc} = \sum_{i=1}^{i=n} \|\dot{\gamma}_i^{cr}\| \Delta t_i \quad (2.13)$$

Where the  $i$  index denotes the time step and  $\Delta t_i$  is the time step duration. The strain energy  $\Delta W$  can be calculated using:

$$\Delta W = \sum_{i=1}^{i=n} \dot{\gamma}_i^{cr} \tau_i \Delta t_i \quad (2.14)$$

The increase in either  $\gamma^{acc}$  or  $\Delta W$  per thermal cycle can be used in a fatigue law to predict the number of cycles to fail. Due to its simplicity this method will provide results with less effort and less computation time than FEA, and because it uses a constitutive law to model the solder's creep behaviour it should provide more accurate results over a wider range of conditions than an analytical method.

A more advanced example of this kind of approach is provided by Clech [14] with the capability of modelling local as well as global thermal expansion mismatches, and the effect of underfill. It has been calibrated against 19 experimental results with an error of about  $\pm 2.5\times$ , and validation was performed against a further 14 experimental results.

A hybrid method is suggested by Darveaux [13] where two purely elastic FEA analyses are conducted to provide 1) the stiffness of the assembly surrounding the joint and 2) the displacement between the top and bottom pads assuming the solder joint is not present. These are then used in a numerical model similar to that described above which uses a constitutive law to predict the average response of the solder joint over a thermal cycle. This strikes a compromise between the accuracy of FEA and the computational ease of a simpler numerical method. However it will not predict the damage caused by the local thermal expansion mismatch between the solder and the component or substrate.

Possibly the main advantage of the alternative methods described here is their computational ease in comparison to FEA but with the advances in computational power over the years this is becoming less of an issue.



### 2.2.3 Solder Constitutive Laws

A constitutive law for a material governs its mechanical behaviour when subject to different stresses at different temperatures. The importance of using the correct constants for the constitutive laws is highlighted by a sensitivity study [15] which shows that the differences in SnPb Young's modulus, CTE (Coefficient of Thermal Expansion) and creep activation energies within the range of variation reported in the literature can lead to inaccurate lifetime predictions when used in FEA modelling. Using a Young's modulus for SnPb solder of 10 GPa, the predicted lifetime of a PQFP (Plastic Quad Flat Pack) component was 3.3 times greater than when using a Young's modulus of 38 GPa. By varying the CTE the lifetimes changed by about 2 times and by varying the activation energies the lifetimes changed by about 11 times.

### 2.2.4 Elasticity

The elastic properties of solder are usually determined from a strain rate controlled tensile test. From this test the Young's modulus can be determined along with the ultimate tensile/shear strength of the solder. There is a large strain rate and temperature effect and the Young's modulus will appear lower at lower strain rates or higher temperatures [16]. The temperature dependence is usually modelled but no work was found which modelled the strain rate dependence.

The elastic deformation of the solder is governed by the Young's modulus  $E$ , and Poisson's ratio. In one dimension the relationship between stress  $\sigma$ , and strain  $\varepsilon$ , is given by Hooke's law:

$$\sigma = E\varepsilon^{el} \quad (2.15)$$

In 3D the relationship is more complex and will be covered in chapter 3. The Young's modulus is both temperature and strain rate dependent, and a formula for calculating the Young's modulus of SnAgCu is provided by Pang [16]:

$$E(T, \dot{\varepsilon})_{SnAgCu} = (-0.0005T + 6.4625) \log \dot{\varepsilon} + (-0.2512T + 71.123) \quad (2.16)$$

The temperature dependence is usually modelled but no modelling work was found which included the strain rate dependence. More temperature dependent Young's



---

## 2.2. Constitutive Law + Fatigue Law Methods

---

modulus values of SnAgCu have been reviewed by Syed [12], there is some scatter in the values reported which may be as a result of differences in the strain rate used. It is pointed out by Basaran and Jiang [17] that when modelling SnPb, the use of different values of Young's modulus (literature values range from 9GPa to 48GPa) can adversely effect the results of a simulation and that ideally a modulus measurement should be made on an actual manufactured package using a nano-indentation technique. The CTE (Coefficient of Thermal Expansion) of the solder governs the amount by which it expands under changing temperatures:

$$\alpha = \frac{d\varepsilon^{th}}{dT} \quad (2.17)$$

A CTE of 25 ppm/°C has been reported for SnPb15, and a CTE of 20 ppm/°C has been reported for SnAgCu16.

### 2.2.5 Creep

Creep is a time dependent plastic deformation which occurs to metals under stress at high homologous temperatures, since solder has a melting point of 183°C (SnPb) or 217°C (SnAgCu) then it creeps at room temperature. During a creep test a constant load is applied to a solder specimen at a constant temperature. The character of the response of the solder is illustrated in figure 2.4. At the instant the force is applied, the solder will experience a strain which is part elastic and part instantaneous plasticity. The elastic part can be predicted given the Young's Modulus of the solder as discussed earlier. The instantaneous plastic part can be modelled using laws from Darveaux et.al. [10] and Wiese and Rzepka [18], although the distinction between this instantaneous plasticity and the primary creep region is not well defined. As the test continues the strain increases, first rapidly (primary region) and gradually slowing to a steady strain rate (secondary region). This additional strain is due to creep. After the secondary region comes the tertiary region during which the strain rate increases until rupture. This occurs due to both necking (shrinking of the cross section resulting in increased stress) and damage (cracking) occurring in the solder.

The standard method for FEA modelling of solder joints involves modelling only the steady state creep and it is possible to get reasonable predictions using this approach [10], [12]. However it is possible that better accuracy may be achieved by

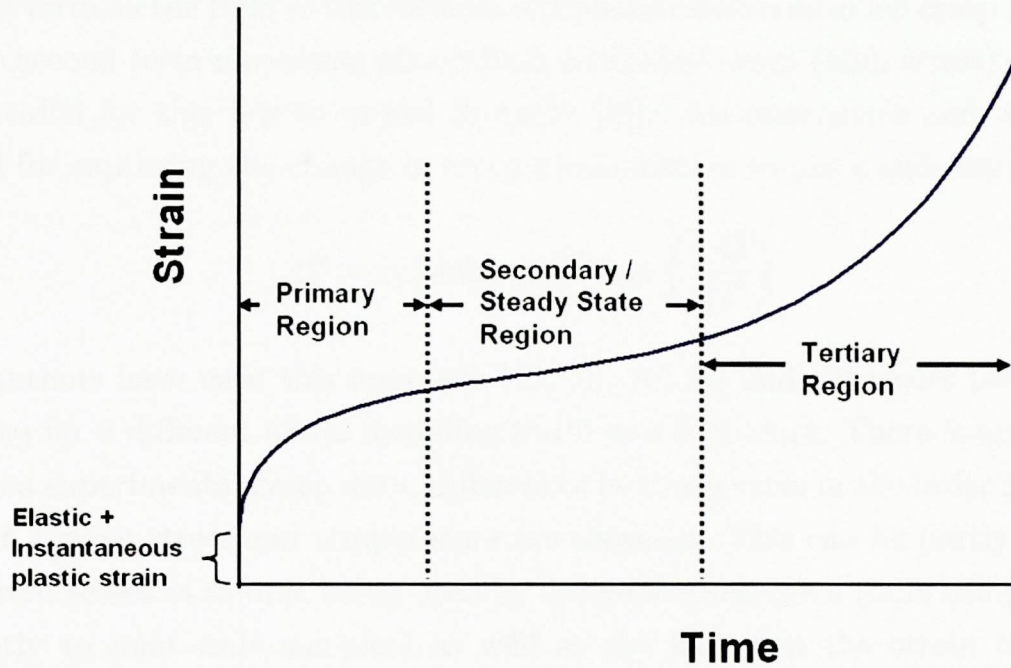


Figure 2.3: Graph showing the three regions of the creep curve for solder

incorporating primary creep and instantaneous plasticity into the model. If the goal of a simulation is to accurately predict the amount of deformation occurring in the solder, then including primary creep is essential.

### 2.2.6 Steady-state creep

The secondary creep, also called steady-state creep, is commonly the only kind of creep to be modelled. The simplest steady-state creep law is the Norton law:

$$\dot{\epsilon}^{ss} = c_1 \sigma^{c_2} \exp\left(\frac{-Q}{kT}\right) \quad (2.18)$$

Where  $\dot{\epsilon}^{ss}$  is the steady state creep strain rate,  $Q$  is the activation energy, and  $k$  is Boltzman's constant. This law has been used to model SnPb10 but doesn't capture the change in creep mechanism between low stresses and high stresses. To capture this change Wiese [19] has used a double-power model to model SnAgCu:

$$\dot{\epsilon}^{ss} = c_1 \left(\frac{\sigma}{\sigma_n}\right)^{c_2} \exp\left(\frac{-Q_1}{kT}\right) + c_3 \left(\frac{\sigma}{\sigma_n}\right)^{c_4} \exp\left(\frac{-Q_2}{kT}\right) \quad (2.19)$$



---

## 2.2. Constitutive Law + Fatigue Law Methods

---

The first term on the RHS of this formula represents climb controlled creep (low stress) and the second term represents glide/climb controlled creep (high stress). Constants are provided for this law to model SnAgCu [19]. An alternative and widely used method for capturing the change in creep mechanism is to use a sinh law:

$$\dot{\epsilon}^{ss} = c_1 [\sinh(c_2 \sigma)]^{c_3} \exp\left(\frac{-Q}{kT}\right) \quad (2.20)$$

Many authors have used this approach [13, 18, 20, 21] and Darveaux has published constants for 4 different alloys including SnPb and Sn3.5Ag4. There is spread in the published experimental creep data, differences in strain rates in the order of 10 to 100 times at a given stress and temperature are common. This can be partly attributed to different scales of sample being used by different researchers (bulk samples behave differently to joint-scale samples) as well as the fact that the strain rate is very sensitive to small changes in stress.

### 2.2.7 Primary creep

Good lifetime predictions are made using only steady state creep laws [10], because although the absolute values of strain predicted are inaccurate, the fatigue laws have been calibrated to these results and thus provide reasonable lifetime predictions. Even better predictions should be possible by modelling primary creep. Three different approaches have been found to model primary creep, the use of a time-variable, isotropic hardening, and kinematic hardening. Of these, only kinematic hardening is suitable to model the solder behaviour during thermo-mechanical cycling.

Darveaux et.al. [10] and Schubert et. al. [20] have reported laws which make use of a time variable in the creep strain rate function. Darveaux's law is represented by equation (12), while Schubert uses a slightly more complex formula.

$$\dot{\epsilon}_{cr} = \dot{\epsilon}_s (1 + c_1 c_2 \exp(-c_2 \dot{\epsilon}_s t)) \quad (2.21)$$

Where  $t$  is the time since the start of the loading. This may be adequate for modelling a monotonic creep test, but modelling of cyclic temperature cycling or fatigue cycling where the stress and therefore  $\dot{\epsilon}_s$  is constantly changing this law is not appropriate. Cheng et. al. [22] used the Anand model to model the primary and secondary regions



---

## 2.2. Constitutive Law + Fatigue Law Methods

---

of the creep curve using isotropic hardening:

$$\dot{\epsilon}_{cr} = c_1 \left[ \sinh \left( c_2 \frac{\sigma}{s} \right) \right]^{1/c_3} \exp \left( -\frac{Q}{RT} \right) \quad (2.22)$$

Where  $s$  is a scalar internal variable which represents the averaged isotropic resistance to plastic flow. It changes according to the following formula:

$$\dot{s} = \left\{ c_4 \left| 1 - \frac{s}{s^*} \right|^{c_5} \cdot \text{sign} \left( 1 - \frac{s}{s^*} \right) \right\} \dot{\epsilon}_{cr} \quad (2.23)$$

Where  $s^*$  is the saturation value of  $s$  given by:

$$s^* = c_6 \left[ \frac{\dot{\epsilon}_{cr}}{c_1} \exp \left( \frac{Q}{kT} \right) \right]^{c_7} \quad (2.24)$$

Where  $c_1$  in equation (15) is the same as  $c_1$  in equation (2.22). The material properties for 60Sn40Pb, 62Sn36Pb2Ag and 96.5Sn3.5Ag were fitted from the conventional - Darveaux model parameters.

The use of an isotropic hardening law to capture the hardening during a creep test is questionable as a large part of the hardening is due to kinematic hardening, Stolkarts et. al. [23] have even reported that isotropic hardening does not occur in SnPb solder. Another study by Kim et al. [24] has shown that kinematic hardening, and not isotropic hardening, is suitable for modelling Sn3.5Ag0.75Cu solder. So although an isotropic hardening model may capture the behaviour of a monotonic creep test it will not capture the true behaviour in cyclic testing where the load is reversed. Despite this the model has been used in FEA analysis of chip assemblies by many researchers, often with good agreement to experimental results [13, 22, 25, 24].

### 2.2.8 Kinematic hardening

To understand how the solder behaves under cyclic loading, mechanical fatigue tests are used. During this test a cyclic strain, either shear or tensile, is imposed on a solder joint or bulk sample. The response of the solder is dependent on the elastic, creep and fatigue properties making it a useful test to validate the accuracy of constitutive laws.

## 2.2. Constitutive Law + Fatigue Law Methods

Kinematic hardening laws with material parameters for SnPb have been found [26, 27, 28] which can accurately predict the behaviour shown in isothermal fatigue tests. A simple form of kinematic hardening law is the Armstrong-Frederick law used in [26] to model SnPb:

$$\dot{\underline{S}} = c_1 (\dot{\varphi} c_2 - \dot{\varphi}_{\text{eff}} \underline{S}) \quad (2.25)$$

Where  $\underline{S}$  is the back stress,  $\dot{\varphi}$  is the creep strain rate, and  $\dot{\varphi}_{\text{eff}}$  is the effective creep strain rate. No laws with material parameters for SnAgCu have been found.

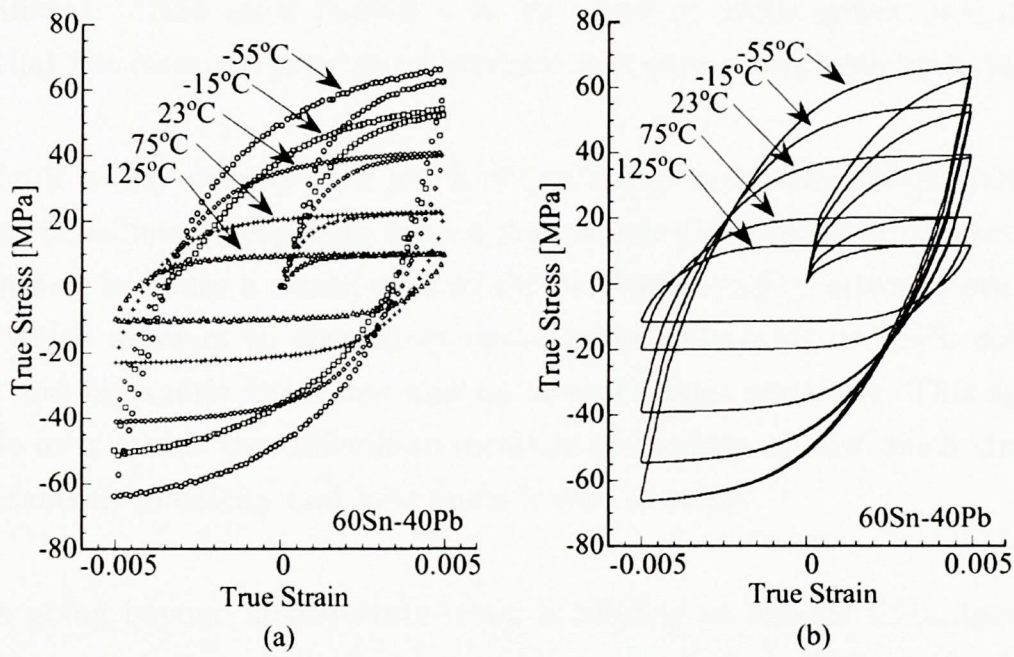


Figure 2.4: Experimental and Simulated hysteresis curves using the McDowell USP model (graph from Neu et. al. [27])

Figure 2.4 shows experimental and simulated hysteresis loops of isothermal fatigue tests from Neu [27] predicted using the McDowell UCP (Unified Creep Plasticity) model [29] which includes both isotropic and kinematic hardening terms.

### 2.2.9 Instantaneous Plasticity

Darveaux used the following law to capture the instantaneous plasticity which occurs in creep tests in many solders including SnPb and Sn3.5Ag:

$$\varepsilon^{in} = c_1 \left( \frac{\sigma}{E} \right)^{c_2} \quad (2.26)$$



---

## 2.2. Constitutive Law + Fatigue Law Methods

---

Where  $\varepsilon^{in}$  is the instantaneous plastic strain. Unfortunately, this law cannot be applied to other loading conditions such as temperature cycling where the stress would be constantly changing. Wiese has used the multilinear elastic-plastic model of ANSYS to simulate the time-independent behaviour of Sn37Pb, Sn3.5Ag and Sn4Ag0.5Cu. This was shown to accurately predict the behaviour of the solder in isothermal fatigue testing with cycle periods of 1s to 3600s. Wiese shows that for fatigue tests with a frequency of 1Hz, the instantaneous plasticity dominates but for cycles with a period of 3600s the creep dominates and the instantaneous plasticity is insignificant. Since most testing is in the order of 3600s cycles then this would suggest that the common practise of ignoring instantaneous plasticity is justified.

It is difficult to say exactly how much of the strain is instantaneous plasticity and how much is primary creep, and even if it is worth distinguishing between the two. An alternative is to use a model such as the McDowell unified creep-plasticity model [29, 27] which appears to accurately capture the behaviour of SnPb solder using isotropic and kinematic hardening and no instantaneous plasticity. This approach is preferable as it avoids the difficult-to-measure distinction of how much strain is due to instantaneous plasticity and how much is due to creep.

Although going beyond steady-state creep modelling to include instantaneous plasticity and/or hardening results in more accurate predictions of the solder behaviour, it remains unproven as to whether this will yield significantly improved life-time predictions.

### 2.2.10 Fatigue laws

Fatigue laws are required to predict the number of cycles to fail when provided with either the accumulated effective creep strain or the strain energy from a simulation. A review of fatigue laws for solder is provided by Lee et. al. [30]. The simplest fatigue laws are the Coffin Manson law equation (2.27) and the strain energy based law equation (2.28) used by Akay [31].

$$\Delta\gamma = c_1 N_f^{c_2} \quad (2.27)$$

---

## 2.2. Constitutive Law + Fatigue Law Methods

---

$$N_f = \left( \frac{\Delta W}{c_1} \right)^{1/c_2} \quad (2.28)$$

If a creep law is used which outputs more than one kind of plastic strain then the fatigue law may make use of this added data to predict the contributions to lifetime from different damage mechanisms. The following equation can then be used to calculate the overall  $N_f$ :

$$\frac{1}{N_f} = \frac{1}{N_f^1} + \frac{1}{N_f^2} + \dots + \frac{1}{N_f^n} \quad (2.29)$$

Where  $N_f^1, N_f^2, \dots, N_f^n$  are the number of cycles to fail predicted separately for each of the  $n$  damage mechanisms. An example of this is provided by Syed [12] where the low-stress creep and high-stress creep contributions predicted using the Wiese double power law equation (2.19) were used to predict the fatigue life:

$$N_f = (0.013\varepsilon_{acc}^I + 0.036\varepsilon_{acc}^{II})^{-1} \quad (2.30)$$

This law along with strain and energy based laws (equations (2.2) and (2.28) respectively) were calibrated with a set of experimental data on assemblies with four different ball pitches and sizes, three different substrate materials and three different accelerated temperature profiles using SnAgCu solder. All of the models were found to predict the characteristic lifetimes to within 25% in most cases [12].

Darveaux published a methodology [10] using fatigue laws which predict the time to crack initiation and the growth rate of the primary and secondary cracks in a SnPb solder bump joint. The crack growth rates are assumed to be constant making the prediction of overall lifetime possible. This has since been updated and simplified [13] by combining the primary and secondary crack propagation rates. Darveaux used FEA and calculated  $\Delta W$  by averaging over a layer of solder  $25\mu\text{m}$  thick adjacent to the package interface where the cracks are expected to develop. This was then used in a law for predicting time to crack initiation  $N_0$ , and a law for the crack propagation rate  $\frac{da}{dN}$ :

$$N_o = c_1 \Delta W^{-c_2} \quad (2.31)$$

$$\frac{da}{dN} = c_3 \Delta W^{c_4} \quad (2.32)$$

The characteristic life  $\eta$ , and failure free life  $N_{ff}$  can then be calculated from:

$$\eta = N_o + \frac{a}{da/dN} \quad (2.33)$$


---



---

### 2.3. Damage Mechanics Method

---

$$N_{ff} = \frac{\eta}{2} \quad (2.34)$$

Also provided [13] is a formula to calculate the overall characteristic life based on the number of worst-case joints present in the whole system (typically only the 4 or 8 highest-stressed joints contribute in a BGA package as this is where the vast majority of failures occur). The method predicted lifetimes with an accuracy of  $\pm 2\times$  or better<sup>2</sup>.

When using any fatigue law it is important to understand that it will work best under conditions similar to that for which the constants were validated. Changing conditions such as chip geometry or temperature profile, or the volume over which averaging of  $\varepsilon_{acc}$  or  $\Delta W$  is performed will effect the accuracy of the lifetime model and its predictions. The accuracy of predictions was found to be in error by a factor of up to  $7\times$  when using a modelling procedure not consistent with that used in crack growth correlation [13]. The use of relative predictions is recommended [13] when there is at least one data set of measured fatigue lifetime for the package in question. The procedure is to first calculate the lifetime for the known case, then any further calculations on different cases can be ‘calibrated’ using the experimental data. The accuracy of relative predictions were found to be in the range of  $\pm 25\%$  or better.

FEA + Fatigue laws can be useful in rating potential designs and undertaking trade-off analysis. But the approach is an empirical method tailored to a specific experimental data set. One of the reasons that many researchers are investigating the use of damage mechanics methods is that these will hopefully remain accurate over a wider data set without having to be re-calibrated.

## 2.3 Damage Mechanics Method

In order to overcome the geometry dependence inherent in the fatigue law approach to predicting lifetime, or to allow crack paths to be predicted, damage-based constitutive laws can be used. A number of researchers have published results from such laws for SnPb solder although the approach is still in the experimental stage. A review covering several methods is provided by Desai [32]. Detailed validation against a

---

<sup>2</sup>Please bear in mind that the accuracies quoted for the different models are not directly comparable as they are based upon different sets of experimental data.

---

## 2.3. Damage Mechanics Method

---

large set of experimental data has not been found for any of these models and the computational cost involved is high. Given time, with the increase in computational power and continued research including more validation against experimental life-time data, this approach may prove useful in predicting reliability.

### 2.3.1 J-integral

The J-integral is used in fracture-mechanics and represents the energy released per unit crack area for a nonlinear-elastic material. It is not intended for use in materials which exhibit plasticity away from the crack tip and therefore is perhaps not suitable for modelling solder. However Ghavifekr and Michel [33] determine the relationship between the J-integral of a notched solder tensile test specimen and the crack growth rate and suggest that it can be applied to the prediction of growth rate in solder joints. And Gu and Nakamura [34] use the method to determine the direction (but not rate) of crack propagation in a solder bump joint.

A simplistic use of the method may be to predict the crack growth rate at the small notch and assume a constant propagation speed. Darveaux has shown that in BGA bump joints the crack propagation speed is roughly constant, making this viable, however other kinds of joint do not show constant crack speed (e.g. resistor joints [35]). A more advanced approach would be to advance the crack through the mesh by small amounts, refining the mesh to achieve a high mesh density around the crack tip, and predict the crack propagation speed at each point in the cracks life. One drawback to the use of the J-integral method for predicting reliability is the necessity to manually introduce small cracks (notches). It can't predict the time or location of crack initiation. No work has been found which validates lifetime predictions using the J-integral method against experimental data.

### 2.3.2 Disturbed State Concept

Using a continuum damage approach, the damage builds up within the bulk of the material, allowing for the modelling of regions of cracking rather than one sharp crack as in the J-integral method. This can capture the phenomena seen in solder of small



---

## 2.3. Damage Mechanics Method

---

microcracks gradually forming within a region and coalescing to form macro-cracks [36].

A framework for implementing a continuum damage model is the Disturbed State Concept which is described by Desai and Whitenack [32]. This regards a material as a composite, containing two different parts - the intact part and the adjusted/disturbed/damaged part, each of which has its own set of material properties. In the case of modelling fatigue damage, the adjusted (or damaged) part would have no resistance to shear stresses and possibly no resistance to hydrostatic stresses. The implementation of this approach is simpler than the J-integral methods in that the mesh does not need to be split (although refining could aid accuracy). Another big advantage is that no prior information on the location of the crack is required. An example of this approach is the damage law described on page 72.

A formula based on accumulated effective strain in the solder can be used to calculate damage:

$$D = 1 - \exp(-c_1 \varepsilon_{acc}^{c_2}) \quad (2.35)$$

However it is stated by Basaran et al. [37] that although  $\varepsilon_{acc}$  is often used to calculate damage, entropy is a better damage metric. Volume averaging is necessary to avoid mesh dependence [38], this raises the issue of the size of the volume to use. In reality, the influence of microcrack interaction occurs over a fairly small length scale, however if the scale is made smaller than the mesh element size then volume averaging will have no effect.

### 2.3.3 Cohesive zone

This technique models the gradual degradation in the adhesion between surfaces, making it ideal for modelling delamination at solder/pad interfaces. The method uses flat, 2D elements, called cohesive zone elements, at an interface along which a crack is expected to develop (e.g. the solder to copper pad interface, or the region of intermetallics near the top of a BGA joint). This element has a stiffness which governs how far it separates (in normal and/or shear directions) depending on the applied stress. As the normal and/or shear separation increases or cycles then the damage present in the element increases and this in turn reduces its stiffness. This

### 2.3. Damage Mechanics Method

---

is very similar to the continuum damage approach except using 2D rather than 3D elements.

Abdul-Baqi et. al. [39] have described a method whereby the bulk of the solder is modelled using a linear elastic law, but with cohesive zones at the solder-pad interface, the interfaces between the phases of SnPb (Pb-rich islands within a Sn-rich matrix) and even in the grain boundaries within each phase. The cohesive zones each have an associated damage parameter  $D$  which evolves according to:

$$\dot{D} = c_1 |\dot{\mu}| (1 - D + c_2)^{c_3} \left( \frac{|Y|}{1 - D} - c_4 \right) \quad (2.36)$$

An increase in the damage leads to a decrease of stiffness as governed by:

$$Y = h(1 - D)\mu \quad (2.37)$$

By using cohesive zones to model four kinds of interface (solder to pad, Sn-rich phase to Pb-rich phase, Sn-rich grain boundary, Pb-rich grain boundary) the method offers a potentially very accurate description of the solder behaviour. However a model is useless without accurate material constants and it is not mentioned how the material properties for these different cohesive zones should be found. Finding the parameters of just one kind of cohesive zone could be done reasonably by using an inverse analysis / optimisation approach, but though the approach could be applied in this case, it is likely that the relative proportion of damage occurring in each kind of cohesive zone (solder to pad, grain boundaries, etc.) will be very difficult to predict.

A consequence of using many layers of cohesive zone elements throughout a joint is that the compliance of the cohesive zone will affect the compliance of the bulk of solder. This is an unwanted side affect and Abdul-Baqi et. al. [39] have in their work ensured that the contribution on the joint compliance from the cohesive zones in their initial, undamaged state is negligible. The cohesive zones remain stiff under compression, thus preventing the unrealistic occurrence of overlapping crack surfaces.

A model is proposed by Yang et. al. [40] in which a single cohesive zone element is used to model SnPb solder in a pure shear cyclic fatigue test. Strangely, the cohesive zone in this model has a thickness, therefore strains are discussed rather than separations or displacements, making it fit the description of a continuum damage model better than the cohesive zone model they describe it as. Separate laws are



---

### 2.3. Damage Mechanics Method

---

used to describe the damage evolution under monotonic strain  $D_{\text{mon}}$  and cyclic strain  $D_{\text{cyc}}$ :

$$\frac{\partial D_{\text{mon}}}{\partial \gamma} = 0.166\gamma^{-0.648} \quad (2.38)$$

$$\frac{\partial D_{\text{cyc}}}{\partial \gamma} = 0.067\gamma^{-0.543} \quad (2.39)$$

This reflects the fact that it takes considerably less accumulated strain to destroy a joint under monotonic loading, than it does under cyclic loading. The way that these are used in a simulation is to use equation (2.38) to model the 1st half cycle, and then use equation (2.39) for all the remaining cycles. In actual fact the use of equation (2.38) to model the 1st half-cycle is probably insignificant, given that 1000s of cycles are typically necessary to cause failure.

#### 2.3.4 Hybrid

Towashiraporn et. al. [41] describe a method in which a damage parameter is calculated based on the accumulated effective strain according to equation (2.35), as might be done with a continuum damage approach. But unlike a continuum damage approach, the damage doesn't effect the stiffness of the bulk of the material, instead, the damage is monitored across the critical interface where the crack is expected to develop. When the damage at a node in this interface reaches a critical value, the connectivity at that node is released, thus creating a crack. In order to reduce computation time, a global-local submodelling method was used. This involves first performing a simulation on a 1/8 symmetry mesh of the whole BGA package. From this, the displacements at the top and bottom interfaces of the most critical solder joint are used as boundary conditions in a more detailed simulation of the critical joint. This was found to be inadequate due to the changing response of the solder as the crack grows. To capture this a more sophisticated method was used where the refined submodel was coupled to the whole assembly model by multiple constraints. However this involved considerably more computational effort.

To save on computational expense, an approximate solution procedure is used which utilises a critical disturbance range rather than a single value. The damage accumulation rate is calculated from a simulation of two cycles. This rate is assumed to remain constant and used to work out the cycle before the most damaged node

---

## 2.4. Discussion

---

will increase beyond the upper bound of the critical disturbance range. At this cycle, all nodes with damage falling within the critical range are disconnected, and the process is repeated iteratively until 70% of the interface is cracked, at which point the joint is considered to have failed. The 70% figure is chosen because it was found experimentally that only 70% of a BGA joint crack is caused by creep-fatigue and the remaining 30% is caused from shear overload. This is also supported by simulations continuing beyond 70% cracking which predict a roughly constant rate of crack growth up to 70%, followed by an exponential increase in crack growth rate. It was found that increasing the critical disturbance range from (0.75-0.85) to (0.5-0.9) did not affect lifetime predictions adversely, but it did reduce the accuracy of crack front predictions.

This is an interesting approach but as with all the damage mechanics methods is in need of further experimental validation. Also the fact that the critical surface must be specified beforehand makes this method unsuitable for modelling new or more complicated geometries.

## 2.4 Discussion

For many engineers, an analytical method is attractive due to its ease of use. Furthermore both Engelmaier [8] and Clech [14] have achieved lifetime predictions with an error of less than  $\pm 2\times$  with analytical approaches. However, these methods do not model the creep behaviour of the solder and are therefore limited in their capability to model a wide range of temperature conditions and geometries. The caveat restricting its use under large temperature ranges ( $-50^{\circ}\text{C}$  -  $80^{\circ}\text{C}$ ) makes Engelmaier's method unsuitable to model many accelerated thermal profiles of interest.

A constitutive law + fatigue model will offer more accurate results, with fewer caveats to its range of applicability. Darveaux [13] has shown that lifetimes can be predicted with an accuracy of 25% for relative predictions, and  $\pm 2\times$  for absolute predictions. Syed [12] has also shown a good correlation with experimental results. The use of the Anand isotropic hardening law [22] is popular but arguably inappropriate since the kinematic hardening may have a greater influence over solder behaviour. The inclusion of kinematic hardening laws should improve prediction of solder strains



## 2.4. Discussion

---

but the impact on reliability predictions is at present unproven. The disadvantage of Finite Element methods is the expertise and time required to set up the analysis. This can be partly overcome by using simpler numerical methods such as Clech's SRS software [14], but these approaches do not capture all the geometry details possible using FEA.

All of the above methods make use of an empirical fatigue law whose constants are geometry dependent, the more advanced damage mechanics based methods avoid the geometry dependence to a large extent by explicitly modelling the crack propagation. They offer the potential for even better accuracy of results over an even wider range of conditions, but are in need of further development and experimental validation before they can be recommended to industry.

# Chapter 3

## FEA Theory

This chapter will describe the theory necessary to solve linear structural problems using FEA. The FEA code FATMAN (Finite-element Analysis Tool, Multiphysics And Nonlinear) was developed for this work and its results are validated against ANSYS on a test case at the end of this chapter.

The minimisation of total potential energy principle is used to derive the FEA discretisation. This method and other alternatives such as the weighted residuals method are covered in standard FEA texts [42, 43].

The FEA discretisation is conceptually simple, it involves:

1. Imposing a mesh of elements and nodes over the domain.
2. Limiting the number of DOFs (Degrees Of Freedom, or displacements) to a finite number, each acting in either  $x$ ,  $y$  or  $z$  on a node in the mesh.
3. Providing a method to interpolate between the DOFs to determine the displacement at any point in the domain (shape functions). From this the internal stored strain energy  $W^{int}$  can be calculated for any given arrangement of DOFs.
4. Lumping all externally applied forces/pressures into discrete forces acting on the nodes. The external potential energy  $W^{ext}$  decreases when these forces do work.



---

### 3.1. Physics

---

5. Finding the combination of DOFs which minimise the overall potential energy  $W^{total} = W^{int} + W^{ext}$ .

OR (another way of understanding the same thing):

Finding the combination of DOFs which balance the externally applied force with the internal reaction force at each node (the internal reaction force being the derivative of strain energy w.r.t. the direction of the associated DOF)

The method will now be described in more detail.

## 3.1 Physics

The deformation of a solid material can be described by the displacement field  $\underline{u}$ .

$$\underline{u} = \begin{bmatrix} u \\ v \\ w \end{bmatrix} \quad (3.1)$$

Where  $u, v$  and  $w$  represent the displacement in  $x, y$  and  $z$  respectively. The elastic strain,  $\underline{\varepsilon}^{el}$  consists of gradients of the displacement:

$$\underline{\varepsilon}^{el} = \begin{bmatrix} \varepsilon_{xx} \\ \varepsilon_{yy} \\ \varepsilon_{zz} \\ \gamma_{xy} \\ \gamma_{yz} \\ \gamma_{zx} \end{bmatrix} = \begin{bmatrix} \frac{\partial}{\partial x} & 0 & 0 \\ 0 & \frac{\partial}{\partial y} & 0 \\ 0 & 0 & \frac{\partial}{\partial z} \\ \frac{\partial}{\partial y} & \frac{\partial}{\partial x} & 0 \\ 0 & \frac{\partial}{\partial z} & \frac{\partial}{\partial y} \\ \frac{\partial}{\partial z} & 0 & \frac{\partial}{\partial x} \end{bmatrix} \underline{u} \quad (3.2)$$

The stress  $\underline{\sigma}$  is related to the strain by the elasticity matrix  $[\mathbf{D}]$ :

$$[\mathbf{D}] = \frac{E}{(1+\nu)(1-2\nu)} \begin{bmatrix} 1-\nu & \nu & \nu & 0 & 0 & 0 \\ \nu & 1-\nu & \nu & 0 & 0 & 0 \\ \nu & \nu & 1-\nu & 0 & 0 & 0 \\ 0 & 0 & 0 & \frac{1-2\nu}{2} & 0 & 0 \\ 0 & 0 & 0 & 0 & \frac{1-2\nu}{2} & 0 \\ 0 & 0 & 0 & 0 & 0 & \frac{1-2\nu}{2} \end{bmatrix} \quad (3.3)$$


---

---

## 3.2. Discretisation

---

$$\underline{\sigma} = \begin{bmatrix} \sigma_{xx} \\ \sigma_{yy} \\ \sigma_{zz} \\ \sigma_{xy} \\ \sigma_{yz} \\ \sigma_{zx} \end{bmatrix} = [\mathbf{D}]\underline{\varepsilon} \quad (3.4)$$

The strain energy stored within a volume  $V$  is given by:

$$W = \frac{1}{2} \int_V \underline{\varepsilon}^T \underline{\sigma} dV \quad (3.5)$$

## 3.2 Discretisation

### 3.2.1 Geometry

In the Finite Element Method the domain is split into nodes and elements. The values being solved for are stored at the nodes, in the case of elasticity this is the displacement. Force loads are also stored at the nodes. Within each element are integration points used to perform numerical integration during the building of the system matrix. Other values such as material properties and stress and strain values are typically stored at the element centers (although storage at the integration points is also possible).

### 3.2.2 The Element

Many element types can be used, each having different shapes and different numbers of nodes. In FATMAN two element types are defined – the wedge with 6 nodes and the brick with 8 nodes. Both are solid elements, other element types such as beam and shell elements are not discussed in this work.

The global coordinate system  $(x, y, z)$  is used to describe the whole Finite Element mesh. But an element type is defined in terms of a local coordinate system  $(r, s, t)$ ,



### 3.2. Discretisation

for example an 8-noded 3D brick element is defined as a perfect cube centered at the origin and with sides of 2 units length in local coordinates as shown in figure 3.1. The local coordinates  $[\mathbf{r}_i] = [r_i \ s_i \ t_i]$  for each node  $i$  are listed below for the brick element in table 3.1.

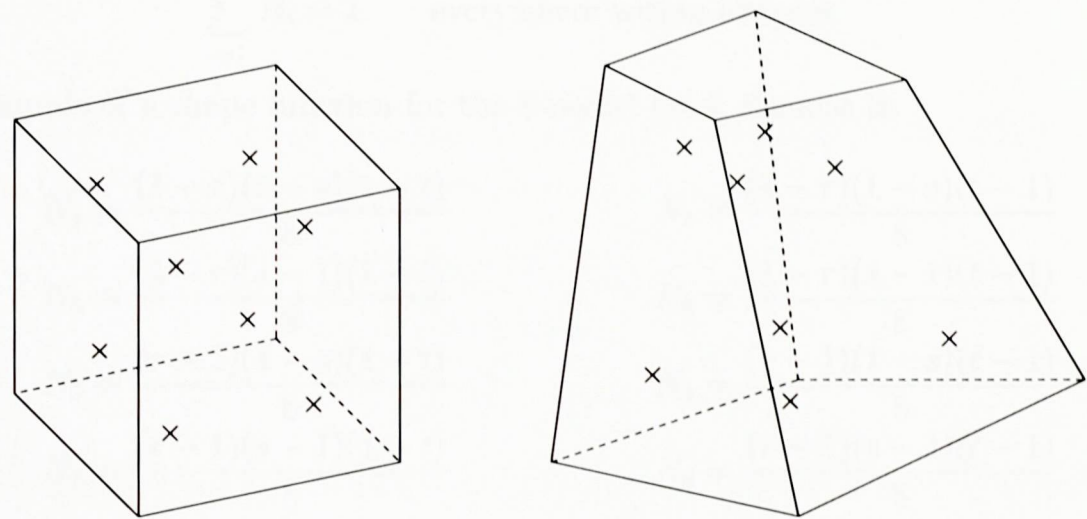


Figure 3.1: Example of an 8 noded brick element in local  $(r, s, t)$  coordinates (left) and global  $(x, y, z)$  coordinates (right). The approximate locations of the integration points are marked with Xs.

node $i$	$r_i$	$s_i$	$t_i$
1	-1	-1	-1
2	-1	-1	1
3	-1	1	-1
4	-1	1	1
5	1	-1	-1
6	1	-1	1
7	1	1	-1
8	1	1	1

Table 3.1: The coordinates of the nodes for the 8-node brick element

#### 3.2.3 Shape Functions

Values stored at the nodes are interpolated within each element using a shape function  $[\mathbf{N}]$ :

$$[\mathbf{N}] = \begin{bmatrix} N_1 & \dots & N_n \end{bmatrix} \tag{3.6}$$

Where  $N_i$  is the weight associated with node  $i$  and is a function of the position within the element. At node  $i$ ,  $N_i$  must be equal to 1 and at every point in the element the

### 3.2. Discretisation

---

sum of all weights must be 1:

$$N_i = 1 \quad \text{at} \quad \underline{s}_i \quad (3.7)$$

$$\sum_{i=1}^n N_i = 1 \quad \text{everywhere within element} \quad (3.8)$$

An example of a shape function for the 8-noded brick element is:

$$\begin{aligned} N_1 &= \frac{(1-r)(1-s)(1-t)}{8} & N_2 &= \frac{(1-r)(1-s)(t-1)}{8} \\ N_3 &= \frac{(1-r)(s-1)(1-t)}{8} & N_4 &= \frac{(1-r)(s-1)(t-1)}{8} \\ N_5 &= \frac{(r-1)(1-s)(1-t)}{8} & N_6 &= \frac{(r-1)(1-s)(t-1)}{8} \\ N_7 &= \frac{(r-1)(s-1)(1-t)}{8} & N_8 &= \frac{(r-1)(s-1)(t-1)}{8} \end{aligned}$$

Given the values of a scalar field  $\phi$  at each of the element nodes ( $\phi = \phi_i$  at node  $i$ ), the value of  $\phi$  any point within the element is given by:

$$\phi = \sum_{i=1}^n N_i \phi_i \quad (3.9)$$

The same thing can be written in matrix notation as:

$$\phi = [\mathbf{N}] \begin{bmatrix} \phi_1 \\ \vdots \\ \phi_n \end{bmatrix} \quad (3.10)$$

The shape function is also used to relate the local coordinate system to the global coordinate system:

$$[\mathbf{x}] = \begin{bmatrix} x & y & z \end{bmatrix} = [\mathbf{N}] \begin{bmatrix} [\mathbf{x}_1] \\ \vdots \\ [\mathbf{x}_n] \end{bmatrix} \quad (3.11)$$

Where  $[\mathbf{x}]$  is the position in the global coordinate system corresponding to the current local coordinates and  $[\mathbf{x}_i] = \begin{bmatrix} x_i & y_i & z_i \end{bmatrix}$  is the position of node  $i$  in global coordinates.



---

## 3.2. Discretisation

### 3.2.4 Degrees of Freedom

The displacement at node  $i$  is represented by:

$$[\mathbf{u}_i] = \begin{bmatrix} u_i & v_i & w_i \end{bmatrix} \quad (3.12)$$

Where  $(u_i, v_i, w_i)$  is the displacement at node  $i$  in global coordinates. Each  $n$ -noded element has  $3n$  degrees of freedom represented by matrix  $[\hat{\mathbf{u}}]$ :

$$[\hat{\mathbf{u}}] = \begin{bmatrix} [\mathbf{u}_1] \\ \vdots \\ [\mathbf{u}_n] \end{bmatrix} = \begin{bmatrix} u_1 & v_1 & w_1 \\ \vdots & \vdots & \vdots \\ u_n & v_n & w_n \end{bmatrix} \quad (3.13)$$

Just as for the global coordinates (3.11), the shape function is used to interpolate the displacement within the element from the nodal values:

$$[\mathbf{u}] = [\mathbf{N}][\hat{\mathbf{u}}] \quad (3.14)$$

### 3.2.5 Local & Global Derivatives

The derivative of each of the shape function weights with respect to the local coordinates is:

$$[\mathbf{N}^1] = \begin{bmatrix} \frac{\partial[\mathbf{N}]}{\partial r} \\ \frac{\partial[\mathbf{N}]}{\partial s} \\ \frac{\partial[\mathbf{N}]}{\partial t} \end{bmatrix} = \begin{bmatrix} \frac{\partial N_1}{\partial r} & \cdots & \frac{\partial N_n}{\partial r} \\ \frac{\partial N_1}{\partial s} & \cdots & \frac{\partial N_n}{\partial s} \\ \frac{\partial N_1}{\partial t} & \cdots & \frac{\partial N_n}{\partial t} \end{bmatrix} \quad (3.15)$$

When the nodal degrees of freedom (displacements)  $[\hat{\mathbf{u}}]$  is multiplied by  $[\mathbf{N}^1]$  it gives the matrix  $[\mathbf{L}]$  of local derivatives of the displacement:

$$[\mathbf{L}] = \begin{bmatrix} \frac{\partial[\mathbf{u}]}{\partial r} \\ \frac{\partial[\mathbf{u}]}{\partial s} \\ \frac{\partial[\mathbf{u}]}{\partial t} \end{bmatrix} = [\mathbf{N}^1][\hat{\mathbf{u}}] \quad (3.16)$$

### 3.2. Discretisation

---

And when the global coordinates  $[\mathbf{x}]$  are multiplied by  $[\mathbf{N}^l]$  it gives the Jacobian matrix  $[\mathbf{J}]$ :

$$[\mathbf{J}] = \begin{bmatrix} \frac{\partial x}{\partial r} & \frac{\partial y}{\partial r} & \frac{\partial z}{\partial r} \\ \frac{\partial x}{\partial s} & \frac{\partial y}{\partial s} & \frac{\partial z}{\partial s} \\ \frac{\partial x}{\partial t} & \frac{\partial y}{\partial t} & \frac{\partial z}{\partial t} \end{bmatrix} = [\mathbf{N}^l][\mathbf{x}] \quad (3.17)$$

The global displacement derivatives (which we need for further calculations) are represented by  $[\mathbf{G}]$ :

$$[\mathbf{G}] = \begin{bmatrix} \frac{\partial [\mathbf{u}]}{\partial x} \\ \frac{\partial [\mathbf{u}]}{\partial y} \\ \frac{\partial [\mathbf{u}]}{\partial z} \end{bmatrix} = [\mathbf{N}^g][\hat{\mathbf{u}}] \quad (3.18)$$

When  $[\mathbf{G}]$  is multiplied by the Jacobian  $[\mathbf{J}]$  it gives the local displacement derivatives  $[\mathbf{L}]$ :

$$[\mathbf{J}][\mathbf{G}] = [\mathbf{L}] \quad (3.19)$$

Multiplying both sides by  $[\mathbf{J}]^{-1}$ :

$$[\mathbf{G}] = [\mathbf{J}]^{-1}[\mathbf{L}] \quad (3.20)$$

Substituting in (3.16):

$$[\mathbf{G}] = [\mathbf{J}]^{-1}[\mathbf{N}^l][\hat{\mathbf{u}}] \quad (3.21)$$

We now have the global derivatives  $[\mathbf{G}]$  as a linear combination of the nodal displacements  $[\hat{\mathbf{u}}]$ . By inspection with (3.18) we see that:

$$[\mathbf{N}^g] = [\mathbf{J}]^{-1}[\mathbf{N}^l] \quad (3.22)$$

#### 3.2.6 Stress & Strain

The components of the strain tensor  $\varepsilon_{ij}$  are composed of a linear combination of components from the global displacement derivatives  $[\mathbf{G}]$  and are represented as a



### 3.2. Discretisation

---

vector  $\underline{\varepsilon}$  for convenience:

$$\underline{\varepsilon}^{el} = \begin{bmatrix} \varepsilon_{xx}^{el} \\ \varepsilon_{yy}^{el} \\ \varepsilon_{zz}^{el} \\ \gamma_{xy}^{el} \\ \gamma_{yz}^{el} \\ \gamma_{zx}^{el} \end{bmatrix} = \begin{bmatrix} \frac{\partial u}{\partial x} \\ \frac{\partial v}{\partial x} \\ \frac{\partial w}{\partial x} \\ \frac{\partial u}{\partial y} + \frac{\partial v}{\partial x} \\ \frac{\partial v}{\partial z} + \frac{\partial w}{\partial y} \\ \frac{\partial w}{\partial x} + \frac{\partial u}{\partial z} \end{bmatrix} = \begin{bmatrix} G_{11} \\ G_{22} \\ G_{33} \\ G_{12} + G_{21} \\ G_{23} + G_{32} \\ G_{31} + G_{13} \end{bmatrix} \quad (3.23)$$

Where  $\varepsilon_{ii}$  are the normal strains and  $\gamma_{ij}$  are the engineering shear strains.

In order to simplify the following maths it is necessary to represent the element's nodal displacements  $[\hat{\mathbf{u}}]$  as a vector  $\underline{U}$ :

$$\underline{U} = \begin{bmatrix} u_1 \\ v_1 \\ w_1 \\ u_2 \\ v_2 \\ w_2 \\ \vdots \\ u_n \\ v_n \\ w_n \end{bmatrix} \quad (3.24)$$

Where  $(u_i, v_i, w_i)$  is the displacement at node  $i$  and  $n$  = number of nodes in the element.

The strain can now be calculated by multiplying  $\underline{U}$  by the  $[\mathbf{B}]$  matrix:

$$\underline{\varepsilon}^{el} = [\mathbf{B}]\underline{U} \quad (3.25)$$

### 3.2. Discretisation

---

Where the  $[\mathbf{B}]$  matrix is defined based on equations (3.18) and (3.22):

$$[\mathbf{B}] = \begin{bmatrix} N_{11}^g & 0 & 0 & N_{12}^g & 0 & 0 & \dots & N_{1n}^g & 0 & 0 \\ 0 & N_{21}^g & 0 & 0 & N_{22}^g & 0 & \dots & 0 & N_{2n}^g & 0 \\ 0 & 0 & N_{31}^g & 0 & 0 & N_{32}^g & \dots & 0 & 0 & N_{3n}^g \\ N_{21}^g & N_{11}^g & 0 & N_{22}^g & N_{12}^g & 0 & \dots & N_{2n}^g & N_{1n}^g & 0 \\ 0 & N_{31}^g & N_{21}^g & 0 & N_{32}^g & N_{22}^g & \dots & 0 & N_{3n}^g & N_{2n}^g \\ N_{31}^g & 0 & N_{11}^g & N_{32}^g & 0 & N_{12}^g & \dots & N_{3n}^g & 0 & N_{1n}^g \end{bmatrix} \quad (3.26)$$

The stress is related to the strain by the elasticity matrix  $[\mathbf{D}]$  defined in equation (3.3):

$$\underline{\sigma} = \begin{bmatrix} \sigma_{xx} \\ \sigma_{yy} \\ \sigma_{zz} \\ \sigma_{xy} \\ \sigma_{yz} \\ \sigma_{zx} \end{bmatrix} = [\mathbf{D}]\underline{\varepsilon} = [\mathbf{D}][\mathbf{B}]\underline{U} \quad (3.27)$$

#### 3.2.7 Elastic Energy

The stored elastic potential energy  $W'$  over a volume  $V$  is given by:

$$W' = \frac{1}{2} \int_V \underline{\varepsilon}^T \underline{\sigma} dV \quad (3.28)$$

In order to calculate this over an element, numerical integration is performed using integration points. The brick element has 8 integration points and the definition of each point  $i$  includes a position  $[\mathbf{r}']_i = \begin{bmatrix} r'_i & s'_i & t'_i \end{bmatrix}$  and volume  $V'_i$  in the local coordinate system. The sum of the volumes of the integration points must equal the total volume of the element:

$$\sum_{i=1}^n V'_i = \text{total volume of element} \quad (3.29)$$

Where  $n$  = number of integration points in the element. The volume in the global coordinate system  $V^g$  can be calculated using the determinant of the Jacobian:

$$V_i^g = \det([\mathbf{J}])V_i \quad (3.30)$$



## 3.2. Discretisation

---

The integral (3.28) is approximated by  $W^{int}$  using numerical integration:

$$W' \simeq W^{int} = \frac{1}{2} \sum_{i=1}^n V_i^g \underline{\underline{\epsilon}}^T \underline{\underline{\sigma}}|_{[\mathbf{r}]=[\mathbf{r}']_i} \quad (3.31)$$

### 3.2.8 Forces

In the FEA discretisation all the forces acting on the element are considered to be concentrated at the nodes. The external force acting on all the nodes of the element is represented by the load vector  $\underline{\underline{F}}$ :

$$\underline{\underline{F}} = \begin{bmatrix} f_{x1} \\ f_{y1} \\ f_{z1} \\ f_{x2} \\ f_{y2} \\ f_{z2} \\ \vdots \\ f_{xn} \\ f_{yn} \\ f_{zn} \end{bmatrix} \quad (3.32)$$

Where  $(f_{xi}, f_{yi}, f_{zi})$  are the components of the external force acting on node  $i$  in  $x, y$  and  $z$  respectively, these consist of forces from neighboring elements plus external boundary conditions,  $n$  = number of nodes in element. The resultant forces  $\underline{\underline{R}}_i$  consist of an internal component  $\underline{\underline{F}}^{int}$  caused by the stress in the element and an external component  $\underline{\underline{F}}$ . A solution is found when the system is in equilibrium and the resultant force at every node is 0:

$$\underline{\underline{R}} = \underline{\underline{F}}^{int} + \underline{\underline{F}} = \underline{\underline{0}} \quad (3.33)$$

The internal force is defined in terms of the derivative of internal strain energy w.r.t. displacement:

$$\underline{\underline{F}}^{int} = -\frac{\partial W^{int}}{\partial \underline{\underline{U}}} \quad (3.34)$$

---

### 3.2. Discretisation

---

Substituting (3.34) into (3.33):

$$\frac{\partial W^{int}}{\partial \underline{U}} = \underline{F} \quad (3.35)$$

#### 3.2.9 Energy Minimisation

An alternative way to arrive at (3.35) is to use the minimum total potential energy principle which states that a system is in equilibrium when its total potential energy is minimised. Consider the total energy of the whole system  $W^{total}$ :

$$W^{total} = W^{int} + W^{ext} \quad (3.36)$$

Where  $W^{ext}$  is the potential energy which decreases when the external forces  $\underline{F}$  do work:

$$W^{ext} = - \int_{\underline{U}'=0}^{\underline{U}'=\underline{U}_i} \underline{F}'^T d\underline{U}' \quad (3.37)$$

Where  $\underline{F}'$  is the transient external force which increases linearly from  $\underline{0}$  when  $\underline{U}' = 0$  to  $\underline{F}$  when  $\underline{U}' = \underline{U}$ :

$$\underline{U}' = x\underline{U} \quad (3.38)$$

$$\underline{F}' = [\mathbf{Q}]\underline{U}' \quad (3.39)$$

Where  $[\mathbf{Q}]$  is the diagonal matrix:

$$Q_{ij} = \begin{cases} F_i/U_i & \text{if } i = j \\ 0 & \text{if } i \neq j \end{cases} \quad (3.40)$$

This linear relationship between force and displacement ensures equilibrium during loading so that all of the energy is converted to strain energy and none to kinetic energy.

Substituting (3.38) and (3.39) into (3.37):

$$W^{ext} = - \int_{x=0}^{x=1} x U_i Q_{ii} U_i dx = \frac{1}{2} U_i Q_{ii} U_i \quad (3.41)$$



---

### 3.2. Discretisation

---

The derivative of the work done by external forces w.r.t. the nodal displacements is:

$$\begin{aligned}\frac{\partial W^{ext}}{\partial U_i} &= -\frac{\partial(\frac{1}{2}U_i Q_{ii} U_i)}{\partial U_i} \\ &= Q_{ii} U_i \\ &= F\end{aligned}\tag{3.42}$$

The total energy of the system is minimised when:

$$\begin{aligned}\frac{\partial W^{total}}{\partial \underline{U}} &= \frac{\partial W^{int}}{\partial \underline{U}} + \frac{\partial W^{ext}}{\partial \underline{U}} = 0 \\ &= \frac{\partial W^{int}}{\partial \underline{U}} - \underline{F} = 0\end{aligned}\tag{3.43}$$

This is the same result as (3.35).

#### 3.2.10 Calculating stiffness

The energy  $W$  can be represented as a function of  $\underline{U}$  by substituting (3.25) and (3.27) into (3.31):

$$W = \sum_{i=1}^n V_i^g \Delta W_i\tag{3.44}$$

$$\begin{aligned}\Delta W_i &= \frac{1}{2}([\mathbf{B}]\underline{U})^T [\mathbf{D}][\mathbf{B}]\underline{U}|_{\underline{r}=\underline{r}'_i} \\ &= \frac{1}{2}\underline{U}^T [\mathbf{B}]^T [\mathbf{D}][\mathbf{B}]\underline{U}|_{\underline{r}=\underline{r}'_i} \quad (i = \text{integration point})\end{aligned}\tag{3.45}$$

Writing using index notation and the Einstein summation convention:

$$\begin{aligned}\Delta W_i &= \frac{1}{2}U_k B_{jk} D_{jl} B_{lm} U_m \\ &= \frac{1}{2} [U_n^2 B_{jn} D_{jl} B_{ln} + U_k B_{jk} D_{jl} B_{lm} U_m (1 - \delta_{mk})]\end{aligned}\tag{3.46}$$

### 3.2. Discretisation

---

Where  $\delta_{ij}$  is the Kronecker delta. Differentiating w.r.t.  $U_n$ :

$$\begin{aligned} \frac{\partial \Delta W_i}{\partial U_n} = & U_n B_{jn} D_{jl} B_{ln} \quad (\text{no summation over } n) \\ & + \frac{1}{2} U_k B_{jk} D_{jl} B_{ln} (1 - \delta_{kn}) \\ & + \frac{1}{2} U_m B_{jn} D_{jl} B_{lm} (1 - \delta_{mn}) \end{aligned} \quad (3.47)$$

But  $[\mathbf{D}]$  is symmetric  $D_{ij} = D_{ji}$  so:

$$\frac{\partial \Delta W_i}{\partial U_n} = B_{jn} D_{jl} B_{lk} U_k \quad (3.48)$$

Writing in matrix form:

$$\frac{\partial \Delta W_i}{\partial \underline{U}} = [\mathbf{B}]^T [\mathbf{D}] [\mathbf{B}] \underline{U} \quad (3.49)$$

Equation (3.35) (or (3.43)) can now be written as a linear system for all the nodes in the element:

$$[\mathbf{K}_e] \underline{U} = \underline{F} \quad (3.50)$$

Where  $[\mathbf{K}_e]$  is the stiffness matrix for the element:

$$[\mathbf{K}_e] = \sum_{i=1}^n [\mathbf{B}]^T [\mathbf{D}] [\mathbf{B}] \quad (3.51)$$

Note that the the form of equation (3.51) means that  $[\mathbf{K}_e]$  is symmetric so long as  $[\mathbf{D}]$  is symmetric. The stiffness matrix  $[\mathbf{K}]$  relating the degrees of freedom (displacements) to the nodal forces over the whole mesh is the sum of all the element stiffness matrices:

$$[\mathbf{K}] = \sum_{e=1}^M [\mathbf{K}_e] \quad (3.52)$$

$$[\mathbf{K}] \underline{U}_s = \underline{F}_s \quad (3.53)$$

Where  $M$  is the total number of elements in the mesh and  $[\mathbf{K}_e]$  is the stiffness matrix for element  $e$ . The final system matrix will be sparse (populated mostly by zeros) for all but the most trivial problems, the data structure used to store the matrix is described in appendix B.



### 3.2.11 Boundary Conditions

The load vector consists of multiple components:

$$\underline{F} = \underline{F}^{ext} + \underline{F}^{th} + \underline{F}^{pl} \quad (3.54)$$

Where  $\underline{F}^{ext}$  = prescribed external load,  $\underline{F}^{pl}$  = plastic load and  $\underline{F}^{th}$  = thermal load.

The plastic and thermal contributions to the load vector  $\underline{F}$  do not represent actual physical forces but are used to ensure the correct overall strain  $\underline{\varepsilon}$  in the solution:

$$\underline{\varepsilon} = \underline{\varepsilon}^{el} + \underline{\varepsilon}^{th} + \underline{\varepsilon}^{pl} \quad (3.55)$$

Where  $\underline{\varepsilon}^{th}$  is:

$$\underline{\varepsilon}^{th} = \alpha \Delta T \quad (3.56)$$

Where  $\alpha$  = the coefficient of thermal expansion and  $\Delta T$  = the temperature relative to the  $\underline{\varepsilon}^{th} = \underline{0}$  state. To determine  $\underline{F}^{th}$ , first use (3.25) to represent the nodal displacements  $\underline{U}^{th}$  corresponding to  $\underline{\varepsilon}^{th}$  (assuming no elastic or plastic strain) :

$$\underline{U}^{th} = [\mathbf{B}]^{-1} \underline{\varepsilon}^{th} \quad (3.57)$$

The load vector corresponding to this displacement is:

$$\underline{F}^{th} = \sum_{e=1}^M [\mathbf{K}_e] \underline{U}^{th} \quad (3.58)$$

Substituting (3.57):

$$\underline{F}^{th} = \sum_{e=1}^M [\mathbf{K}_e] [\mathbf{B}]^{-1} \underline{\varepsilon}^{th} \quad (3.59)$$

And similarly for the plastic load:

$$\underline{F}^{pl} = \sum_{e=1}^M [\mathbf{K}_e] [\mathbf{B}]^{-1} \underline{\varepsilon}^{pl} \quad (3.60)$$

### 3.2.12 Need for DOF constraints

As it stands the system cannot be solved as it is not sufficiently constrained - there is no unique solution. To sufficiently constrain a 1D system requires that at least 1 DOF is fixed, a 2D system requires at least 3 DOFs are fixed, and a 3D system requires at least 6 DOFs are fixed. This can be understood by the following reasoning:

The system matrix for a 1D problem with an independent variable  $x$ , when multiplied by the displacements  $\underline{U}$ , gives a vector (the force) which is dependent only on the derivatives of the displacements w.r.t.  $x$ . Therefore any solution  $\underline{U}$  of  $[\mathbf{K}]\underline{U} = \underline{F}$  will have a corresponding family of solutions:

$$\begin{bmatrix} U_1 + u \\ U_2 + u \\ \vdots \\ U_n + u \end{bmatrix} \quad \text{for any displacement } u \quad (3.61)$$

because the derivatives of the displacement are invariant w.r.t. translations in  $x$ .

Similarly, for a 2D problem on the  $xy$  plane,  $[\mathbf{K}]\underline{U}$  consists of a linear combination of the following 3 terms:

1.  $\frac{\partial u}{\partial x}$  - invariant w.r.t. translations in  $x$
2.  $\frac{\partial v}{\partial y}$  - invariant w.r.t. translations in  $y$
3.  $(\frac{\partial u}{\partial y} + \frac{\partial v}{\partial x})$  - invariant w.r.t. rotations in  $xy$  plane

and for a 3D problem,  $[\mathbf{K}]\underline{U}$  consists of a linear combination of the following 6 terms:

1.  $\frac{\partial u}{\partial x}$  - invariant w.r.t. translations in  $x$
2.  $\frac{\partial v}{\partial y}$  - invariant w.r.t. translations in  $y$
3.  $\frac{\partial w}{\partial z}$  - invariant w.r.t. translations in  $z$
4.  $(\frac{\partial u}{\partial y} + \frac{\partial v}{\partial x})$  - invariant w.r.t. rotations in  $xy$  plane



---

### 3.2. Discretisation

---

5.  $(\frac{\partial v}{\partial z} + \frac{\partial w}{\partial y})$  - invariant w.r.t. rotations in  $yz$  plane
6.  $(\frac{\partial w}{\partial x} + \frac{\partial u}{\partial z})$  - invariant w.r.t. rotations in  $zx$  plane

Sufficient DOF constraints need to be introduced to prevent all of the displacements being translated or rotated in any of the above ways. Only then will a unique solution exist.

#### 3.2.13 Implementing DOF constraints

There are at least two ways to set a DOF (degree of freedom)  $i$  to a fixed displacement  $u$ :

1. Remove the  $i^{\text{th}}$  row and column system matrix and add the necessary contribution to the load vector.
2. Set the system matrix diagonal:  $K_{ii} = \text{HUGE\_VAL}$  and the load vector component:  $F_i = \text{HUGE\_VAL} \times u$

The first option is preferable as it will reduce the size of the system matrix to be solved and it doesn't require the definition of an arbitrary HUGE\_VAL which needs to be large enough to sufficiently swamp the other system matrix values for a given problem. However the 2<sup>nd</sup> method has been chosen as it is simpler to implement.

Sometimes it is necessary to make DOFs a function of each other, for example when implementing a symmetry boundary condition on the  $x = y$  plane the  $u$  displacement should equal the  $v$  displacement at each node. To achieve this, the two rows and columns corresponding to each related pair of DOFs can be combined into one row and one column.

3.3 Laplace equation (thermal / electrical)

The Laplace equation is:

$$S = \nabla(-k\nabla V) \tag{3.62}$$

Where  $V$  is a potential field,  $S$  is a source term and  $k$  is a constant. This equation is used to describe steady-state thermal conductivity and electrical conductivity by substituting the variables shown in table 3.2. The discretisation is simpler than for stress analysis as we are solving for a scalar field  $V$  rather than a vector field. A full description can be found in FEA textbooks [42, 43].

Laplace term	Thermal	Electrical
$V$	$T$ (temperature)	$V$ (voltage)
$S$	$Q$ (heat source)	$Q$ (charge source)
$k$	$k$ (thermal conductivity)	$1/\rho$ ( $\rho$ = resistivity)
$-k\nabla V$	$q$ (heat flux)	$\underline{J}$ (current density)

Table 3.2: The meaning of  $V$ ,  $S$  and  $k$  in steady-state thermal and electrical applications of the Laplace equation

3.4 Solvers

This section will discuss the solvers used to solve the system matrix (3.52) resulting from the above discretisation. There are two main classes of linear solver - direct and iterative. A direct solver will generate a solution in a fixed number of steps whereas an iterative solver will gradually refine the solution over a number of steps until the desired accuracy is achieved.

The following solvers have been implemented in software and will be compared:

- 1. Conjugate gradient with Jacobi Preconditioner (iterative)
- 2. Conjugate Gradient with Incomplete Cholesky Preconditioner (iterative)
- 3. Cholesky Factorisation (Direct)



---

### 3.4. Solvers

---

All three solvers are designed to solve sparse symmetrical systems. Generally, symmetrical systems can be solved in roughly half the time it takes to solve a similarly sized unsymmetrical system. Typical non-symmetrical solvers include the Bi-Conjugate Gradient method (iterative) and LU factorisation based methods (direct)

#### 3.4.1 Cholesky Factorisation

This method factors the system matrix  $[\mathbf{K}]$  (which must be symmetrical) into two matrices  $[\mathbf{L}]$  and its transpose  $[\mathbf{L}]^T$ :

$$[\mathbf{K}] = [\mathbf{L}][\mathbf{L}]^T \quad (3.63)$$

Where the matrix  $[\mathbf{L}]$  is a lower triangular matrix:

$$L_{ij} = 0 \quad \text{if } j > i \quad (3.64)$$

The algorithm to perform this factorisation on a dense matrix is straightforward but has prohibitively large storage requirements. These can be reduced considerably if using operating on a sparse matrix by using a more complex algorithm. For this work a public domain implementation was used from Davis [44, 45, 46] and integrated with FATMAN.

Once  $[\mathbf{L}]$  has been found, backsubstitution can be used to solve for  $\underline{U}$  relatively quickly.

#### 3.4.2 Preconditioned Conjugate Gradient Method

This is an iterative solver which solves  $[\mathbf{K}]\underline{U} = \underline{F}$  for any symmetric positive definite matrix  $[\mathbf{K}]$  (the FEA discretisation always produces symmetric positive definite matrices for linear elasticity). It is the most widely used iterative method for solving sparse symmetric systems. A detailed description of the method is provided by Shewchuk [47].

The method is almost always used with a preconditioner, this is a matrix  $[\mathbf{M}]$  which

---

### 3.4. Solvers

---

approximates  $[\mathbf{K}]$  but is easy to invert. In this work a Jacobi preconditioner and an incomplete Cholesky preconditioner are compared.

The Jacobi preconditioner includes only the diagonal elements of  $K$ , therefore the inverse  $[\mathbf{M}]^{-1}$  is given by:

$$M_{ij}^{-1} = \begin{cases} 1/K_{ij} & \text{if } i = j \\ 0 & \text{if } i \neq j \end{cases} \quad (3.65)$$

The incomplete Cholesky preconditioner involves performing a modified Cholesky factorisation algorithm where the resulting factor  $[\mathbf{L}]$  contains the same arrangement of non-zeros as  $[\mathbf{K}]$ . The preconditioner matrix is then given by:

$$[\mathbf{M}]^{-1} = ([\mathbf{L}][\mathbf{L}]^T)^{-1} \quad (3.66)$$

This inverse isn't calculated explicitly, but whenever a multiplication by  $[\mathbf{M}]^{-1}$  is required backsubstitution can be used.

Using the incomplete Cholesky preconditioner is far more time consuming than using the Jacobi preconditioner in terms of the one-off setup cost ( $[\mathbf{L}][\mathbf{L}]^T$  factorisation vs.  $(\text{diag}[\mathbf{K}])^{-1}$ ) and the time taken to perform the  $[\mathbf{M}]^{-1}\underline{x}$  multiplications every iteration. However, because the incomplete Cholesky preconditioner offers a better approximation of  $[\mathbf{K}]^{-1}$  it will generally take fewer iterations to converge than the Jacobi preconditioner.

#### 3.4.3 Comparison of solvers

The main benefits of using a direct solver are a) it completes in a pre-defined number of steps, b) the solution accuracy is usually higher, and c) the factorisation or matrix inversion only needs to be performed once – solutions for different load vectors are then obtained very quickly.

The main benefit of iterative solvers is that they consume much less memory so can solve larger problems. The number of iterations required is very problem dependent



---

### 3.4. Solvers

---

and they tend to be slower than direct solvers (although for some problems they can be quicker).

To compare the speed and accuracy of the solvers, two different problems have been chosen. The first is very simple - a cube under shear loading. The second is a simulation of the fatigue test apparatus used by the NPL to obtain the experimental results presented in chapter 6, this contains a far more intricate geometry but has fewer elements and nodes than the first problem. The run time of the solvers was tested on Windows 2000 running on a 2.53GHz Pentium 4 processor with no other applications running.

Part of the difference between the speed of the solvers is due to the efficiency of the implementation, the Cholesky Factorisation routines were obtained from Davis [44, 45, 46] and have been shown to be a very efficient implementation [48]. On the other hand the incomplete Cholesky preconditioner algorithm was implemented for this work with no effort spent on code optimisation - a better implementation would reduce the simulation times.

In the following results the residual stated for all solvers is the L2-norm of the residual  $\underline{R}$  of the whole system (3.52):

$$\underline{R} = [\mathbf{K}_s]\underline{U}_s - \underline{F}_s \quad (3.67)$$

This isn't the same value used by the iterative solvers to test for convergence - the iterative solvers were considered to have converged when the L2-norm of the vector  $\underline{R}'$  reached the prescribed tolerance:

$$\underline{R}' = [\mathbf{M}]^{-1}[\mathbf{K}_s]\underline{U}_s - [\mathbf{M}]^{-1}\underline{F}_s \quad (3.68)$$

where  $[\mathbf{M}]$  is the preconditioner matrix.

#### Cube in Shear

The mesh is shown in figure 3.2 and contains 17576 nodes ( $26 \times 26 \times 26$ ). A smaller mesh of 9261 nodes ( $21 \times 21 \times 21$ ) is also investigated.

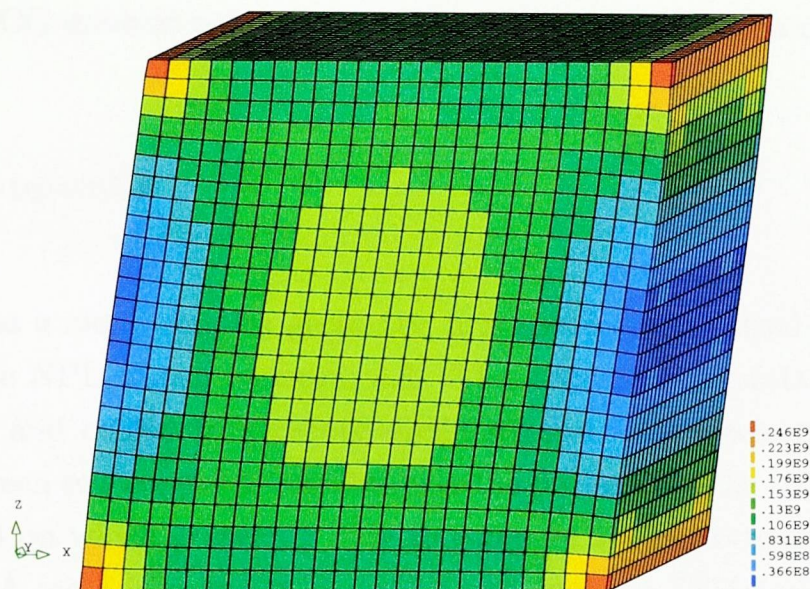


Figure 3.2: Cube under shear test case - deformation exaggerated by 30 $\times$ . Contours represent effective stress.

The bottom surface is held at zero displacement and the top surface is subjected to a 1 $\mu$ m displacement to achieve a shear deformation mode. The convergence criteria used for the two iterative solvers was  $\| \underline{R}' \| < 1 \times 10^{-14}$ .

No. of nodes		CG (Jacobi precondition)	CG (Incomplete Cholesky precondition)	Cholesky Factorisation
21 $\times$ 21 $\times$ 21	Iterations	124	44	N/A
	Time taken	4	52	18
	$\  \underline{R} \ $	8.6E-8	3.3E-8	1.7E-14
26 $\times$ 26 $\times$ 26	Iterations	155	55	N/A
	Time taken	9	180	74
	$\  \underline{R} \ $	7.9E-8	3.7E-8	2.1E-14

Table 3.3: The performance of the three solvers using two different mesh densities.

The performance of the different solvers when tackling this problem is compared in table 3.3. In both cases the Jacobi preconditioned CG (Conjugate Gradient) solver was best, followed by the Cholesky factorisation and lastly the incomplete Cholesky preconditioned CG solver. Although less iterations were required using the incomplete Cholesky preconditioner compared to the Jacobi, this is offset by the time to perform the factorisation and the increased time taken per cycle (a more efficient implementation may drastically reduce the run-time).

The reason for the good performance of the Jacobi CG solver is likely due to a low condition number of the system matrix  $[\mathbf{K}]$  for this problem. The number of iterations



required for the CG method is lower for matrices with low condition numbers [47].

**Fatigue Test Apparatus**

This test case has a more complex geometry, it is based on an actual test apparatus developed by the NPL shown in figure 3.3. The apparatus consists of a steel rod which is heated and cooled to generate cyclic stresses in a specimen containing a solder joint between two copper arms. However the purposes of the test are irrelevant to this investigation which is seeking only to compare the performance of the three solvers. The FEA mesh is shown in figure 3.4 and contains 7524 nodes, in the FEA model the specimen is approximated by a solid block of copper, ignoring the solder joint. The behaviour of the specimen will be investigated in detail in chapter 6.

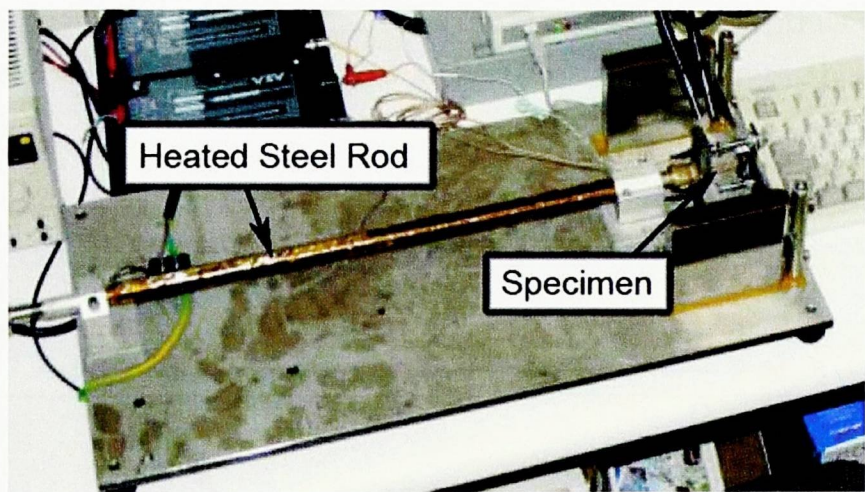


Figure 3.3: A photo of the NPL fatigue test apparatus.

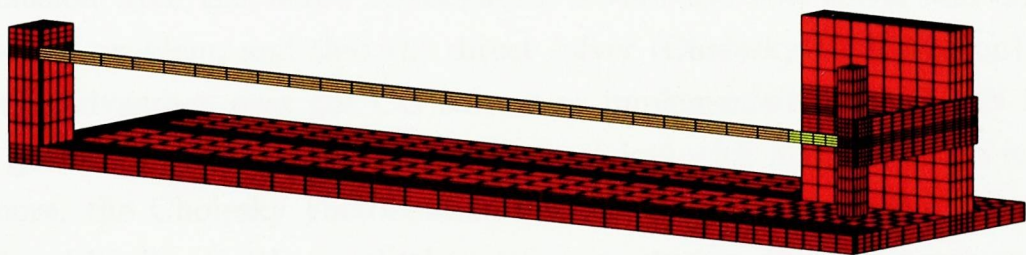


Figure 3.4: Fatigue test mesh - the orange section is at 100°C, the red and yellow sections are at 25°C.

The result of the simulation is shown in figure 3.5, the heated part has expanded

### 3.4. Solvers

causing the whole apparatus to bend. The performance of the different solvers is

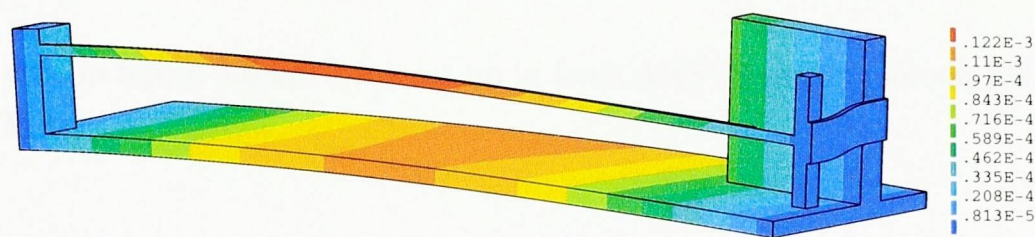


Figure 3.5: Fatigue test results. The deformation is exaggerated by 80× and the contours represent the vertical displacement

compared in table 3.4.3. The convergence criteria used for the iterative solvers was  $\| \underline{R}' \| < 1 \times 10^{-12}$ . The results are the mirror opposite of the previous test case. This time the more complex geometry favoured the direct Cholesky Factorisation solver over the iterative CG solvers. It is likely that the condition number of the system matrix for this problem is a lot higher than for the previous test, thus explaining the greater number of iterations required for the CG solvers despite there being fewer nodes and DOFs.

	CG (Jacobi precond)	CG (Incomplete Cholesky precondition)	Cholesky Factorisation
Iterations	12356	2914	N/A
Time taken	161	131	4
$\  \underline{R} \ $	3.9E-6	1.1E-6	2.4E-8

### Conclusion

The conclusion from this short investigation is that the best solver will depend on the particular problem, and that the direct solver (Cholesky Factorisation) appears to have the advantage over the CG solvers as implemented in FATMAN for more complex geometries (specifically for system matrices with high condition numbers). Furthermore, the Cholesky Factorisation has the advantage of being able to solve for additional loadings with very little extra computation, this will prove very useful when used with the implicit creep solution procedure described on page 61.



### 3.5 Verifying accuracy compared to ANSYS

The test case in figure 3.6 has been set up in both ANSYS (a commercial FEA code) and FATMAN:



Figure 3.6: The mesh for the test case run in FATMAN and ANSYS. The yellow beam is at 100 °C and the rest of the mesh is at 25 °C.

The mesh and boundary conditions are identical in both ANSYS and FATMAN. The model is made purely of copper and consists of a beam at 100 °C held between arms of 25 °C. The thermal expansion causes the whole model to bend.

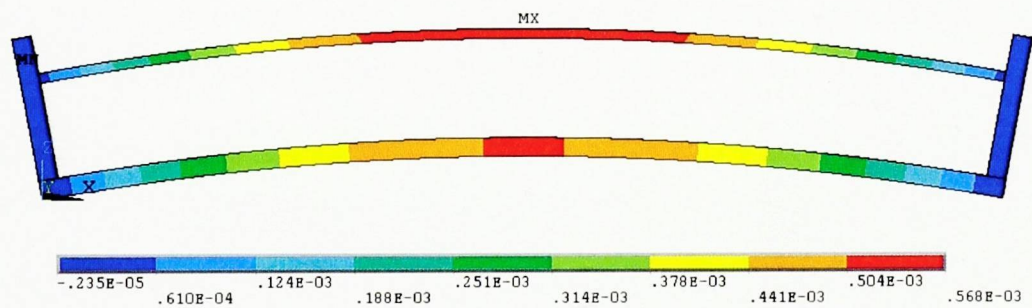


Figure 3.7: w displacements predicted by ANSYS

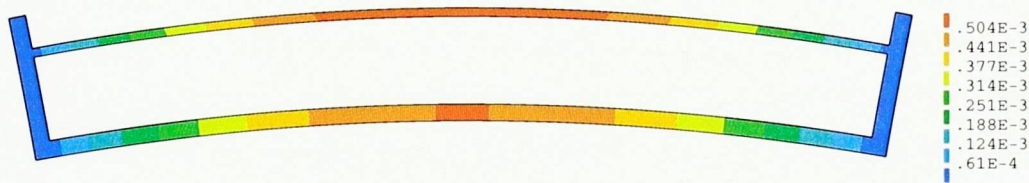


Figure 3.8: w displacements predicted by FATMAN

The results given by ANSYS (figure 3.7) and FATMAN (figure 3.8) are identical, with the maximum predicted vertical displacement at the center of the beam being 0.573mm in both cases. In FATMAN, the Cholesky Factorisation, CG with Jacobi

### 3.5. Verifying accuracy compared to ANSYS

---

preconditioner and CG with incomplete Cholesky preconditioner solvers were tested, all giving identical results.

## Chapter 4

# Solder Constitutive Law

The constitutive law for the solder joints is to be given in the following chapters and then implemented in the FEM code. The law is to be implemented as:

1. Elastic-plastic hardening law: The modulus  $E$  is a constant, this is described in the literature and is to be given in the next chapter of the book.

2. Kinematic hardening law: The kinematic hardening law is to be given in the next chapter of the book and is to be implemented in the FEM code.

3. Isotropic hardening law: The isotropic hardening law is to be given in the next chapter of the book and is to be implemented in the FEM code.

A hardening law is to be given in the next chapter of the book and is to be implemented in the FEM code. The hardening law is to be implemented in the FEM code and is to be implemented in the FEM code.

Finally a damage evolution law is described along with a criterion to be implemented in the FEM code and is to be implemented in the FEM code.



# Chapter 4

## Solder Constitutive Law

This chapter will describe the constitutive laws to be used in the following chapters and their implementation in FATMAN. The three laws implemented are:

1. **Steady state creep law.** The sinh law (2.20) was chosen, this is described in the literature review and is widely used to model creep of solder.
2. **Kinematic hardening law.** The Armstrong Frederick law (2.25) is used to capture the primary region of the creep curve shown in figure 2.4.
3. **Damage law.** The disturbed state concept is used to represent damage along with a simple damage evolution law based on the accumulated creep strain.

A novel scheme called LENI (Linear-Elastic, Nonlinear-Inelastic), used to solve for creep using an implicit discretisation is presented and its application to both the sinh law (2.20) and the Armstrong Frederick kinematic hardening law is discussed. Test cases are presented which demonstrate the benefit of an implicit discretisation over an explicit discretisation.

Finally a simple damage evolution law is described along with a method to test for failure using electrical resistance as a failure criteria. A volume averaging technique is described which partially overcomes the mesh dependence of the law. A number of test cases investigate the mesh dependence under different loading conditions.

## 4.1 Creep Law

The creep laws in chapter 2 are in a form suitable to model only one component, either pure tensile loading or pure shear loading:

$$\dot{\varphi}_{ii} = f(\sigma_{ii}) \quad \text{or} \quad \dot{\varphi}_{ij} = g(\sigma_{ij}) \quad (4.1)$$

Where  $\dot{\varphi}_{ij}$  is the creep strain rate tensor. To implement in an FEA code, this form must be generalised to provide all 6 components of the strain rate tensor when given the 6 components of the stress tensor. A creep law designed for tensile loading in the form of (4.1) can be converted to 3D form using the following equation:

$$\dot{\varphi}_{ij} = f(\sigma_{\text{eff}}) \frac{3}{2} \frac{\hat{\sigma}_{ij}}{\sigma_{\text{eff}}} \quad (4.2)$$

where  $\sigma_{\text{eff}}$  is the effective stress (also known as the Von Mises stress):

$$\sigma_{\text{eff}} = \sqrt{\frac{1}{2} [(\sigma_{xx} - \sigma_{yy})^2 + (\sigma_{yy} - \sigma_{zz})^2 + (\sigma_{zz} - \sigma_{xx})^2] + 3 [\sigma_{xy}^2 + \sigma_{yz}^2 + \sigma_{zx}^2]} \quad (4.3)$$

and  $\hat{\sigma}$  is the deviatoric stress:

$$\hat{\sigma}_{ij} = \begin{cases} \sigma_{ij} & \text{if } i \neq j \\ \frac{2\sigma_{ii} - \sigma_{kk} - \sigma_{ll}}{3} & \text{if } i = j \quad (i \neq k \neq l) \end{cases} \quad (4.4)$$

This results in a creep strain with no hydrostatic component - i.e. with no volume change.

### 4.1.1 Explicit and Implicit Time Discretisation

The simplest way to implement a creep law is to use an explicit solution procedure:

$$\underline{\varphi}^{k+1} = \underline{\varphi}^k + \dot{\underline{\varphi}}^k \Delta t^k \quad (4.5)$$

$$\Delta t^k = t^{k+1} - t^k \quad (4.6)$$

Where the superscript represents the time step and  $t^k$  is the time at time-step  $k$ . This method is susceptible to numerical instability. Due to the exponential increase of



---

## 4.1. Creep Law

---

strain rate with stress, the generation of extremely large strain rates may occur which requires very small time steps to avoid an unrealistic result or numerical overflow. The use of an implicit solution scheme avoids this:

$$\underline{\varphi}^{k+1} = \underline{\varphi}^k + \underline{\dot{\varphi}}^{k+1} \Delta t^k \quad (4.7)$$

A stress-relaxation test case highlighting the benefit of the implicit scheme is provided on page 67.

### 4.1.2 LENI (Linear-Elastic / Nonlinear-Inelastic) Scheme

This section describes the LENI scheme which utilises the linear elastic solver methods described in chapter 3 as part of an iterative scheme to solve the implicit creep discretisation (4.7). Methods exist for solving creep implicitly such as the one described by Langtangen [49]. The scheme presented here differs from the method described by Langtangen [49] in that the LENI scheme does not require the entire system matrix to be altered on each iteration. This has the benefit that the matrix factorisation or inversion only needs to be performed once per time step.

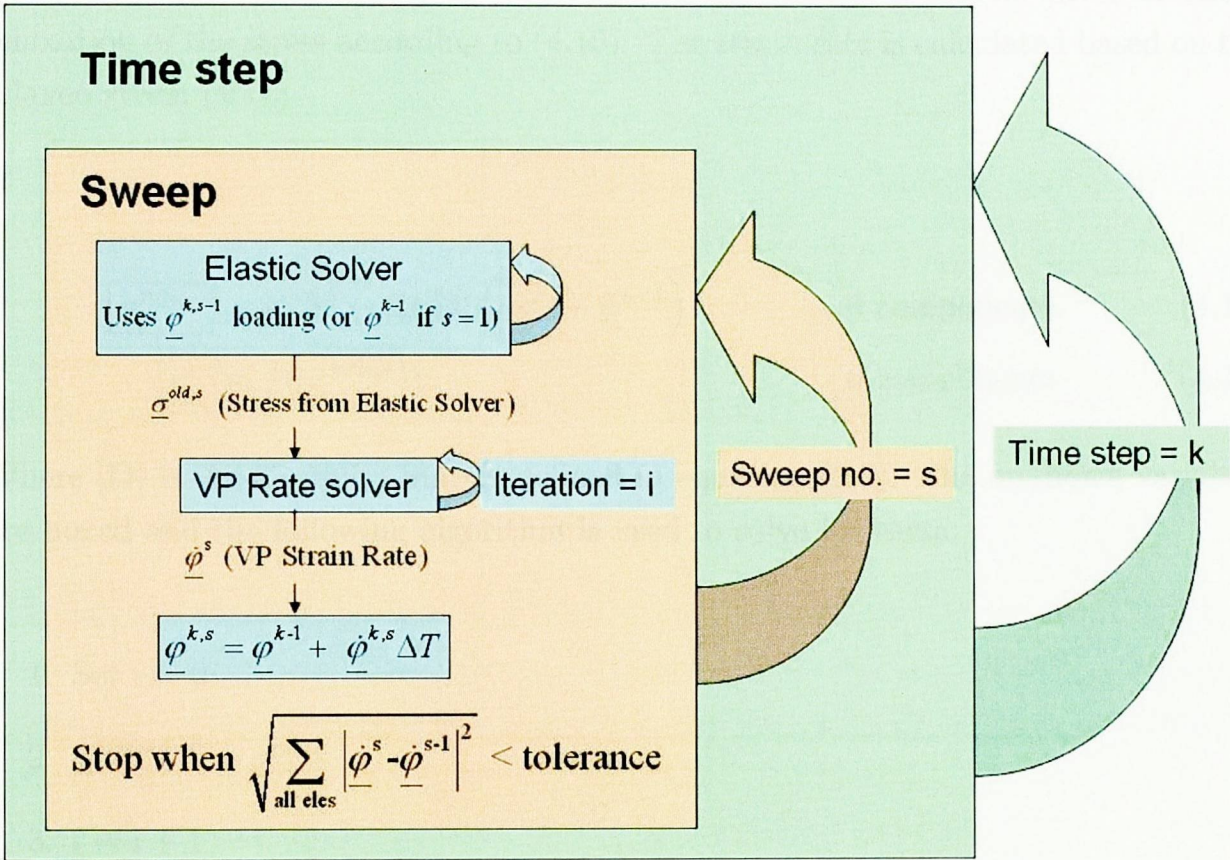
In the following description, the  $k$  superscript refers to the time step, the  $s$  superscript refers to the sweep (outer iteration), and the  $i$  superscript refers to the inner iteration. if there is no  $s$  or  $i$  superscript then assume it is the solved value - i.e.,  $s$  or  $i$  will be the no. of sweeps or iterations taken to converge. If there is no  $k$  superscript then assume it refers to the current time step.

The LENI scheme is summarised in figure 4.1. It works by alternately calculating a) the displacement and stress over the whole mesh with the linear elastic solver and b) a better approximation of the creep strain rate for each element using a per-element plasticity solver (VP Rate solver in figure 4.1). This continues until the amount by which the creep strain rate changes between iterations  $\xi_{\text{eff}}$  is smaller than the prescribed tolerance<sup>1</sup>:

$$\underline{\xi} = \underline{\dot{\varphi}}^s - \underline{\dot{\varphi}}^{s-1} \quad (4.8)$$

---

<sup>1</sup> Alternatively the residual of equation (4.11) may be a better value to judge convergence, unfortunately this was not considered in time to investigate further.



- $\underline{\varphi}^{k,s,i}$  = VP strain at time step  $k$ , sweep  $s$ , iteration  $i$   
 $\underline{\dot{\varphi}}^{k,s,i}$  = VP strain rate at time step  $k$ , sweep  $s$ , iteration  $i$   
 $\underline{\sigma}^{old,k,s}$  = stress after elastic solver at time step  $k$ , sweep  $s$   
 $\underline{\sigma}^{new,k,s,i}$  = stress in VP Rate solver at time step  $k$ , sweep  $s$ , iteration  $i$

Figure 4.1: This diagram shows the workings of the implicit solution scheme



---

#### 4.1. Creep Law

---

$$\xi_{\text{eff}} = \sqrt{\sum_{\text{all eles}} \frac{2}{9} [(\xi_{ii} - \xi_{jj})^2 + (\xi_{jj} - \xi_{kk})^2 + (\xi_{kk} - \xi_{ii})^2] + \frac{1}{3} [\xi_{ij}^2 + \xi_{jk}^2 + \xi_{ki}^2]} \quad (4.9)$$

The per-element VP Rate solver works by assuming that the nodal displacements (and therefore overall strain) are fixed and so any change of plastic strain causes a relaxation of the stress according to (4.10). The strain rate is calculated based on the relaxed stress (4.11).

$$\boxed{\underline{\sigma}^{\text{new},s}} = \underline{\sigma}^{\text{old},s} - \Delta t[\mathbf{D}] \left( \boxed{\underline{\dot{\varphi}}^s} - \underline{\dot{\varphi}}^{s-1} \right) \quad \text{- 6 components} \quad (4.10)$$

$$\boxed{\underline{\dot{\varphi}}^s} = \underline{f}(\boxed{\underline{\sigma}^{\text{new},s}}) \quad \text{- 6 components} \quad (4.11)$$

Where  $[\mathbf{D}]$  is the elasticity matrix defined in equation (3.3). The unknown variables are boxed and the following algorithm is used to solve for them:

1. Set  $i = 0$
2.  $\underline{\sigma}^{\text{new},s,i=0} = \underline{\sigma}^{\text{old},s}$
3.  $i = i + 1$
4. First define  $F_{ij}$  to be the residual of (4.11):

$$F_{ij}(\underline{\dot{\varphi}}, \underline{\sigma}) = f_{ij}(\underline{\sigma}) - \dot{\varphi}_{ij} \quad (4.12)$$

Then perform the following Newton-Raphson iterative step to obtain a better approximation of  $\varphi_{ij}^s$  which seeks to minimise  $F_{ij}$ :

$$\dot{\varphi}_{ij}^{s,i} = \dot{\varphi}_{ij}^{s,i-1} - \frac{F_{ij}(\underline{\dot{\varphi}}^{s,i-1}, \underline{\sigma}^{\text{new},s,i-1})}{\left[ \frac{\partial F_{ij}(\underline{\dot{\varphi}}^{s,i-1}, \underline{\sigma}^{\text{new},s,i-1})}{\partial \dot{\varphi}_{ij}^{s,i-1}} \right]} \quad (4.13)$$

5. Calc new stress:

$$\underline{\sigma}^{\text{new},s,i} = \underline{\sigma}^{\text{old},s} - \Delta t[\mathbf{D}] (\underline{\dot{\varphi}}^{s,i} - \underline{\dot{\varphi}}^{s-1}) \quad (4.14)$$


---

---

## 4.2. Steady-state creep (explicit vs. implicit)

---

6. If  $i = \text{maximum no. of inner iterations}$ , then  $\text{exit}^2$ , else goto 3

Step 4 requires differentiation of the creep constitutive law, this has been performed for the sinh law on page 64 and the kinematic hardening law on page 71.

Since the scheme involves solving the linear elastic system many times under different loading conditions, a matrix inversion or factorisation approach such as the Cholesky factorisation described on page 51 is generally much faster than an iterative solver.

## 4.2 Steady-state creep (explicit vs. implicit)

The sinh law (2.20) is written in full 3D in the form of (4.2) below:

$$\dot{\epsilon}_{ij} = A[\sinh(\alpha\sigma)]^n e^{-Q/kT} \frac{3}{2} \frac{\hat{\sigma}_{ij}}{\sigma_{\text{eff}}} \quad (4.15)$$

This has been implemented in FATMAN using both explicit and implicit discretisations. The implementation of the implicit discretisation using LENI will be discussed followed by some test cases to demonstrate the effect of the explicit and implicit discretisation.

### 4.2.1 Implementing using LENI Scheme

The  $\underline{f}(\underline{\sigma}^{new,s})$  function from equation (4.11) is defined to be equal to  $\underline{\dot{\varphi}}$  from equation (4.15). It is written in the following form to simplify the differentiation:

$$f_{ij} = g(\sigma_{\text{eff}}^{new,s}) \hat{\sigma}_{ij}^{new,s} \quad (4.16)$$

where  $\hat{\sigma}_{ij}$  is the deviatoric stress and  $g(\sigma_{\text{eff}}^{new,s})$  is:

$$g(\sigma_{\text{eff}}^{new,s}) = A[\sinh(\alpha\sigma_{\text{eff}}^{new,s})]^n e^{-Q/kT} \frac{3}{2} \frac{1}{\sigma_{\text{eff}}^{new,s}} \quad (4.17)$$

---

<sup>2</sup> A convergence test could also be made based on the residual of equation (4.11).



---

## 4.2. Steady-state creep (explicit vs. implicit)

---

To simplify the following, the  $\underline{\sigma}$  refers to  $\underline{\sigma}^{new,s}$  and  $\dot{\varphi}$  refers to  $\dot{\varphi}^s$ . Differentiating (4.17) w.r.t. effective stress:

$$\frac{\partial g}{\partial \sigma_{\text{eff}}} = \frac{3}{2} \frac{A e^{-Q/kT}}{\sigma_{\text{eff}}} \left[ n \alpha [\sinh(\alpha \sigma_{\text{eff}})]^{n-1} \cosh(\alpha \sigma_{\text{eff}}) - \frac{[\sinh(\alpha \sigma_{\text{eff}})]^n}{\sigma_{\text{eff}}} \right] \quad (4.18)$$

Differentiating the effective stress (4.3) w.r.t. stress components:

$$\frac{\partial \sigma_{\text{eff}}}{\partial \sigma_{ij}} = \begin{cases} \frac{2\sigma_{ii} - \sigma_{kk} - \sigma_{ll}}{2\sigma_{\text{eff}}} & \text{if } i = j \quad (i \neq k \neq l) \\ \frac{3\sigma_{ij}}{\sigma_{\text{eff}}} & \text{if } i \neq j \end{cases} \quad (4.19)$$

Differentiating equation (4.10) w.r.t. the current strain rate<sup>3</sup>:

$$\frac{\partial \sigma_{ij}}{\partial \dot{\varphi}_{ij}} = \begin{cases} -\frac{\Delta T E (1-\nu)}{(1+\nu)(1-2\nu)} & \text{if } i = j \\ -\frac{\Delta T E}{2(1-2\nu)} & \text{if } i \neq j \end{cases} \quad (4.20)$$

Differentiating (4.12) w.r.t.  $\underline{\dot{\varphi}}_{ij}$ :

$$\begin{aligned} \frac{\partial F_{ij}}{\partial \dot{\varphi}_{ij}} &= \frac{\partial f_{ij}}{\partial \dot{\varphi}_{ij}} - 1 \\ \frac{\partial F_{ij}}{\partial \dot{\varphi}_{ij}} &= \sum_{k=1}^3 \sum_{l=1}^k \frac{\partial f_{ij}}{\partial \sigma_{kl}} \frac{\partial \sigma_{kl}}{\partial \dot{\varphi}_{ij}} - 1 \end{aligned} \quad (4.21)$$

Differentiating  $\hat{\sigma}_{ij}$  w.r.t.  $\sigma_{ij}$ :

$$\frac{\partial \hat{\sigma}_{ij}}{\partial \sigma_{ij}} = 1 - \frac{\delta_{ij}}{3} \quad (4.22)$$

Where  $\delta_{ij}$  is the Kronecker delta. Due to their small contribution, and in order to simplify the equations, terms in which  $kl \neq ij$  are ignored:

$$\begin{aligned} \frac{\partial F_{ij}}{\partial \dot{\varphi}_{ij}} &= \frac{\partial f_{ij}}{\partial \sigma_{ij}} \frac{\partial \sigma_{ij}}{\partial \dot{\varphi}_{ij}} - 1 \\ &= \left( \frac{\partial g}{\partial \sigma_{ij}} \hat{\sigma}_{ij} + g \frac{\partial \hat{\sigma}_{ij}}{\partial \sigma_{ij}} \right) \frac{\partial \sigma_{ij}}{\partial \dot{\varphi}_{ij}} - 1 \\ &= \left( \frac{\partial g}{\partial \sigma_{\text{eff}}} \frac{\partial \sigma_{\text{eff}}}{\partial \sigma_{ij}} \hat{\sigma}_{ij} + g \frac{\partial \hat{\sigma}_{ij}}{\partial \sigma_{ij}} \right) \frac{\partial \sigma_{ij}}{\partial \dot{\varphi}_{ij}} - 1 \end{aligned} \quad (4.23)$$

Now by substituting (4.18), (4.19), (4.20) and (4.22) into (4.23) we can calculate the value required to perform the Newton-Raphson iteration in equation (4.13) for each

---

<sup>3</sup>In the actual implementation exists a mistake/simplification:  $\frac{\partial \sigma_{ii}}{\partial \varphi_{ii}} = \Delta T E$ , this doesn't affect the final solution, but perhaps increases the no. of iterations required

---

---

## 4.2. Steady-state creep (explicit vs. implicit)

---

of the six components of  $\varphi_{ij}^s$ .

### 4.2.2 Shear test (explicit)

In following simulation a gradually increasing displacement was applied to the top face of a cuboid shaped block of SnAgCu solder to achieve an overall shear strain rate of  $2.33 \times 10^{-4} \text{ s}^{-1}$ . Creep was calculated using an explicit implementation of the sinh creep law using material constants from Schubert [50] and listed in Appendix A.

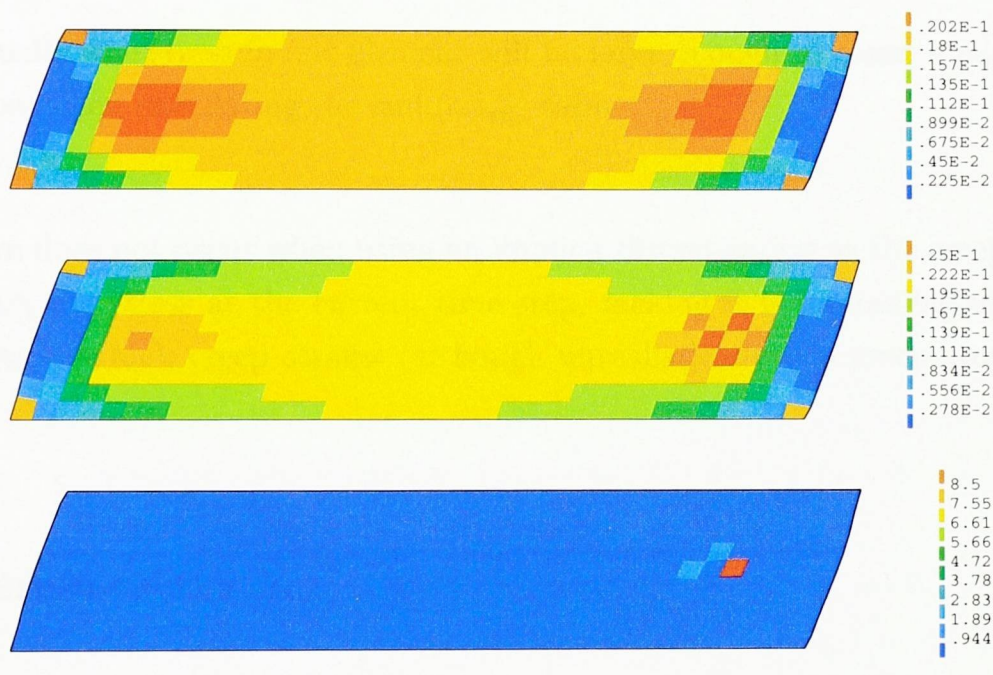


Figure 4.2: Showing the  $\varphi_{acc}$  contours for the last three time steps before simulation failure due to sinh overflow

The results are shown in figure 4.2 and a ‘checkerboard’ effect is seen to develop before the simulation stops running due to numerical overflow (i.e. the calculation of  $\dot{\varphi}_{ij}$  resulted in a value too large to be stored as a double precision floating point number). A reasonable explanation for this effect is given below:

1. One element has a slightly higher stress than its surrounding elements.
2. This causes a high creep strain rate causing the creep strain  $\varphi$  to increase by an unrealistically large amount in this element by the next time step.



---

## 4.2. Steady-state creep (explicit vs. implicit)

---

3. The high creep strain in this element causes it to become overly distorted compared to its 4 neighbours. Therefore the neighbouring elements will exert stresses on it which attempt to lower its distortion, and the central element exerts forces on the surrounding elements which causes them to become more distorted. If the time step were small enough, this would make all the elements' strains closer. But because the time step size is too large, by the next time step the central element is distorted in the opposite direction and the surrounding elements have become distorted.
4. The process continues and spreads outwards from each of the surrounding elements.
5. Eventually, the stress in one element will be large enough to cause a numerical overflow when calculating the  $\sinh(\alpha\sigma_{\text{eff}})$  term.

This problem does not occur when using an implicit discretisation as the creep strain is based upon the stress at the current time step, making it is impossible to generate unrealistically high creep strains (although unrealistically *low* creep strains are possible).

### 4.2.3 Stress relaxation

In this test, a fixed strain of 0.25% is applied to a single element of solder at 25 °C. The solder is modeled using the sinh steady-state creep law and the response over a 60s time period is compared using implicit and explicit discretisations.

The explicit discretisation could only be used using a time step of 0.003s or less. If a greater time step is used then the sinh term yields a number too big to be represented by a double precision floating point and the program crashes. The implicit scheme can be run with any size time step without crashing.

As shown in figure 4.3, using the explicit scheme with a time step of 0.003s yields a very inaccurate result. The creep strain generated during the first time step is actually greater than the total imposed strain, causing the sign of the stress and subsequent strain rate to reverse. With time steps of 0.001s and smaller, the results

---

## 4.2. Steady-state creep (explicit vs. implicit)

---

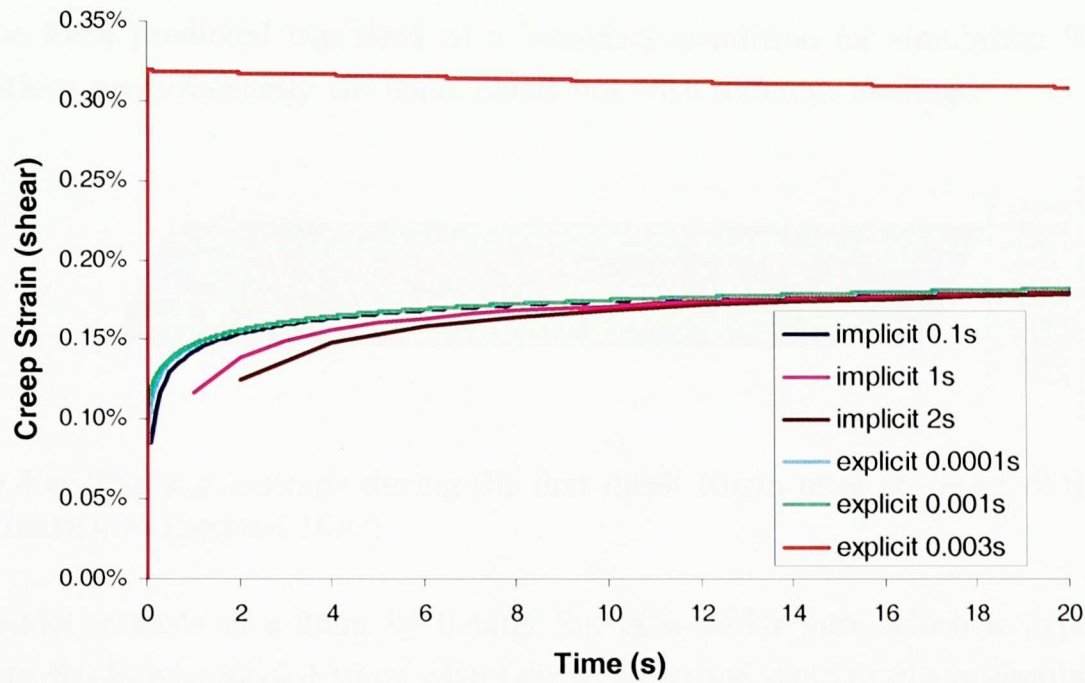


Figure 4.3: The creep strains predicted using explicit and implicit discretisations with different time step sizes

from the explicit scheme converge to the correct result. The implicit scheme on the other hand, predicts similar results using a far larger time step size of 0.1s. With time steps of 1s or greater, the implicit scheme still provides a solution but the initial part of the curve becomes increasingly inaccurate with greater time step sizes.

The explicit scheme may be better in rare situations of purely force-controlled loading such as a monotonic creep test, because the stress doesn't change over time thus making the stress-relaxation approach of LENI's per-element solver inefficient. But the improved stability and ability to use fewer time steps make the implicit scheme more appropriate than the explicit scheme for most simulations.

### 4.2.4 Force-controlled vs. Displacement-controlled loading

The LENI scheme is better suited to displacement-controlled loading conditions than to force-controlled loadings. The reason is that when solving for the strain rate using the per-element solver, the displacements are assumed to remain constant and the stress can be relaxed.

In the following, simulation A was run using a fixed displacement boundary condition,



---

## 4.2. Steady-state creep (explicit vs. implicit)

---

and the force predicted was used as a boundary condition for simulation B. Both simulations predict exactly the same result but with different loadings.

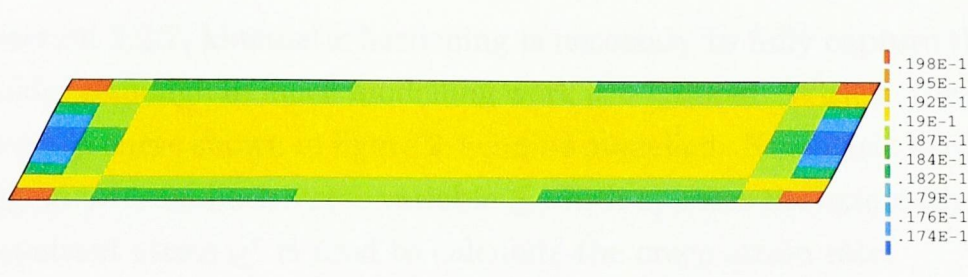


Figure 4.4: The  $\phi_{\text{eff}}$  contours during the first dwell 10min after the start of the test. (Deformation exaggerated  $16\times$ .)

The model consists of a 2mm by 0.4mm SnAgCu solder joint which is exposed to shearing displacements of  $\pm 10\mu\text{m}$  with 14min ramps and 6min dwells in simulation A. The  $\phi_{\text{eff}}$  contours and deformation during the test are shown in figure 4.4. Simulation A took 166s to complete two cycles.

The predicted force from simulation A was used as a boundary condition in simulation B which predicted the displacement profile of  $\pm 9.98\mu\text{m}$ , very close to the original simulation. The time taken for this simulation was 349s – over double the time taken using the fixed displacement boundary condition.

The reason that simulation B took over twice as long as simulation A is due to the inner per-element VP Rate solver which calculates a new strain rate on the basis that the nodal displacements are fixed but the stress relaxes according to (4.10). This prevents numerical overflow of the sinh term but requires more iterations under fixed stress conditions.

In thermal cycling tests, the loading on the solder joint is not purely displacement-controlled (fixed strain amplitude) or force-controlled (fixed stress amplitude) but somewhere in between. If the relative stiffness of the surrounding assembly is very high then the loading is more strain-controlled, if the relative stiffness of the surrounding assembly is very low then the loading is more stress-controlled.

## 4.3 Kinematic Hardening Law

As noted in section 2.2.7, kinematic hardening is necessary to fully capture the creep behavior of solder although in much modelling work it is ignored. With it, the primary section of the creep curve shown in figure 2.4 can be modelled. Kinematic hardening is achieved using an internal back stress variable  $\underline{S}$  which opposes the externally applied stress. The resultant stress  $\underline{\sigma}^r$  is used to calculate the creep strain rate:

$$\underline{\sigma}^r = \underline{\sigma} - \underline{S} \quad (4.24)$$

$$\underline{\dot{\epsilon}} = \underline{f}(\underline{\sigma}^r) \quad (4.25)$$

In this work, the following Armstrong-Frederick law is used to model the back stress evolution.

$$\underline{\dot{S}} = h (\underline{\dot{\epsilon}} S_{\max} - \underline{\dot{\epsilon}}_{\text{eff}} \underline{S}) \quad (4.26)$$

Where the effective strain rate  $\underline{\dot{\epsilon}}_{\text{eff}}$  is given by:

$$\underline{\dot{\epsilon}}_{\text{eff}} = \sqrt{\frac{2}{9} [(\dot{\epsilon}_{ii} - \dot{\epsilon}_{jj})^2 + (\dot{\epsilon}_{jj} - \dot{\epsilon}_{kk})^2 + (\dot{\epsilon}_{kk} - \dot{\epsilon}_{ii})^2] + \frac{1}{3} [\dot{\epsilon}_{ij}^2 + \dot{\epsilon}_{jk}^2 + \dot{\epsilon}_{ki}^2]} \quad (4.27)$$

An obvious flaw of this method is that when the external stress is less than  $S_{\max}$  the back stress can completely cancel out the stress resulting in a steady state strain rate of 0 which is not realistic. To overcome this problem the maximum back stress  $S_{\max}$  could be made dependent on the current applied stress:

$$S_{\max} = b\sigma_{\text{eff}} \quad (4.28)$$

However, for simplicity's sake the Armstrong Frederick form (4.26) will be used. It should be suitable to predict lifetime under cyclic loading where creep is generally well in the primary region (the creep curves from Xiao [51] investigated in chapter 5 show that the primary region extends for many hours while accelerated tests usually have cycle periods in the order of 1 hour).

All subsequent mentions of the 'kinematic hardening law' in this work refer to this law.



#### 4.3.1 Implementing using LENI

To implement the kinematic hardening law using the LENI scheme, the function  $f(\underline{\sigma}^{new,s})$  is defined as:

$$f_{ij} = g(\sigma_{\text{eff}}^{r,new,s}) \hat{\sigma}_{ij}^{r,new,s} \quad (4.29)$$

where  $g()$  is the same function defined in equation (4.17), and  $\sigma^r$  is the resultant stress:

$$\underline{\sigma}^r = \underline{\sigma} - \underline{S} \Delta t^k \quad (4.30)$$

The evolution of the back stress  $S$  is discretised implicitly as follows:

$$\underline{S}^k = \underline{S}^{k-1} + \underline{\dot{S}}^k \quad (4.31)$$

The current back stress  $\underline{S}^{k,s,i}$  is updated on each iteration of the per-element solver using equations (4.31) and (4.26).

In the following,  $\sigma^r$  refers to  $\sigma^{r,new,s}$  and  $\dot{\varphi}$  refers to  $\dot{\varphi}^s$ . Differentiating equation (4.30) w.r.t. the stress components:

$$\frac{\partial \sigma_{ij}^r}{\partial \sigma_{kl}} = \delta_{ik} \delta_{jl} - \frac{\partial S_{ij}}{\partial \sigma_{kl}} \quad (4.32)$$

Where  $\delta_{ij}$  is the Kronecker delta. To simplify the implementation the  $\frac{\partial S_{ij}}{\partial \sigma_{kl}}$  terms are ignored:

$$\frac{\partial \sigma_{ij}^r}{\partial \sigma_{kl}} = \delta_{ik} \delta_{jl} \quad (4.33)$$

This simplification doesn't affect the final result but may increase the number of iterations required.

The derivative of the resultant stress w.r.t. the strain rate is:

$$\frac{\partial \sigma_{ij}^r}{\partial \dot{\varphi}_{ij}} = \sum_{k=1}^3 \sum_{l=1}^k \frac{\partial \sigma_{ij}^r}{\partial \sigma_{kl}} \frac{\partial \sigma_{kl}}{\partial \dot{\varphi}_{ij}} \quad (4.34)$$

Substituting (4.33):

$$\frac{\partial \sigma_{ij}^r}{\partial \dot{\varphi}_{ij}} = \frac{\partial \sigma_{ij}}{\partial \dot{\varphi}_{ij}} \quad (4.35)$$

---

#### 4.4. Damage Law

---

The derivative of the residual  $F_{ij}$  has the exactly the same form as equation (4.23) but with  $\sigma_{ij}^r$  replacing  $\sigma_{ij}$ :

$$\frac{\partial F_{ij}}{\partial \dot{\varphi}_{ij}} = \left( \frac{\partial g}{\partial \sigma_{\text{eff}}^r} \frac{\partial \sigma_{\text{eff}}^r}{\partial \sigma_{ij}^r} \hat{\sigma}_{ij}^r + g \frac{\partial \hat{\sigma}_{ij}^r}{\partial \sigma_{ij}^r} \right) \frac{\partial \sigma_{ij}^r}{\partial \dot{\varphi}_{ij}} - 1 \quad (4.36)$$

Substituting in (4.35):

$$\frac{\partial F_{ij}}{\partial \dot{\varphi}_{ij}} = \left( \frac{\partial g}{\partial \sigma_{\text{eff}}^r} \frac{\partial \sigma_{\text{eff}}^r}{\partial \sigma_{ij}^r} \hat{\sigma}_{ij}^r + g \frac{\partial \hat{\sigma}_{ij}^r}{\partial \sigma_{ij}^r} \right) \frac{\partial \sigma_{ij}}{\partial \dot{\varphi}_{ij}} - 1 \quad (4.37)$$

By substituting (4.18), (4.19), (4.20) and (4.22) (using  $\sigma_{ij}^r$  in place of  $\sigma_{ij}$ ) into (4.37) we can calculate the value required to perform the Newton-Raphson iteration in equation (4.13) for each of the six components of  $\varphi_{ij}^s$ .

## 4.4 Damage Law

A damage law has been implemented to allow the degradation and cracking of the solder to be captured. The law is based on the disturbed state concept [32] where each element of solder material is composed of two fractions - an intact fraction and a damaged fraction. The damaged fraction is stored as an internal variable  $D$  for each element in the mesh and starts at 0 (completely intact) and gradually increases to 1 (completely damaged) as the material is deformed. This is illustrated in figure 4.5.

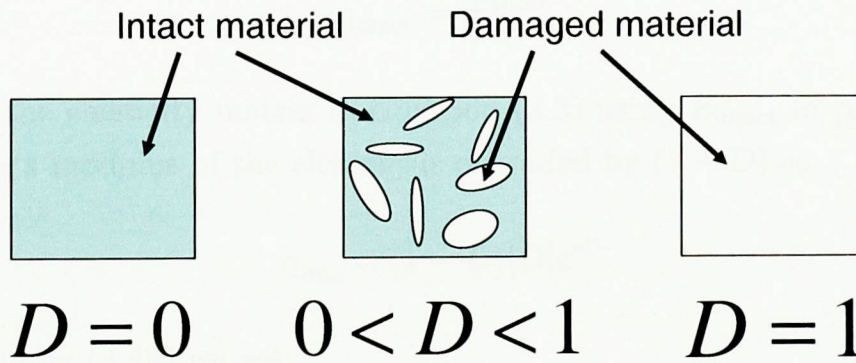


Figure 4.5: Diagram illustrating the increase in damaged material within an element as  $D$  increases from 0 to 1

The intact and damaged parts have different material properties and the properties



---

#### 4.4. Damage Law

---

of the element are interpolated based on  $D$ :

$$\Phi = (1 - D)\Phi_{\text{intact}} + D\Phi_{\text{damaged}} \quad (4.38)$$

Where  $\Phi$  is any material constant. The simplest way to model the damage is to make the Young's modulus zero in the damaged fraction. This means that having a completely damaged element is equivalent to removing the element from the mesh. In this case the Young's modulus is given by:

$$E = (1 - D)E_{\text{intact}} \quad (4.39)$$

Unfortunately, in the implementation the Young's modulus of an element can't be reduced to exactly 0 as this can result in a singular matrix with no unique solution. An easy way around this is to provide a small lower bound for the modulus. This is achieved by placing an upper limit on the damage variable  $D$  (for this work 0.999999999 has been used). A better way of dealing with this situation would be to remove the nodes from the mesh when all their adjacent elements satisfy  $D > D_{\text{critical}}$ , however this would involve added computational cost.

If we assume that the elastic strain is equal throughout the element:

$$\underline{\varepsilon}^{el} = \underline{\varepsilon}_{\text{intact}}^{el} = \underline{\varepsilon}_{\text{damaged}}^{el} \quad (4.40)$$

Then the stress in the intact part is given by:

$$\underline{\sigma}_{\text{intact}} = [\mathbf{D}]\underline{\varepsilon}^{el} \quad (4.41)$$

Where  $[\mathbf{D}]$  is the elasticity matrix in equation (3.3) using  $E_{\text{intact}}$  in place of  $E$ . The average Young's modulus of the element is degraded by  $(1 - D)$  so:

$$\underline{\sigma}_{\text{avg}} = (1 - D)[\mathbf{D}]\underline{\varepsilon}^{el} \quad (4.42)$$

Dividing (4.41) by (4.42) we get:

$$\underline{\sigma}_{\text{intact}} = \frac{\underline{\sigma}_{\text{avg}}}{(1 - D)} \quad (4.43)$$

This equation is used to obtain  $\underline{\sigma}_{\text{intact}}$  after the elastic solver has generated  $\underline{\sigma}_{\text{avg}}$  as the creep strain rate is calculated based on  $\underline{\sigma}_{\text{intact}}$ .

---

## 4.4. Damage Law

---

In reality, damaged material may still be able to withstand compressive hydrostatic stresses, but implementing this is tricky. It is possible to split the Young's modulus into separate deviatoric and hydrostatic components and make only the deviatoric component degrade with damage. This keeps the ability of the damaged material to withstand compressive stresses but has the unwanted side effect of also allowing the material to withstand tensile stresses. To make the material withstand compressive but not tensile stresses a non-linear response is ideally required. This has not been implemented in FATMAN.

All subsequent mentions of the 'damage law' in this work refer to this law.

### 4.4.1 Damage evolution

Following work by other researchers including Towashiraporn [41] the damage is based on the accumulated effective creep strain  $\varphi_{\text{acc}}$ :

$$\varphi_{\text{acc}} = \sum_{\text{time-steps}} \dot{\varphi}_{\text{eff}} \Delta t \quad (4.44)$$

Where the effective strain rate  $\dot{\varphi}_{\text{eff}}$  is given by:

$$\dot{\varphi}_{\text{eff}} = \sqrt{\frac{2}{9} [(\dot{\varphi}_{ii} - \dot{\varphi}_{jj})^2 + (\dot{\varphi}_{jj} - \dot{\varphi}_{kk})^2 + (\dot{\varphi}_{kk} - \dot{\varphi}_{ii})^2] + \frac{1}{3} [\dot{\varphi}_{ij}^2 + \dot{\varphi}_{jk}^2 + \dot{\varphi}_{ki}^2]} \quad (4.45)$$

The following law is used in this work to calculate the damage:

$$D = e^{B\varphi_{\text{acc}}} \quad (4.46)$$

This is the simplest possible damage evolution law, containing only one material constant, more sophisticated versions have been published (e.g. equation (2.35)) but none have been sufficiently validated against experimental results. For this work, the simple law above was thought to be the best place to start from.

A problem with the law (4.46) is that it is highly mesh dependent. This occurs because a local concentration of stress will lead to a local concentration of damage, which can turn into a very thin crack limited only by the mesh spacing.



---

#### 4.4. Damage Law

---

To overcome this problem the law can be modified to make the damage dependent on a weighted average of  $\varphi_{\text{acc}}$  over a region around the element. The following law uses a Gaussian distribution to perform the weighted average:

$$\varphi_{\text{acc}}^{\text{avg}} = \frac{\int_V \varphi_{\text{acc}} \exp\left(-\frac{r^2}{2\omega^2}\right) dV}{\int_V \exp\left(-\frac{r^2}{2\omega^2}\right) dV} \quad (4.47)$$

where  $r$  is the distance from the center of the element and  $\omega$  is the standard deviation of the distribution which we will call the damage length scale. Since the influence of  $\varphi_{\text{acc}}$  over a unit volume at distances of  $d > 3\omega$  is only 1.1% or less compared to  $d = 0$ , these are ignored to save computational resources. The effect of using different  $\omega$  values is investigated in sections 4.4.4 and 4.4.5.

#### 4.4.2 Explicit scheme

An explicit discretisation is used for the damage evolution due to ease of implementation:

$$D^i = e^{B\varphi_{\text{acc}}^{i-1}} \quad (4.48)$$

Where  $i$  is the time step. This results in optimistic predictions (less damage) rather than the conservative predictions an implicit law would predict. In a typical thermal/mechanical cycling simulation, the damage builds up gradually over many cycles, therefore the damage change per time step is usually quite small and the difference between an implicit and explicit scheme should be negligible.

#### 4.4.3 Determining Lifetime

To predict the lifetime using the above damage law a failure criteria is required. One method is to use the increase in electrical resistance across the joint. It works by assuming the electrical conductivity  $k$  is a linear function of the damage just like the Young's Modulus:

$$k = k_{\text{intact}}(1 - D) \quad (4.49)$$

---

#### 4.4. Damage Law

---

A fixed potential difference  $V$  is applied across the joint and the current  $I$  is predicted. The resistance  $R$  is given by Ohm's law:

$$R = V/I \quad (4.50)$$

The resistance of a completely intact joint is calculated as  $R_0$ . The failure condition is defined as the time at which the relative resistance  $R/R_0$  has increased to a certain value. This technique is used for many of the simulations in this thesis.

##### 4.4.4 Displacement-controlled cyclic loading

The mesh dependence of the above damage law will now be investigated for a simple test case. A test-case is shown in figure 4.6 in which a solder joint is subjected to mechanical cycling. The bottom is kept fixed and the top displacement is cycled between  $-12\mu\text{m}$  and  $+12\mu\text{m}$  with 5min ramps and 5min dwells.

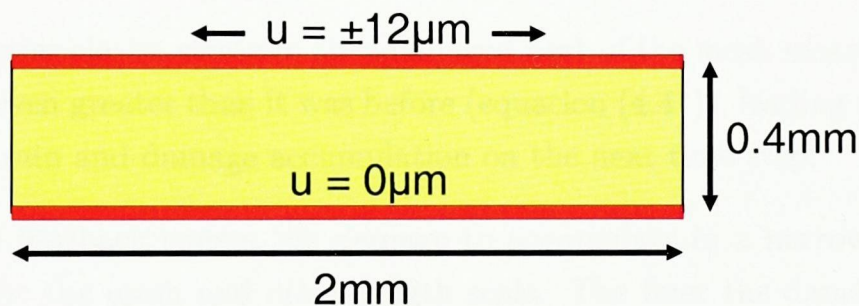


Figure 4.6: The dimensions and boundary conditions of the displacement controlled cyclic loading test case. ( $u$  = displacement)

The damage law has been used to predict  $N_f$  for this problem using different mesh densities and length scales. The failure point has been defined as the point at which the electrical resistance between the top and bottom faces has reached  $10\times$  its initial value (i.e.  $R/R_0 = 10$ ).

Using a mesh spacing of  $40\mu\text{m}$  and a length scale of  $40\mu\text{m}$  the damage contours at the point of failure are shown in figure 4.7.

The effect of changing both the mesh density and the length scale can be seen in figure 4.8. This shows that when a length scale of 0 is used,  $N_f$  is highly mesh dependent.



#### 4.4. Damage Law

---



Figure 4.7: The damage contours after 12 displacement controlled cycles (just before the resistance increase reaches  $10\times$ )

The reason is as follows:

1. Early in the simulation there will be slightly more damage occurring in one part of the mesh.
2. The greater damage means that this part of the mesh is now weaker than the surrounding elements and so will subsequently experience a greater elastic strain.
3. The greater elastic strain in this damaged part of the mesh means that  $\sigma_{\text{eff,intact}}$  will be even greater than it was before (equation (4.41)), leading to even greater creep strain and damage accumulation on the next time step.
4. Positive feedback causes the damage to accumulate in a narrow band limited in size by the mesh and crack length scale. The finer the damaged band, the greater the strain will be within the band and thus the quicker that failure will occur.

When a length scale of  $\omega = 133\mu\text{m}$  is used,  $N_f$  is completely mesh independent over the range investigated because even for the coarsest mesh used, the large  $\omega$  is the limiting factor regarding the fineness of the crack. The length scales in between show intermediate levels of mesh dependence. A length scale of  $40\mu\text{m}$  appears to be mesh independent at  $60\mu\text{m}$  and below (although simulations at finer mesh densities are necessary to confirm this).

#### 4.4. Damage Law

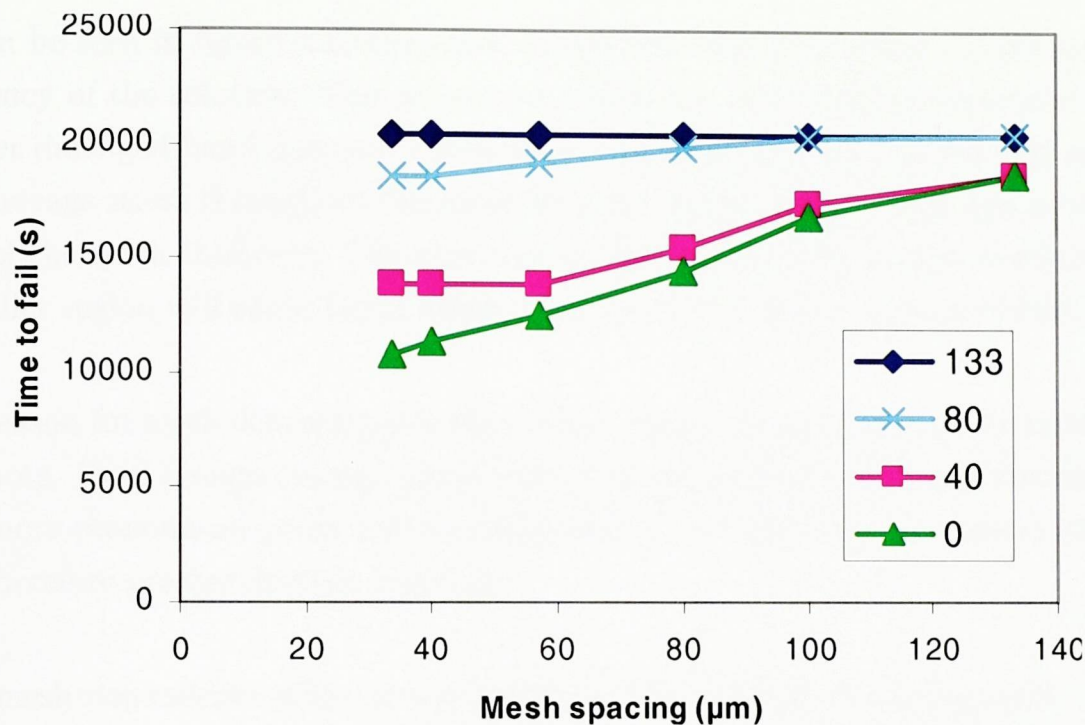


Figure 4.8: The effect of mesh density and crack length scale on the time to fail under displacement controlled loading. (The graph legend shows the crack length scale in  $\mu\text{m}$ )

#### 4.4.5 Force-controlled cyclic loading

Similar to the displacement controlled test described above, this test case instead uses a prescribed cyclic force boundary condition as shown in figure 4.9.

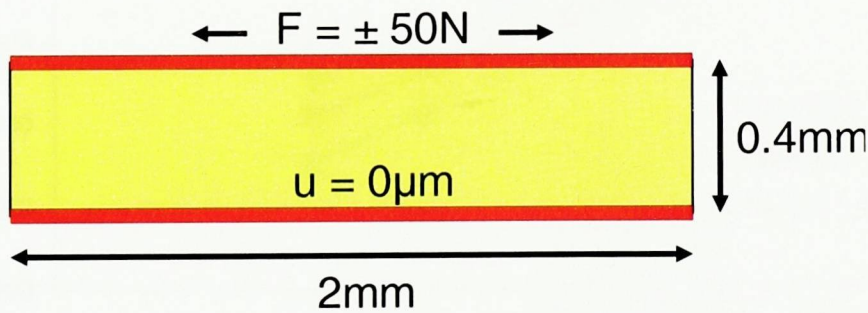


Figure 4.9: The dimensions and boundary conditions of the displacement controlled cyclic loading test case. ( $F$  = force and  $u$  = displacement)

The damage contours at failure look identical to those predicted for the displacement controlled test in figure 4.7. But the effect of using different mesh densities and damage length scales is quite different from the displacement-controlled test.



#### 4.4. Damage Law

As can be seen in figure 4.10 the crack length scale has little effect on the mesh dependency of the solution. This is because unlike the displacement-controlled test, a thinner damaged band does not necessarily experience a greater strain and  $\sigma_{\text{eff,intact}}$ . The average stress throughout the mesh depends on the applied force and is independent of the crack thickness. The only reason that  $\omega$  affects  $N_f$  is that averaging over a smaller region will cause faster damage accumulation in the regions of high  $\varphi_{\text{acc}}$ .

The reason for mesh dependence is that a finer mesh means more concentrated stress hot spots. Even though average stress in a region may be the same, a greater variation (i.e. more pronounced peaks and troughs) leads to a higher average creep strain rate and therefore greater damage build up.

This mesh dependence effect is not unique to the damage law being used – it also occurs using the standard constitutive law + fatigue law methods. Where there is a stress hot-spot or singularity, the mesh density will have an affect on the average accumulated creep strain in that area.<sup>4</sup>

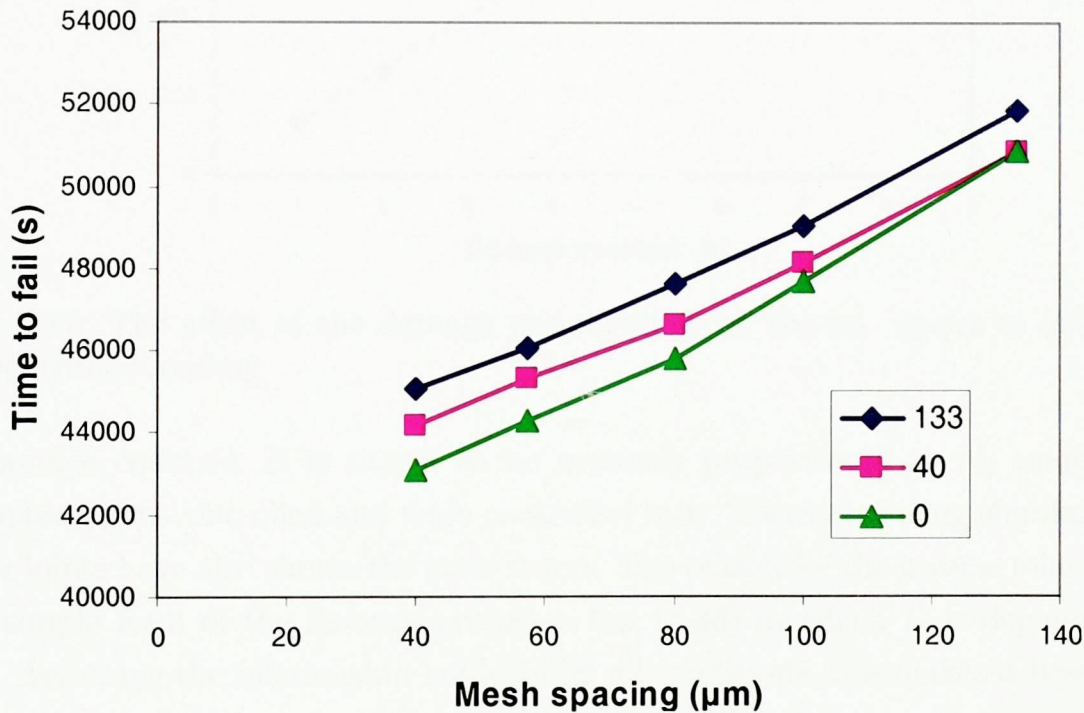


Figure 4.10: The effect of mesh density and crack length scale on the time to fail under force controlled loading. (The legend shows the damage length scale in  $\mu\text{m}$ .)

<sup>4</sup>So why doesn't this apply to the displacement controlled test? After all there will also be stress hot spots with a more detailed mesh resulting in a higher creep rate. But no matter how quickly the solder creeps, the actual amount it creeps is limited by the prescribed displacement. Since it's the amount of creep not the speed which governs the amount of damage accumulation, the existence of stress hot spots doesn't make much difference to the lifetime in the displacement controlled test.

### 4.4.6 Speeding up computation

One of the drawbacks of using the damage law to predict reliability is that 1000s of cycles are routinely performed during accelerated testing. To model all these cycles using FEA can be prohibitively expensive computationally so a method is presented here to reduce this.

For the displacement-controlled and force-controlled problems described above, simulations have been run using different  $B$  constants and the results shown in figures 4.12 and 4.11.

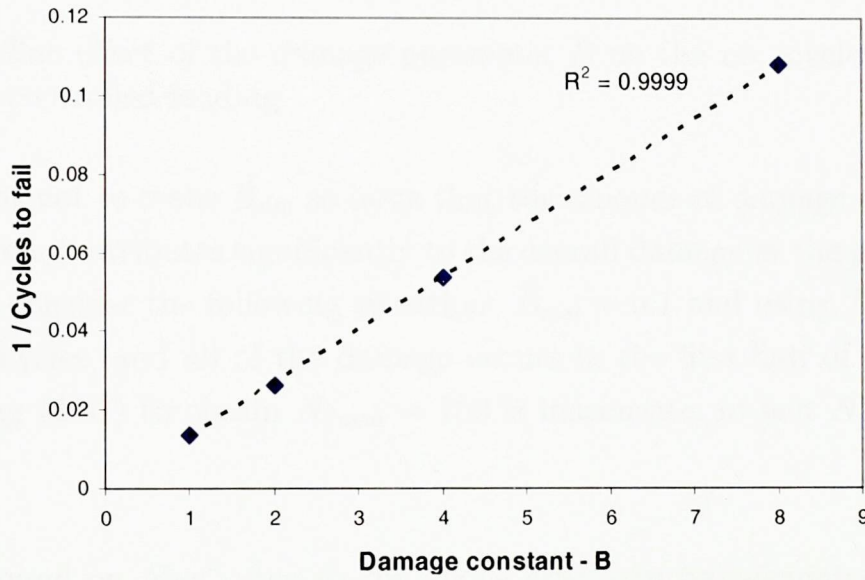


Figure 4.11: The effect of the damage parameter  $B$  on the no. cycles to fail under force controlled loading

The damage constant  $B$  is shown to be inversely proportional to  $N_f$  under both the displacement-controlled and force-controlled test. Thermal cycling simulations of resistor joints have also shown the same trend. The reason for the inverse relationship is the simple form of the damage evolution law (4.46) in which  $D$  is dependent on  $B\varphi_{acc}$ . Assuming the relationship holds under all conditions, this makes it possible to shorten the computation time by using the damage law with an unrealistically high  $B$  constant and finding the actual  $N_f$  as follows:

If the real  $B$  value is  $B_{real}$  and  $B_{sim}$  is used for the simulation yielding  $N_{f:sim}$ , the real cycles to fail  $N_{f:real}$  can be found with:

$$N_{f:real} = N_{f:sim} \frac{B_{sim}}{B_{real}} \quad (4.51)$$



## 4.5. Summary

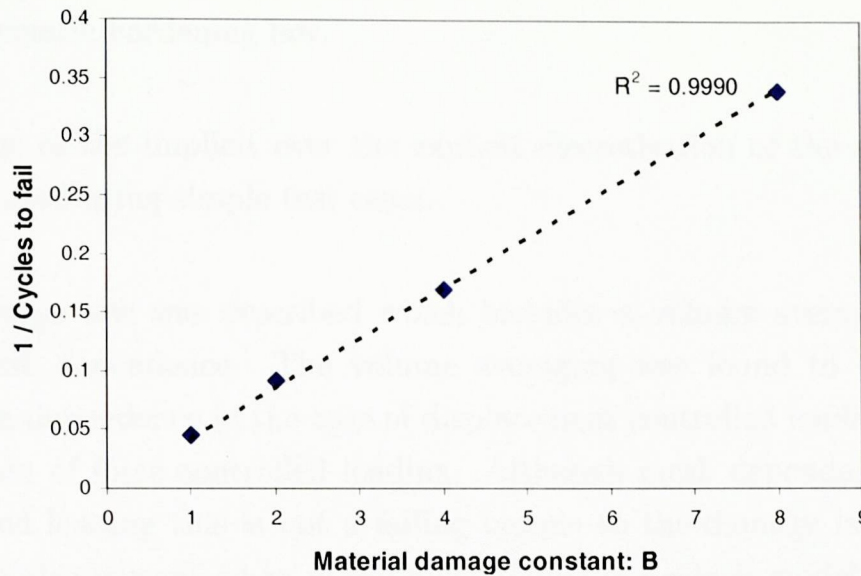


Figure 4.12: The effect of the damage parameter  $B$  on the no. cycles to fail under displacement controlled loading

It is important not to make  $B_{\text{sim}}$  so large that the amount of damage contributed by part of one cycle contributes significantly to the overall damage at the point of failure. For example, consider the following situation:  $B_{\text{real}} = 0.1$  and using  $B_{\text{sim}} = 10$  gives  $N_{f:\text{sim}} = 1.5$  cycles, and all of the damage occurs in the first half of each cycle. In this case using (4.51) to obtain  $N_{f:\text{real}} = 150$  is inaccurate, in fact  $N_{f:\text{real}}$  should be 200 cycles.

The upper bound on  $N_{f:\text{real}}$  due to the above error can be calculated by rounding  $N_{f:\text{sim}}$  up to the nearest integer before using (4.51) and similarly the lower bound can be obtained by rounding  $N_{f:\text{sim}}$  down. As long as  $N_{f:\text{sim}}$  is kept to a reasonably high number the error in using (4.51) to obtain  $N_{f:\text{real}}$  should be small.

This method allows the damage law to be used to model any number of cycles in a reasonable time. If a more complex damage evolution law was used, for instance (2.35), this speedup method may be inappropriate.

## 4.5 Summary

The novel (to the best of the author's knowledge) LENI scheme for solving implicit creep was described and implemented for the sinh creep law and the Armstrong-

## 4.5. Summary

---

Frederick kinematic hardening law.

The advantage of the implicit over the explicit discretisation of the sinh creep law was demonstrated using simple test cases.

A simple damage law was described which includes a volume averaging technique to reduce mesh dependence. The volume averaging was found to be effective in reducing mesh dependence in the case of displacement controlled loading but ineffective in the case of force controlled loading. Although mesh dependence remains in force-controlled loading this is not a failing unique to the damage law – this mesh dependence is also present when performing simulations which model creep with no damage mechanics.

A method was proposed to speedup the computational time of the damage law by increasing the material constant  $B$  by a factor to perform the simulation and compensating for this by increasing the predicted value of  $N_f$  by the same factor.



## Chapter 5

# Determining Material Constants

In this chapter, work on determining material constants for the kinematic hardening law developed in chapter 4 will be presented. Inverse analysis techniques are described and validated before being used to determine constants for the sinh law and the kinematic hardening law which match a set of 12 creep curves obtained from the literature [51]. Finally, a method to obtain the constant for the damage law described in chapter 4 is presented.

### 5.1 Inverse methods

For some constitutive laws, determining the material constants from experimental results is trivial. For example, to determine the Young's modulus from a tensile strength test, the gradient can be read from a stress-strain graph. This is not usually the case for constitutive laws for creep and kinematic hardening. The material constants for these laws are not directly measurable but are chosen to provide an empirical fit of the model to experiment. So inverse analysis methods are required to infer material properties from experimental data.

Inverse analysis can be roughly described as any problem where the answer is known but not the question. In terms of FEA – a normal, direct analysis involves specifying the geometry, boundary conditions and material properties and predicting the

## 5.1. Inverse methods

---

displacements, forces, stresses and strains as outputs. In an inverse analysis some of the outputs become inputs and some of the inputs become outputs. In this work the strain becomes an input and some of the solder kinematic hardening law constants become outputs.

The inverse analysis technique for determining material constants can be summarised by the following:

1. Choose initial guess for material constants
2. Run simulation
3. Calculate error between simulation results and experimental results
4. If the error is less than the tolerance then exit
5. Refine constants in an attempt to minimise error
6. Goto step 2

This process is also known as optimisation as constants are chosen which minimise (i.e. optimise) the error value. The error is a measure of how different the simulation result is from the experimental result, in this work the strain is being compared and the method used is described later. The different inverse techniques differ in the method used to calculate the error (step 3) and to refine the material constants on each iteration (step 5).

The simplest method of refining the constants is to judge the error by visual inspection and to use trial and error. This relies on using intuition to judge how changing each constant will affect the simulated results. It can work for some problems if there are only one or two constants and the simulation runs quickly, otherwise this technique would likely be both time consuming and inaccurate. Sophisticated optimisation algorithms are available which can minimise the error using fewer iterations than it would have taken a human relying on intuition.

The software VisualDoc was used which has a choice of the Fletcher-Reeves conjugate gradient method or the Broydon-Fletcher-Goldfarb-Shannon variable metric method



---

## 5.2. Creep tests

---

to perform the optimisation. The later was chosen as it is considered theoretically better than the Fletcher-Reeves method [52]. It is an iterative gradient based method.

The method requires the definition of an error value  $\xi$  as a function of the material constants  $c_1, c_2, \dots, c_n$ :

$$\xi = f(c_1, c_2, \dots, c_n) \quad (5.1)$$

This function must be continuous with respect to the material constants as the gradient is approximated using a finite difference discretisation:

$$\frac{\partial \xi}{\partial c_i} \simeq \frac{f(\dots, c_i + \frac{1}{2}\Delta c_i, \dots) - f(\dots, c_i - \frac{1}{2}\Delta c_i)}{\Delta c_i} \quad (5.2)$$

Where  $\Delta c_i$  is the finite difference step size associated with material constant  $i$ . This gradient is calculated for each constant  $c_i$  on each iteration and used by the algorithm to search for a better set of material constants which attempt to minimise the error  $\xi$ . A more detailed description of the algorithm can be found in the VisualDoc documentation [52].

## 5.2 Creep tests

Two tests commonly used to determine the creep properties of solder include monotonic creep tests and isothermal fatigue tests. Both of these can be used to indirectly determine constants for a kinematic hardening law. Isotropic hardening is not modelled as it was found to be inappropriate for modelling solder (see page 23).

In the following work the inverse analysis technique is validated by predicting material constants for idealised creep curves. Then material constants for the Armstrong-Frederick kinematic hardening law (4.26) are determined from published monotonic creep results on SnAgCu solder. Material constants for the steady state sinh creep law are also generated to match this data. The curves generated by the kinematic hardening law and the steady state creep laws are compared.

---

## 5.2. Creep tests

---

### 5.2.1 Method

The experimental data published in [51] consists of 12 strain vs. time graphs each representing a different stress and temperature condition (see table 5.1). These were chosen as they were the largest collection of whole creep curves found in the literature for SnAgCu solder (most publications only report the steady-state strain rates).

Case	Temperature ( °C)	Stress (MPa)
001	80	11.59
002	80	13.8
003	80	12.78
004	80	11.59
005	115	15.01
006	115	11.13
007	115	10.07
008	115	8.73
009	150	14.91
010	150	11.52
011	150	9.82
012	150	6.32

Table 5.1: Stress and temperatures for the 12 creep tests.

To model the test in FATMAN an FEA mesh consisting of just one element is used and force is applied to achieve a tensile stress as shown in figure 5.1. Only one element is needed because the test is designed to apply a uniform stress and strain on the solder test specimen. In fact, the use of FEA was not strictly necessary – the calculation for creep with only one component at a known temperature and stress is simple. The integration with the FATMAN FEA code was done in preparation for any further optimisation work which might be done requiring more complex geometries.

The VisualDOC software is used along with FATMAN to perform the optimisation. Communication between the programs is conducted via files as shown in figure 5.2. Files for each of the cases are kept in a separate directories *case001/*, *case002/*, ..., *case012/*. *FATMAN.exe* calculates the error from each simulation and writes it to an output file *strainComp.txt*. Another small program *calcError.exe* sums the error from each of the simulations and places the total error in *resp.vef* for VisualDOC to read. VisualDOC uses this error to guide its search and outputs material constants for the next iteration in *dvar.vef*. A Perl script modifies the material constants in all the inform files based on *dvar.vef*.



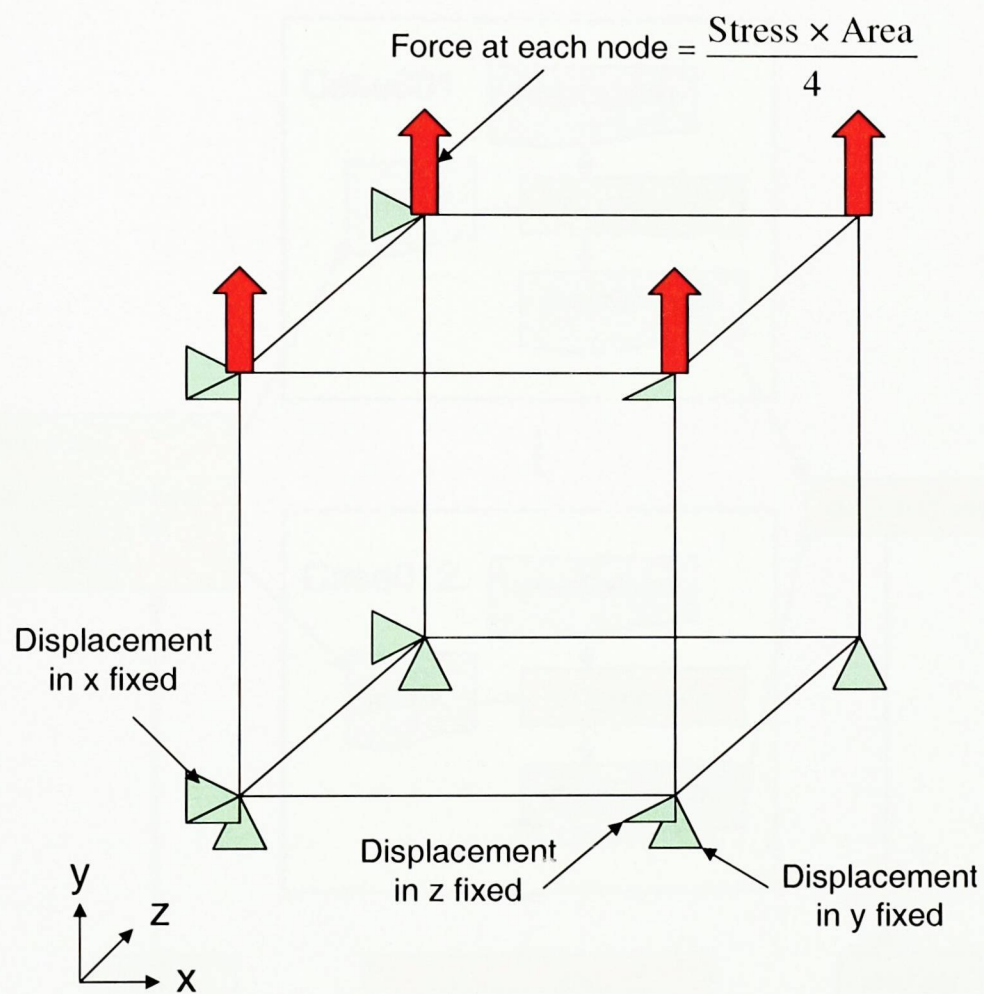


Figure 5.1: The boundary conditions used in the one element model used to model the monotonic creep test

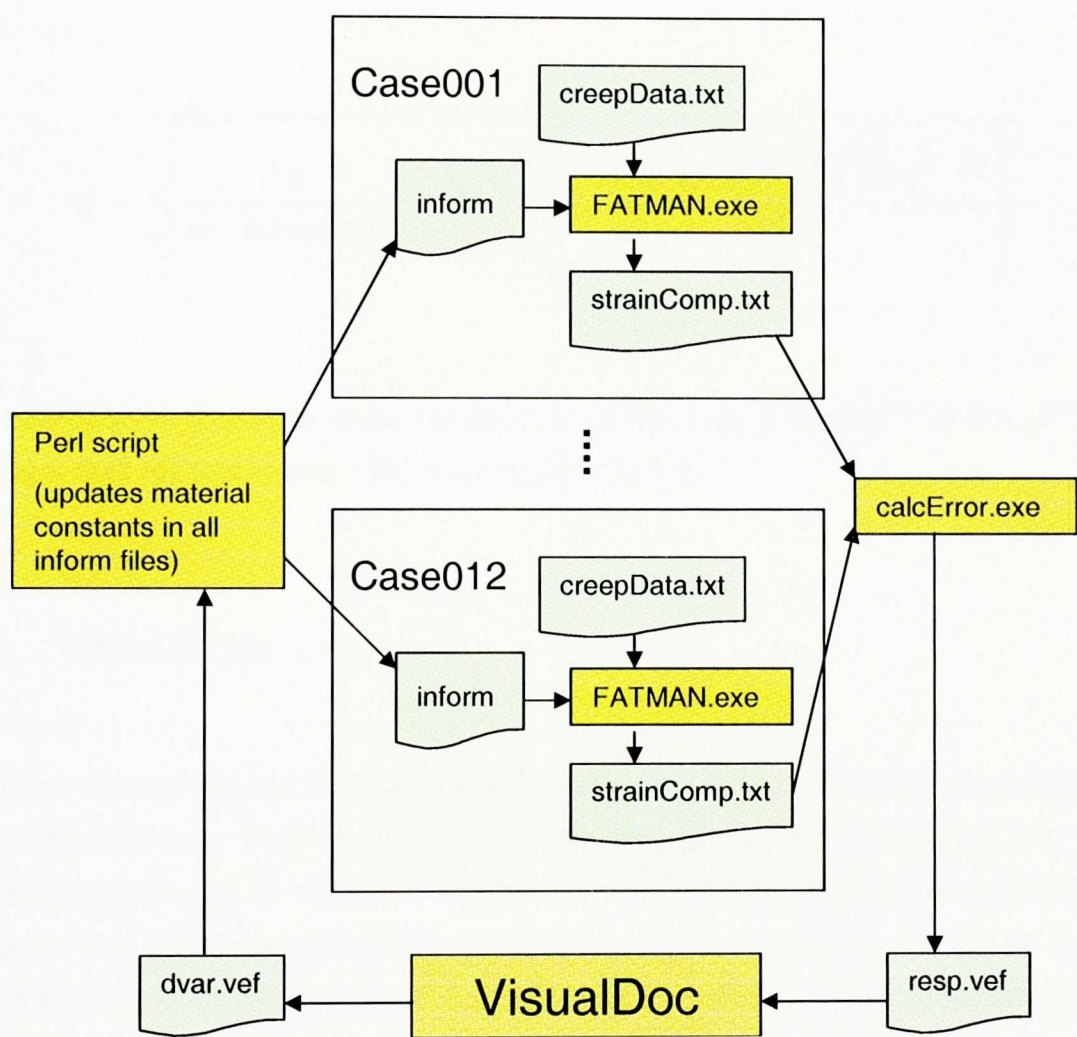


Figure 5.2: The FATMAN - VisualDOC integration



## 5.2. Creep tests

---

VisualDoc uses the Broyden-Fletcher-Goldfarb-Shanno conjugate gradient algorithm [52] to search for the material constants. The algorithm requires the gradient of the error w.r.t. the material constants at each iteration, this is obtained using a finite difference approximation. The relative step size and a minimum absolute step size are specified, the effect of changing these will be investigated.

The error  $\xi$  was used to judge the correlation between the simulated and experimental curves<sup>1</sup>:

$$\xi = \sqrt{\frac{1}{\text{no. creep tests}} \sum_{\text{creep-tests}} \left[ \frac{\sum_{\text{time-steps}} \left( \frac{\varphi^{\text{exp}} - \varphi^{\text{sim}}}{\min(\varphi^{\text{exp}}, \varphi^{\text{sim}})} \right)^2 \delta t}{t_{\text{total}}} \right]} \quad (5.3)$$

As an example of what the error represents, in the case where  $\varphi^{\text{exp}} = 2 \times \varphi^{\text{sim}}$  for all time steps and all test cases, the error would be 2.0.

### 5.2.2 Validation

To confirm the method works, simulations were performed of the 12 monotonic creep tests using arbitrary reference constants for the kinematic hardening law. These simulations produced 12 reference creep curves. The idea behind the validation was to imagine the reference constants were lost and new constants needed to be found which could generate curves matching the reference curves. The constants found by the optimisation method were then compared with the original reference constants to see how closely the new constants match the reference constants.

The results of this validation are shown in table 5.2. The parameters being optimised are  $A$  from the sinh law and  $h$  and  $S_{\text{max}}$  from the kinematic hardening law (the remaining three sinh parameters  $\alpha, n$  and  $Q/k$  are fixed at the values provided by Schubert [50]). The first column shows the reference constants used to generate the ‘experimental’ creep curves, the second column shows the starting point of the optimisation

---

<sup>1</sup>Implementation detail: In VisualDoc  $\epsilon^2$  was the parameter being optimised as this was originally chosen as the error function before altering it to the more meaningful one in equation (5.3)

## 5.2. Creep tests

Property	Reference	Starting Point	After Optimisation
$A$ ( $1 \times 10^5$ Pa)	2.77984	10.0	1.005145
$h$ ( $1 \times 10^{-6}$ s)	5.0	3.0	6.135117
$S_{\max}$ (MPa)	10.0	3.0	8.386562
$\xi$	$7.789 \times 10^{-4}$	11.51	$8.732 \times 10^{-3}$

Table 5.2: The results of the validation. The constants  $\alpha$ ,  $n$ , and  $Q/k$  are as given by Schubert [50].

and the third column contains the constants generated by the optimisation.

Although the constants generated are quite different from the reference constants, the error between the curves is extremely small, so that when plotted on a graph the curves are indistinguishable. This indicates that the problem is ill-conditioned, with a range of material constants which will provide a similar low error. But since it is the result of the laws which are important and not the constants themselves, this is not a concern.

### 5.2.3 Fitting to experimental creep curves

Optimisations were performed using the sinh law (SS1 and SS2) and using the kinematic hardening law (KH1 and KH2). For the sinh law all four constants were optimised and for the kinematic hardening law only  $A$ ,  $h$ , and  $S_{\max}$  were optimised. The starting point for SS1 is the set of constants from Schubert in appendix 5. It makes sense to choose previously published constants as a starting point as providing a good initial estimate will help the optimisation algorithm find the solution quicker. The other starting points were chosen arbitrarily, and are listed in table 5.3.

The results of optimisations from these four starting points is shown in table 5.4. For these optimisations the finite difference step size used to calculate the gradient  $\frac{\partial \epsilon}{\partial x}$  for a material constant  $x$  was  $0.01x$  (or  $1 \times 10^{-5}$ , whichever is larger). This resulted in the SS1 parameters remaining very close to their starting values. The other three optimisations started at points with higher errors which were decreased drastically.

The above optimisations were repeated using a smaller finite difference step size of



### 5.2. Creep tests

Property	SS1	SS2	KH1	KH2
$A$ ( $1 \times 10^5$ Pa)	<b>2.77984</b>	<b>2.0</b>	<b>2.77984</b>	<b>2.0</b>
$\alpha$ ( $1 \times 10^{-8}$ Pa $^{-1}$ )	<b>2.447</b>	<b>2.0</b>	2.447	2.447
$n$	<b>6.41</b>	<b>5.0</b>	6.41	6.41
$Q/k$ ( $1 \times 10^3$ °K)	<b>6.5</b>	<b>7.5</b>	6.5	6.5
$h$ ( $1 \times 10^{-6}$ s)	N/A	N/A	<b>5.0</b>	<b>0.2</b>
$S_{\max}$ (MPa)	N/A	N/A	<b>10.0</b>	<b>2.0</b>
$\xi$	2.946	16.91	3.245	3.366

Table 5.3: The starting points for optimisation (the values in bold are the ones to be optimised)

Property	SS1	SS2	KH1	KH2
$A(1 \times 10^5$ Pa)	2.77996	1.96981	25.71240	28.33986
$\alpha$ ( $1 \times 10^{-8}$ Pa $^{-1}$ )	2.44720	1.81216	2.447	2.447
$n$	6.40198	5.22226	6.41	6.41
$Q/k(1 \times 10^3$ °K)	6.48451	6.34477	6.5	6.5
$h(1 \times 10^{-6}$ s)	N/A	N/A	3.117858	4.606939
$S_{\max}$ (MPa)	N/A	N/A	11.32412	8.554231
$\xi$	2.937	2.666	0.7040	0.7098

Table 5.4: Results of optimisation using FD steps of 1E-2 relative, 1E-5 absolute

0.001 $x$  (or  $1 \times 10^{-6}$ , whichever is higher). This had a good effect on SS1, yielding a significantly lower error. However the errors achieved for the other cases are worse using the smaller finite difference steps.

In all cases the kinematic hardening law produced lower errors than the sinh law. This is as expected since the sinh law is not intended to capture the primary region of the creep curve present in the experimental data.

The results show that for this problem, the starting point does influence the optimised constants. This occurs because the search algorithm is designed to find a local min-

Property	SS1	SS2	KH1	KH2
$A(1 \times 10^5$ Pa)	2.487167	2.244033	25.63893	28.56856
$\alpha$ ( $1 \times 10^{-8}$ Pa $^{-1}$ )	1.599673	1.824163	2.447000	2.447000
$n$	4.994432	5.243524	6.410000	6.410000
$Q/k(1 \times 10^3$ °K)	6.335794	6.393744	6.500000	6.500000
$h(1 \times 10^{-6}$ s)	N/A	N/A	2.662011	5.230417
$S_{\max}$ (MPa)	N/A	N/A	12.98002	7.800450
$\xi$	2.650	2.673	0.7202	0.7128

Table 5.5: Results of optimisation using FD steps of 1E-3 relative, 1E-6 absolute

### 5.3. Damage

imum - there is no guarantee that this will be the best possible solution. Therefore it is wise to run the algorithm a number of times from different starting points to increase the chances of finding the true global minimum. Despite the different material constants predicted when using different starting points, the curves produced using the KH1 and KH2 constants from table 5.4 were virtually indistinguishable, and the curves from the SS1 and SS2 constants were close.

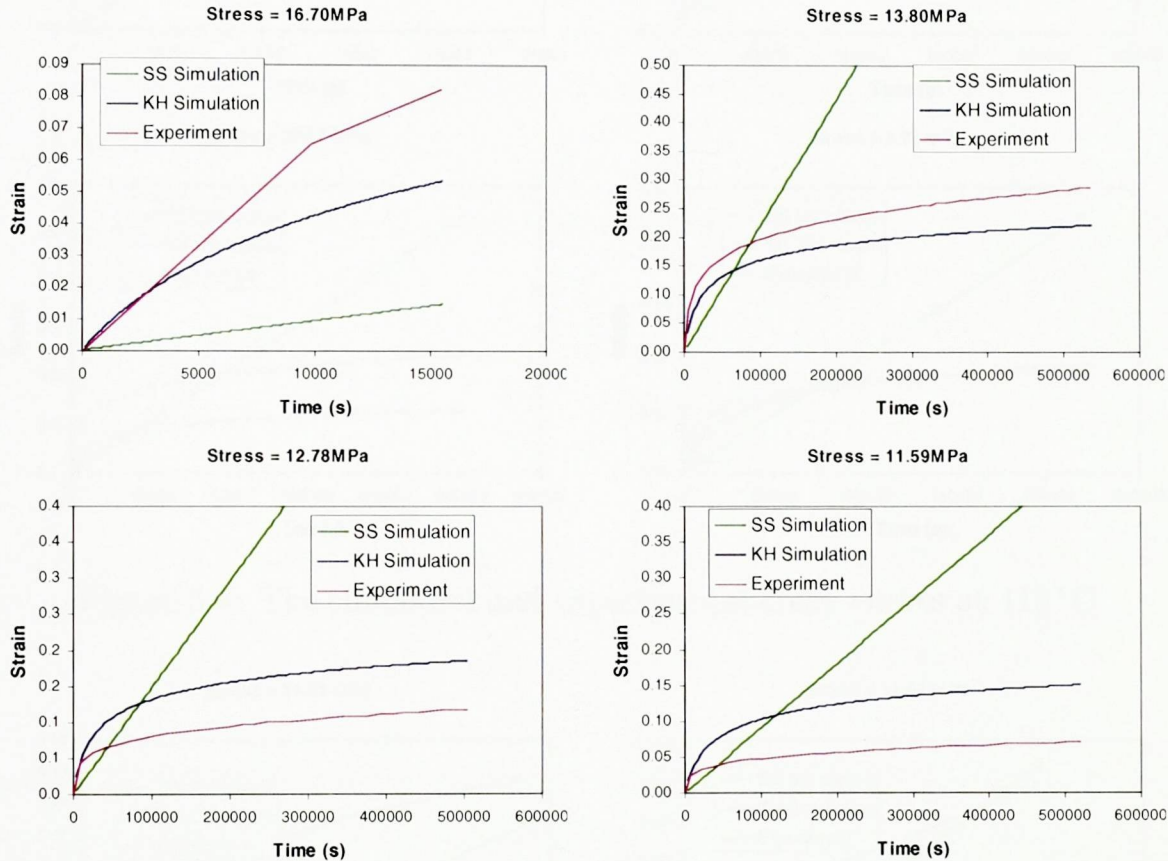


Figure 5.3: The simulated and experimental creep curves at 80 °C

The best set of constants for the steady state law is SS1 from table 5.5, and the best set of constants for the kinematic hardening law is KH1 from table 5.4. Results of simulations using these constants are plotted in figures 5.3, 5.4 and 5.5. It is plain to see that the kinematic hardening law provides a much better match to the experimental curves compared to the steady state law.

### 5.3 Damage

The damage law presented on page 72 contains only one material constant  $B$ . Due to the inversely proportional relationship between  $B$  and  $N_f$  identified on page 80 the



5.3. Damage

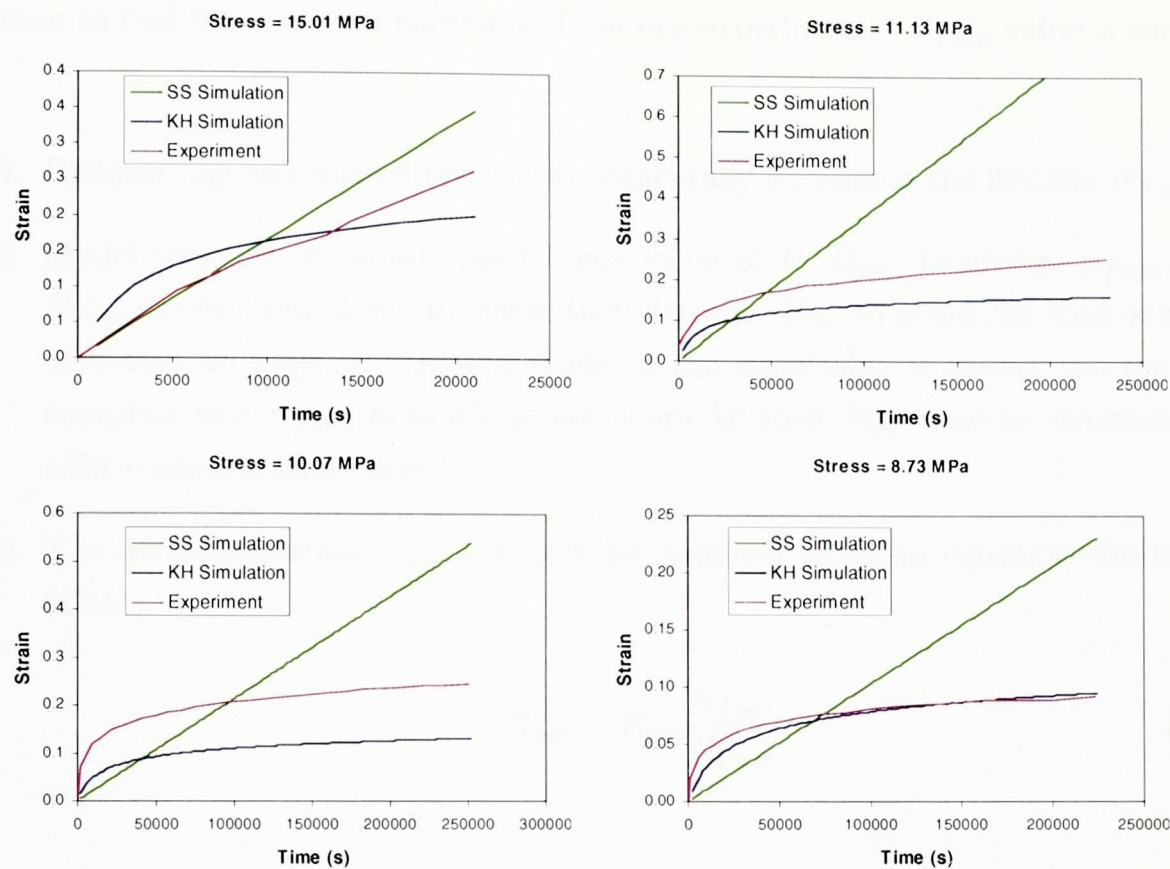


Figure 5.4: The simulated and experimental creep curves at 115 °C

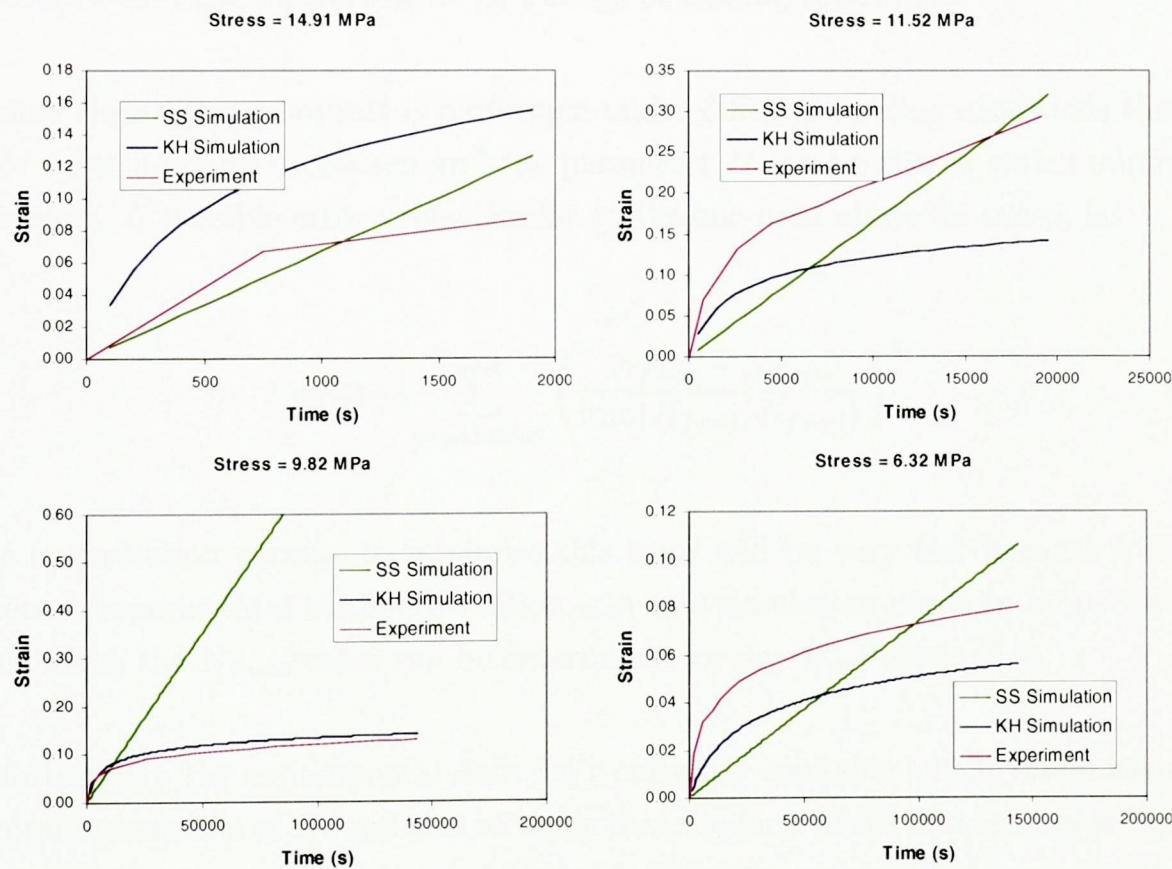


Figure 5.5: The simulated and experimental creep curves at 150 °C

### 5.3. Damage

---

process to find this material parameter from one experimental  $N_{f:\text{exp}}$  value is simple:

1. Perform any accelerated test to experimentally determine the lifetime  $N_{f:\text{exp}}$
2. Model this test using an approximate value of  $B$ ,  $B_{\text{sim}}$ , to obtain  $N_{f:\text{sim}}$ . (If  $N_{f:\text{sim}}$  is less than about 10 cycles then decrease  $B_{\text{sim}}$  to avoid the kind of error discussed on page 81. Alternatively, if the simulation is taking too long to complete and  $N_{f:\text{sim}}$  is much greater than 10 then  $B_{\text{sim}}$  may be increased to reduce computation time.)
3. The correct constant  $B_{\text{real}}$  can now be obtained using an equation similar to (4.51):

$$B_{\text{real}} = B_{\text{sim}} \frac{N_{f:\text{sim}}}{N_{f:\text{exp}}} \quad (5.4)$$

When a simulation runs using  $B_{\text{real}}$  it will yield  $N_{f:\text{real}}$  which will be equal to  $N_{f:\text{exp}}$ . However since only one experimental value was used the constant  $B_{\text{real}}$  is likely to be inaccurate and not representative of a range of loading conditions.

If more than one experiment is performed under different loading conditions then an error value needs to be chosen and the parameter  $B$  can be chosen which minimises this error. A possible error value, similar to the one used above for creep, is:

$$\text{error} = \sum_{\text{experiments}} \left( \frac{N_{f:\text{exp}} - N_{f:\text{real}}}{\min(N_{f:\text{exp}}, N_{f:\text{real}})} \right)^2 \quad (5.5)$$

The optimisation process to minimise this error will be very fast because for each different experimental loading condition only one simulation needs to be performed, after which the  $N_{f:\text{real}}$  value can be determined for any  $B_{\text{real}}$  using (5.4).

Unfortunately the experimental data isn't currently available which would allow an accurate prediction of  $B$  (and also to verify that the form of the damage law is capable of providing accurate predictions of lifetime). However, on page 104 a rough estimate of  $B$  is made on the basis of the results of the NPL fatigue test.



## 5.4 Summary

1. The inverse analysis approach was described in relation to determining material constants.
2. The VisualDoc optimisation software was integrated with FATMAN to perform the inverse analysis.
3. The method was validated by predicting material constants for the Armstrong-Frederick kinematic hardening law which generate curves matching idealised, reference creep curves. The material constants found were differed from the reference constants but generated practically identical creep curves.
4. Material constants were found for the steady state sinh creep law and the Armstrong-Frederick kinematic hardening law by using published monotonic creep test results.
5. A simple method to determine the  $B$  constant for the damage law using inverse analysis was described.

# Chapter 6

## Analysis: Fatigue Test

This chapter investigates an isothermal fatigue test for solder joints developed by the NPL. The test is intended to apply a prescribed displacement profile to a solder lap joint positioned between two copper arms. Modelling shows that the displacement across the solder joint is not equal to the displacement at the ends of the copper arms. A numerical method is described to compensate for this difference to allow the correct displacement to be achieved experimentally.

The hysteresis (stress vs. strain) curve for an undamaged joint is predicted using the finite element technique and compared to experiment. Damage accumulation is predicted for SnAgCu using the damage law described in chapter 4 and the results are compared to experiment in terms of load drop, electrical resistance and crack shape. Also the effect of prescribed cracks on the electrical resistance across the specimen is predicted.

### 6.1 Description of test

Isothermal fatigue tests are useful as they capture many aspects of solder's mechanical behaviour, two of which are particularly relevant to this work:



---

## 6.1. Description of test

---

1. Kinematic hardening will have an effect on the behaviour of the solder and since the load is reversed the effect of kinematic hardening may be distinguished from isotropic hardening (unlike the monotonic creep test)
2. The rate of weakening and cracking of the solder due to ductile fatigue will have an effect on the load drop measured

This means that material constants which describe (a) kinematic hardening and (b) damage accumulation could potentially be obtained using the techniques in chapter 5. Unfortunately, due to the limited resources available for the tests it was not possible to obtain a sufficient quantity of experimental data to accurately determine these constants. Hence, only a very rough estimate has been made of the damage law constant  $B$  based on the results of a single test on page 104.

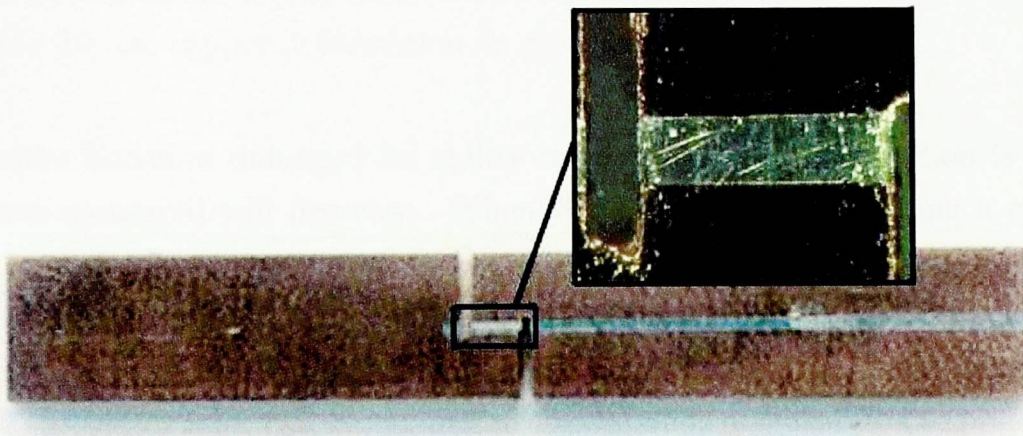


Figure 6.1: The test specimen. A SAC joint between two copper arms

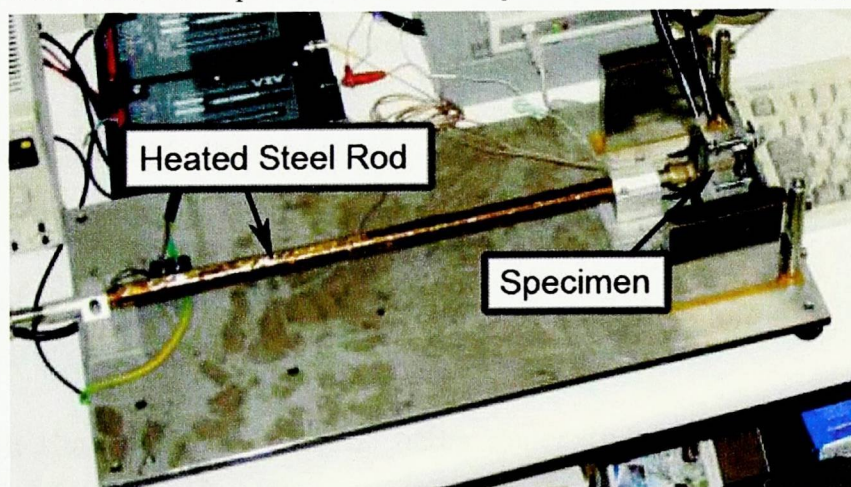


Figure 6.2: A photo of the NPL fatigue test apparatus.

The test specimen consists of a SnAgCu lap joint between two copper arms and is shown in figure 6.1. The apparatus in which the specimen is placed was modelled very



---

## 6.2. Modelling Method

---

crudely on page 55 and is shown in figure 6.2. The apparatus is capable of measuring the force applied across the specimen and the displacement between the ends of the specimen is measured using a pair of LVDTs (Linear Variable Differential Transformers). The temperature of the rod is controlled by passing an electric current through a heating coil wrapped around it. Heating or cooling the rod causes it to expand or contract respectively, thus exerting a force on the specimen. The displacement across the specimen (between the ends of the copper arms) is controlled by adjusting the temperature of the steel rod to ensure the correct displacement as measured by the LVDTs.

In the initial design of the test a periodic displacement profile was applied to the ends of the copper arms with the assumption that the solder will experience the same deformation. This was shown to be false – deformation occurs in the copper arms which results in a lower displacement across the joint. A method will be described to compensate for the copper deformation on page 99.

As the solder becomes damaged its ability to resist further deformation is reduced so the force measured will decrease. When the force amplitude during a cycle has dropped to 50% (or some other arbitrary percentage) of the original value, then the joint is considered to have failed. Alternatively, the electrical resistance across the joint could be used as a failure criteria. In this way, the fatigue resistance (cycles to failure) of the solder joint can be quantified for different magnitudes of applied strain at different temperatures.

## 6.2 Modelling Method

The purpose of the modelling work is:

1. Establish that the displacement being generated across the solder joint is as prescribed:
  - (a) Show that significant deformation occurs in the copper arms. Hence the displacement across the solder is not the same as the displacement controlled at the copper arms.



---

### 6.3. Displacement Compensation

---

- (b) Develop method to compensate for the displacement in the copper, thus achieving the correct displacement across the solder joint.
- 2. Predict the load-drop and crack shape in the solder and compare to experiment.
- 3. Determine how the electrical resistance changes with crack length.

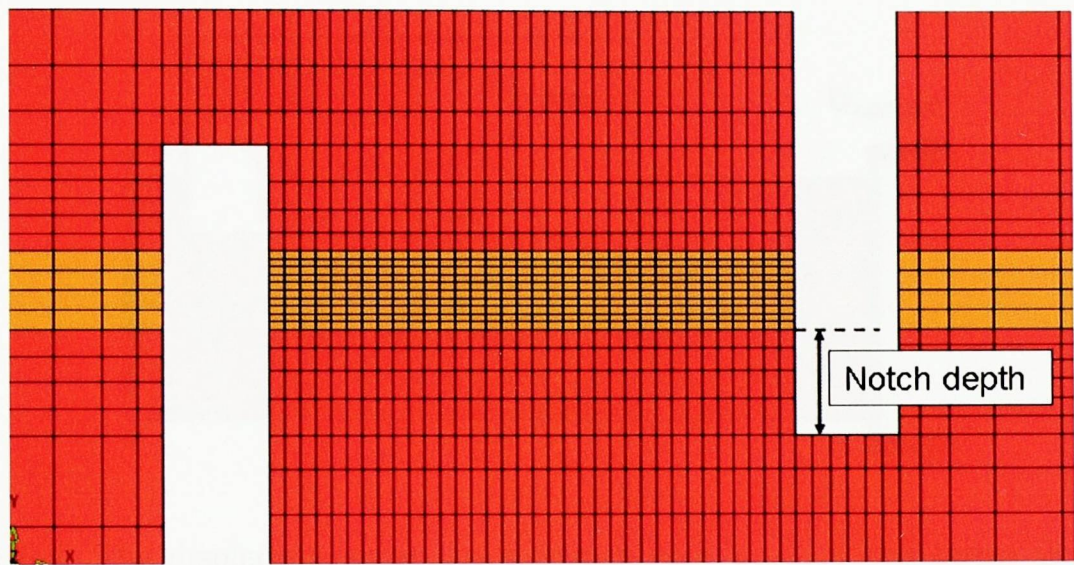


Figure 6.3: The Finite Element mesh showing the notch depth

All the modeling work was conducted using the FATMAN code. Figure 6.3 illustrates the mesh density in the region of the solder joint. The copper is modelled as a linear elastic material and the solder is modelled using the steady-state sinh creep law where the material properties are provided in appendix A. One simulation is also performed using the kinematic hardening law with constants KH1 from table 5.4.

For the prediction of the crack propagation and drop in the maximum force per cycle, the damage-based constitutive law described in chapter 4 was used.

### 6.3 Displacement Compensation

The test is intended to apply a trapezoidal displacement profile to the solder joint. In the initial design of the test this profile was applied directly to the ends of the copper arms ( $u_{\text{applied}}$  in figure 6.4), under the assumption that the displacement in the copper is negligible. However simulations have been performed which show this

### 6.3. Displacement Compensation

to be false. There can be a large discrepancy between the displacement either side of the solder joint and the displacement either side of the copper arms. Figure 6.5 shows a maximum error of about 20% between the displacement at the end ( $u_{\text{applied}}$ ) and across the joint ( $u_{\text{solder}}$ ) at a temperature of 100 °C. When the temperature is decreased to -35 °C (figure 6.6), this error increases to 60% as the increased stiffness and greater creep resistance of the solder results in a lower  $u_{\text{solder}}$ .

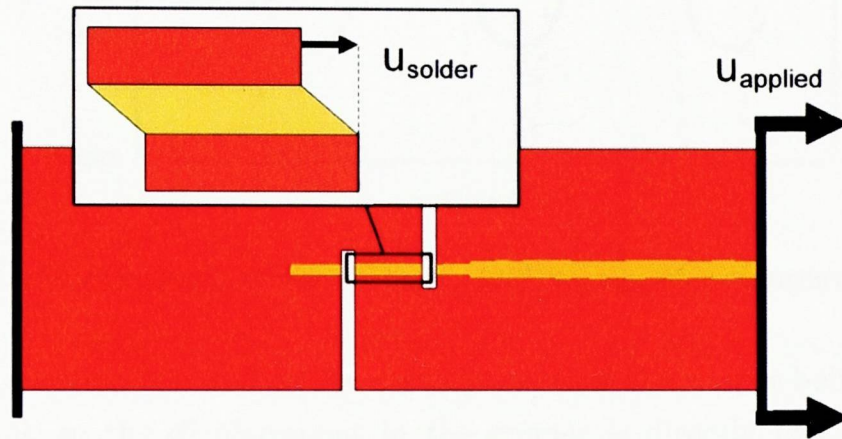


Figure 6.4: The displacements at the specimen end ( $u_{\text{applied}}$ ) and across the solder joint ( $u_{\text{solder}}$ )

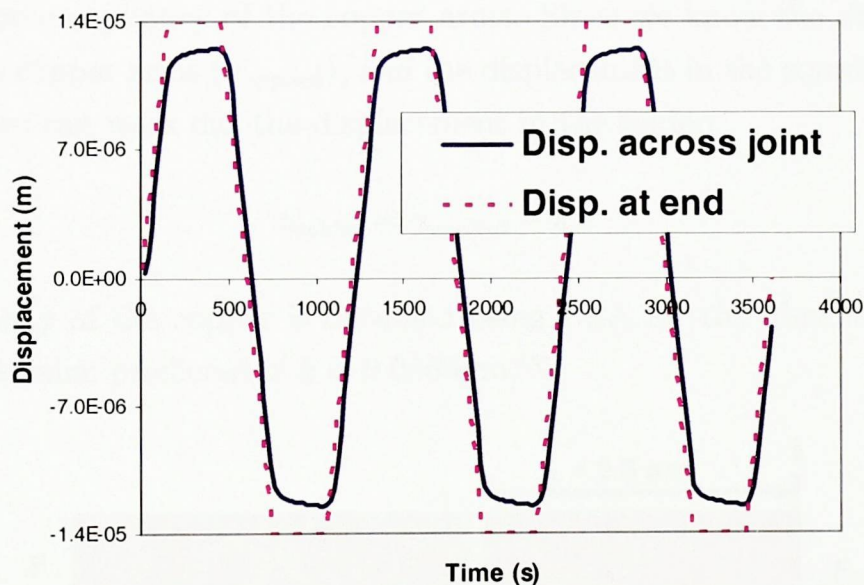


Figure 6.5: The discrepancy between  $u_{\text{solder}}$  and  $u_{\text{applied}}$  at a temperature of 100 °C

In order to achieve the correct displacement profile at the solder joint it is necessary to apply a different displacement profile at the ends of the copper arms. This new displacement profile cannot be worked out in advance because the amount of deformation in the copper depends on the force, which in turn depends on the creep in the solder and this is not known beforehand.



### 6.3. Displacement Compensation

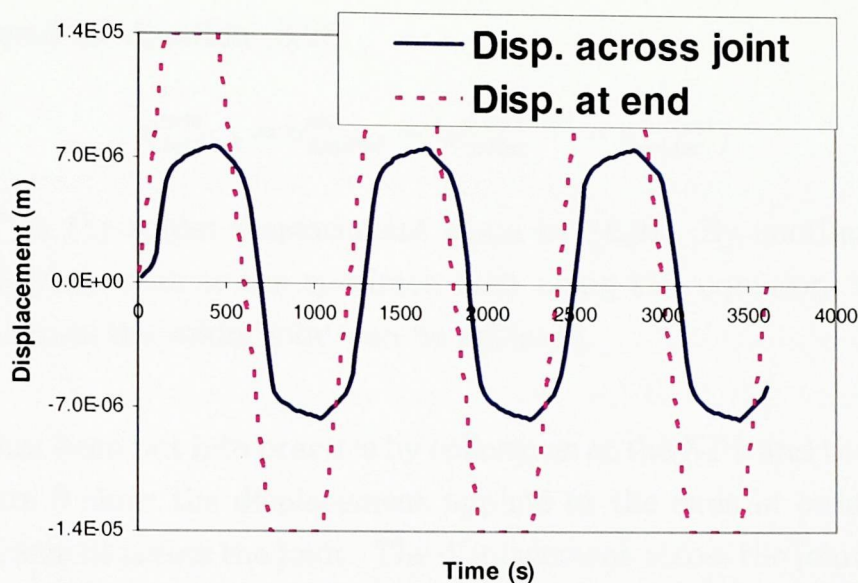


Figure 6.6: The discrepancy between  $u_{\text{solder}}$  and  $u_{\text{applied}}$  at a temperature of  $-35^{\circ}\text{C}$

The following solution is based on the assumption that the copper behaves as a linear elastic material, so the displacement in the copper is directly proportional to the force:

$$u_{\text{copper}} = kF \tag{6.1}$$

Where  $k$  is the compliancy of the copper arms. Since we know the displacement at the end of the copper arms ( $u_{\text{applied}}$ ), and the displacement in the copper is a function of the force, we can work out the displacement in the solder:

$$u_{\text{solder}} = u_{\text{applied}} - kF \tag{6.2}$$

The compliancy of the copper is obtained using FEA for the dimensions shown in figure 6.7, the value predicted is  $k = 0.0566\mu\text{m}/\text{N}$ .

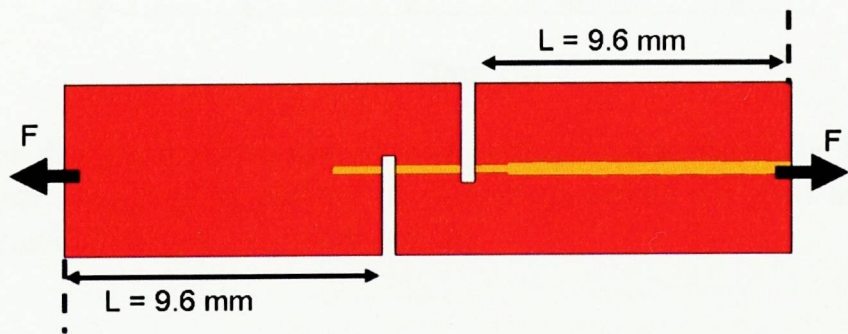


Figure 6.7: The dimensions used to calculate the compliancy of the copper arms  $k$

In order to control the solder displacement it is necessary to implement a feedback

### 6.3. Displacement Compensation

mechanism based on equation (6.2):

$$u_{\text{applied}}^{\text{new}} = u_{\text{applied}}^{\text{old}} + (u_{\text{solder}}^{\text{prescribed}} - u_{\text{solder}}^{\text{current}}) \quad (6.3)$$

Where  $u_{\text{solder}}^{\text{current}}$  is the solder displacement given by (6.2). By continually updating the applied displacement at the specimen ends using this equation, the prescribed displacement across the solder joint can be achieved.

This method has been put into practice by colleagues at the NPL and the experimental results in figure 6 show the displacement applied at the ends in order to achieve a  $\pm 10\mu\text{m}$  displacement across the joint. The displacement across the joint is determined using equation (6.2) and its accuracy depends on the accuracy of  $k$ . There is a slight overshoot of the solder displacement at the start of each dwell, a possible explanation for this is the time lag between measuring the current displacement and applying the adjusted displacement. Nevertheless, the displacement across the solder is very close to that intended (assuming  $k$  is accurate) and far better than would be achieved without using the displacement compensation method.

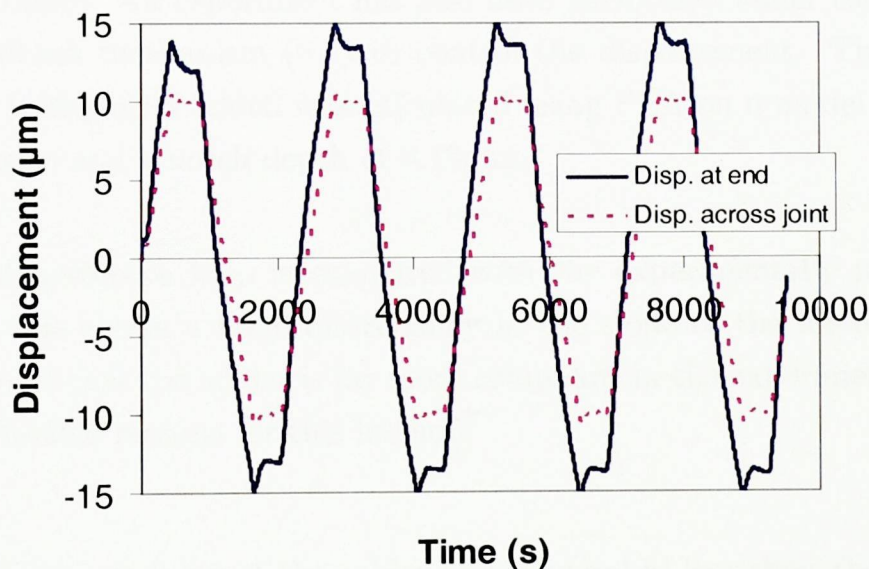


Figure 6.8: The displacements achieved in experiment when using the feedback mechanism to control  $u_{\text{solder}}$ . (The plotted displacement across the joint is not measured directly, it is calculated using equation (6.2))



### 6.4 Fatigue Cycling

In order to achieve the prescribed displacement  $u_{\text{solder}}$  in the FEA simulation, an inverse analysis approach is used. This is an iterative process where at each time step the applied displacement at the ends of the copper arms is adjusted until the displacement measured across the solder joint is as prescribed<sup>1</sup>. This works by performing the following adjustment to  $u_{\text{applied}}$  on each iteration of the LENI scheme:

1. Calculate  $u_{\text{solder}}$  directly based on the  $u$  displacements of the solder joint nodes at the top-center of the joint and the bottom-center of the joint.
2. Adjust  $u_{\text{applied}}$  using equation (6.3).

The simulation was performed at 25 °C, with an applied displacement of  $\pm 10\mu\text{m}$  across the solder joint and with 14 min ramps and 6 min dwells, the notch depth has been reduced to 0.18mm. An experiment has also been performed under these conditions using the feedback mechanism (6.3) to control the displacement. The compliancy used was  $k = 0.064\mu\text{m}/\text{N}$  which was calculated using FEA on a model with 16.1mm long copper arms and a notch depth of 0.18mm.

The predicted hysteresis loop is compared with the experimentally measured loop in figure 6.9, this shows a large discrepancy in the slope of the force-displacement curve. It appears that the solder is far more compliant in the experiment than in the simulation. Possible reasons for this include:

1. The Young's modulus of the solder is considerably less than the 51GPa used in the simulation. (The modulus would need to be about 8GPa - far less than reported in the literature)
2. The copper arms are more compliant than assumed. If the compliancy were double then the actual behaviour of the solder during the test would be as shown by the  $k = 0.13\mu\text{m}/\text{N}$  green curve in figure 6.9. This would imply that the geometry and/or Young's modulus of the copper in the experiment is significantly different to that simulated.

---

<sup>1</sup>Alternatively the same feedback mechanism used in the experiment could have been modelled.

---

## 6.4. Fatigue Cycling

---

3. There is additional unaccounted-for deformation occurring between the ends of the copper arms and the LVDTs (Linear Variable Differential Transformers) which measure the displacement.

It is currently unclear which, if any, of the above explanations is correct. Also of interest is that the force predicted using the kinematic hardening law is lower than that predicted by the steady state creep law, this is because the kinematic hardening law captures the increased creep strain rates within the primary region of the creep curve.

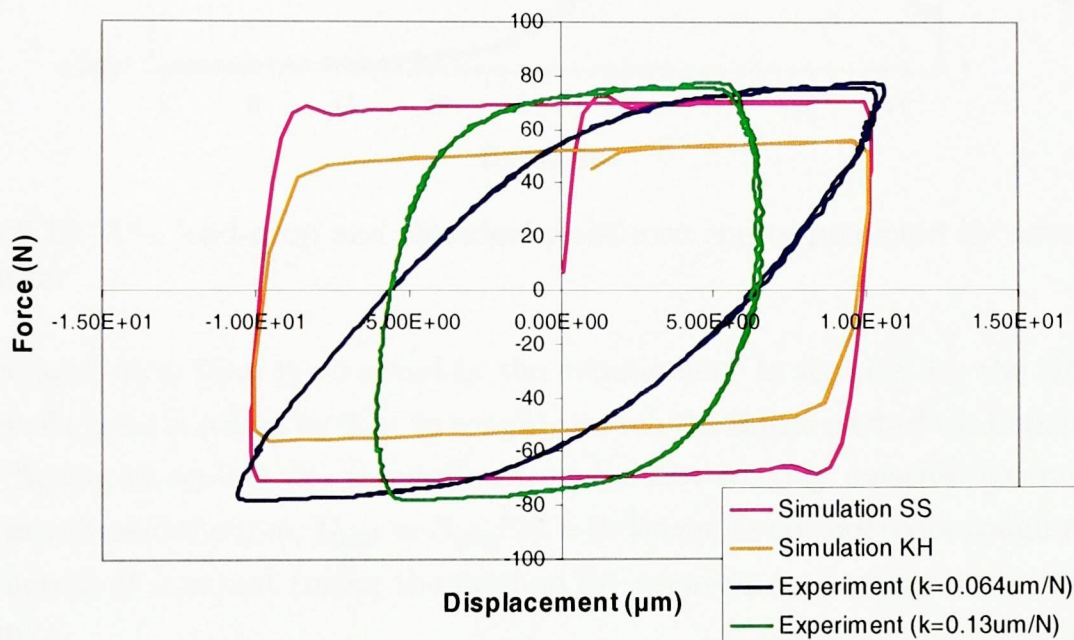


Figure 6.9: The predicted hysteresis loop using both steady state (SS) and kinematic hardening (KH) laws compared with the experimental loop, using both the correct compensation  $k = 0.064 \mu\text{m}/\text{N}$  and  $k = 0.13 \mu\text{m}/\text{N}$ .

### 6.4.1 Load drop

The above experiment was continued for 700 cycles, over which time the load amplitude dropped to about 1/3 its original value. This load drop has been simulated using the damage law with parameter  $B_{\text{sim}} = 1.0$  and the load-drop over time is presented in figure 6.10 along with the increase in electrical resistance predicted using the method described in 4.4.3.

The simulation uses the unrealistic damage constant  $B_{\text{sim}} = 1.0$ , which results in



### 6.4. Fatigue Cycling

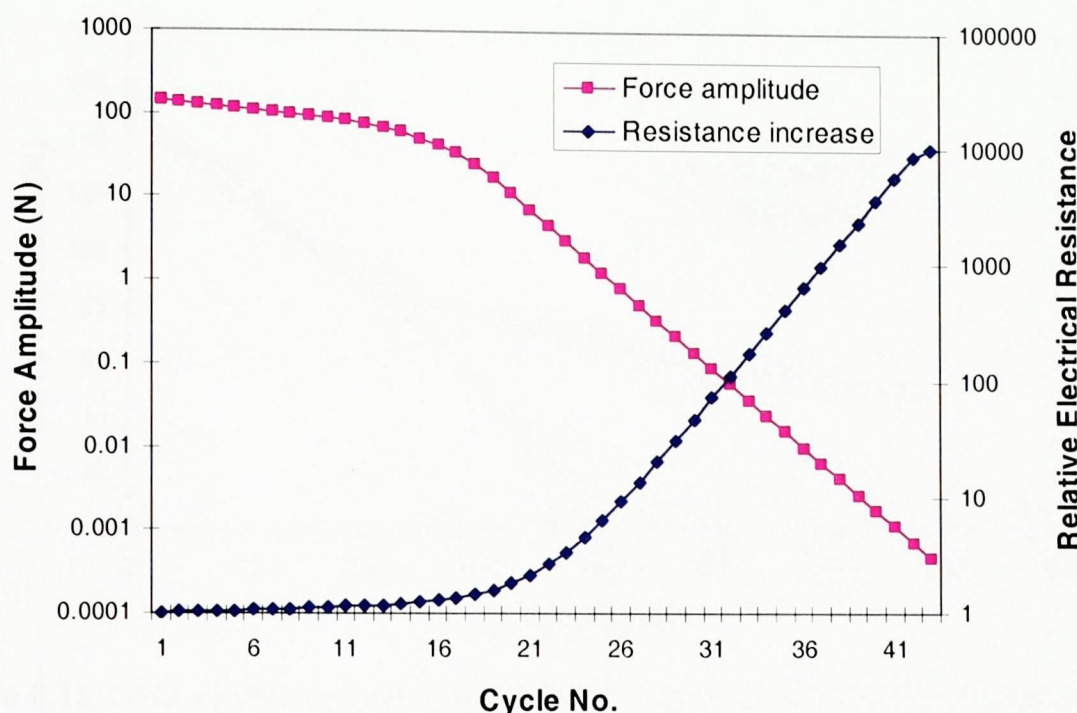


Figure 6.10: The load-drop and electrical resistance curves predicted by damage-law simulation

a faster load drop than is observed in the experiment. In figure 6.11, the simulated number of cycles is scaled by  $20\times$  to roughly match the initial part of the experimental curve. Seeing as scaling the simulation time by  $20\times$  roughly matches the beginning of the experimental curve,  $B_{\text{real}} = B_{\text{sim}}/20 = 0.05$  can be considered a rough measure of the actual  $B$  constant (using the method for speeding up damage computation on page 80).

After 200 cycles, figure 6.11 shows a discrepancy between the simulated and experimental results, the rate of load drop in the simulated curve drops rapidly whereas the experiment shows a slowing of the load drop rate. There are many possible reasons for this which include:

1. The crack shape predicted is different to the experiment. This is likely as the random variation in the solder properties due to its granular microstructure will make the exact crack shape unpredictable. No cross sections are available matching this test case but an example of a joint damaged by the fatigue test is shown below in figure 6.12.
2. In reality the crack surfaces will touch each other and therefore resist compressive stresses. In the simulation, completely damaged elements do not resist

## 6.4. Fatigue Cycling

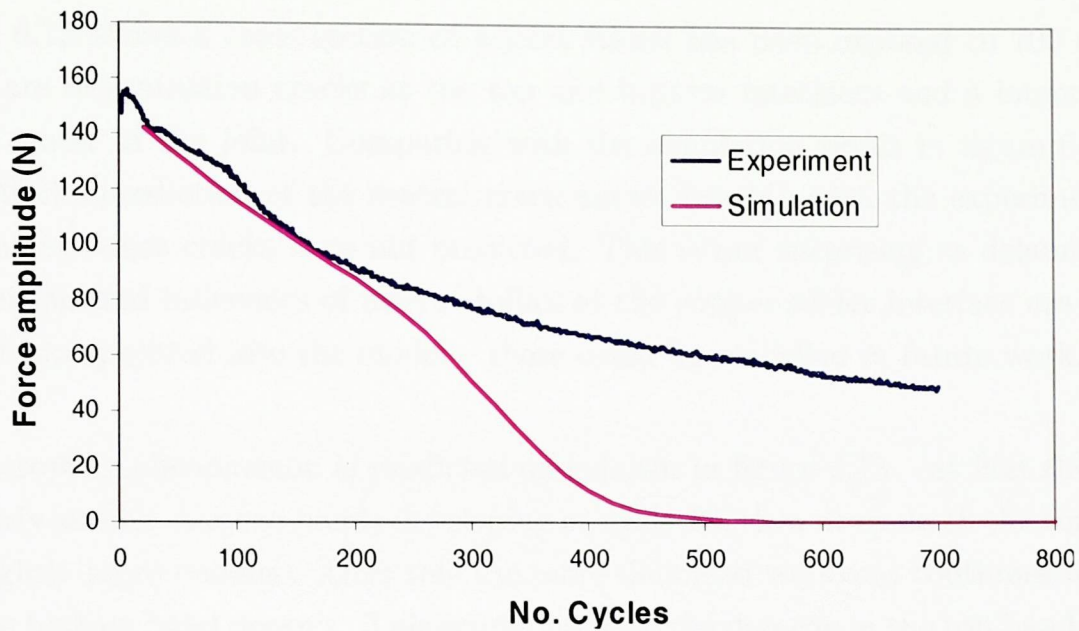


Figure 6.11: The predicted load drop curve scaled to match the experimental curve

compressive stresses.

3. The constitutive damage law doesn't accurately model the change in solder properties caused by creep fatigue.
4. The geometry of the FEA model doesn't match the experiment exactly, in particular the size of the notch can vary slightly between experimental samples.

Unfortunately the lack of experimental data means that the true cause(s) of the discrepancy cannot be identified at present.

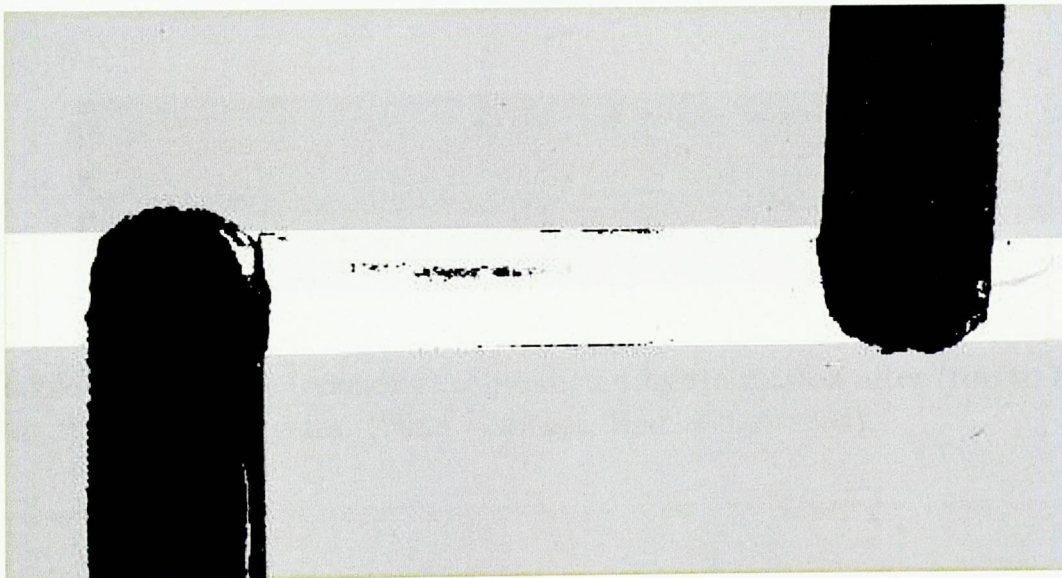


Figure 6.12: An SEM image of cracks after 700 cycles



---

#### 6.4. Fatigue Cycling

---

Figure 6.12 shows a cross section of a joint which has been exposed to 700 cycles. There are delamination cracks at the top and bottom interfaces and a larger crack in the center of the joint. Comparing with the simulation result in figure 6.13 we see that the prediction of the central crack agrees roughly with the experiment except the interface cracks were not predicted. This is not surprising as delamination mechanisms and influences of intermetallics at the copper-solder interface are not at present incorporated into the model – these could be modelled in future work.

An interesting phenomenon is predicted and shown in figure 6.13 – at first there are two fairly similar damage bands developing at cycle 13, then at cycle 18 the top band has slightly more damage. After this the more damaged top band continues to grow and the bottom band doesn't. This occurs because the damage in the top band makes it weaker and therefore it deforms more, alleviating the strain in the bottom band.

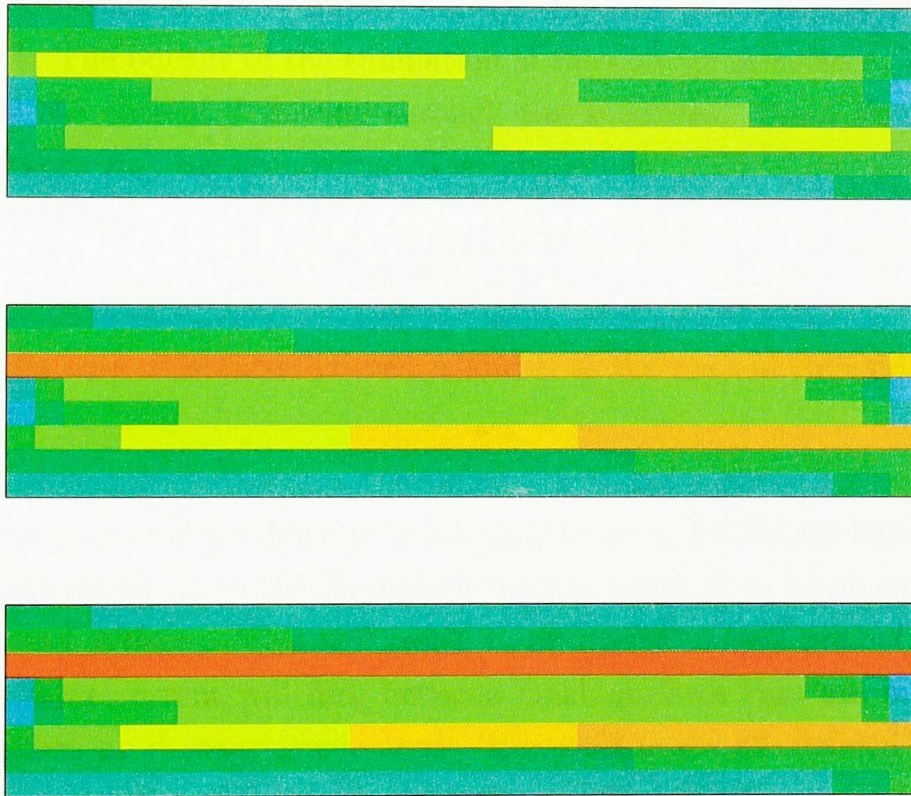


Figure 6.13: The damage (cracking) as predicted by simulation after (top to bottom) 13 cycles, 18 cycles, 43 cycles. (Blue = intact, Red = damaged)

## 6.5 Electrical Resistance

In order to monitor the degradation of the solder joint during the experiment, a value similar to electrical resistance (which we will call pseudo-resistance) is monitored. As cracks grow in the solder joint, the pseudo-resistance increases.

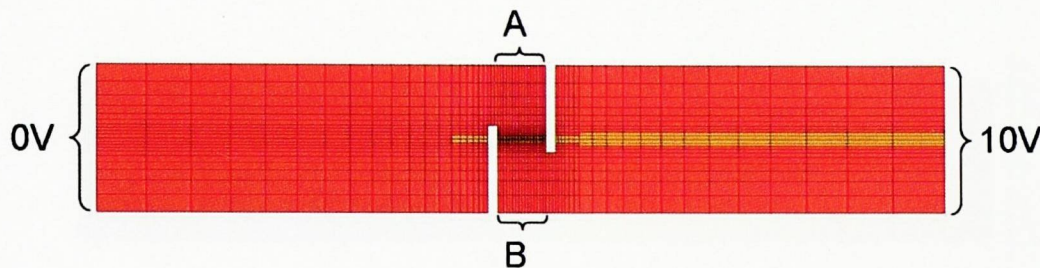


Figure 6.14: Diagram showing the mesh and boundary conditions

A potential difference of 10V is applied between the ends of the copper arms as shown in figure 6.14. The output of the simulation is the voltage at surfaces A and B ( $V_A$  and  $V_B$ ) and the current  $I$  flowing through the specimen. From these values the pseudo-resistance  $R_{AB}$  between A and B is calculated:

$$R_{AB} = \frac{(V_B - V_A)}{I} \quad (6.4)$$

This is not the true resistance between A and B as the current isn't flowing directly from A to B.

This has been simulated for different crack lengths using FATMAN and the material constants in appendix A. In the simulation there is assumed to be no current flowing between cracked surfaces. This will result in an overestimated predicted resistance as in reality some current will flow between crack surfaces that are in contact. In these simulations no damage law is used – the crack paths are defined manually by disconnecting the nodes of the mesh along the crack interface.

Figure 6.15 shows voltage contours for different crack lengths and figure 6.16 shows the relationship between crack length and resistance. When two cracks are present in the joint the pseudo-resistance increases considerably for crack lengths 50% and above. This occurs because the electric current is forced to flow horizontally through the joint in a narrow channel.



6.5. Electrical Resistance

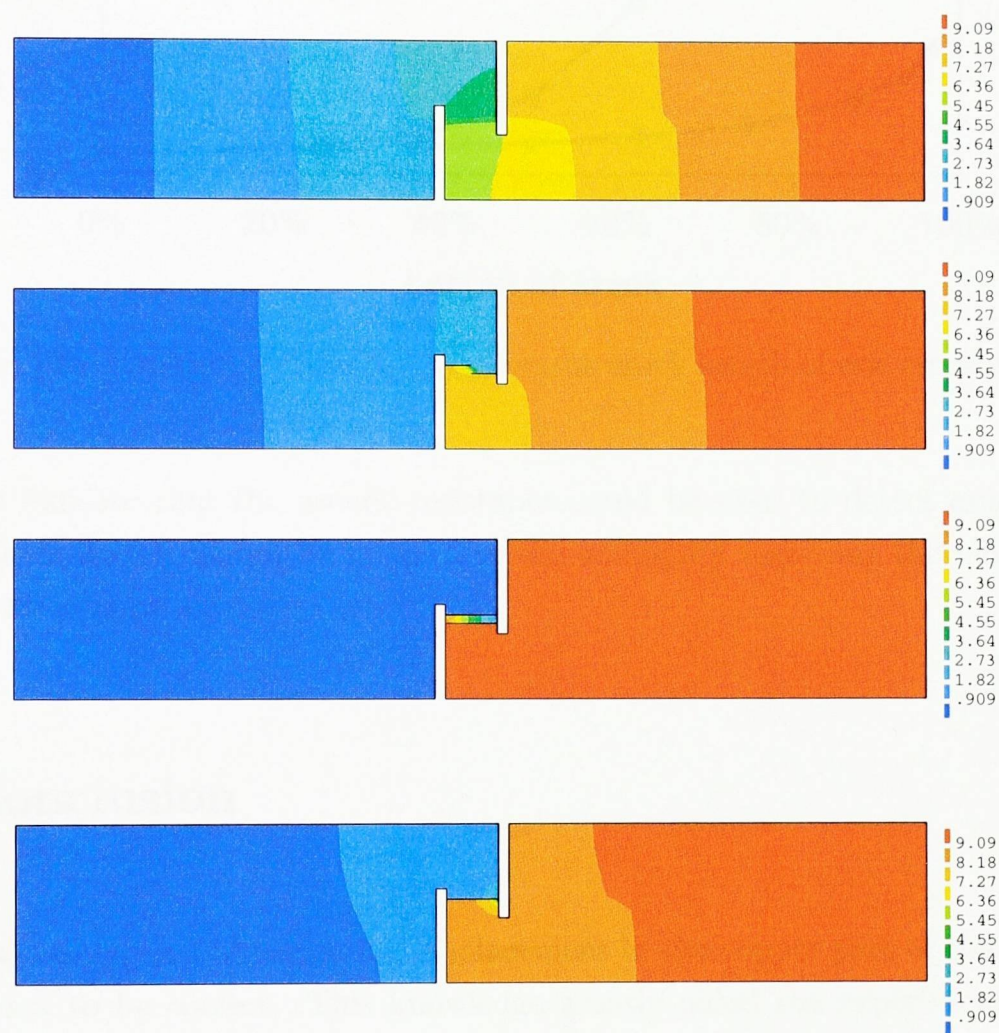


Figure 6.15: The voltage field with (top to bottom) no crack present, two 50% cracks, two 97% cracks, one 97% crack. (Red = 10 Volts, Blue = 0 Volts)

## 6.6. Conclusion

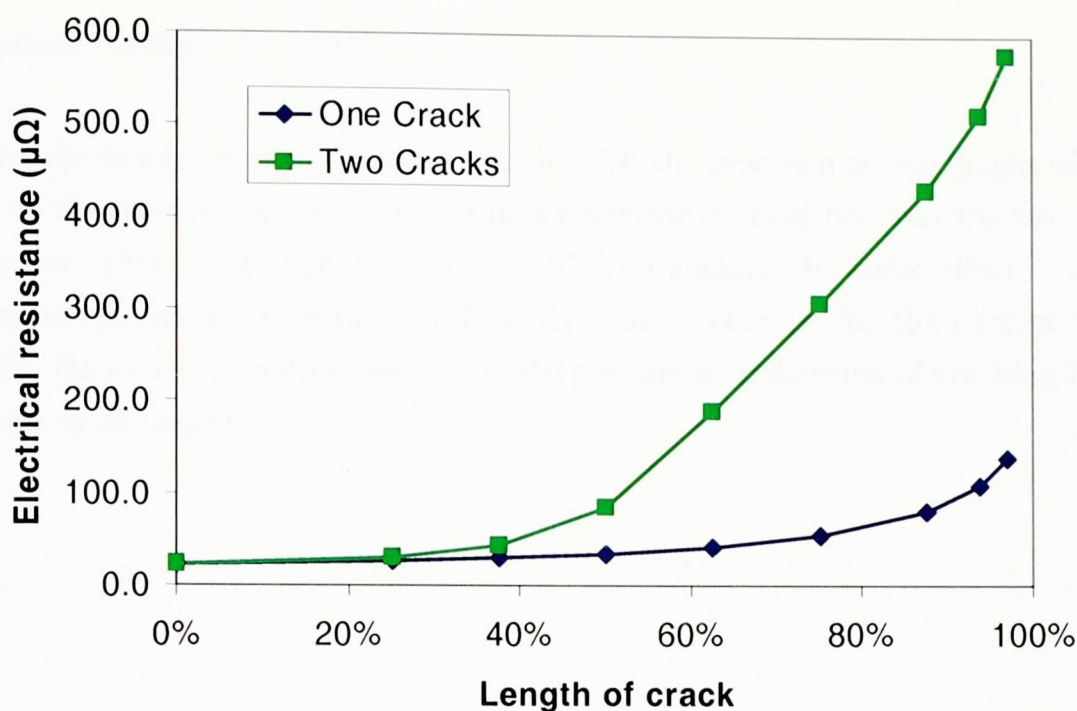


Figure 6.16: The change in resistance ( $R_{AB}$ ) versus crack length of one crack and two cracks

The results indicate that the pseudo-resistance could be used to detect cracks but the exact crack length cannot be inferred to the ambiguity regarding the number of cracks and their exact shape.

## 6.6 Conclusion

The original assumption of neglecting displacement in the copper part of the sample was found not to be correct. This knowledge greatly aided the experimental programme at the NPL. It was shown that the deformation in the solder accounted for only 40% to 80% of the total displacement, depending on the temperature. The remaining 20% to 60% of the total displacement is due to elastic deformation in the copper specimen. However by implementing the feedback mechanism in equation (6.3), the correct displacement across the solder joint can be achieved.

The predicted hysteresis curve for an intact joint did not match the experimental curve. Three possible explanations were presented on page 103 but further investigation is required to determine the true reason. The predicted load drop curve was fitted to the experimental data for the first 200 cycles to obtain a rough estimate of



## 6.6. Conclusion

---

the damage constant  $B = 0.05$ .

The pseudo-resistance was shown to double with the presence of two cracks of  $>39\%$  length as the electric current is forced into a narrow channel between the two cracks. If only one crack is present it must be  $>67\%$  to achieve the same effect – it takes a longer single crack to create a sufficiently narrow channel for the current to flow through. Hence the pseudo-resistance could provide an indication of cracking but not the exact crack length.

## Chapter 7

# Analysis: Thermal Cycling of Resistor Joints

In a thermal cycling test, the specimen is placed in an oven where the temperature is repeatedly cycled between two extremes. This chapter presents modelling and experiments to predict the effect of thermal cycling profiles on the damage buildup in surface mount resistors. Three sizes of resistor are investigated: 2512, 1206 and 0603, using both SnAgCu solder and Sn3.5Ag solder.

Experimental work performed by the NPL (National Physical Laboratory) is presented which compares the degradation in ultimate shear strength (USS) caused by thermal cycling using the six temperature profiles shown in figure 7.1. FEA models are used to predict the severity of the six thermal profiles, creep is modelled with the sinh law (4.15). Accumulated creep strain  $\varphi_{acc}$ , and accumulated creep energy density  $\Delta W$  are used to predict damage. Results are compared to the experimental data showing a reasonable correlation between predicted damage and drop in USS. Hysteresis loops showing the stress-strain response in the solder are used to show how the solder behaves during the different regions of the thermal cycles.

FEA modelling using the sinh creep law is used to predict the sensitivity of the damage to changes in the shape of an idealised trapezoidal thermal profile. The effect of changing the temperature extremes and the ramp and dwell times are predicted.



---

### 7.1. Experimental Method

---

The ability of the sinh law, the Armstrong-Frederick kinematic hardening law, and the damage law from chapter 4 to model the thermal cycling are compared. The damage law is also compared to the sinh law with regards comparing the lifetime of joints with different geometries.

Finally the crack shapes and electrical resistance increase are predicted using the damage law with different mesh densities and crack length scale parameters to illustrate the mesh dependence of the damage law.

## 7.1 Experimental Method

For this work 3 sizes of resistor were investigated: 1206, 0805 and 0603. For each of these three resistors, two solder alloys were investigated: Sn-3.5Ag, Sn-3.8Ag-0.7Cu. For each of these 6 combinations of resistor and alloy, the 6 thermal cycles A-F shown in figure 7.1 were investigated. (The actual thermal profiles were measured and are shown in figure 7.1.) For each of these 36 combinations of resistor, alloy and thermal cycle, both 0 thermal cycles and 1200 thermal cycles were tested. For each of the above 72 combinations, about 26 specimens were tested, the results which follow represent an average of these 26 specimens.

Cycle	Low Temp [°C]	High Temp [°C]	Ramp Time [min]	Dwell Time [min]	Total Period [min]
A	-55	125	17.5	5	45
B	-55	125	10	10	40
C	-20	125	15	5	40
D	-12	125	0.5	5	11
E	-20	80	10	5	30
F	-55	125	3.3	0	6.6
Median	-34	103	9	5	28

Table 7.1: The six thermal profiles used to experimentally validate the model and the median profile used for the sensitivity analysis

Each specimen was thermal cycled (for either 0 or 1200 cycles) and then tested for ultimate shear strength (USS). The USS test works by pushing the side of the resistor with a shearing arm until the joints break completely as shown in figure 7.2. The maximum reaction force from the resistor is recorded as the USS. The relative drop in USS between 0 and 1200 cycles is used to represent the damage in the joint. This

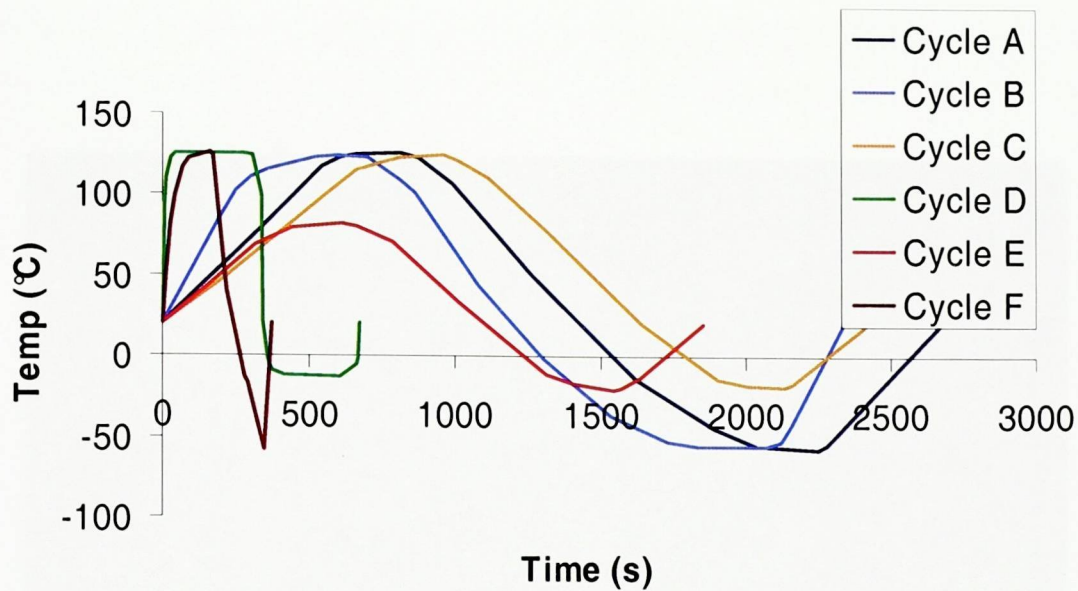


Figure 7.1: The actual temperature profiles as measured using a thermocouple on the test boards

method allows the damage in a joint to be measured without having to wait until the joint has completely failed. (However the accuracy of the results may not be as good as for tests in which joints are cycled to complete failure to obtain  $N_f$  values.) The results will be shown later in comparison with the modelling results.

## 7.2 Modelling method

The approach to damage prediction is to model the creep behaviour of the solder over 3 thermal cycles. The average accumulated creep strain and creep energy density in the stand-off region (see figure 7.3) during the 3<sup>rd</sup> cycle is then extracted as an indication of the amount of damage in the joint. All the materials except for the solder are treated as linear-elastic. Despite having a highly anisotropic CTE and Young's modulus the FR4 is assumed to behave isotropically as the vertical expansion w.r.t. figure 7.3 has no influence on the solder joint behaviour.

The solder is modelled using either the sinh creep law or the Armstrong-Frederick kinematic hardening law and some simulations are performed using the sinh law along with the damage law. These laws are discussed in chapter 4.

The mesh used for the 1206 resistor is shown in figure 7.4. The 0805 and 0603 meshes



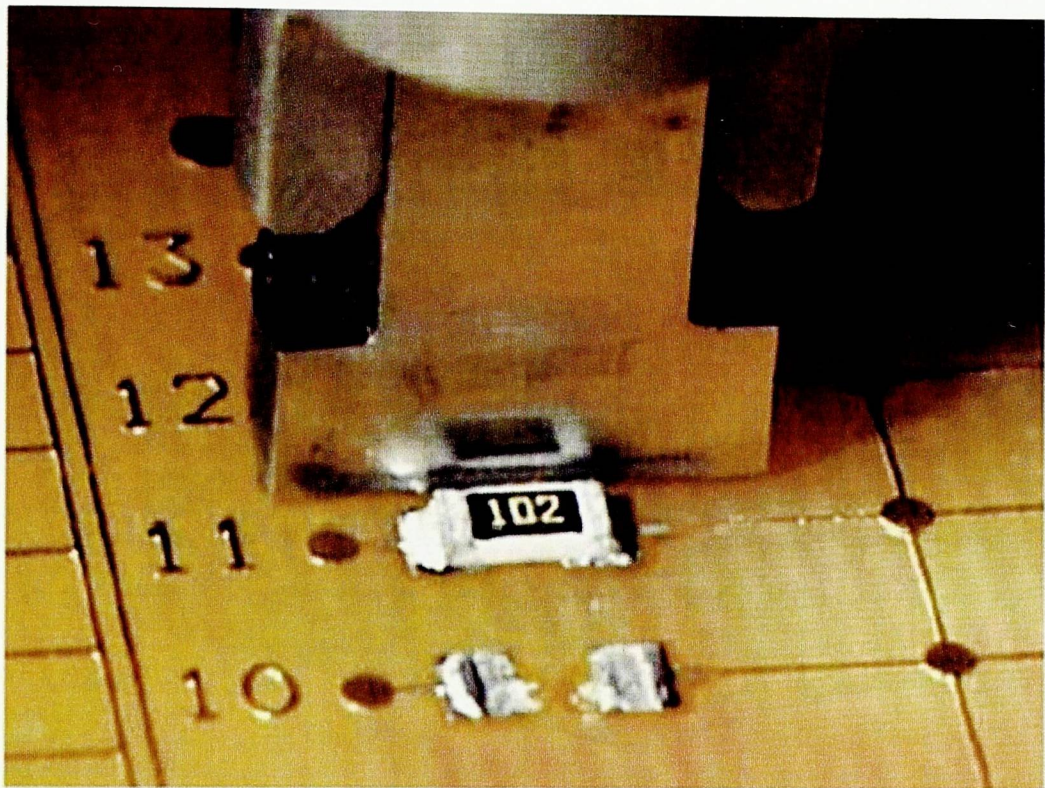


Figure 7.2: The ultimate shear strength test

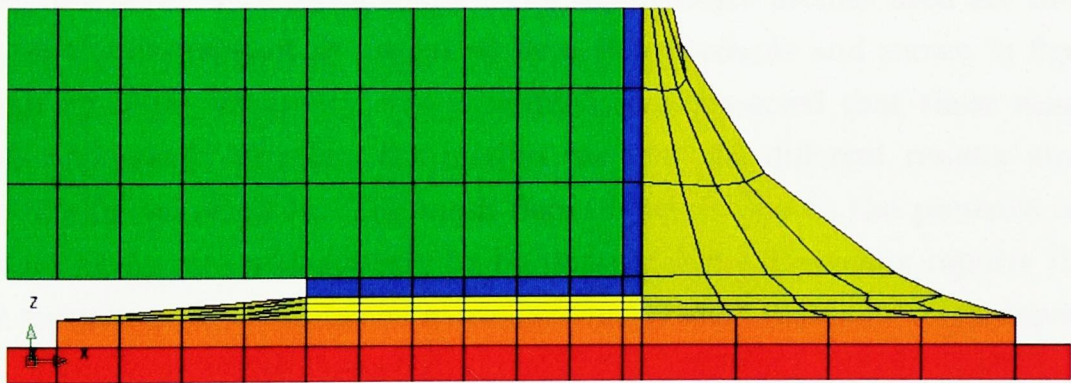


Figure 7.3: The stand-off region - the first part of the joint to become damaged



---

### 7.3. Modelling vs. Experiment

---

are similar to this but with different dimensions. An additional high resolution mesh for the 1206 resistor is shown in figure 7.5 and is used to compare the effect of different length scales using the damage law.

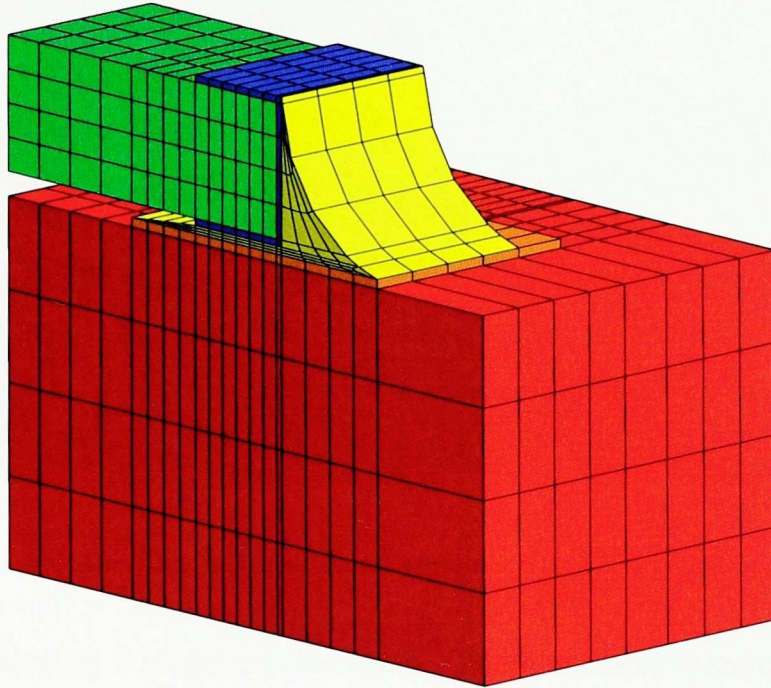


Figure 7.4: The mesh for a 1206 resistor (quarter-symmetric)

### 7.3 Modelling vs. Experiment

Simulations were run using the 1206, 0805 and 0603 meshes with SnAgCu solder and the 1206 mesh with SnAg solder. The temperature profiles used are the actual profiles of the experiment as measured by a thermocouple and shown in figure 7.1. Although no mesh sensitivity was performed it is expected that these results will be mesh dependent, therefore the meshes used for the different resistor sizes were kept as similar as possible. The mesh dependence is due to the presence of stress hotspots/singularities and appears to be unavoidable – Darveaux reports [13] that volume averaging of the strain energy reduces but doesn't eliminate mesh dependence.

The comparison of the SnAgCu (abbreviated to SAC) predictions to experiment are shown in figures 7.6 and 7.7. The results show a comparison of the model predictions with the experimental results using VP (Visco-Plastic or creep) strain and VP strain energy as damage indicators respectively. The 1206 experimental USS values have



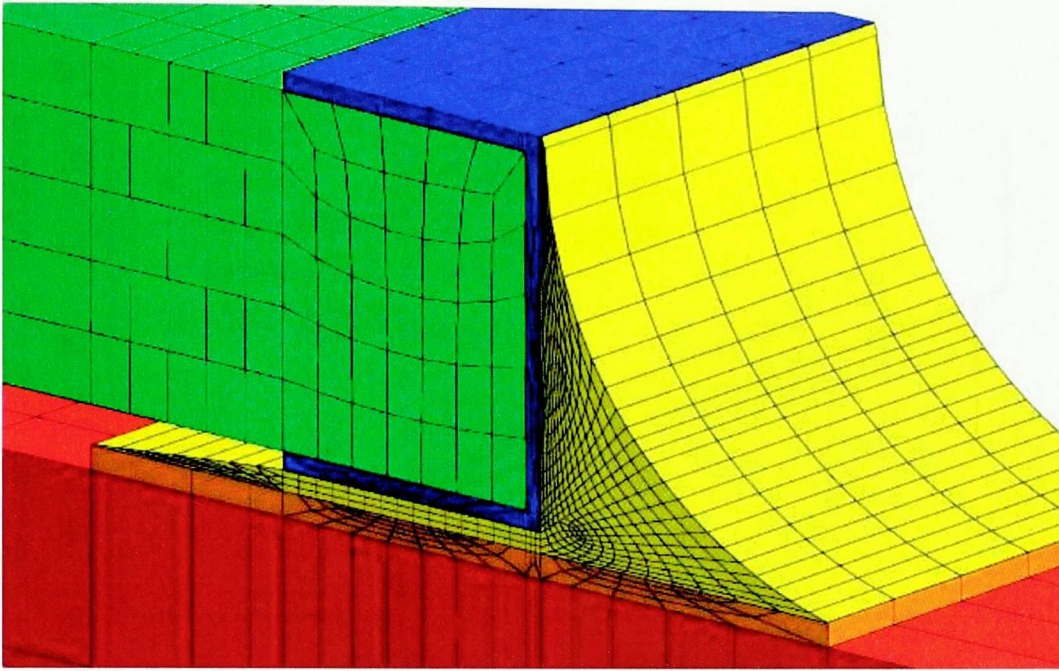


Figure 7.5: The detailed mesh for a 1206 resistor

error bars representing 1 standard deviation. There is disagreement in the literature over whether VP strain or VP energy density should be used as a damage indicator [30].

From the above results the accumulated strain gives a better correlation with the measured damage than the strain energy density. The correlation of the creep strain is still not perfect - it is not clear to what extent this is due to the (considerable) spread in the experimental results and to what extent it is due to inaccuracies of the modelling.

For SnAg solder only the 1206 resistor was modelled. The results are shown in figures 7.8 and 7.9. As for SnAgCu, the experimental damage (drop in USS) is predicted more accurately by the VP strain than the VP energy density.

## 7.4 Hysteresis Loops

A hysteresis loop is a stress-strain graph of a plastic material undergoing cyclic loading. The loops shown here represent the average shear stress and strain over the

7.4. Hysteresis Loops

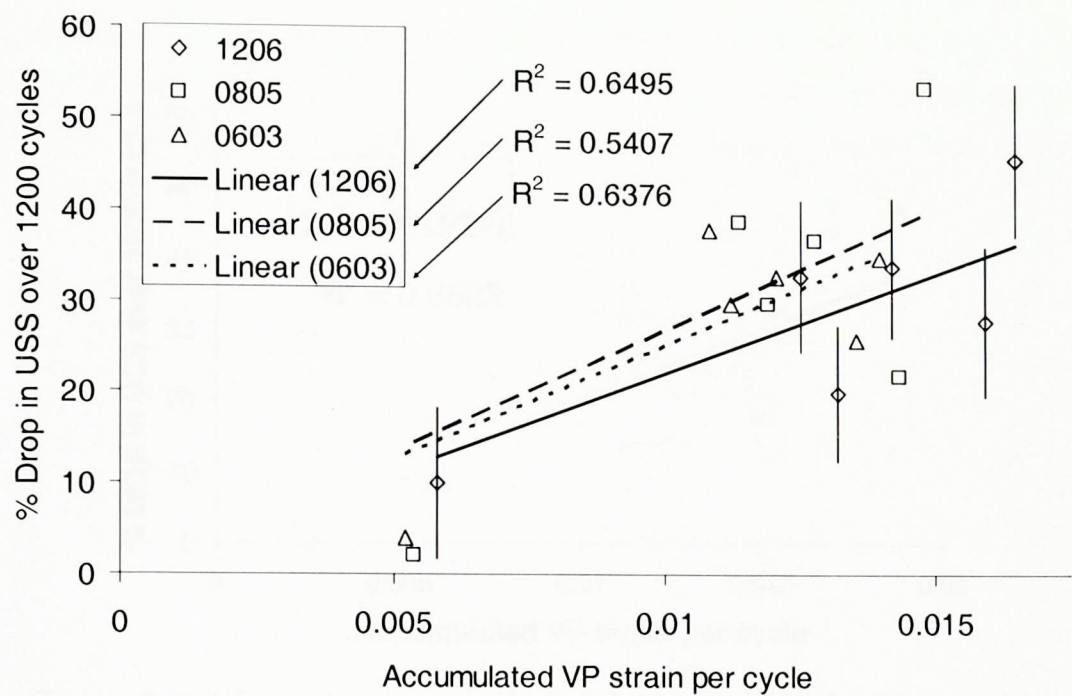


Figure 7.6: 6: Drop in USS vs. accumulated strain for SAC solder. For each size of resistor - 1206, 0805 and 0603, there are 6 data points - one for each of the cycles A-F.  
(R2 is the correlation to a linear relationship)

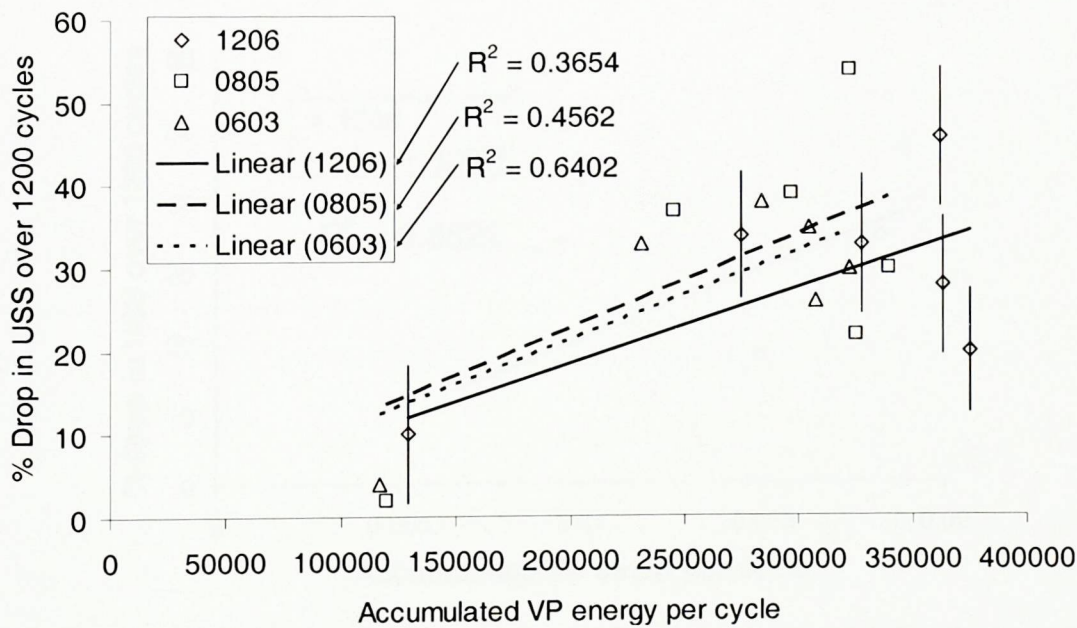


Figure 7.7: 7: Drop in USS vs. accumulated strain energy for SAC solder. For each size of resistor there are 6 data points - one for each of the cycles A-F.  
(R2 is the correlation to a linear relationship)



7.4. Hysteresis Loops

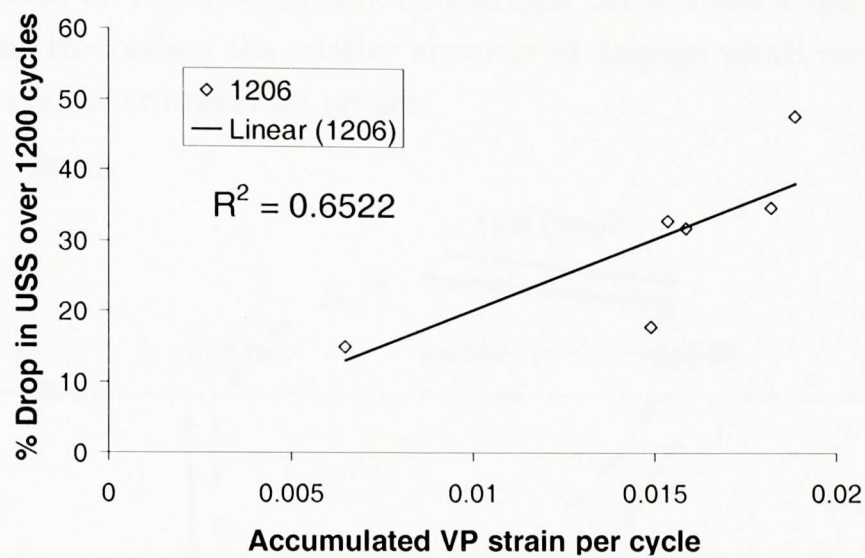


Figure 7.8: VP strain vs. experimental drop in USS for SnAg solder (R2 is the correlation to a linear relationship)

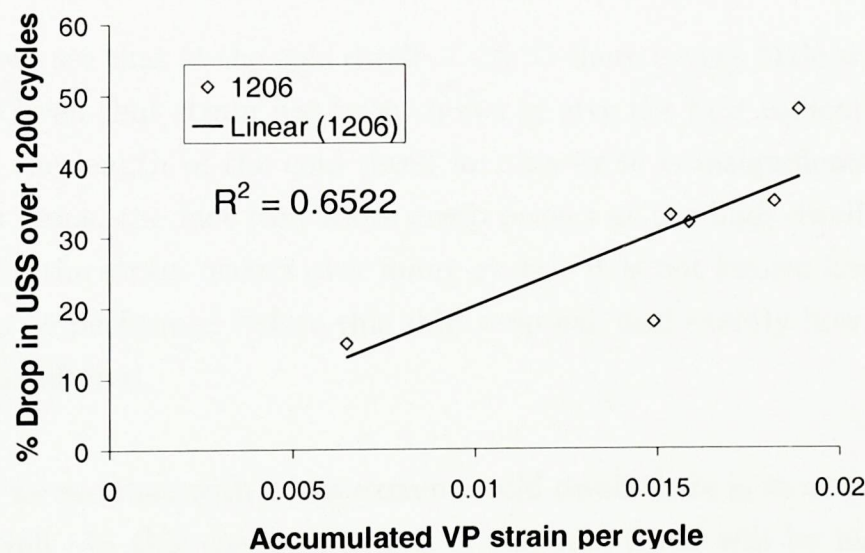


Figure 7.9: VP energy density vs. experimental drop in USS for SnAg solder (R2 is the correlation to a linear relationship)

#### 7.4. Hysteresis Loops

stand-off region of the joint in the plane of figure 7.3 for the third thermal cycle. It should be noted that there is very significant variation between the inner and outer parts of the stand-off region which will be averaged out in these loops. Nevertheless, they help in understanding the relative amounts of damage which occur during the different parts of the temperature profile.

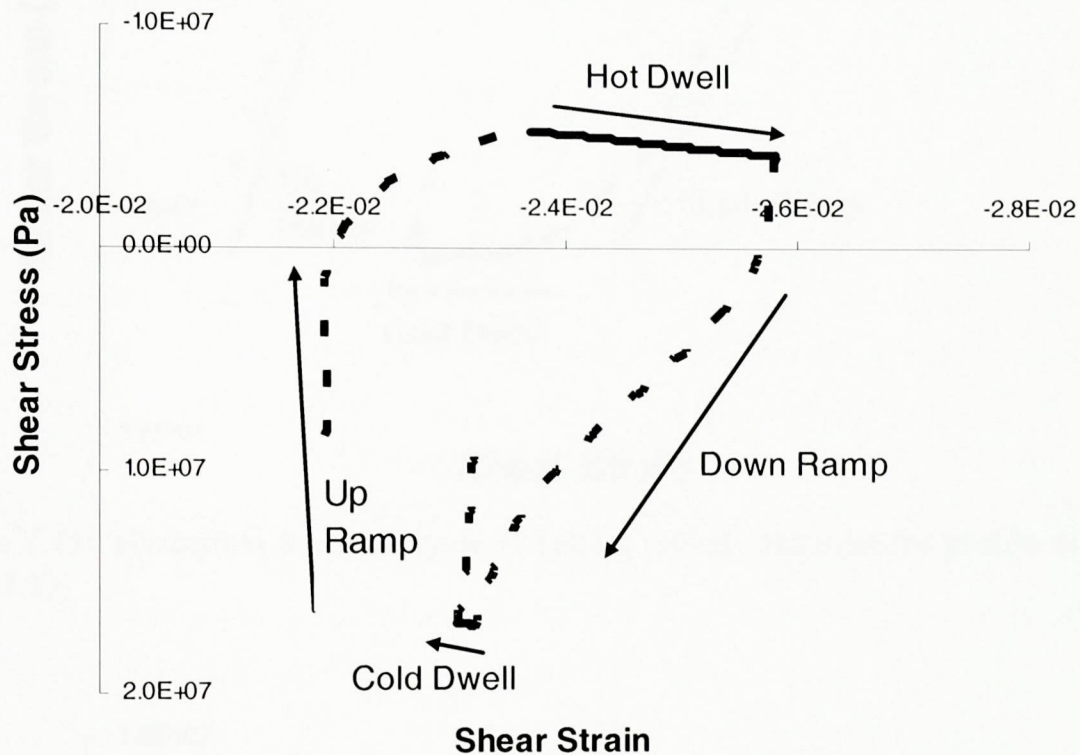


Figure 7.10: Hysteresis loop for cycle B (using idealised trapezoidal temp. profile)

In figure 7.10 we see that at the cold dwell of  $-55^{\circ}\text{C}$  there is very little strain (although high stress). Given that strain has been shown to give the best indication of damage it seems that the length of the cold dwell for this cycle is insignificant. As with all the hysteresis loops, the fact that more creep occurs at the high dwell means that a gradual shift in the strain occurs over many cycles. It is not known how many cycles would need to be performed before this shift stopped, and exactly how the hysteresis loops would be altered.

In figure 7.11 we see that with a less extreme cold dwell there is more creep occurring during the dwell. In this case the length of the cold dwell will be more significant than for cycle B but still nowhere near as significant as the length of the hot dwell (assuming strain and not energy to be the true damage indicator).

Figure 7.12 shows the hysteresis loop for cycle F. Note that the actual temperature profile for cycle F has a hot dwell (figure 7.1) which is not specified in the cycle



7.4. Hysteresis Loops

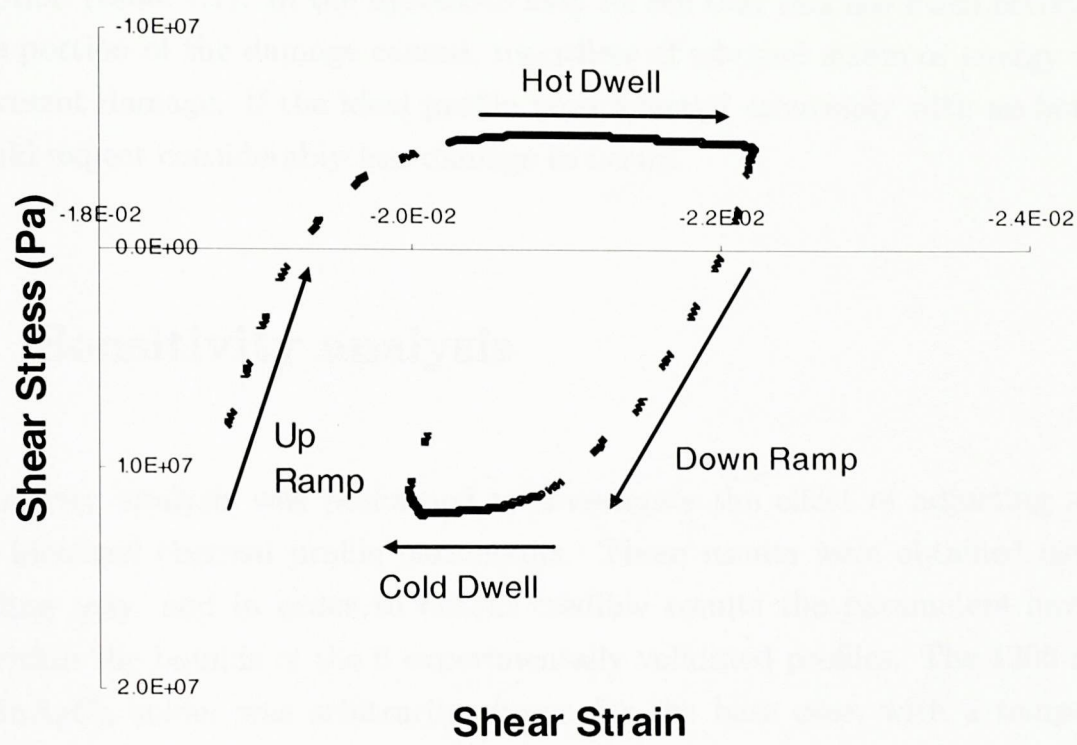


Figure 7.11: Hysteresis loop for cycle D (using actual temperature profile as shown in fig 7.1))

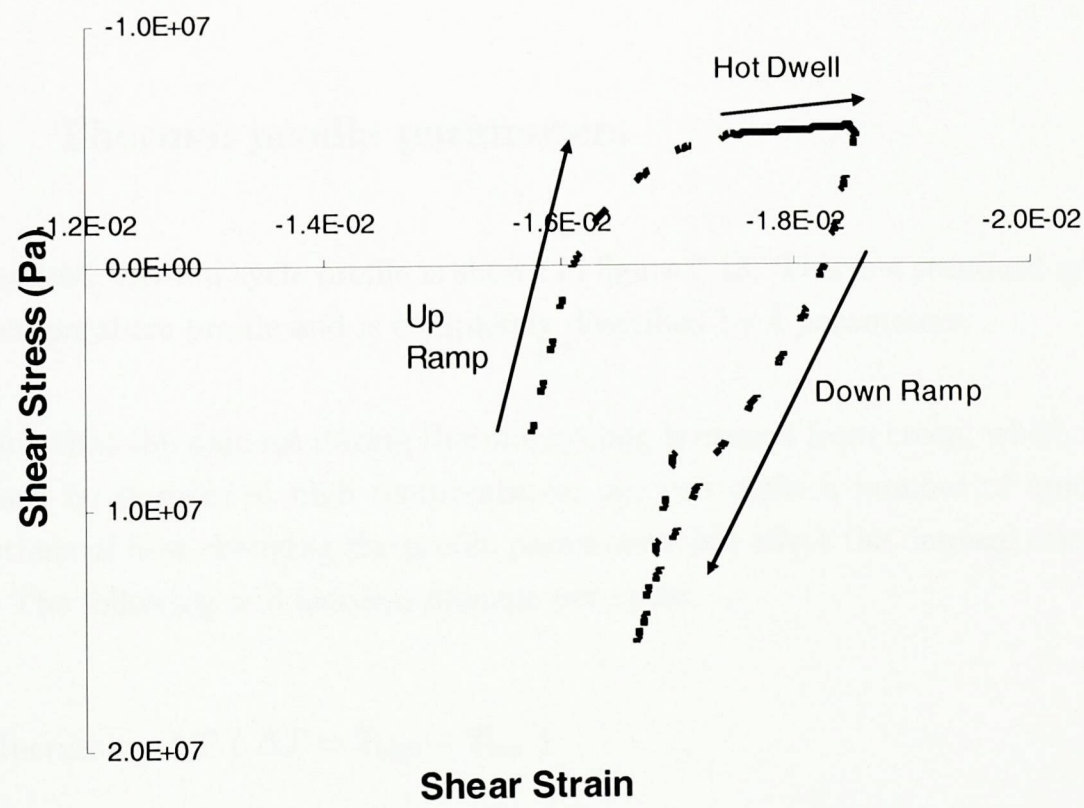


Figure 7.12: Hysteresis loop for cycle F (using actual temperature profile as shown in fig 7.1))

description (table 7.1). In the hysteresis loop we see that this hot dwell accounts for a large portion of the damage caused, regardless of whether strain or energy is used to represent damage. If the ideal profile were followed accurately with no hot dwell we could expect considerably less damage to occur.

## 7.5 Sensitivity analysis

A sensitivity analysis was performed to investigate the effect of adjusting all four of the idealised thermal profile parameters. These results were obtained using FE modelling only, and in order to obtain credible results the parameters have been kept within the bounds of the 6 experimentally validated profiles. The 1206 resistor with SnAgCu solder was arbitrarily chosen for the base case, with a temperature profile whose parameters are the median of the 6 experimentally verified profiles (see figure 7.1). For each parameter under investigation, 5 simulations were run with different parameter values spanning the whole range of values which appeared in the experimentally validated profiles. The results are shown below.

### 7.5.1 Thermal profile parameters

An idealised thermal cycle profile is shown in figure 7.13. This is a standard symmetrical temperature profile and is completely described by 4 parameters:

Knowing that the damage during thermal cycling is caused from creep, which in turn is caused by stresses at high temperatures, one can make a number of qualitative predictions of how changing the profile parameters will affect the damage caused per cycle. The following will increase damage per cycle:

1. Increasing  $\Delta T$  (  $\Delta T = T_{\text{high}} - T_{\text{low}}$  )
2. Increasing  $T_{\text{avg}}$  (  $T_{\text{avg}} = [T_{\text{low}} + T_{\text{high}}]/2$  )
3. Increasing  $t_{\text{dwell}}$



7.5. Sensitivity analysis

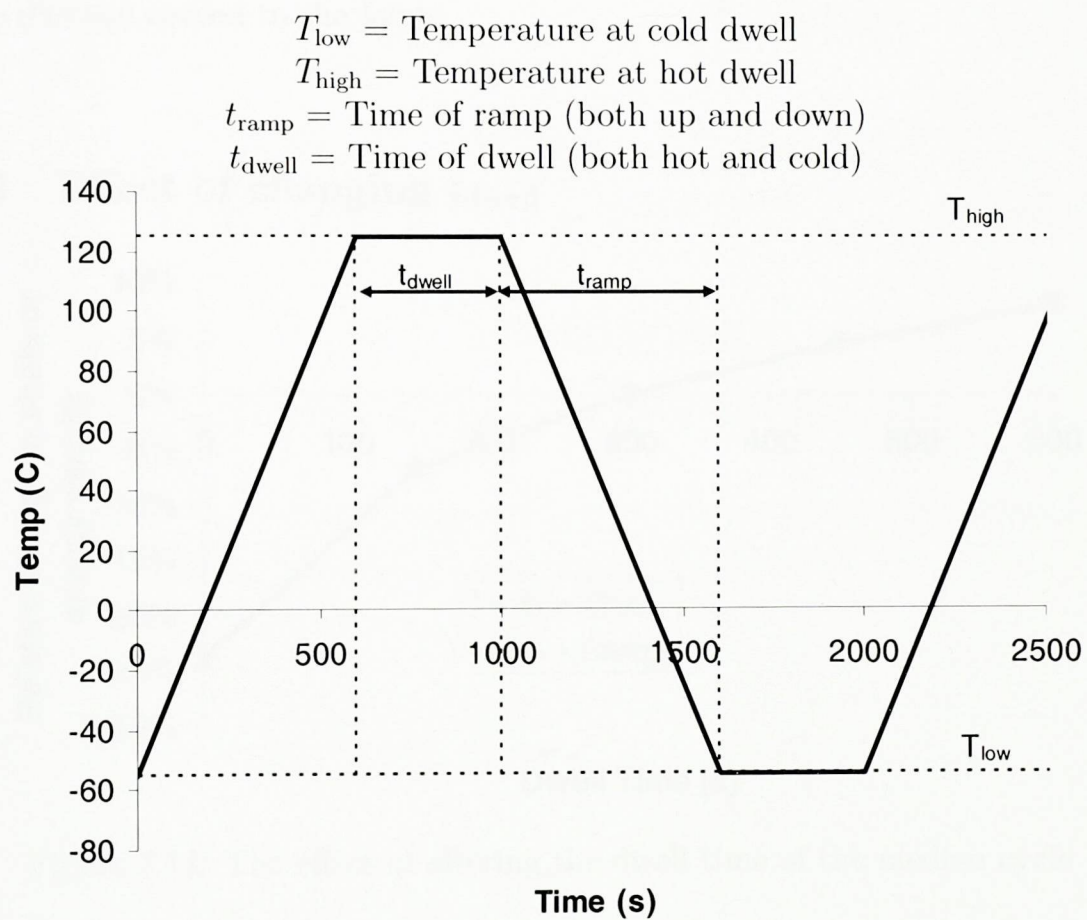


Figure 7.13: An idealised temperature cycle profile.

## 7.5. Sensitivity analysis

But the effect of the following is unclear:

1. Increasing  $t_{\text{ramp}}$  (Although a slower ramp would allow more time therefore causing a greater accumulated creep strain, the stress will be lower.)
2. Decreasing  $T_{\text{low}}$  (Although  $\Delta T$  is increased,  $T_{\text{avg}}$  is decreased.)

The results presented below give a clearer idea of the effect of all the above parameters on the damage caused to the joints.

### 7.5.2 Effect of changing $t_{\text{dwell}}$

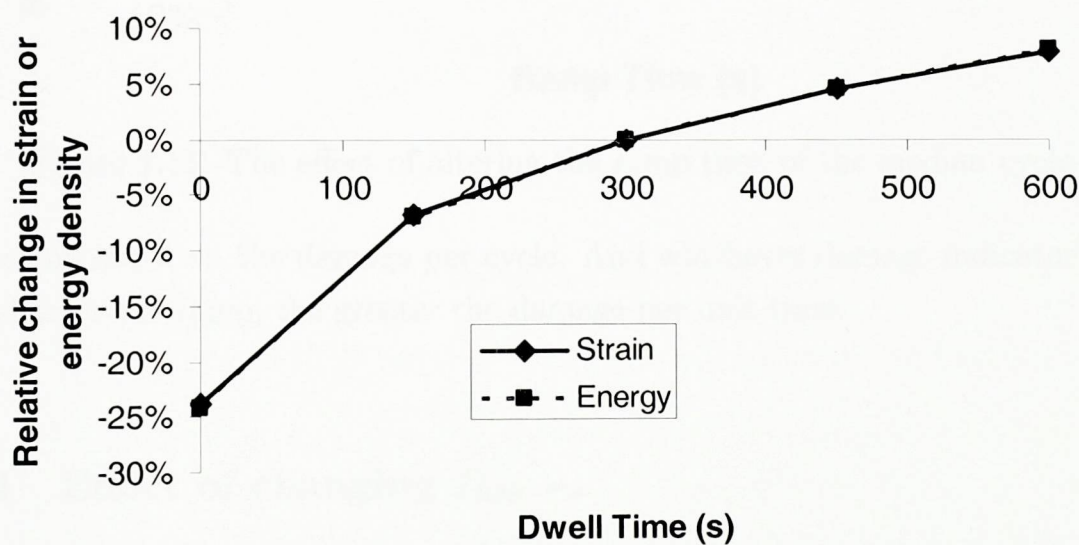


Figure 7.14: The effect of altering the dwell time of the median cycle

Increasing the dwell time provides more damage per cycle. But the rate of damage over time is highest with the shortest dwell time of 0. Remember that this applies for the specific values of  $T_{\text{high}}$ ,  $T_{\text{low}}$  and  $t_{\text{ramp}}$  and the graph may look very different after altering these values.

### 7.5.3 Effect of changing $t_{\text{ramp}}$

In figure 7.15 we see the biggest difference between the strain and the energy predictions. The reason that the energy increases for faster ramps is that the temperature



### 7.5. Sensitivity analysis

changes without giving the solder as much time to adjust, which increases the stress. For a slower ramp the solder deformation can ‘keep up’ with the temperature change better and so the stress and the energy are lower, even though the solder has deformed more. If, as seems likely, the strain is the true indicator of damage, the ramp time

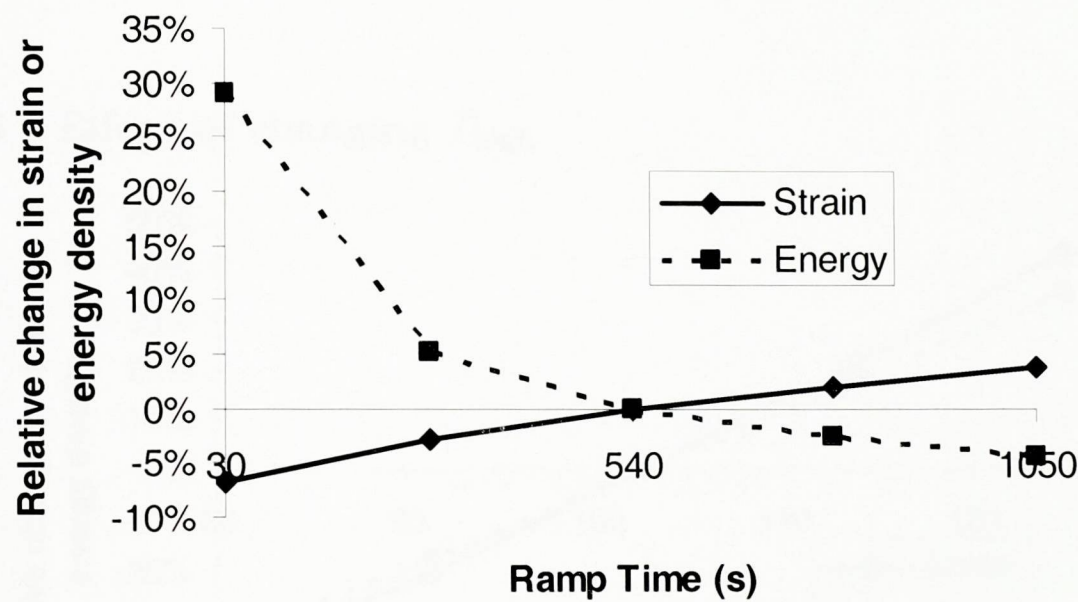


Figure 7.15: The effect of altering the ramp time of the median cycle

has a small effect on the damage per cycle. And whichever damage indicator we use - the shorter the ramp, the greater the damage per unit time.

#### 7.5.4 Effect of changing $T_{low}$

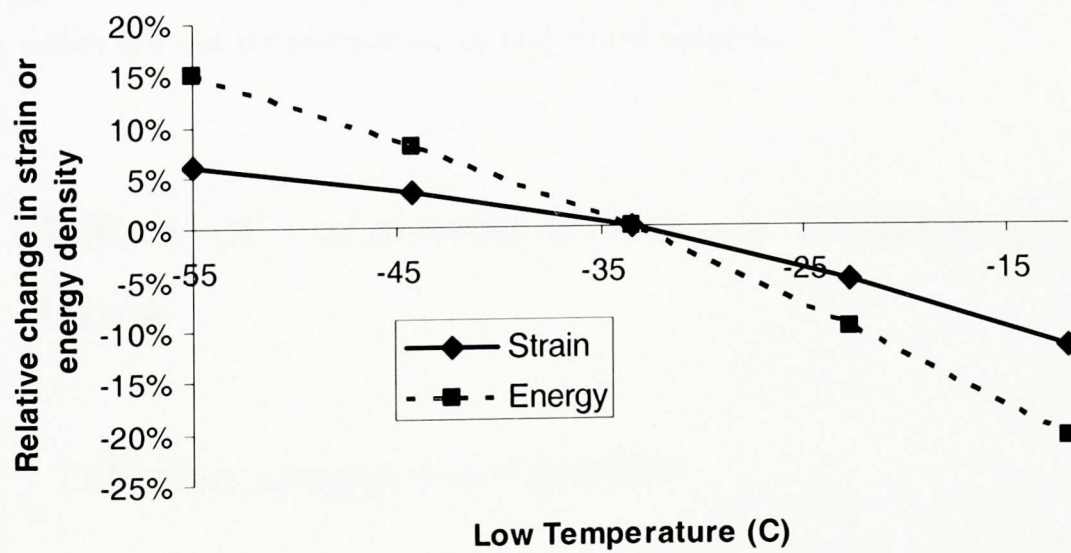


Figure 7.16: The effect of altering the low temperature of the median cycle

---

## 7.6. Effect of constitutive law on lifetime predictions

---

With a lower cold temperature we get increased strain, but not a great deal more. The effect on the energy is significantly greater due to high stresses being generated at the cold extreme. It is probably not wise to choose too low a temperature for  $T_{\text{low}}$  as a brittle damage mechanism may become dominant under the high stress conditions.

### 7.5.5 Effect of changing $T_{\text{high}}$

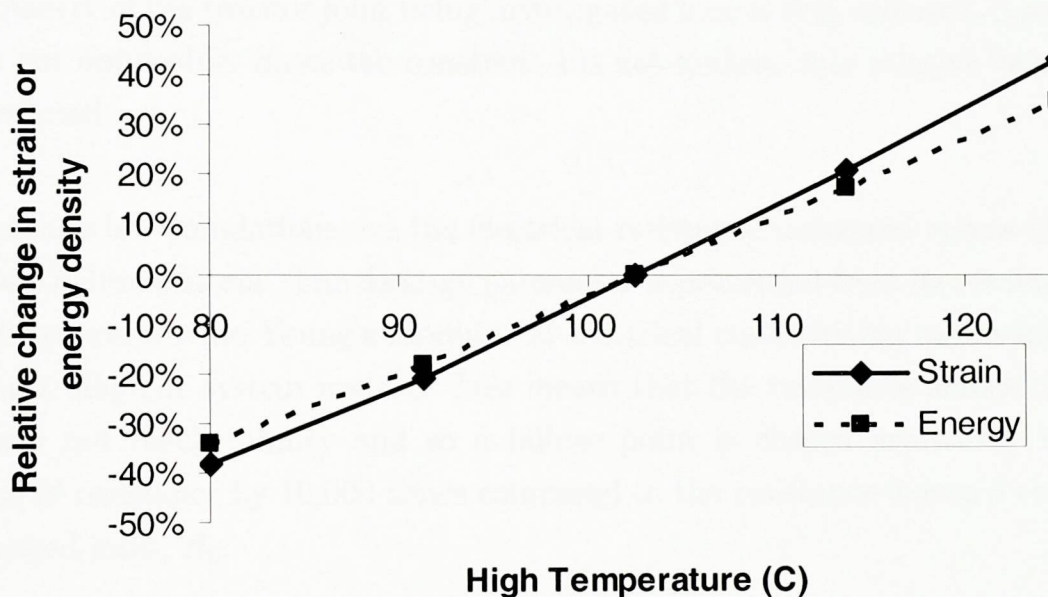


Figure 7.17: The effect of altering the high temperature of the median cycle

Figure 7.17 shows that of all the 4 parameters, the high temperature appears to be by far the most significant in its effect on the damage per cycle, using either strain or energy as the damage indicator. However, raising  $T_{\text{high}}$  too much may generate test results which are not representative of real world failures.

## 7.6 Effect of constitutive law on lifetime predictions

### 7.6.1 Different temperature profiles

Simulations were performed for thermal cycling of a 1206 resistor under the 6 different thermal cycle profiles in figure 7.1 using the steady-state sinh creep law (SS), the



---

## 7.6. Effect of constitutive law on lifetime predictions

---

kinematic hardening law (KH) and the damage law. The material properties are given in appendix A apart from the constants for the KH law which were obtained using the optimisation method in chapter 5. To determine  $N_f$  the following fatigue law published by Syed [12] is used:

$$N_f = A\varphi_{acc}^{-1} \quad (7.1)$$

Syed determined a value for  $A$  which is appropriate for area array packages, but since the geometry of the resistor joint being investigated here is very different, Syed's value of  $A$  is not applicable. Since the constant  $A$  is not known, only relative values of  $N_f$  are predicted.

The damage law simulations use the electrical resistance measured across the solder joint as a failure criteria. The damage parameter is prevented from increasing beyond 0.99999 to prevent the Young's modulus or electrical conductivity to reaching 0 and creating a singular system matrix. This means that the resistance across the solder joint will not reach infinity and so a failure point is chosen arbitrarily to be an increase of resistance by 10,000 times compared to the resistance across a completely undamaged joint,  $R_0$ .

The damage constant used in the simulation  $B_{sim}$  is chosen to be 1 as this seems a reasonable compromise between solution time and accuracy. As discussed on page 81, it is not necessary to use an accurate  $B_{sim}$  parameter in the simulation, so long as the  $N_{f,sim}$  predicted is not too small to introduce errors. A length scale parameter  $\omega = 100\mu\text{m}$  was used to reduce the mesh dependence of the result. This large value means that the crack path is not predicted very precisely.

The fixed voltage boundary conditions for the electrical calculation are: 0V at the solder-joint/copper pad interface and +10V at the solder-joint/component termination interface. The current  $I$  is then predicted by the simulation and Ohm's law can be used to calculate the resistance. When the relative resistance  $R/R_0$  increases to 10000 times its initial value the joint is considered to have failed.

Since the  $N_f$  values predicted by the SS, KH and damage laws are not directly comparable, they have been normalised such that the average of the  $N_f$  values of all 6

## 7.6. Effect of constitutive law on lifetime predictions

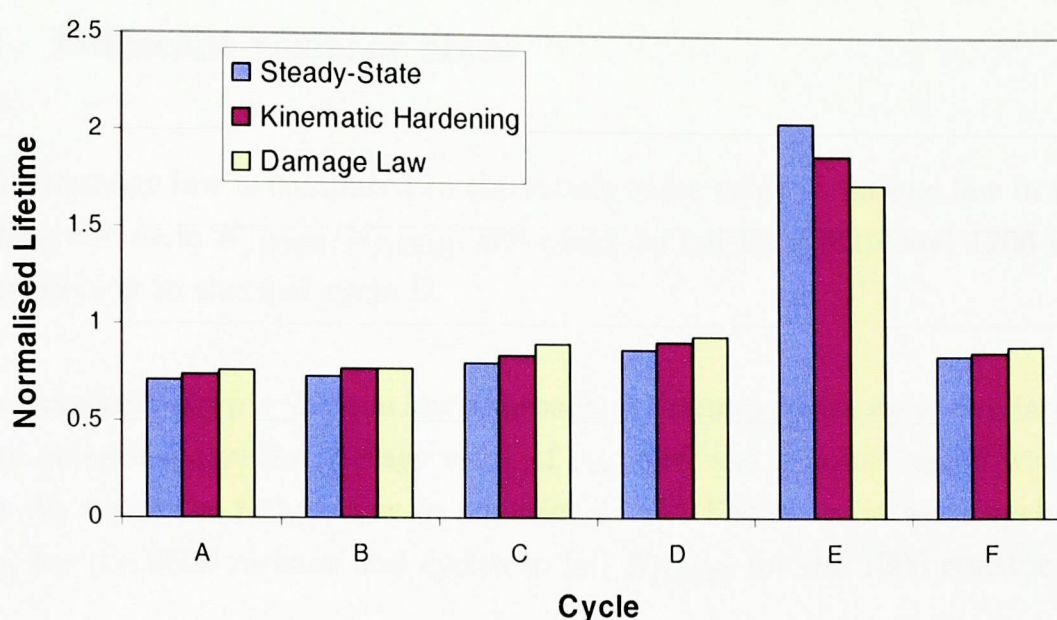


Figure 7.18: The difference in relative lifetime prediction between the Steady-State (SS), Kinematic-Hardening (KH) and Damage constitutive laws

cycles A to F is 1:

$$\frac{1}{6} \sum_{\text{cycle}=A}^F N_f^{\text{SS}} = 1, \quad \frac{1}{6} \sum_{\text{cycle}=A}^F N_f^{\text{KH}} = 1, \quad \frac{1}{6} \sum_{\text{cycle}=A}^F N_f^{\text{damage}} = 1, \quad (7.2)$$

The results in figure 7.18 show the relative difference between the constitutive laws to be fairly small. The order of severity of the cycles as predicted by the SS and KH law is:

(most damaging) A, B, C, F, D, E (least damaging)

Cycle A is the most damaging due to its large temperature range and long cycle time. Cycle E is the least damaging because its temperature range is the smallest. This order differs only slightly when using the damage law: F becomes slightly more damaging than C. The small difference between the laws suggests that their capability to predict the effect of different applied thermal loading conditions is roughly similar.



## 7.6.2 Different resistor sizes

Here the damage law is compared to the steady state creep + fatigue law in terms of predicting the ratio  $N_{f(0603)}/N_{f(1206)}$ , the cycles to fail for a 0603 and 1206 resistor—when subjected to thermal cycle B.

For the standard creep + fatigue law approach, 3 thermal cycles were simulated using the sinh creep law and the average value of  $\varphi_{acc}$  over the standoff region was used to predict  $N_f$  using the fatigue law in equation (7.1). The ratio between cycles to fail  $N_{f(0603)}$  for the 0603 resistor and cycles to fail  $N_{f(1206)}$  for the 1206 resistor is given by:

$$\frac{N_{f(0603)}}{N_{f(1206)}} = \frac{A\varphi_{acc(0603)}^{-1}}{A\varphi_{acc(1206)}^{-1}} \quad (7.3)$$

$$= \frac{\varphi_{acc(1206)}}{\varphi_{acc(0603)}} \quad (7.4)$$

For the damage law simulations a constant of  $B_{sim} = 10.0$  is used and the predicted number of cycles is converted to a roughly realistic number  $N_{real}$  using the method on page 80 with the value  $B_{real} = 0.05$  determined from the fatigue test on page 104. A length scale of  $\omega = 100\mu\text{m}$  was used.

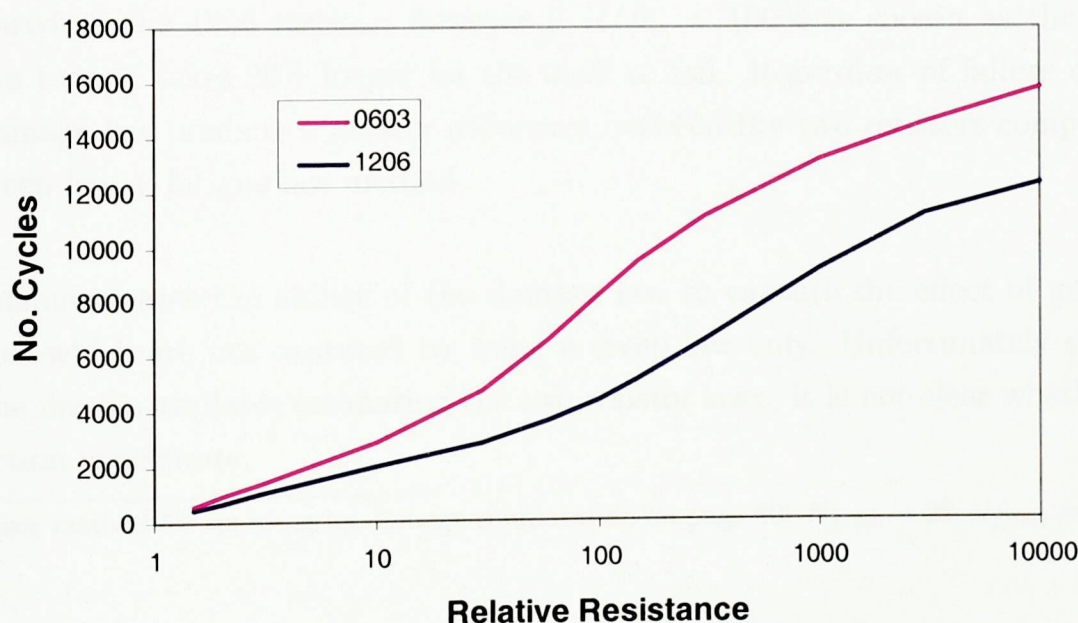


Figure 7.19: The number of cycles  $N_{real}$  versus the relative resistance  $R/R_0$

The relative resistance predicted for the two resistors is shown in figure 7.19. The

## 7.6. Effect of constitutive law on lifetime predictions

damage contours at cycle 4400 and at  $R/R_0 = 10000$  are shown in figure 7.20, they show that after 4400 cycles<sup>1</sup> the standoff region in the 1206 resistor is completely damaged and the standoff region in the 0603 resistor is almost completely damaged.

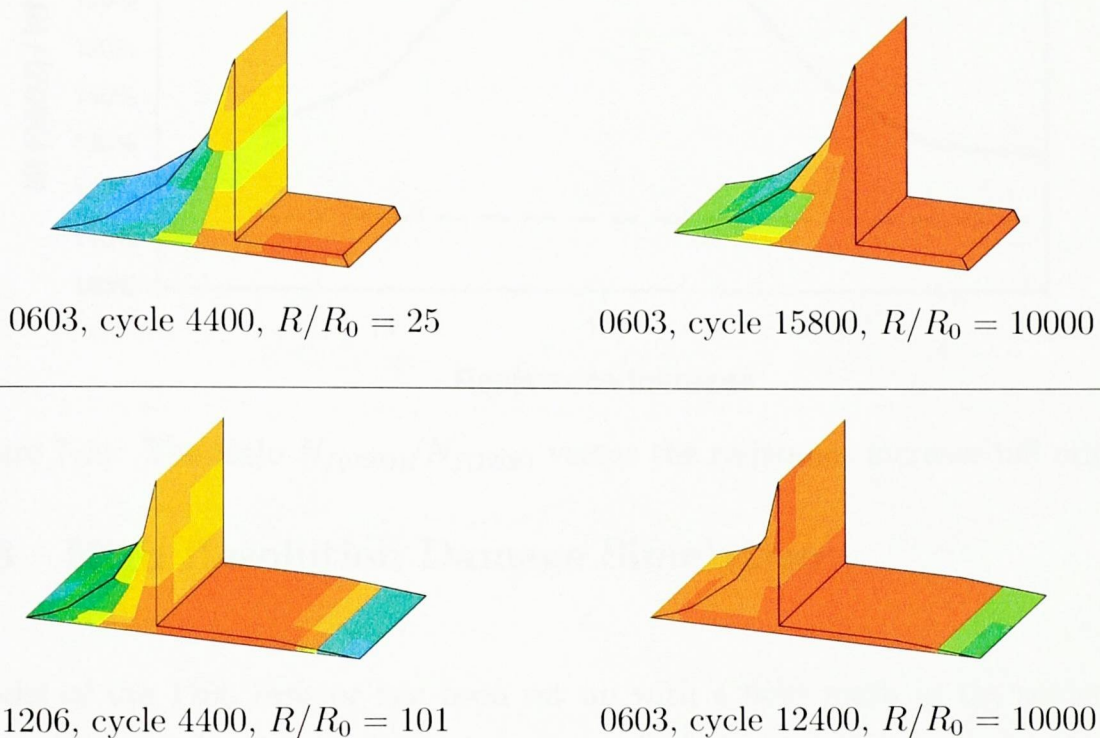


Figure 7.20: The damage distribution for the 0603 and 1206 resistors

The ratio  $N_{f(0603)}/N_{f(1206)}$  is very dependent on the failure criteria chosen, this is seen clearly in figure 7.21. It takes 88% longer for the 0603 resistor to reach  $R/R_0 = 100$  compared to the 1206 resistor, however if  $R/R_0 = 10000$  is chosen as the failure criteria then it takes 29% longer for the 0603 to fail. Regardless of failure criteria, the damage law predicts a greater difference between the two resistors compared to the creep law + fatigue law method.

This demonstrates the ability of the damage law to capture the effect of geometry changes which are not captured by using a creep law only. Unfortunately since no lifetime data is available comparing the two resistor sizes, it is not clear whether this prediction is accurate.

<sup>1</sup>Using method for speeding up damage computation on page 80:  $N_{f:\text{sim}} = 22, N_{f:\text{real}} = 4400$



## 7.6. Effect of constitutive law on lifetime predictions

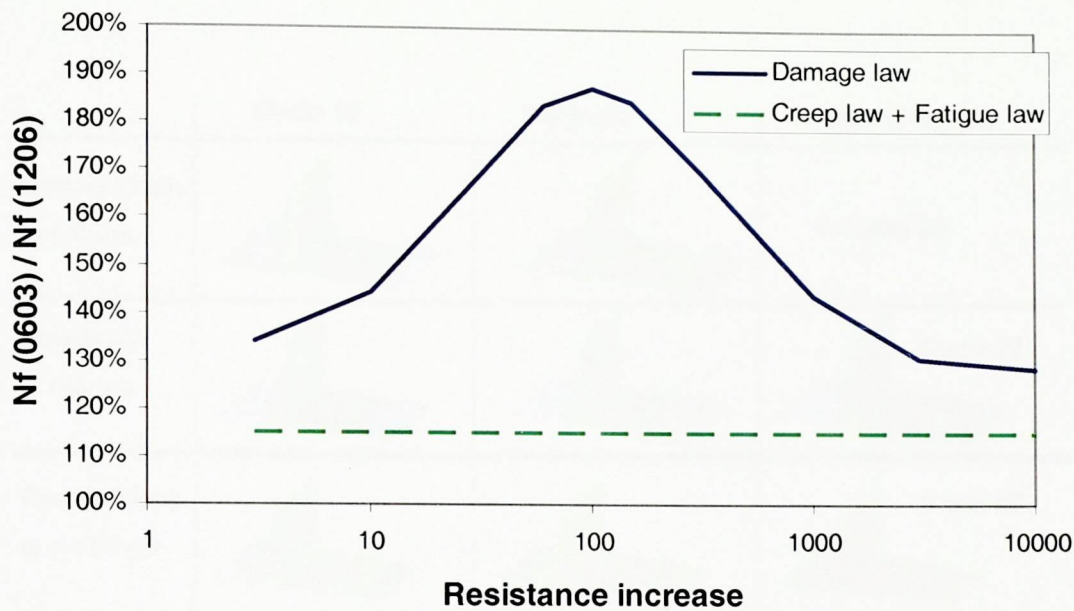


Figure 7.21: The ratio  $N_{f(0603)}/N_{f(1206)}$  versus the resistance increase fail criteria

### 7.6.3 High Resolution Damage Simulation

A model of the 1206 resistor has been set up with a finer mesh in the solder joint compared to the simulations presented above. This is used to investigate the mesh sensitivity of this problem and the effect of using different length scales parameters.

The first and second rows of figure 7.22 compare the effect of changing the mesh density when a length scale of  $\omega = 0\mu\text{m}$  is used. With a coarse mesh the crack propagates horizontally through the fillet region but when a fine mesh is used the propagation occurs vertically. This indicates that the crack shape is very mesh dependent when no length scale averaging is used. The similarity in the number of cycles to fail (20 versus 22) is regarded as a coincidence given the different crack paths.

When a length scale of  $\omega = 100\mu\text{m}$  is used the coarse and fine meshes both produce a vertical crack propagation direction in the fillet. So the length scale averaging has proved successful in reducing the mesh dependence of the crack direction. However, there is still a mesh dependence regarding the number of cycles to fail. This can be explained by the presence of stress hotspots present in the fine mesh which are not captured by the coarser mesh. This higher stress leads to faster creep and faster damage accumulation.

### 7.6. Effect of constitutive law on lifetime predictions

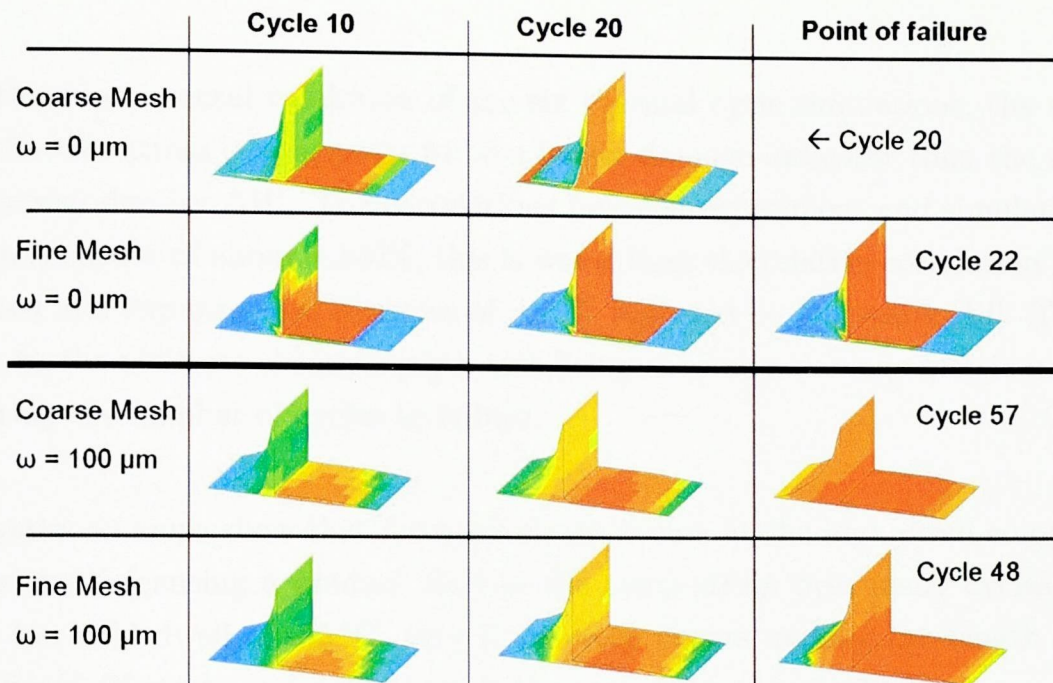


Figure 7.22: The damage distribution predicted using a coarse and fine mesh and length scales of  $\sigma = 0\mu\text{m}$  and  $\sigma = 100\mu\text{m}$ . The left column is after 10 cycles, the central column is after 20 cycles and the right column is at the point of failure. (Blue = intact, Red = damaged)

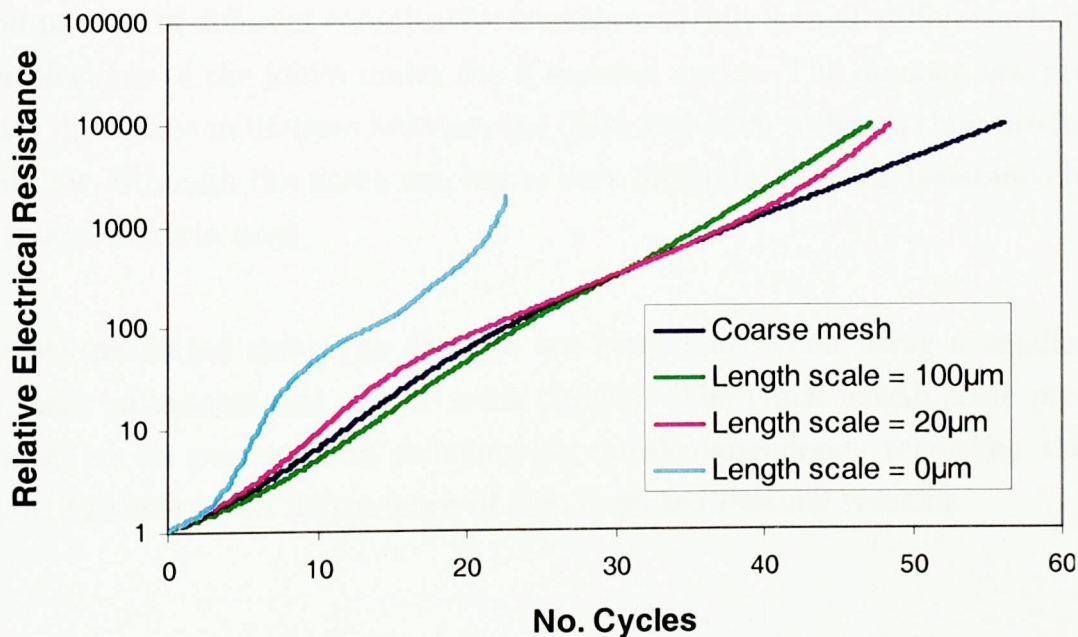


Figure 7.23: The resistance versus cycle no. for the coarse mesh and the fine mesh with different crack length scale



## 7.7 Conclusions

From the experimental validation of the six thermal cycle simulations, the accumulated effective strain  $\varphi_{\text{acc}}$  appears to be a better damage indicator than the accumulated energy density  $\Delta W$ . The correlations between experiment and simulation here have an accuracy of about  $\pm 100\%$ , this is worse than the relative correlation between predicted and experimental lifetimes of  $\pm 25\%$  reported by Darveaux [13]. This may be due to the ultimate shear strength test being used as a damage metric instead of measuring the number of cycles to failure.

The hysteresis loops show that far more strain occurs at the high dwell compared to the low dwell (causing a gradual shift in the creep strain over many cycles). With a very low cold dwell of  $-55^\circ\text{C}$ , very little creep occurs making the length of dwell insignificant (if strain and not energy is the true damage indicator).

The sensitivity analysis showed that for the range of parameters investigated, shorter ramps and dwells both lead to more damage per unit time. Decreasing the low temperature causes slightly more damage per cycle and increasing the high temperature causes a lot more damage per cycle.

The comparison of different constitutive laws showed only a small difference in predicting the lifetimes of the joints under the 6 thermal cycles. The damage law predicted a greater difference in lifetime between the 0603 and 1206 resistors than predicted by the sinh law although the exact amount is very dependent on the resistance increase  $R/R_0$  failure criteria used.

The cracks predicted using the damage law were finer when using a smaller crack length scale parameter and a finer mesh density. The crack length scale parameter was shown to be successful in reducing the mesh dependency regarding the crack direction, however mesh dependence of the predicted lifetime remains.

## Chapter 8

# Analysis: Crack Detection Tests

This chapter presents both modelling and experimental test data to characterise the performance of five non destructive tests. The focus is on determining the length of thermal fatigue cracks within the solder joints for a surface mount resistor on a strip of FR4 PCB. Four of the tests operate by applying mechanical loads to the PCB and monitoring the strain response at the top of the resistor. The fifth test applies a heat source to the PCB and monitors the temperature response at the top of the resistor. The modelling results show that of the five tests investigated, three are sensitive to the presence of a crack in the joint and its magnitude. Hence these tests show promise in being able to detect cracking caused by accelerated testing. The experimental data supports these results although more validation is required.

### 8.1 Introduction

When performing accelerated cycling tests it is necessary to determine the cycle at which failure occurs. Typically a component will be monitored for electrical continuity, however this approach will only provide the number of cycles to complete failure  $N_f$  (i.e. when a crack has grown completely through the joint). This can take a very long time and it can be useful to determine the amount of damage which has been done to the joint before it ultimately fails. One method used is to cut the sample in half and inspect its cross section with a microscope [35, 53, 54]. Another method is



---

## 8.2. Cracks caused by Thermal Cycling

---

to use dye penetration. In this way, the fatigue cracks can be observed and measured. However, these methods are destructive to the component and the solder joints.

The tests presented in this chapter are intended to be a quicker and cheaper, non-destructive method to detect crack length within the two Sn-3.5Ag solder joints of a 2512 surface mount resistor (6mm long, 2.6mm wide, 0.55mm high), mounted at the center of a strip of FR4 PCB (360mm long, 5mm wide, 1.3mm thick). They are not intended to detect damage on a PCB with many components. These tests could potentially allow the growth of a crack through a single specimen to be recorded by testing after different numbers of thermal cycles which is not possible using destructive methods such as cross sectioning.

The chapter will first discuss the kinds of cracks which are caused by thermal cycling, following this is a description of each of the tests under investigation. Modelling methods are then discussed, before presenting the results of the simulations. For each of the tests investigated, a prediction is given of the sensitivity of each test to the different kinds of cracks which occur.

## 8.2 Cracks caused by Thermal Cycling

In order to model the crack detection tests presented in this paper, it is first necessary to determine the geometry of the cracks caused by thermal cycling.

Modelling conducted to predict the crack shape in the solder using the damage law is shown in figure 8.1. (This result is from chapter 7 and the details of the simulation are discussed on page 131.) The predicted crack propagation direction is shown diagrammatically in figure 8.2, after the standoff region is completely cracked the simulations predict the crack propagating along the interface with the component termination which is represented as the vertical crack in figure 8.3.

A number of experiments have been reported in which thermal cycled joints have been cross sectioned [35, 53, 54]. A limitation of the cross-section technique is that the full 3D shape of the crack is not observed, Shangguan [35] assumed that the crack propagated from left to right with respect to figure 8.3. As the modelling in figure

## 8.2. Cracks caused by Thermal Cycling

---

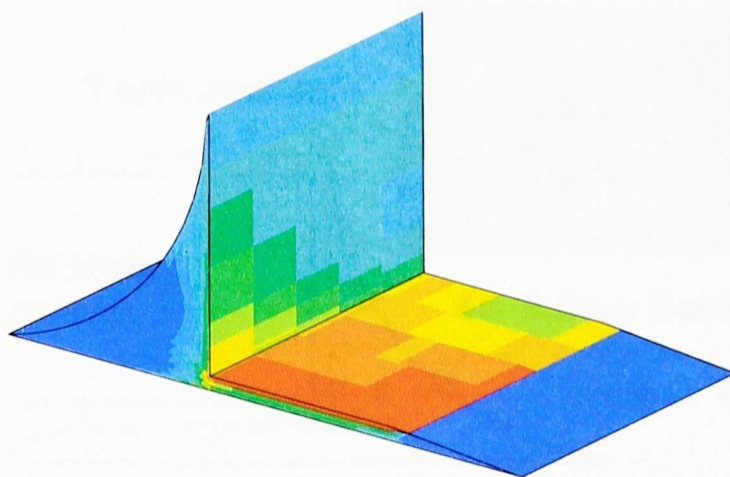


Figure 8.1: Predicted crack shape in standoff region. (Red = completely cracked, Blue = completely intact)

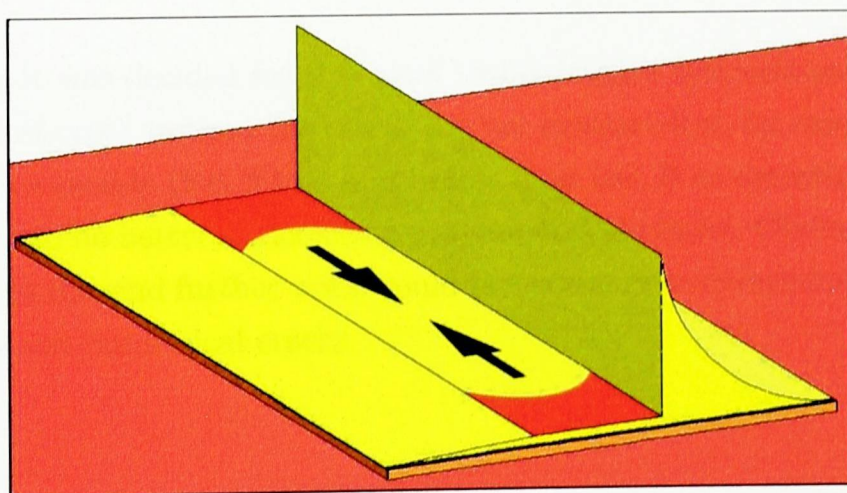


Figure 8.2: Crack propagation in standoff region



---

### 8.3. Test Methods

---

8.1 shows, the crack propagation direction is perpendicular to this and therefore his measurement of the time for crack propagation through the standoff region is likely to be underestimated.

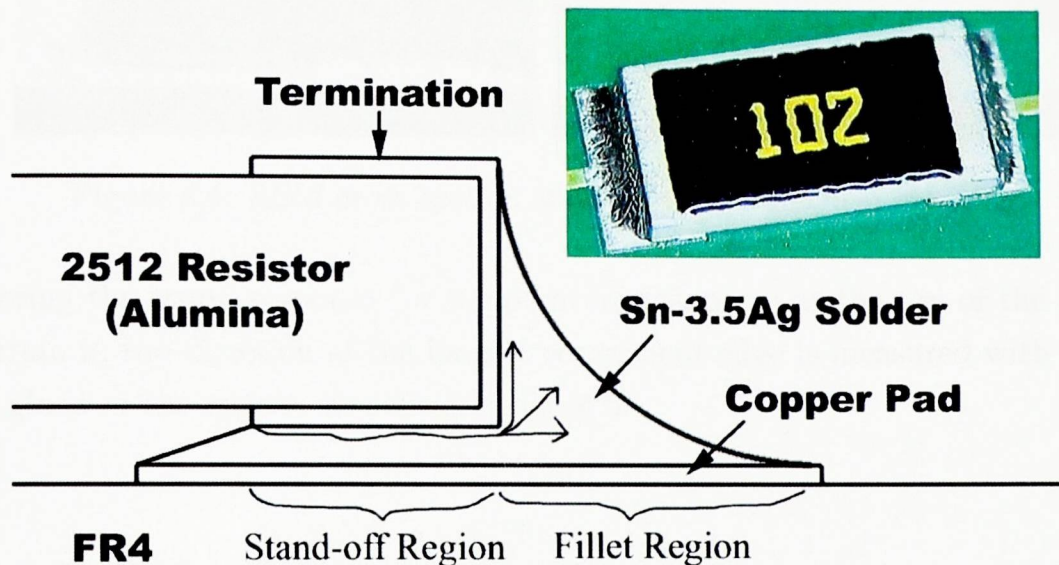


Figure 8.3: Crack propagation directions

The experimental results from [35, 53, 54] show a number of different directions of crack propagation which are illustrated in figure 8.3. They include the vertical direction predicted by the modelling along with horizontal and diagonal cracks through the fillet. In this work, the sensitivity of the tests to all three crack directions will be investigated.

For simplicity, it was decided for this work to investigate symmetrical cracks only – although in most cross sections the cracks are not symmetrical, for example see figure 8.4. It seems reasonable that if test A is better than test B at detecting symmetrical cracks, it will also be better at detecting unsymmetrical cracks. Obviously there may be exceptions to this and further work would be necessary to determine the behaviour of the tests on unsymmetrical cracks.

## 8.3 Test Methods

The following tests have been designed so that cross sectioning is not required. All the tests work by applying a mechanical (or thermal) loading to the specimen and

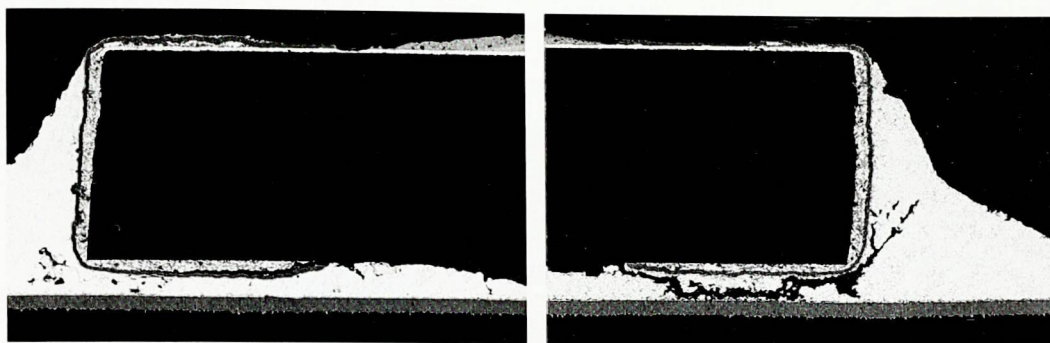


Figure 8.4: SEM cross section showing unsymmetrical cracking

monitoring the strain response (or temperature response) at the top of the resistor. The strain in the direction of the longest component edge is measured with a strain gauge glued to the resistor as shown in figure 5.

#### 8.3.1 Pull Test

The test specimen is subjected to a 100N tensile load using the apparatus shown in figure 8.5 and the strain on the resistor's top surface is monitored with a strain gauge. This measured strain will depend on the magnitude of the cracks in the joints since the presence of a crack will affect the way the load (and therefore strain) is distributed through the specimen.

#### 8.3.2 3 Point bend test

In this test, displacements are imposed on the test specimen at three points causing it to bend as illustrated in figure 8.6. The apparatus used for this test is the modified micrometer screw gauge shown in figure 8.7, the central point rotates as the screw gauge is turned.



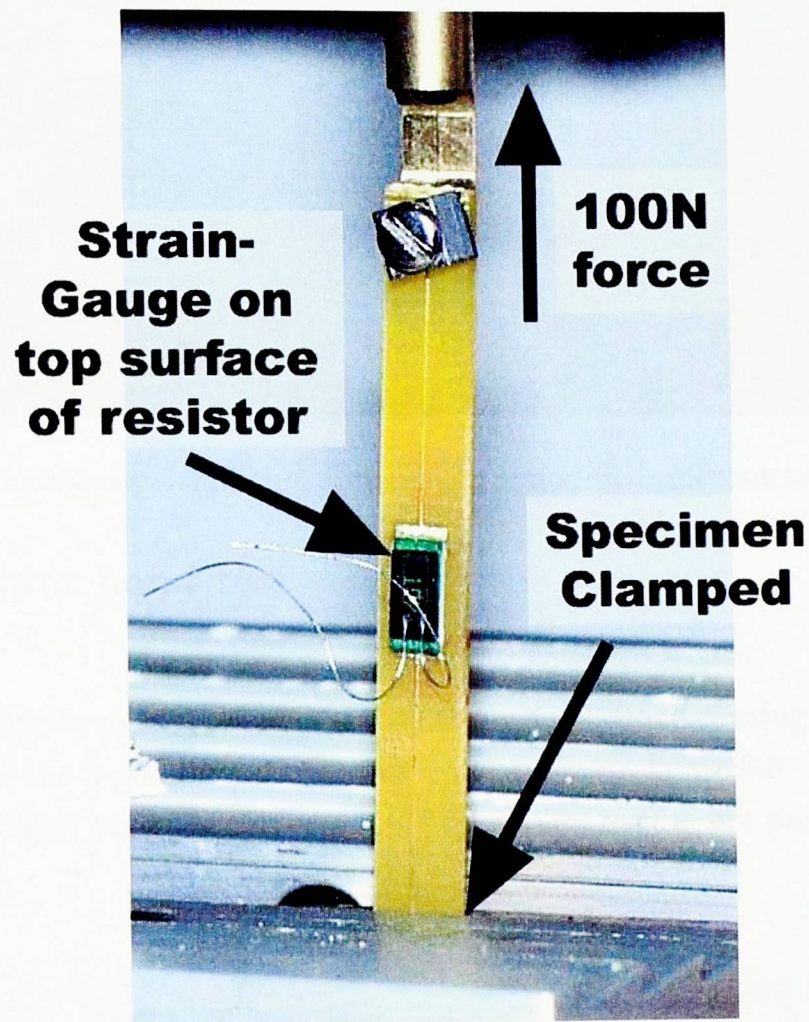


Figure 8.5: The pull test apparatus (a tensile testing machine)

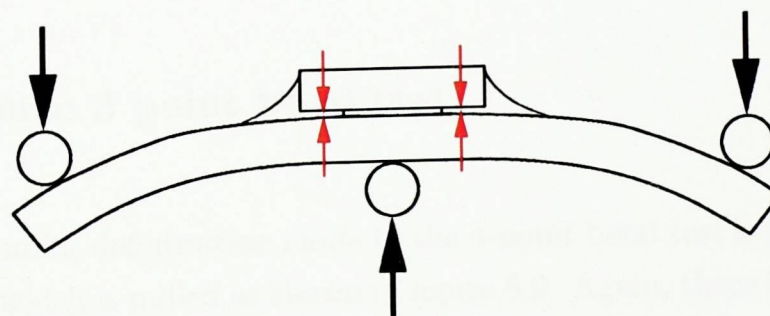


Figure 8.6: The 3-point bend test

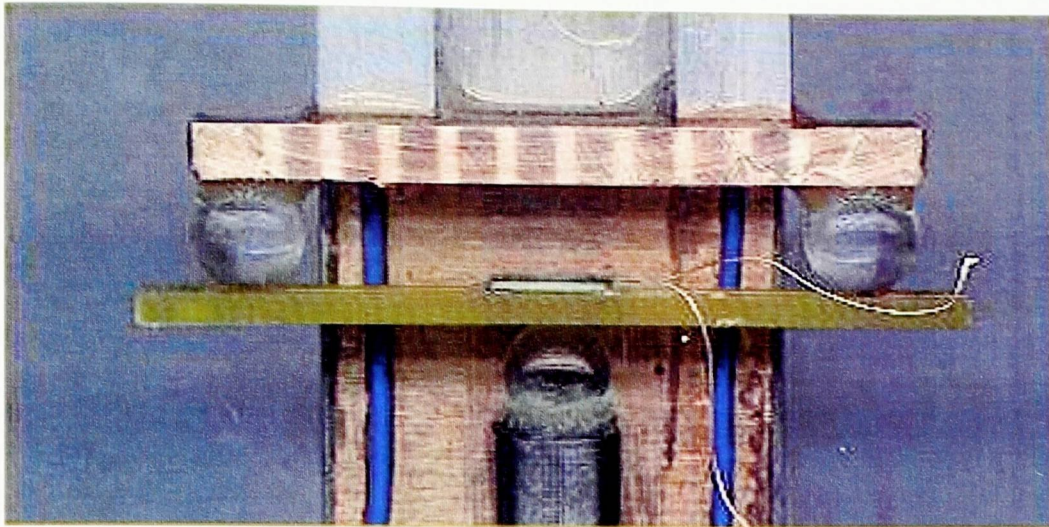


Figure 8.7: The 3-point bend test apparatus (a modified micrometer screw gauge)

#### 8.3.3 4 Point bend test

In this test, 4 displacements are imposed on the test specimen causing it to bend in the opposite way to the 3-point bend test, this is illustrated in figure 8.8. No experimental apparatus has been built for this test, only modelling results are presented.

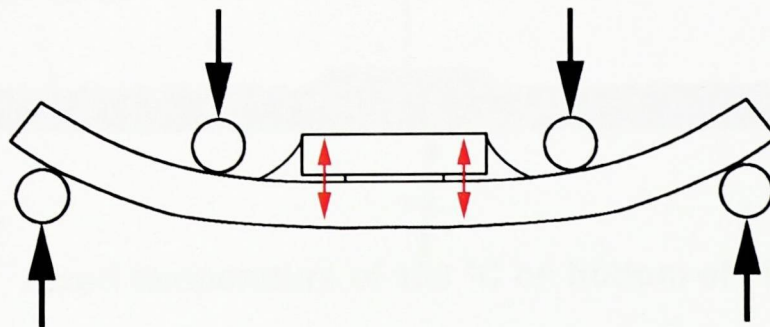


Figure 8.8: The 4-point bend test

#### 8.3.4 Reverse 3 point bend test

In this test, a similar deformation mode to the 4-point bend test is produced by using a central point which is pulled as shown in figure 8.9. Again, there is no experimental apparatus built to perform the test, but modelling work has been conducted to predict its sensitivity to cracks.



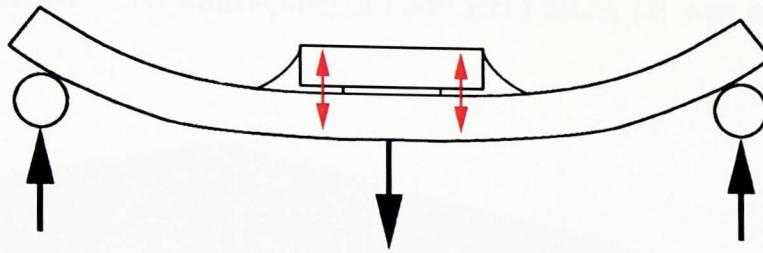


Figure 8.9: The reverse 3-point bend test

### 8.3.5 Thermal conductivity test

The whole specimen is initially at room temperature and the bottom of the PCB is placed in contact with a hot plate at  $100^{\circ}\text{C}$  as shown in figure 8.10. (The exact temperature is not important, the analysis is linear and material properties temperature independent so the trends will be the same regardless of the temperature magnitude.)

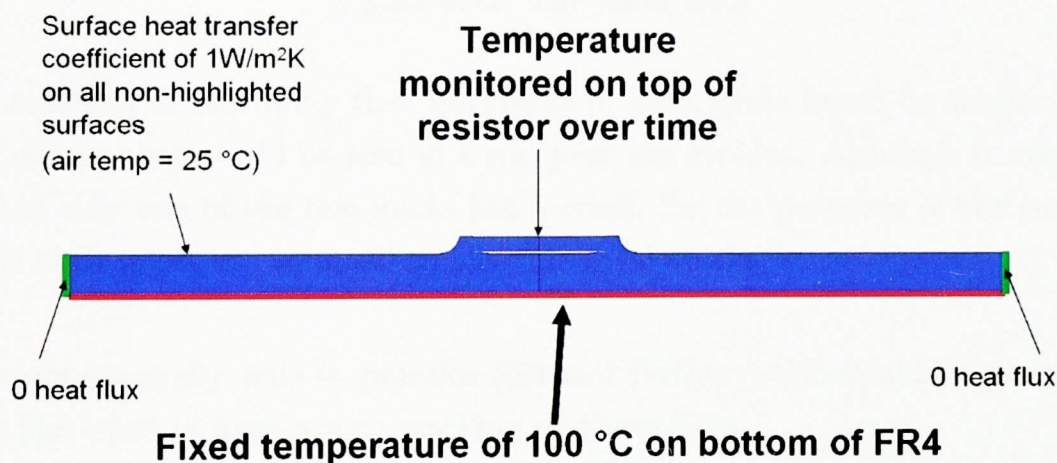


Figure 8.10: The boundary conditions for the thermal conductivity test

## 8.4 Modelling Method

In order to predict the sensitivity of the various tests described above, many meshes were constructed, each with a different crack length. An example of the mesh used is shown in figure 8.11, slight variations to this model were required when introducing the different sized cracks. The correct boundary conditions were imposed to simulate each of the tests and the strain at the top of the resistor (the location of the strain

---

## 8.4. Modelling Method

---

gauge) was recorded. The multi-physics code PHYSICA [4] was used to run all the simulations<sup>1</sup>.

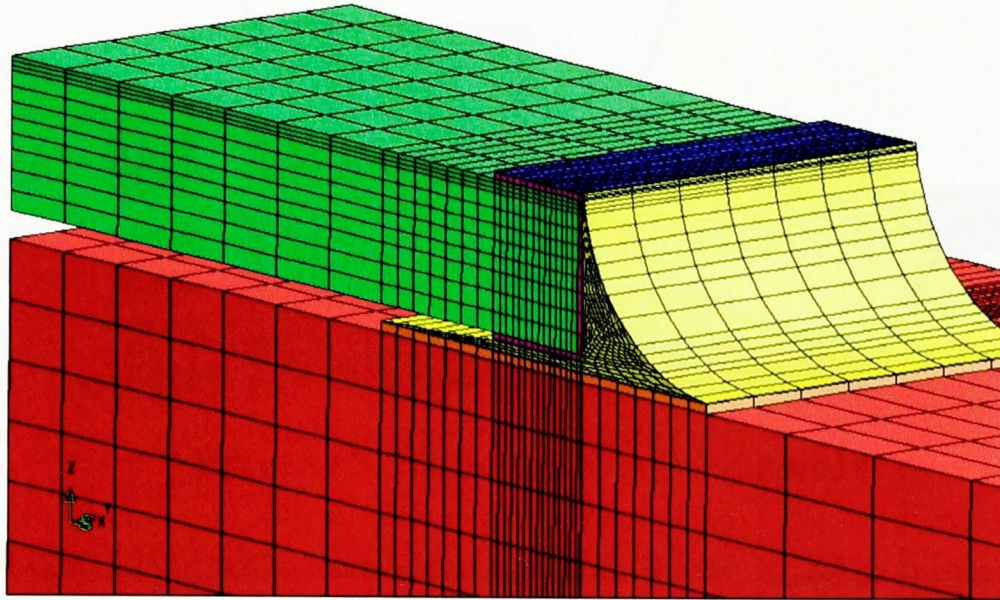


Figure 8.11: The mesh used

It was assumed in this study that the cracks in both joints would be similar and the jagged details that would be seen in a real joint are avoided. Although it may be the case that only one of the two joints has a crack, for the purposes of the sensitivity analysis both joints are assumed to have identical cracks.

This is not generally true in practice [35] and further work would be necessary to predict the effect of asymmetric cracking on these tests.

The materials which the specimen is made of are shown in figure 8.12. For all the materials except the solder, the behaviour is assumed to be linear elastic at room temperature. The material properties used are listed in appendix A. Note that two Elastic moduli are used for the FR4. Various sources report a modulus of between 12 to 28 GPa. In this work, simulations have been performed at 12.4GPa (as measured by the NPL), and 22 GPa [55], the effect of the different values is discussed later.

For most of the results presented, the creep in the solder is ignored and it is treated as a linear-elastic material. But a number of simulations have been performed using

---

<sup>1</sup>Since this work was conducted before the FATMAN module was implemented, this work used the EVP (Elastic Visco-Plastic) module which solves elasticity problems using the Finite Volume Method.



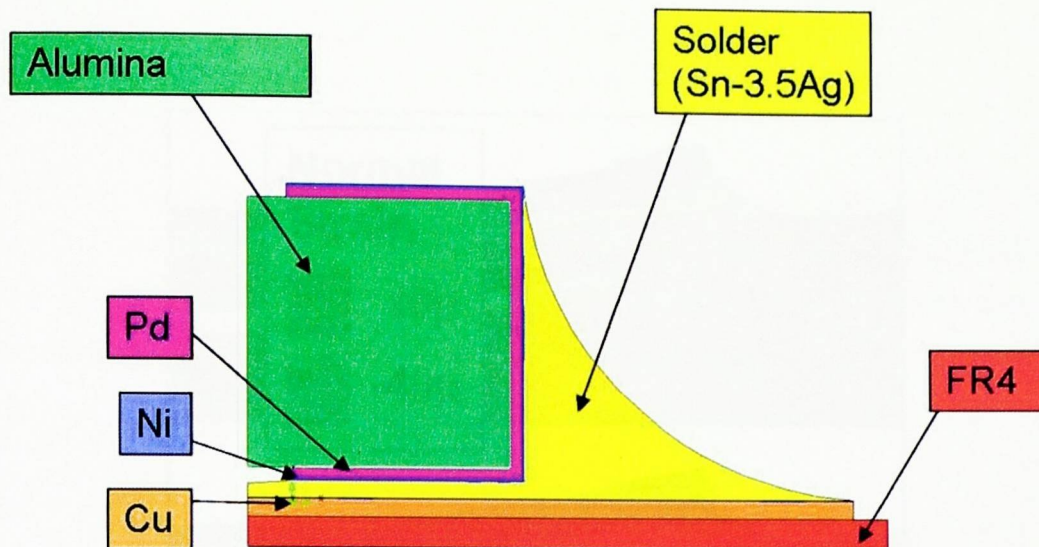


Figure 8.12: The materials used in the model

the sinh law (4.15) with material constants from Darveaux [10] to capture creep.

It is assumed that the loading applied during the test opens up the crack. Therefore contact analysis between the crack interfaces was not performed. In certain conditions this is not true and the crack surfaces are pushed together, this is discussed further in the results section.

## 8.5 Results

### 8.5.1 Pull Test

The elastic simulation with an FR4 Young's Modulus  $E$  of 12.4 GPa as measured by the NPL will be presented first. On loading, the test piece deforms as shown in figure 8.13, the left hand side of the images represents a symmetry plane, so the position of the strain gauge is at the top left corner of each diagram.

With no crack present the bending causes the top surface of the resistor to be in compression. When a crack has grown across the stand-off region the bending of the resistor is reduced by a small amount, leading to a 29% change in the strain at the strain gauge. When the crack grows further, either vertically or diagonally into the

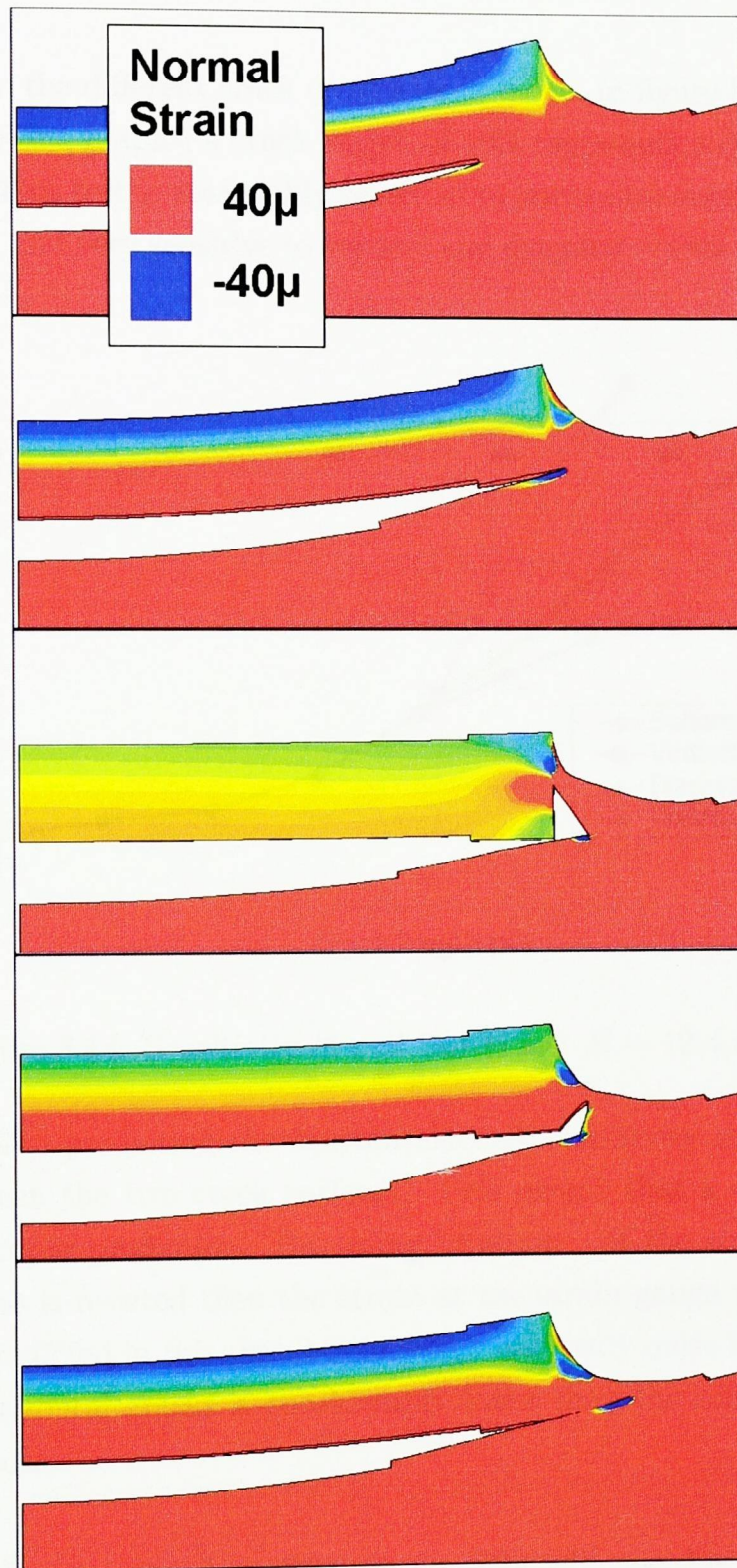


Figure 8.13: Pull test simulation results showing the strain contours at the symmetry plane. Deformation exaggerated by 150 $\times$ . From top to bottom: no crack, 100% standoff crack, vertical crack, diagonal crack, horizontal crack.



---

## 8.5. Results

---

fillet region, then a more dramatic change is seen causing the strain to eventually turn from compressive to tensile ( $>100\%$  change).

The sensitivity to the different crack directions is shown in figure 8.14. Note that in this and the following graphs, a crack length of 50% represents a completely cracked standoff region. This test is reasonably sensitive to horizontal cracks in the stand-off and fillet regions, and very sensitive to vertical and diagonal cracks in the fillet region.

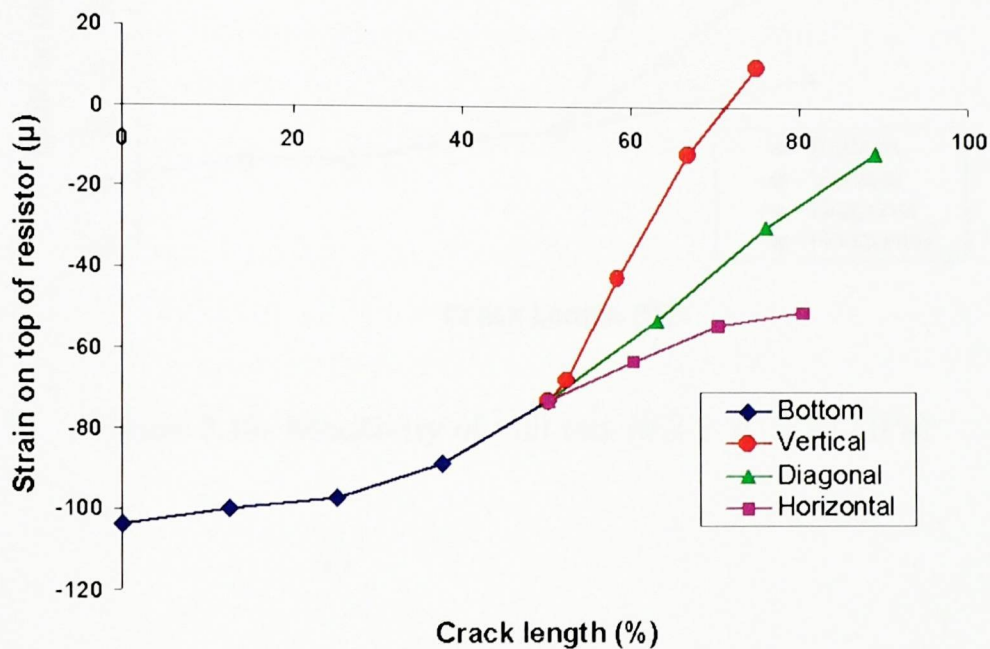


Figure 8.14: Sensitivity of pull test (FR4:  $E = 12.4$  GPa)

There is a problem predicting the horizontal crack sensitivity as the results show an overlap between the two crack surfaces. This means that a contact analysis is required for a proper prediction. But using intuition – if the contact between the two crack surfaces is resisted then the strain at the strain gauge will change by less than the value predicted in this simulation, which is already quite low. Therefore, the sensitivity to horizontal cracks is considerably lower than the sensitivity to vertical and diagonal cracks.

The elastic simulation using  $E = 22$  GPa for FR4 will now be discussed. As can be seen from figure 8.15, the overall shape of the graph is roughly similar to that produced using the lower strength FR4. There are 2 main differences. First, the increased  $E$  causes the magnitude of the strains to be lower. Second, the sensitivity to crack length in the standoff region is only 13%, a considerable decrease compared to the 29% obtained using  $E = 12.49$  GPa.

## 8.5. Results

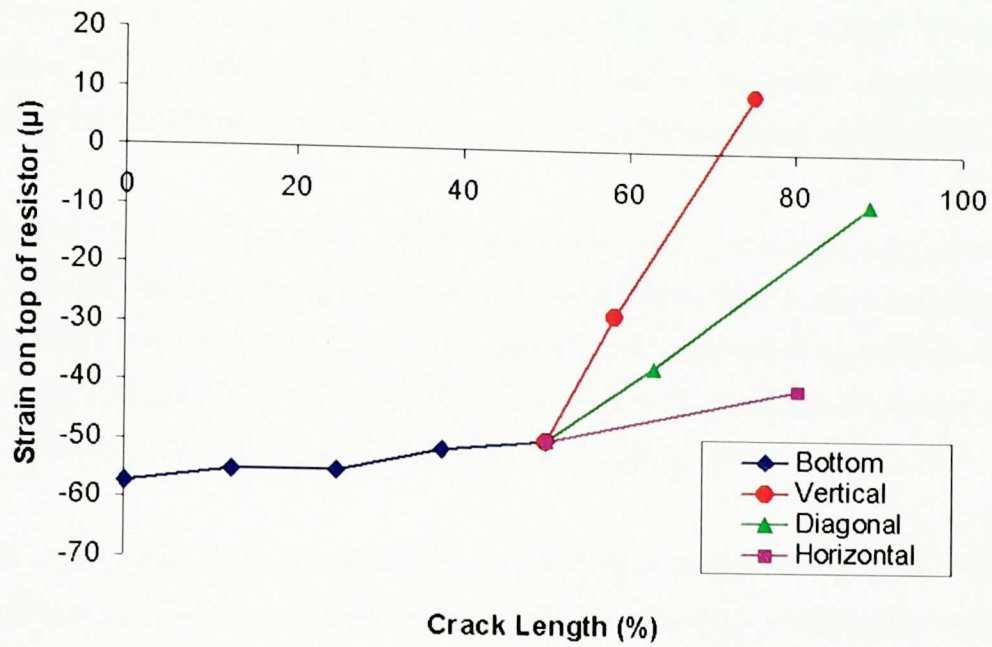


Figure 8.15: Sensitivity of pull test (FR4:  $E = 22$  GPa)

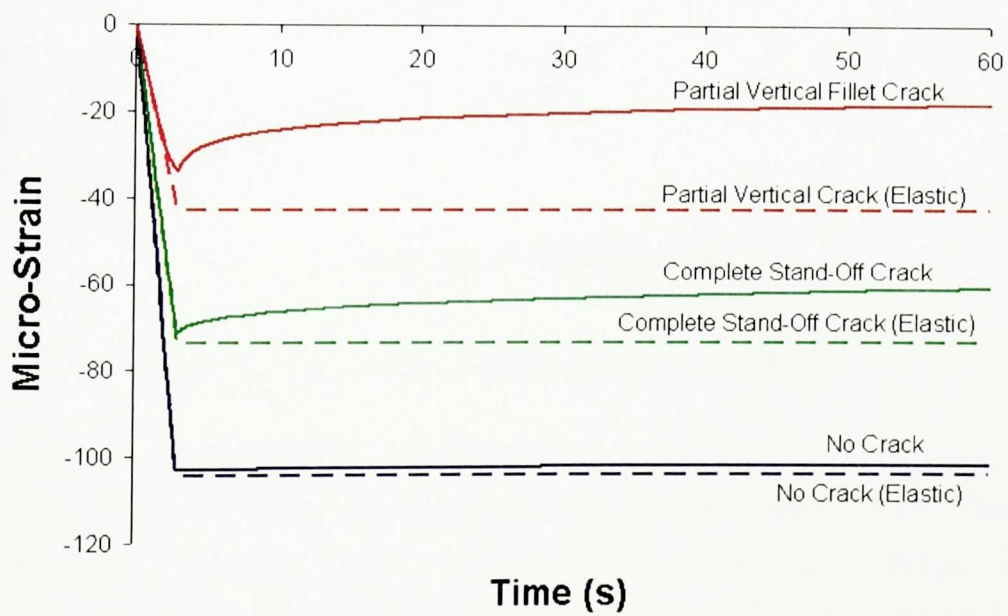


Figure 8.16: Effect of creep on pull test



---

## 8.5. Results

---

The next result is from a simulation incorporating creep in the solder and using the lower  $E$  of 12.4 GPa for the FR4. Figure 8.16 shows that creep has a negligible effect when no crack is present but becomes very prominent for the larger crack sizes. It has the effect of increasing the difference in the strains between the different crack lengths, thereby improving the sensitivity of the tests compared to the elastic results.

It is a concern that significant damage may be done to the solder over the course of the test. The simulation of crack growth is beyond the scope of this investigation but it is intuitively obvious that with a large enough crack initially present in the solder, the high stress concentration generated by the test in the remaining solder will cause the crack to grow, possibly completely destroying the joint.

To restrict creep and crack growth, the applied load could be reduced. This would have the effect of lowering the strains generated, therefore potentially reducing the accuracy of the strain gauge measurements. Hence, a load is required which offers an acceptable compromise between the accuracy and destructiveness of the test.

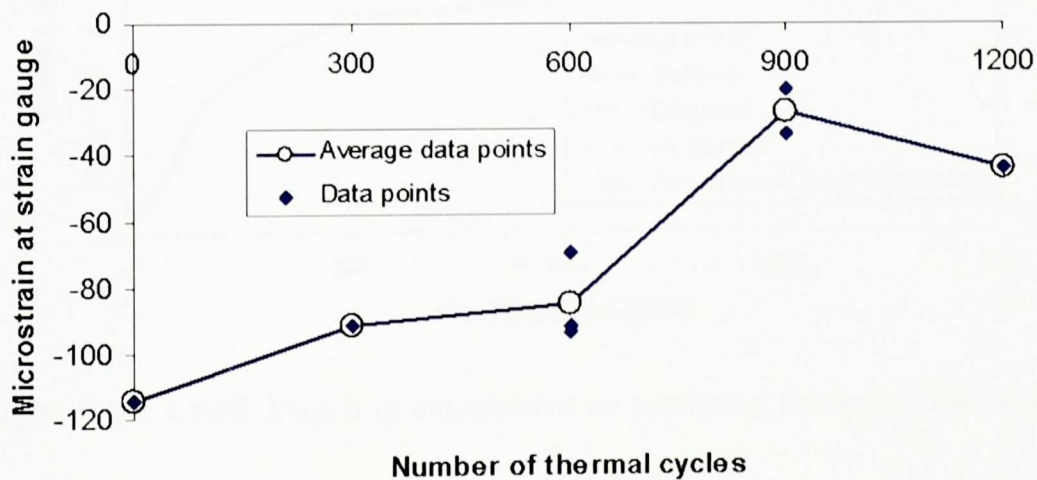


Figure 8.17: Experimental results for pull test

This test has been applied experimentally to a number of specimens exposed to different numbers of thermal cycles and the results are shown in figure 8.17. The number of specimens tested was very small – each of the data points in the graph represents only one test. Also, each of the data points represents a *different* specimen (in future work it would be interesting to test the *same* specimen after different numbers of thermal cycles).

## 8.5. Results

The strain gauge reading taken before any thermal cycles (first point on the graph in figure 8.16) shows reasonable correlation with the prediction in figure 8.14 when no crack is present (but not as good using the higher value  $E = 22\text{GPa}$  for the FR4). This is the only data point for which the modelling results can be directly validated, as the exact crack length within the damaged specimens is unknown.

Using the modelling results, the crack length for the experimentally thermal cycled specimens can be predicted. In order to make the predictions, the modelling results in figure 8.14 are calibrated so that the strain with no crack present matches the experimental data. This calibrated graph is used to lookup the crack length which corresponds to each point in figure 8.17. The predicted crack length versus thermal cycles is shown in figure 8.18.

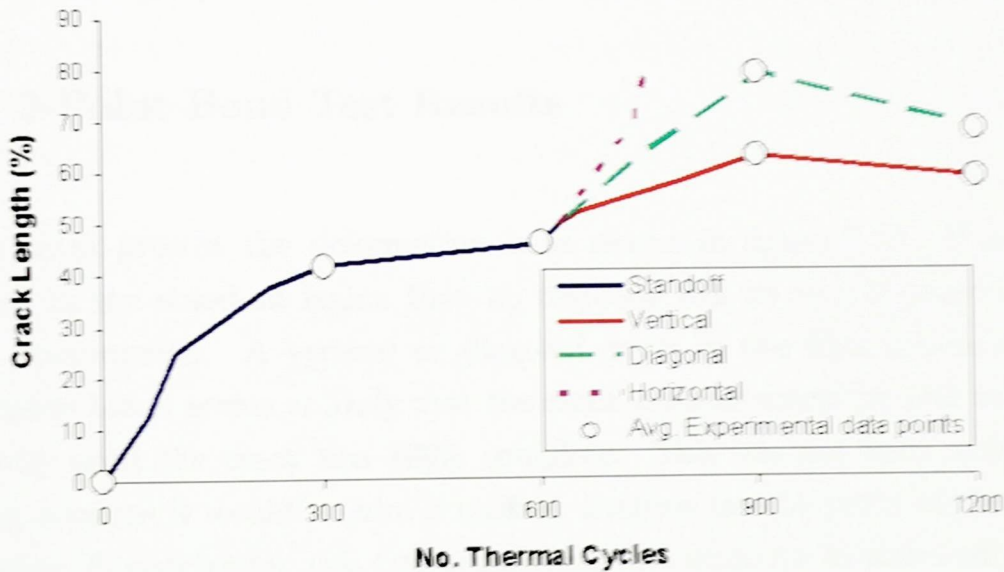


Figure 8.18: Crack length in experiment as predicted from pull test results

From figure 8.18 it seems reasonable to say that the specimens tested at 900 and 1200 cycles couldn't have contained symmetrical horizontal cracks – the strains generated are outside the range which 2 horizontal cracks are capable of generating according to the modelling predictions in figure 8.14. It is likely that at 900 and 1200 cycles there were either symmetric vertical or diagonal cracks, or unsymmetrical cracks. It is impossible to determine the exact length of a crack due to the ambiguity in its direction.



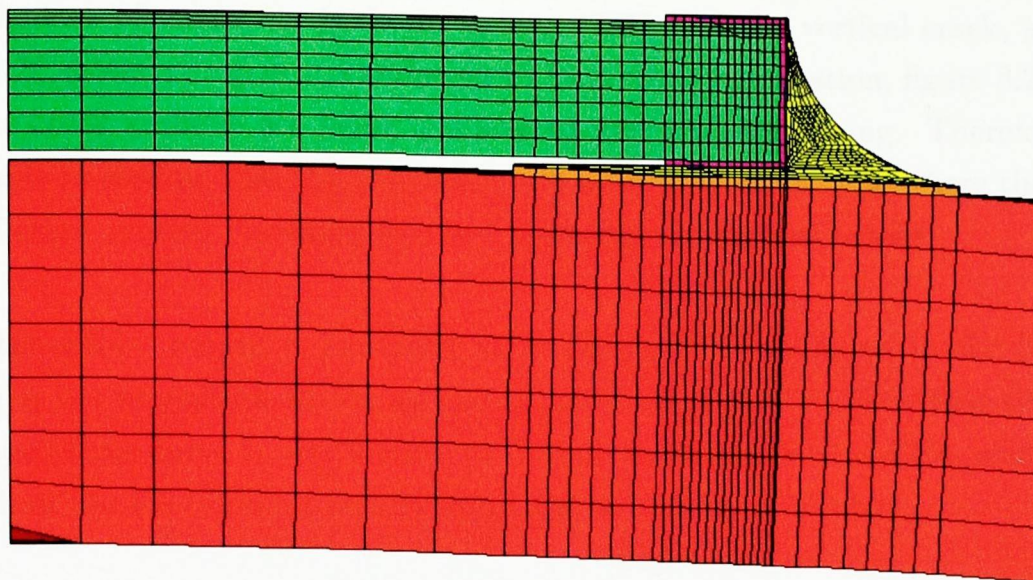


Figure 8.19: Deformation exaggerated  $30\times$  for the 3-point bend test. No crack in the solder.

### 8.5.2 3-Point Bend Test Results

With no crack present the deformation is as shown in figure 8.19. If a crack is introduced in the stand-off region then no response will be seen because the crack is under compression. A vertical or diagonal crack in the fillet region would be under tension but it seems unlikely that the crack surfaces would be able to separate significantly until the crack was 100% complete. This has not been verified with modelling because it would require a contact analysis for the parts of the crack in compression. In conclusion, this test is definitely not sensitive to stand-off cracks at all, and is unlikely to be sensitive to fillet cracks.

### 8.5.3 4-Point Bend Test Results

Unlike the 3-point bend test, the 4-point bend test causes the initial stand-off crack to be under tension. It will therefore be pried apart and will generate a large response in the strain gauge reading as can be seen in figure 8.20 (these results use the NPL measured value of 12.4 GPa for the FR4 Young's Modulus).

The test shows good sensitivity to horizontal cracks. Unfortunately though, there is no sensitivity to vertical or diagonal cracks in the fillet region. For the diagonal



---

## 8.5. Results

---

crack the lack of sensitivity is shown in figure 8.21. For the vertical crack, although figure 8.21 shows a drop in strain during vertical crack propagation, figure 8.20 shows that the crack surfaces are being compressed and are overlapping. Therefore, it is reasonable to assume that the true result will be similar to the case where there is no vertical crack present – making this test insensitive to vertical cracks.

When the FR4 strength is increased to 22 GPa (the value found in the literature [55]) then the magnitude of the strains is increased (figure 8.22). Other than that, the shape of the curve is very similar to that given for the weaker FR4, meaning the strength of the FR4 doesn't greatly affect the sensitivity of the test.

As for the pull test, 3 simulations were performed using a constitutive law for creep and the Young's Modulus of 12.4GPa for the FR4. The response of the strain on the resistor is shown in figure 22. And just as for the pull test, creep in the solder actually improves the sensitivity of this test, but at the expense of permanently deforming the solder, invalidating its description as a non-destructive test.

The results presented above indicate that the test could be useful in determining the length of a crack in the stand-off region, or a horizontal crack in the fillet region. No experiments have been performed on this test.

### 8.5.4 Reverse 3-Point Bend Test Results

The results are shown in figures 23, 24 and 25 and everything that has been said regarding the 4-point test results applies to this. It shows good sensitivity to standoff cracks and horizontal fillet cracks, but vertical and diagonal fillet cracks have little effect on the strain gauge reading as the cracks are under compression.

### 8.5.5 Thermal Conductivity Results

The temperature contours 12 seconds after the start of the test are shown in figure 8.27. There is not a significant change until the crack is greater than 72%. The response at the top of the resistor is shown in figure 8.28, cracks up to 72% cause no



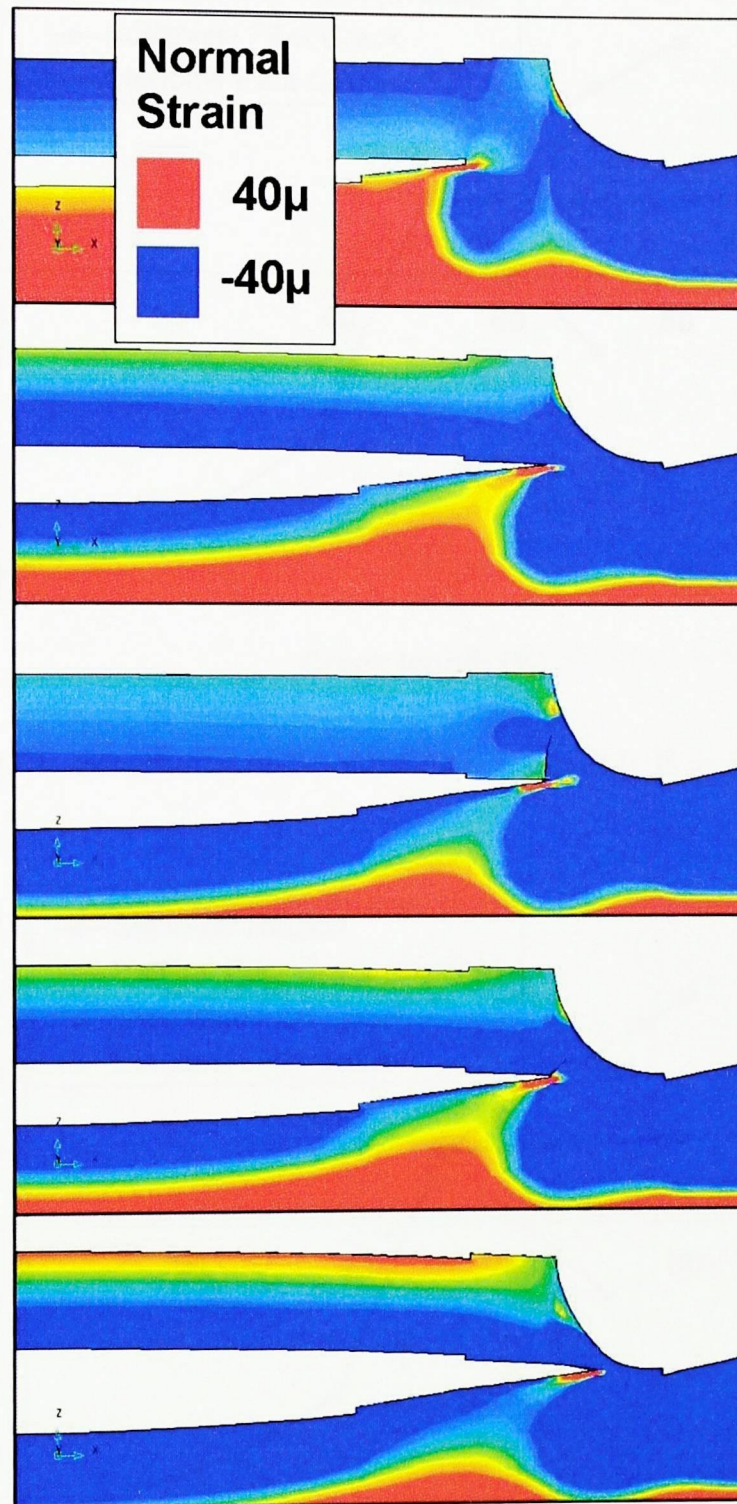


Figure 8.20: 4-point bend test results showing the strain contours at the  $y=0$  symmetry plane. Deformation exaggerated by 150 times. From top to bottom: no crack, 100% standoff crack, vertical crack, diagonal crack, horizontal crack.

8.5. Results

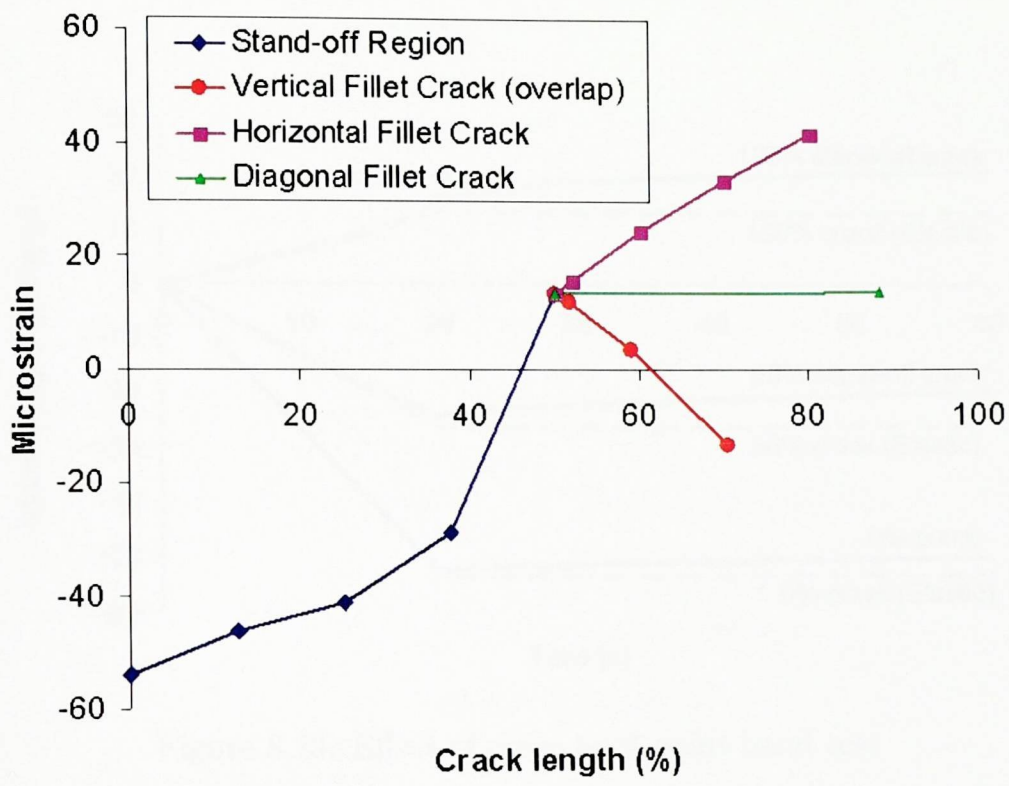


Figure 8.21: Sensitivity of 4-point bend test (FR4:  $E = 12.4$  GPa)

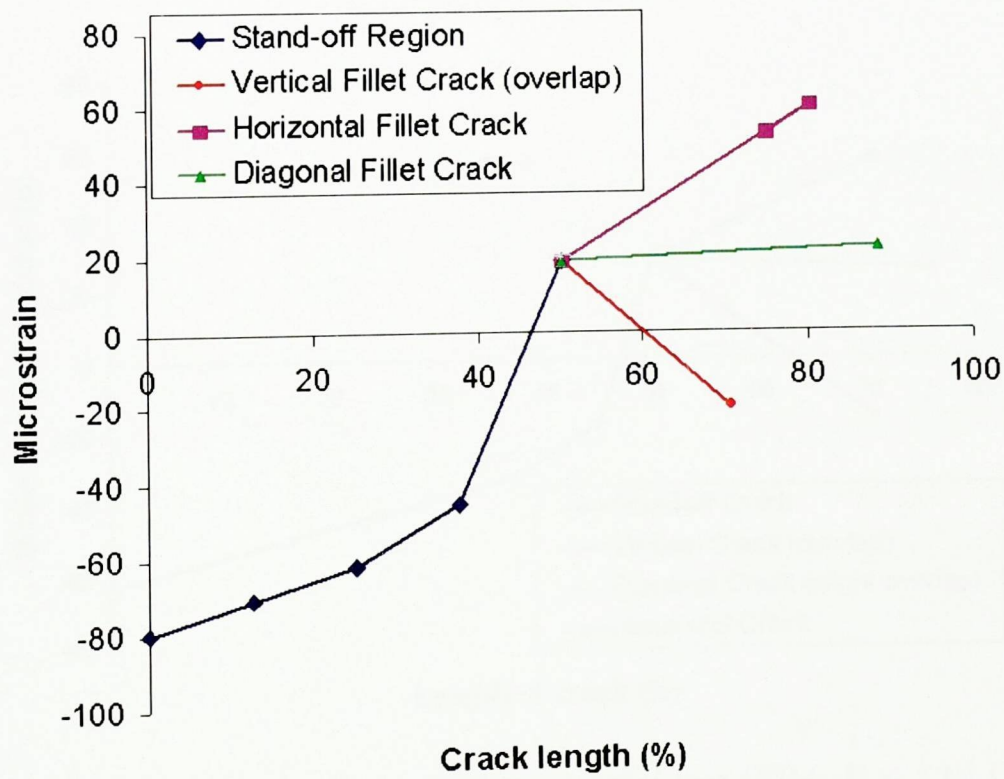


Figure 8.22: Sensitivity of 4-point bend test (FR4:  $E = 22$  GPa)



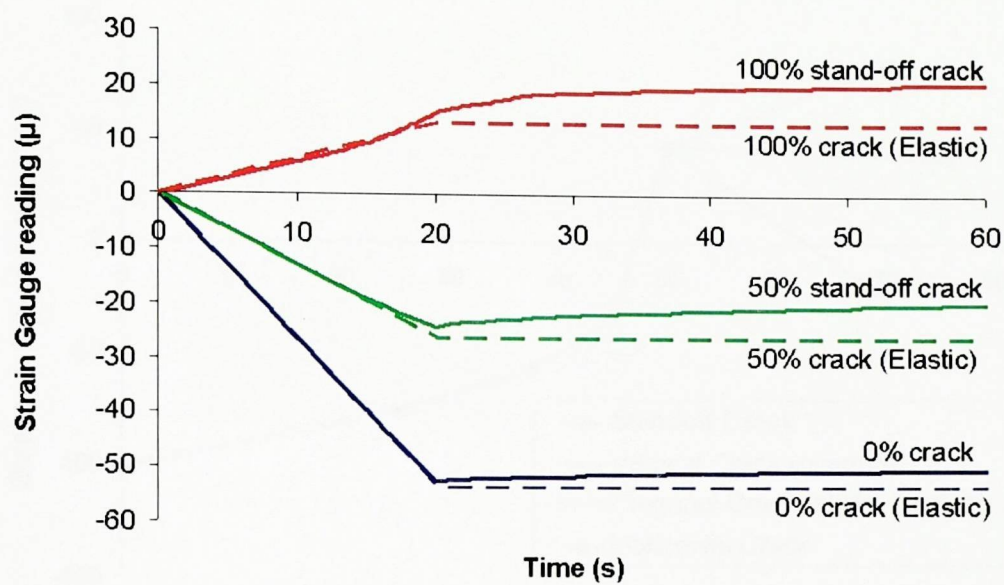


Figure 8.23: Effect of creep on 4-point bend test

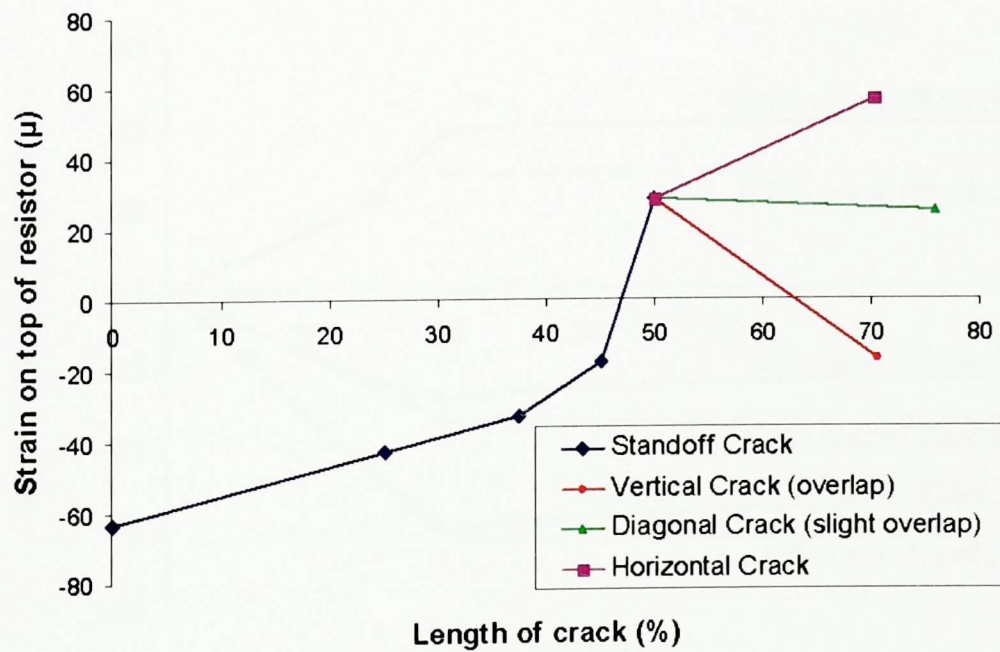


Figure 8.24: Sensitivity of reverse 3-point bend test (FR4:  $E = 12.4$  GPa)

8.5. Results

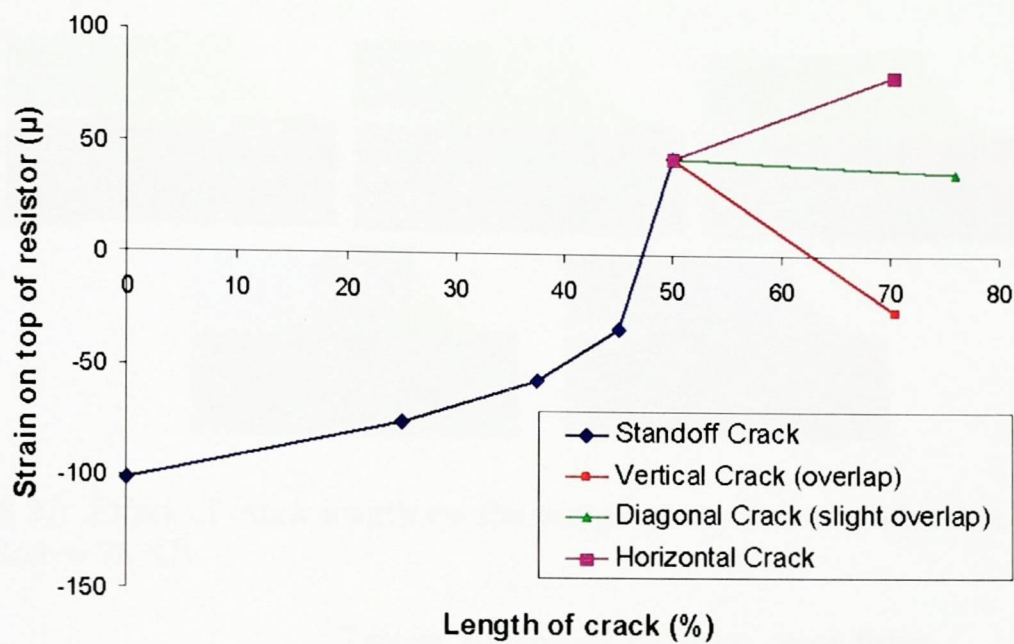


Figure 8.25: Sensitivity of reverse 3-point bend test (FR4: E = 22 GPa)

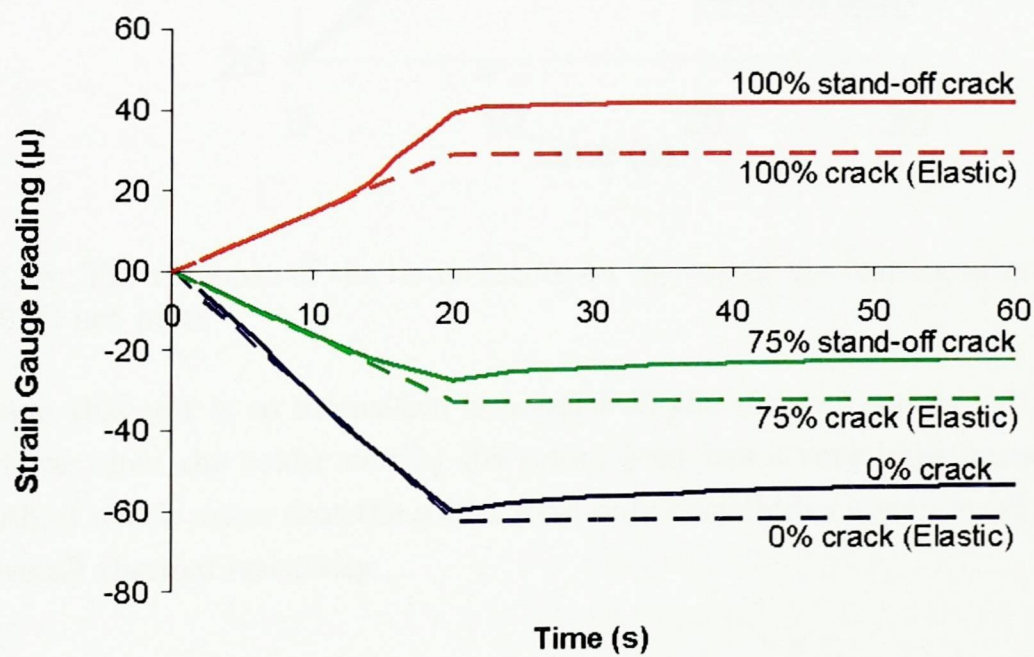


Figure 8.26: Effect of creep on reverse 3-point bend test



## 8.5. Results

significant effect on the temperature response and even cracks up to 99.4% only show a small ( $<10\%$ ) temperature change.

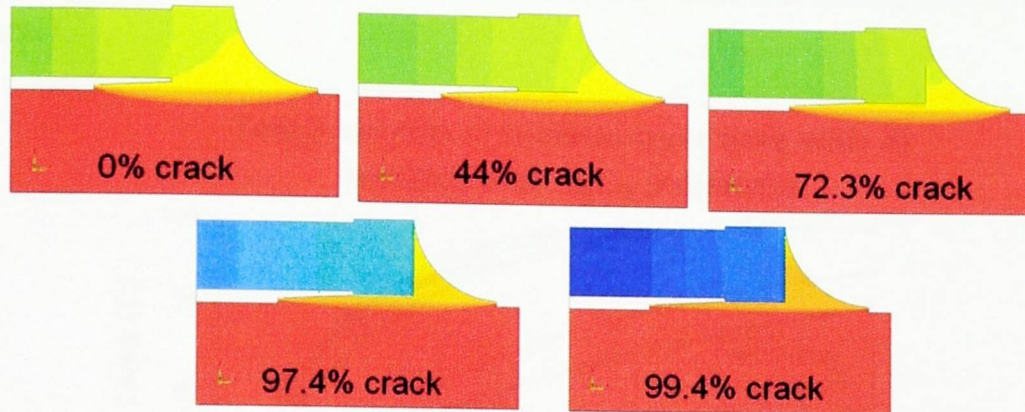


Figure 8.27: Effect of crack length on the temperature contours after 12s. (Blue =  $65^{\circ}\text{C}$ , Red =  $75^{\circ}\text{C}$ )

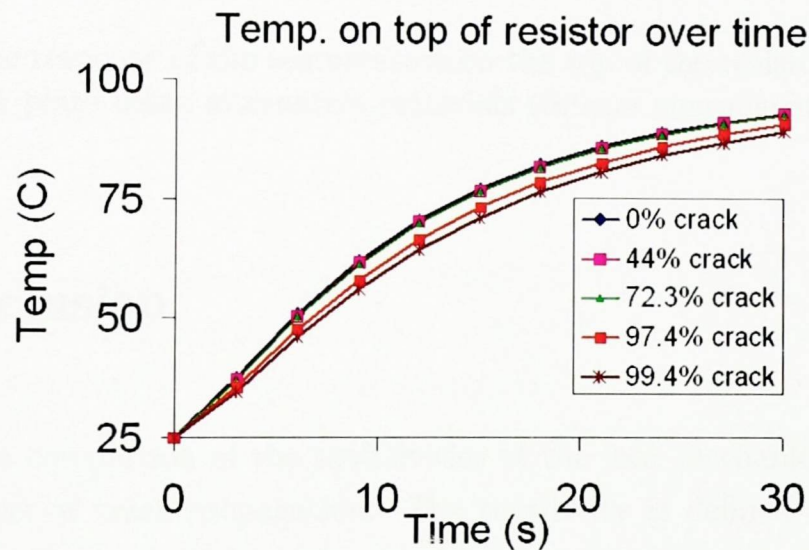


Figure 8.28: The response of the temperature on the top of the resistor after contact with  $100^{\circ}\text{C}$  hot plate

The reason this test is so insensitive is because a) the thermal conductivity of the FR4 is lower than the solder and b) the solder joint has a very large cross section area, both of which mean that the solder joint only contributes a very small amount to the overall thermal resistivity.

To determine the significance of the material properties, other simulations were performed using alumina instead of FR4 as a substrate and silicon instead of alumina for the component. The results of these simulations are shown in figure 8.29. They show a much greater difference in temperature between the different crack lengths,

## 8.6. Conclusion

making the test feasible using both a component and substrate with high thermal conductivity. (However in reality some thermal conduction will occur between the cracked surfaces which is ignored in the model and which will reduce the temperature difference.)

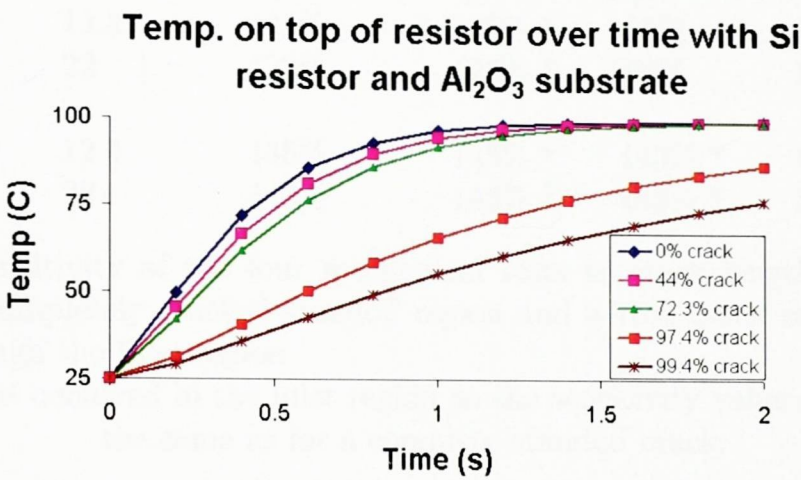


Figure 8.29: The response of the temperature on the top of the resistor after contact with 100 °C hot plate using alternative materials (Silicon component and Alumina substrate)

## 8.6 Conclusion

Table 3 shows a comparison of the sensitivities of the four mechanical tests to the various directions of crack propagation. The sensitivity is defined as the relative change in the strain gauge reading when compared to the case of no crack.

The 3-point bend test has been shown not to work but the other three tests have a good possibility of working. The 4-point test and reverse 3-point test have shown good sensitivity to initial stand-off cracks and horizontal fillet cracks. The pull test has shown some sensitivity to stand-off cracks and good sensitivity to vertical or diagonal fillet cracks. Therefore, a combination of the pull test along with either the reverse 3-point or 4-point test should allow any of the possible standoff and fillet cracks to be detected. Further modelling work could be conducted to determine the response of the test to an unsymmetrical crack.

The thermal conductivity test was shown to be very insensitive to crack length, the reason being the poor thermal conductivity of the FR4 substrate.



## 8.6. Conclusion

Test type	Young's Modulus (GPa)	Stand-off (50%)	Vertical Fillet (75%)	Diagonal Fillet (75%)	Horizontal Fillet (75%)
Pull test	12.4	29%	109%	70%	49%
	22	13%	117%	58%	26%
3-point	12.4 or 22	N/A	N/A	N/A	N/A
4-point	12.4	125%	125% *	125%	169%
	22	123%	123% *	126%	166%
Reverse					
3-point	12.4	145%	145% *	145% *	191%
	22	143%	143% *	143% *	181%

Table 8.1: Sensitivity of the four mechanical tests to crack length. A 50% crack represents a completely cracked standoff region and a 75% crack represents a crack half way through the fillet region.

\* crack contact occurred in the fillet region so the sensitivity value is assumed to be the same as for a complete standoff crack.

The NPL measured Young's Modulus of 12.4 GPa for the FR4 provided a better match between simulation and experiment than the 22 GPa value quoted in the literature [55].

The pull test, the 4-point bend test and the reverse 3-point bend tests show promise but require further experimental validation with specimens whose crack length is known. Such an investigation could also determine how destructive the tests are – whether they cause the cracks to grow significantly when using different forces (pull test) or displacements (bend tests). This would help to find the optimum force or displacements to apply in the tests – an acceptable compromise needs to be made between the size of the strains generated and the damage done to the solder joints for the tests to be classified as non-destructive.

## Chapter 9

### Conclusions

The theory behind the FEA discretisation has been presented and implemented in the FATMAN code. The LENI scheme to solve for creep using an implicit discretisation was presented and shown to be more robust than an explicit scheme.

The literature review suggests that at present FEA using a creep law combined with an empirical fatigue law is the best choice to predict solder joint lifetime  $N_f$  with correlations within  $\pm 25\%$  possible. This approach was used with the sinh creep law to predict damage accumulation in a resistor under different thermal cycle profiles in chapter 7. The correlation to experimental drop in USS (Ultimate Shear Strength) after 1200 cycles was only about  $\pm 2\times$ . This is reasonable but perhaps using experiments which cycle the joints to failure, thus determining  $N_f$  rather than USS, would yield a better correlation.

To capture the creep more accurately than a steady-state creep law the Armstrong Frederick kinematic hardening law was implemented using the LENI scheme. Material constants were obtained using inverse analysis in chapter 5 and it was shown to fit the experimental creep curves much better than the steady state law. However when used to predict  $N_f$  under thermal cycling of resistors in chapter 7 the predicted trend is roughly similar to the steady-state law. So despite providing more accurate predictions of strain rates, kinematic hardening doesn't have a big impact on relative lifetime predictions in this case.



---

A damage law was presented which can capture the crack growth in a solder joint during accelerated cycling, potentially removing the need for an empirical fatigue law. A failure criteria based on electrical resistance increase  $R/R_0$  was presented although  $N_f$  was shown to be very dependent on the value of  $R/R_0$  chosen. In further work it may be worth investigating this further. Perhaps the elements should be totally removed from the mesh once the damage  $D$  increases beyond a certain cutoff point representing the sudden coalescing of microcracks leading to crack formation. This would probably make the point of failure more definite.

A crack length scale parameter was used and was shown to reduce the mesh dependence of the damage law for the idealised test cases in chapter 4 and for the thermal cycling of a resistor on page 131. Further work could investigate this mesh dependence under different conditions and seek ways of reducing it further. To achieve the goal of a lifetime prediction method with no empirical, geometry dependent factors, mesh independence is very important.

A method for speeding up the damage computation was presented on page 80 which allows the prediction of damage over any number of thermal cycles while only simulating a small number using FEA. It relies on the fact that the material constant  $B$  is inversely proportional to  $N_f$  so although it works well for the presented law, it will not work for more complex laws where this relationship no longer holds.

Work was presented on a fatigue test in chapter 6 which demonstrated a method to achieve the correct displacement profile across the solder joint by compensating for the displacement in the copper arms. Even accounting for this displacement, simulations predicting the hysteresis curve using both the steady state sinh law and kinematic hardening law did not match experimental data – the experiments showed a much more compliant solder joint than predicted. The reasons for this are not clear however work is continuing at the NPL on developing the test and future experiments and simulations may help explain the discrepancy. Results from this test could be used in future to determine constants for the kinematic hardening law and damage law using the methods described in chapter 5.

Work in chapter 7 compared simulations of thermal cycled resistor joints to experiment and showed that creep strain provided a better indicator of damage than strain energy. A sensitivity analysis showed the effect of altering the temperature range and

---

## 9.1. Future work

---

the ramp and dwell times. The high temperature was found to have the most significant effect on the severity of the thermal cycle. The damage law was used to predict the crack propagation through the resistor joints and the use of volume averaging was seen to reduce the mesh dependence regarding the crack shape.

Modelling of novel crack detection tests was presented in chapter 8. The pull test, reverse 3-point bend test and the 4-point bend test show sensitivity to cracks in the solder but more experimental work is necessary to validate these predicted results. Experiments in which SEM images or dye penetration techniques are used to determine the length of cracks in tested samples would be useful.

## 9.1 Future work

This is a list of suggestions for projects which could follow on from the work presented in this thesis:

1. Validate FATMAN versus ANSYS (or other commercial code) more thoroughly for both elasticity and nonlinear creep problems.
2. Compare the performance of LENI against other implicit solution schemes.
3. Further develop the damage law with the goal (perhaps unattainable) of mesh independent results.
4. Remove completely damaged elements from the mesh, thus making the point of failure more definite.
5. Attempt to validate the kinematic hardening law constants found in chapter 5 by simulating the first few cycles of a fatigue test and comparing the results against experimental data covering a wide range of loading conditions (e.g. different strain rates and displacement amplitudes).
6. Determine the material constants for the damage law by inverse analysis using experimental fatigue test data.



### 9.1. Future work

---

7. Obtain or validate the damage law constants against experimental lifetime data on a range of different chip assemblies (e.g. resistor, flip-chip, BGA, etc.) under thermal cycling.
8. Investigate the cause of the discrepancy between the experimental and simulated hysteresis loops for the NPL fatigue test.
9. Perform experiments on the NPL fatigue test in which the correlation between pseudo-resistance and crack length is determined.
10. Model the crack detection tests using asymmetric cracks.
11. Determine the sensitivity of the crack detection tests using experimental methods. For example: the joints could be thermal cycled, tested using one of the crack detection tests, then the actual crack length could be determined by cross sectioning or dye penetration.

# Appendix A

## Material Properties

The material constants used in the simulations.

### A.1 Material Properties

Material	Young's Mod (GPa)	Poisson's Ratio	CTE (ppm/°K)	Source
SnAgCu *	61.251-0.0585T (T in °K)	0.36	20.0 (or 16.66 + 0.017T <sup>†</sup> ) (T in °K)	[50]
Sn3.5Ag	45.7	0.31	20	
FR4	22 (or 12.4 <sup>‡</sup> )	0.28	18(xy) 70(z)	[56]
Alumina	282.7	0.22	7.4	[56]
Copper	121	0.35	17	[56]
Palladium	117	0.39	11.5	[57]

Table A.1: Elastic material constants

\* from combined data on Sn3.8Ag0.7Cu, Sn3.5Ag0.75Cu, Sn3.5Ag0.5Cu, and Castin<sup>TM</sup>

<sup>†</sup>obtained from [58]

<sup>‡</sup>obtained from DMA (Dynamic Mechanical Analysis) performed at NPL



### A.1. Material Properties

Solder	A	$\alpha$	n	Q/k	Source
SnAgCu *	277984 s <sup>-1</sup>	0.02447 MPa <sup>-1</sup>	6.41	6500 K	[50] (via [12])
Sn3.5Ag	900000 s <sup>-1</sup>	0.06525 MPa <sup>-1</sup>	5.5	8690 K	[10]

Table A.2: Constants for sinh law

\* from combined data on Sn3.8Ag0.7Cu, Sn3.5Ag0.75Cu, Sn3.5Ag0.5Cu, and Castin<sup>TM</sup>

Solder	Thermal conductivity (W m <sup>-1</sup> K <sup>-1</sup> )	Density (kg m <sup>-3</sup> )	Specific Heat (J kg <sup>-1</sup> K <sup>-1</sup> )	Source
SnAg	70	8400	160	[57]
Alumina	25	3900	880	
FR4	0.29	1800	187.7	
Copper	385	8960	385	[57]
Palladium	71.2	12020	247	[57]
Nickel	60.7	8800	460	[57]

Table A.3: Thermal properties

Solder	Electrical resistivity ( $\mu\Omega$ cm)	Source
SnAgCu	10-15	[59]
SnPb	14.5	[59] (via [60])

Table A.4: Electrical properties

# Appendix B

## Sparse Matrix data structure

For all but the very smallest meshes the final system matrix is sparse, meaning the vast majority of elements are zero. Therefore it is not sensible to store the full  $n \times n$  elements in memory. Instead, the following sparse matrix data structure is used:

	Row 1				Row 2			Row 3	
	1	2	3	4	5	6	7	8	
<b>value[]</b>	$K_{1,1}$	$K_{1,4}$	$K_{1,7}$	$K_{1,8}$	$K_{2,2}$	$K_{2,1}$	$K_{2,6}$	$K_{3,3}$	...
<b>index[]</b>	4	4	7	8	7	1	6	12	...

Figure B.1: Example showing the sparse matrix data structure in use

The non-zero element values are stored in the real array `value[]` on a row-by-row basis. For each row  $i$ , the value of the diagonal element  $K_{ii}$  is stored, followed by all the other non-zero elements in that row. The integer array `index[]` is used to keep track of where the non-zeros are situated in the system matrix:

1. If `value[i]` represents a diagonal  $K_{jj}$ , `index[i]` is a pointer to the last value in row  $j$ . e.g. in figure B.1:

$$\begin{aligned} \text{value}[5] &= K_{22} \\ \text{value}[\text{index}[5] + 1] &= K_{33} \end{aligned}$$



- 
2. If `value[i]` represents a non-diagonal: `index[i]` is the corresponding column number. e.g. in figure B.1:

$$\text{value}[3] = K_{17}$$

$$\text{index}[3] = 7$$

To allow the start of any row to be found without having to search through `index[]`, an integer array `lookup[]` is used:

$$\text{value}[\text{lookup}[i]] = K_{ii}$$

Note that all the diagonals are stored, this is OK since the FEA discretisation will never produce a system matrix diagonal of zero unless the Young's moduli of all the surrounding elements are zero - (if this situation occurs the matrix becomes singular and is likely to generate an error in the solver algorithm).

Since the FEA discretisation produces symmetrical matrices, it is possible to reduce the storage requirements almost by half by neglecting to store elements one side of the diagonal. However, storing the full matrix allows matrix multiplications to be computed quickly so despite the redundancy, both sides of the diagonal are stored in FATMAN.

## Bibliography

- [1] Joseph LaDou. Printed circuit board industry. *International Journal of Hygiene and Environmental Health*, In Press, Corrected Proof.
- [2] S. Ridout, M. Dusek, C. Bailey, and C. Hunt. Finite element modeling of crack detection tests. In *EuroSimE*, pages 141–146, Brussels, 2004. IEEE.
- [3] S. Ridout, M. Dusek, C. Bailey, and C. Hunt. The effect of thermal cycle profiles on solder joint damage. In *EMAP*, pages 436–441. IEEE, 2004.
- [4] Ridout. Modeling and experiments on an isothermal fatigue test for solder joint. In *EuroSimE*, pages 478–482. IEEE, 2005.
- [5] S. Ridout and C. Bailey. Constitutive modeling of kinematic hardening and damage in solder joints. In *ESTC*, pages 927–933. IEEE, 2006.
- [6] S. Ridout, M. Dusek, C. Bailey, and C. Hunt. Assessing the performance of crack detection tests for solder joints. *Microelectronics Reliability*, 46:2122–2130, 2006.
- [7] S. Ridout and C. Bailey. Review of methods to predict solder joint reliability under thermo-mechanical cycling. *Fatigue and Fracture of Engineering Materials and Structures*, ACCEPTED FOR PUBLICATION.
- [8] Werner Engelmaier. Solder attachment reliability, accelerated testing, and result evaluation. In John H. Lau, editor, *Solder Joint Reliability: Theory and Applications*. Van Nostrand Reinhold, New York, 1991.
- [9] IPC. IPC-D-279: Design guidelines for reliable surface mount technology printed board assemblies. Technical report, IPC, 1996.



## Bibliography

---

- [10] Robert Darveaux, Kingshuk Banerji, Andrew Mawer, and Glenn Dody. Reliability of plastic ball grid array assembly. In John Lau, editor, *Ball Grid Array Technology*. New York, 1995.
- [11] Jean Paul Clech. Lead-free and mixed assembly solder joint reliability trends. In *APEX Designers Summit*, volume S28-3, Anaheim, California, 2004. IPC.
- [12] Ahmer Syed. Accumulated creep strain and energy density based thermal fatigue life prediction models for SnAgCu solder joints. In *ECTC*, pages 737–746. IEEE, 2004.
- [13] Robert Darveaux. Effect of simulation methodology on solder joint crack growth correlation (white paper). Technical report, Amkor.
- [14] Jean Paul Clech. Solder reliability solutions: A PC-based design-for-reliability tool. *Soldering & Surface Mount Technology*, 9(2):45–54, 1997.
- [15] Shi-Wei Ricky Lee and Xiaowu Zhang. Sensitivity study on material properties for fatigue life prediction of solder joints under cyclic thermal loading. *Circuit World*, 24(3):26–31, 1998.
- [16] H.L. Pang, B.S. Xiong, C.C. Neo, X.R. Zhang, and T.H. Low. Bulk solder and solder joint properties for lead free 95.5Sn-3.8Ag-0.7Cu solder alloy. In *ECTC 2003*, pages 673–679. IEEE, 2003.
- [17] Cemal Basaran and Jianbin Jiang. Measuring intrinsic elastic modulus of Pb/Sn solder alloys. *Mechanics of Materials*, 34(6):349–362, 2002.
- [18] S. Wiese and S. Rzepka. Time-independent elastic-plastic behaviour of solder materials. *Microelectronics Reliability*, 44(12):1893–1900, 2004. fatigue.
- [19] S. Wiese and K. J. Wolter. Microstructure and creep behaviour of eutectic SnAg and SnAgCu solders. *Microelectronics Reliability*, 44(12):1923–1931, 2004. ss.
- [20] A. Schubert, R. Dudek, R. Doring, H. Walter, E. Auerswld, A. Gollhardt, B. Schuch, H. Sitzmann, and B. Michel. Lead-free solder interconnects: Characterisation, testing and reliability. In *EuroSimE 2002*, pages 62–72, Paris, 2002. IEEE.
- [21] John H. L. Pang, B. S. Xiong, and T. H. Low. Creep and fatigue characterization of lead free 95.5Sn-3.8Ag-0.7Cu solder. In *ECTC 2004*, pages 1333–1337. IEEE, 2004.

## Bibliography

---

- [22] Z.N. Cheng, G.Z. Wang, L. Chen, J. Wilde, and K. Becker. Viscoplastic anand model for solder alloys and its application. *Soldering and Surface Mount Technology*, 12(2):31–36, 2000.
- [23] V. Stolkarts, L. M. Keer, and M. E. Fine. Damage evolution governed by micro-crack nucleation with application to the fatigue of 63Sn-37Pb solder. *Journal of the Mechanics and Physics of Solids*, 47(12):2451–2468, 1999.
- [24] Do-Seop Kim, Qiang Yu, Tadahiro Shibutani, and Masaki Shiratori. Nonlinear behaviour study on effect of hardening rule of lead free solder joint. In *IPACK 2003*, pages 837–843, Hawaii, 2003. ASME.
- [25] John H. L. Pang, Patrick T. H. Low, and B. S. Xiong. Lead-free 95.5Sn-3.8Ag-0.7Cu solder joint reliability analysis for micro-BGA assembly. In *ITHERM*, pages 131–136, Las Vegas, 2004. IEEE.
- [26] Juan Gomez and Cemal Basaran. Damage mechanics constitutive model for Pb/Sn solder joints incorporating nonlinear kinematic hardening and rate dependent effects using a return mapping integration algorithm. *Mechanics of Materials*, 38:585–598, 2006.
- [27] R. W. Neu, D. T. Scott, and M. W. Woodmansee. Measurement and modeling of back stress at intermediate to high homologous temperatures. *International Journal of Plasticity*, 16(3-4):283–301, 2000.
- [28] Xianjie Yang and Sayed Nassar. Constitutive modeling of time-dependent cyclic straining for solder alloy 63Sn-37Pb. *Mechanics of Materials*, 37(7):801–814, 2005. fatigue.
- [29] D.L. McDowell. A nonlinear kinematic hardening theory for cyclic thermoplasticity and thermoviscoplasticity. *International Journal of Plasticity*, 8:695–728, 1992.
- [30] W. W. Lee, L. T. Nguyen, and G. S. Selvaduray. Solder joint fatigue models: review and applicability to chip scale packages. *Microelectronics Reliability*, 40(2):231–244, 2000.
- [31] H. Akay, H. Zhang, and N. Paydar. Experimental correlations of an energy-based fatigue life prediction method for solder joints. In *International Intersociety Electronic and Photonic Packaging Conference (INTERpack)*, volume 2, pages 1567–1574. ASME, 1997.



## Bibliography

---

- [32] Chandra S. Desai and Russell Whitenack. Review of models and the disturbed state concept for thermomechanical analysis in electronic packaging. *Journal of Electronic Packaging*, 123:19–33, 2001.
- [33] H. B. Ghavifekr and B. Michel. Generalized fracture mechanical integral concept jg and its application in microelectronic packaging technology. *Sensors and Actuators A: Physical*, 99(1-2):183–187, 2002.
- [34] Yu Gu and Toshio Nakamura. Interfacial delamination and fatigue life estimation of 3D solder bumps in flip-chip packages. *Microelectronics Reliability*, 44(3):471–483, 2004.
- [35] Donkai Shangguan. Analysis of crack growth in solder joints. *Soldering & Surface Mount Technology*, 11(3):27–32, 1999.
- [36] Shengmin Wen. Damage based fatigue criterion for solders in electronic packaging. In *ITHERM*, pages 184–191. IEEE, 2004.
- [37] C. Basaran, H. Tang, and S. Nie. Experimental damage mechanics of microelectronic solder joints under fatigue loading. *Mechanics of Materials*, 36(11):1111–1121, 2004.
- [38] Chandra S. Desai, Cemal Basaran, and Wu Zhang. Numerical algorithms and mesh dependence in the disturbed state concept. *International Journal for Numerical Methods in Engineering*, 40:3059–3083, 1997.
- [39] A. Abdul-Baqi, P. J. G. Schreurs, and M. G. D. Geers. Fatigue damage modeling in solder interconnects using a cohesive zone approach. *International Journal of Solids and Structures*, 42(3-4):927–942, 2005.
- [40] Q. D. Yang, D. J. Shim, and S. M. Spearing. A cohesive zone model for low cycle fatigue life prediction of solder joints. *Microelectronic Engineering*, 75(1):85–95, 2004.
- [41] P. Towashiraporn, G. Subbarayan, and C. S. Desai. A hybrid model for computationally efficient fatigue fracture simulations at microelectronic assembly interfaces. *International Journal of Solids and Structures*, 42(15):4468–4483, 2005.
- [42] O. C. Zienkiewicz, R. L. Taylor, and J. Z. Zhu. *The Finite Element Method: Its Basis and Fundamentals*. Butterworth-Heinemann, 2005.

## Bibliography

---

- [43] Klaus-Jürgen Bathe. *Finite Element Procedures*. Prentice Hall, New Jersey, 1996.
- [44] T. A. Davis and W. W. Hager. Modifying a sparse cholesky factorization. *SIAM Journal on Matrix Analysis and Applications*, 20(3):606–627, 1999.
- [45] T. A. Davis and W. W. Hager. Multiple-rank modifications of a sparse cholesky factorization. *SIAM Journal on Matrix Analysis and Applications*, 22(4):997–1013, 2001.
- [46] T. A. Davis and W. W. Hager. Row modifications of a sparse cholesky factorization. *SIAM Journal on Matrix Analysis and Applications*, 26(3):621–639, 2005.
- [47] Jonathan Richard Shewchuk. An introduction to the conjugate gradient method without the agonizing pain. Edition 1 $\frac{1}{4}$  (<http://www.cs.cmu.edu/quake-papers/painless-conjugate-gradient.pdf>). 1994.
- [48] Nicholas I. M. Gould, Yifan Hu, and Jennifer A. Scott. Complete results from a numerical evaluation of sparse direct solvers for the solution of large, sparse, symmetric linear systems of equations. Internal report, Numerical Analysis Group, 2005.
- [49] Hans Petter Langtangen. *Computational Partial Differential Equations*. Springer-Verlag, 2003.
- [50] A. Schubert, R. Dudek, E. Auerswald, A. Gollhardt, B. Michel, and H. Reichl. Fatigue life models of SnAgCu and SnPb solder joints evaluated by experiments and simulations. In *ECTC*, pages 603–610. IEEE, 2003.
- [51] Qiang Xiao, Luu Nguyen, and William D. Armstrong. Aging and creep behaviour of Sn<sub>3.9</sub>Ag<sub>0.6</sub>Cu. In *ECTC 2004*, pages 1325–1332. IEEE, 2004.
- [52] Vanderplaats R&D. *Visual Doc Version 5.0 Theoretical Manual*, 2005.
- [53] F.A. Stam and E. Davitt. Effects of thermomechanical cycling on lead-free (snpb and snagcu) surface mount solder joints. *Microelectronics Reliability*, 41:1815–1822, 2001.
- [54] C. Andersson, D. Anderson, P. E. Tegehall, and J. Liu. Effect of different temperature cycle profiles on the crack propagation and microstructural evolution of real lead free joints of different electronic components. In *EuroSimE*, pages 455–464, Brussels, 2004.



## Bibliography

---

- [55] J. H. Lau, C. Chang, T. Y Lee, S. W. R. amd Cheng, D. Cheng, T.J. Tseng, and D. Lin. Thermal-fatigue life of solder bumped flip chip on micro via-in-pad (VIP) low cost substrates. In *Proc. NEPCON-West 2000*, pages 554–562, Anaheim, CA, 2000.
- [56] M. Dusek, J. Nottay, C. Hunt, H. Lu, and C. Bailey. An experimental validation of modelling for Pb-free solder joint reliability. Technical report, NPL / University of Greenwich, Oct 2001.
- [57] Matweb material property database ([www.matweb.com](http://www.matweb.com)).
- [58] J. Lau. Lead-free wave-soldering and reliability of light-emitting diode (LED) display assemblies. In *IPC First International Conference on Lead-Free Electronics*, Brussels, Belgium, 2003.
- [59] Judith Glazer. Judith glazer, "microstructure and mechanical properties of pb-free solder alloys for low-cost electronic assembly: A review," j. electronic materials 23(8), 693 (1994). *J. Electronic Materials*, 23(8):693, 1994.
- [60] Database for solder properties with emphasis on new lead-free solders (<http://www.boulder.nist.gov/div853/lead%20free/props01.html>).